



The  
University  
Of  
Sheffield.

Department of Electrical and Electronic Engineering  
Communication Research Group

# Wideband Circularly Polarized Layered Dielectric Resonator Antennas for X-band and mm Wave Applications

By

Waled A Mohamed Albakosh

Department of Electronic and Electrical Engineering  
University of Sheffield

A thesis submitted in partial fulfilment of the requirements for the degree of  
Doctor of Philosophy

August 2023

## **The impact of the COVID-19 pandemic**

The unprecedented outbreak of the COVID-19 pandemic has profoundly influenced various sectors, including the academic sphere, and its repercussions have been palpably felt in my research endeavors. My investigation, characterized by both theoretical analysis and experimental validation, encountered significant disruptions owing to the pandemic.

From March 2020 to July 2021, the University enacted a closure of its premises, restricting access to essential personnel only. This decisive measure, while vital for public health, resulted in a substantial interruption to my scholarly work. The inability to access vital resources and conduct experimental procedures led to a consequent delay in the research timeline, extending the completion date by an estimated 12 months.

Moreover, the global impact of the pandemic has resonated economically, manifesting in an escalation of the quotation price for fabrication. This unforeseen inflation not only perturbed our budgetary allocation but necessitated a thorough reassessment and recalibration of the thesis plan.

Despite these formidable challenges, our research team exhibited resilience and adaptability. By critically evaluating our original plan and making necessary adjustments, we were able to realign our research trajectory to not only meet but successfully complete the objectives within the stipulated funded period.

In summary, while the COVID-19 pandemic imposed significant challenges and reshaped the landscape of my research, it also provided a testament to our capacity to adapt and persevere. The lessons learned from this experience will undoubtedly contribute to a more robust and flexible approach to future research undertakings.

## **Acknowledgements**

Undertaking this PhD journey has been an enlightening and transformative process, one that would have been impossible without the support and guidance of numerous individuals and organizations. Foremost, my deepest gratitude goes to my respected supervisor, Dr. Salam Khamas, who has provided determined guidance throughout this academic endeavour. His intellectual rigour, scholarly insights, and unflagging encouragement have been pivotal in the actualization of this thesis. His mentorship has not only driven this research but also enriched my personal and professional growth.

Next, I would like to express my sincere appreciation to Mr. Steven Marsden, whose technical prowess was indispensable during the laboratory experiments. His adept skills and knowledge made an invaluable contribution in manoeuvring the practical intricacies of my research.

Additionally, I am deeply indebted to the Ministry of Higher Education in Libya, whose financial backing has been instrumental in the execution and completion of my study. Their generous support underscored the practical aspects of this research and facilitated its completion. My colleagues in the Communication Group at the University of Sheffield have provided an environment of collegiality and intellectual stimulation, for which I am sincerely grateful. Their camaraderie, encouragement, and shared insights have been a beacon throughout this journey. I also wish to acknowledge my colleagues in the communication group at the University of Sheffield, along with all my relatives and friends. Their camaraderie, support, and motivation have been a source of strength throughout this academic journey.

Lastly, and most importantly, I want to convey my deepest appreciation to my wife. Her unwavering support, resilience, and the immense sacrifices she made in managing our family

while I was immersed in this research cannot be understated. She has been the foundation upon which my academic achievements stand.

In conclusion, the completion of this thesis has been a community effort, and for this, I am forever grateful. The wisdom, assistance, and emotional support I have received from these individuals and institutions have been paramount, shaping both this academic work and my own journey within it.

# Publication

## Journal Articles

1. W. Albakosh, R. Asfour, Y. Khalil, and S. K. Khamas, "Wideband Millimeter-Wave Perforated Hemispherical Dielectric Resonator Antenna," *Electronics*, vol. 13, no. 9, p. 1694, 2024
2. W. Albakosh, R. Asfour, T. S. Abdou, Y. Khalil, and S. K. Khamas, "Wideband Millimeter-Wave Perforated Cylindrical Dielectric Resonator Antenna Configuration," *Magnetism*, vol. 4, no. 1, pp. 73-90, 2024.

## Conference Papers

1. W. Albakosh, A. A. Abdulmajid, and S. Khamas, "Spiral slot-fed High Gain Wide Bandwidth Circularly Polarized Layered Cylindrical DRA," in *2020 International Workshop on Antenna Technology (iWAT)*, 2020, pp. 1-3: IEEE. (chapter 2)
2. W. Albakosh, R. Asfour, and S. Khamas, " Wideband Millimetre-Wave Layered Cylindrical Dielectric Resonator Antenna' to the AP-S/URSI 2024 accepted , Paper ID: 1487
3. W. Albakosh, R. Asfour, and S. Khamas, " 60 GHz Wideband Circularly Polarized Layered Hemispherical DRA" to the AP-S/URSI 2024 accepted, Paper ID: 1484
4. R. Asfour, W. Albakosh, and S. Khamas, Edward A Ball, " A Low-Profile Fully Planar Loop Antenna for Polarization Reconfigurability " to the AP-S/URSI 2024 accepted , Paper ID: 1482
5. W. Albakosh ,R. Asfour, and S. Khamas "Measurements of Slot-Fed Circularly Polarized Layered Cylindrical DRA for X-Band Applications" to ATOMS 2024 online submission system, Paper ID: 1487

## **List of Abbreviations**

<b>DRA</b>	<b>Dielectric Resonator Antenna</b>
<b>CDRA</b>	<b>Cylindrical Dielectric Resonator Antennas</b>
<b>TM</b>	<b>Transverse Magnetic</b>
<b>TE</b>	<b>Transverse Electric</b>
<b>HE</b>	<b>Hybrid Electric</b>
<b>HM</b>	<b>Hybrid Magnetic</b>
<b>HEM</b>	<b>Hybrid Electromagnetic</b>
<b>EHF</b>	<b>Extremely High Frequency</b>
<b>RDRA</b>	<b>Rectangular Dielectric Resonator Antennas</b>
<b>HDRA</b>	<b>Hemispherical Dielectric Resonator Antennas</b>
<b>ISM</b>	<b>Industrial Scientifically and Medical</b>
<b>CPW</b>	<b>Coplanar Wave guide</b>
<b>CP</b>	<b>Circularly Polarized</b>
<b>FSS</b>	<b>Frequency Selective Surfaces</b>
<b>IPD</b>	<b>Integrated Passive Device</b>
<b>AR</b>	<b>Axial Ratios</b>
<b>FDM</b>	<b>Fused Deposition Modeling</b>

## **Abstract**

Dielectric resonator antennas (DRAs) are emerging as promising contenders for the forthcoming generation of wireless communication systems due to their capability to deliver expanded bandwidth and increased radiation efficiency. Furthermore, achieving higher gain is feasible by stimulating a higher-order resonance mode, aligning with the demands of high-frequency applications. This thesis provides a comprehensive exploration into the performance optimization of dielectric resonator antennas (DRAs) that are indispensable for high-frequency communication applications like satellite communication, radar systems, and 5G networks. Several methodologies have been explored to augment the gain of dielectric resonator antennas (DRAs), including the utilization of higher-order mode operation in standalone DRAs, integration of dielectric superstrates, and the deployment of DRA arrays. Each of these design strategies is accompanied by inherent limitations, such as narrower impedance bandwidth, impractical dimensional requirements, significant sensitivity to fabrication discrepancies, and the necessity for intricate and lossy feed networks in the case of arrays. Conversely, existing literature primarily focuses on multi-layer DRAs solely for the enhancement of impedance bandwidth. This study attempts to expand the potential of integrating a dielectric coat layer to not only amplify gain and axial ratio but also improve impedance bandwidth. The study investigates the performance shortcomings of traditional single-layer DRAs, particularly in achieving the desired bandwidth and gain. To overcome these limitations, the research delves into the impact of additional dielectric layers and alterations in dielectric constants on the DRA's performance parameters. Moreover, it introduces an alternative approach to prevailing methodologies, which predominantly hinge on either single-mode operation with diminished gain or higher-order mode operation marked by restricted bandwidth and considerable vulnerability to fabrication tolerances.

In a significant finding, a circularly polarized two-layer cylindrical DRA exhibited substantial enhancements, with impedance and axial ratio bandwidths improving to 45% and 18%, respectively. The gain was also amplified to 12.5 dBic, signifying its utility for X-band applications.

Furthermore, the research explores the potential of millimetre-wave layered cylindrical DRAs, focusing on their circular polarization. The proposed design provided promising results, achieving an 88% impedance bandwidth, Axial Ratio bandwidth 23.3% and a 12.29 dBic gain, solidifying its efficacy for 5G applications.

A novel assembly technique was also explored, leveraging a 3D printer to combine two dielectric layers, subsequently eradicating the possibility of air gaps. This approach showed potential, particularly in the performance of circularly polarized perforated cylindrical DRAs in the millimetre-wave band. In addition, a circularly polarized perforated hemispherical DRA (HDRA) was developed and tested at millimetre-wave frequencies, exhibiting improvements in performance metrics

Finally, the research culminates in the development of a two-layer hemispherical DRA designed specifically for millimeter-wave applications operating at 60 GHz. When compared to a single-layer configuration, this novel design exhibited a broader impedance bandwidth of 52.3%, an axial ratio of 10.18%, and a higher gain of 7.6 dBic.

Despite some discrepancies between the simulated and measured results, primarily due to technical constraints, this research has underscored the potential of novel DRA designs in improving performance parameters. The study thus significantly contributes to the broader discourse on antenna technology, offering a platform for further investigation in this domain.

# Table of Contents

The impact of the COVID-19 pandemic.....	i
Acknowledgements.....	ii
Publication .....	iv
List of Abbreviations .....	v
Abstract.....	vi
List of figures.....	xi
List of table .....	xvi
Chapter1 Introduction and Literature Review .....	1
1.1 Introduction:.....	1
1.2 DRAs and Millimetre Wave Communications .....	3
1.3 DRA Gain-enhancement Methods .....	6
1.3.1 Fundamental Mode Excitation.....	6
1.3.2 Higher-order Mode Excitation.....	7
1.4 Circularly Polarized DRAs.....	9
1.5 Multi-layered DRAs .....	12
1.6 3D printing Technology .....	14
1.7 Research problem:.....	15
1.8 Research Objectives: .....	15
1.9 The Structure of the thesis.....	16
Chapter2 Layered Cylindrical DRA for X-band Applications .....	19
2.1 Introduction:.....	19
2.2 Cylindrical DRA modes .....	22
2.3 Design and simulation DRAs.....	23
2.3.1 Concept design from CST simulations.....	23
2.3.2 Antenna Configuration .....	24
2.3.3 Parametric Studies .....	25

2.4 Fabrication and measurements .....	38
2.4.1 Configuration of a single layer circularly polarized CDRA.....	39
2.4.2 A layered circularly polarized CDRA .....	43
2.5 Conclusions .....	47
Chapter3 High Gain Wide-Band Millimetre Wave Cylindrical DRA.....	48
3.1 Introduction .....	48
3.2 Aperture coupling.....	49
3.3 Antenna configuration.....	51
3.3.1 Parametric Studies .....	52
3.4 Experimental Results.....	64
3.5 Conclusion.....	70
Chapter4 High Gain Wide-Band Millimetre Wave Perforated Cylindrical DRA .....	71
4.1 Introduction: .....	71
4.2 Antenna Configuration.....	72
4.2.1 Equivalent Single Layer DRA with Perforated Outer Layer.....	72
4.2.2 Parameter study .....	74
4.3 Experimental Results.....	79
4.4 Conclusion.....	85
Chapter5 Wide-Band Layered Millimetre Wave Hemispherical DRA .....	87
5.1 Introduction: .....	87
5.2 Antenna Configuration.....	91
5.2.1 Layered HDRA.....	91
5.2.2 Parametric Study.....	100
5.2.3 Experimental Results .....	106
5.3 Hemispherical DRA with a perforated Alumina coat .....	112
5.3.1 Antenna conflagration .....	113
5.3.2 Experimental Results.....	118

5.4 Conclusions .....	123
Chapter6 60 GHz Wide-Band Axial Ratio Hemispherical DRA fed by a Coplanar Waveguide .....	125
6.1 Introduction .....	125
6.2 Antenna Configuration.....	127
6.2.1 Experimental study of the layered 60 GHz HDRA .....	137
6.3 Conclusion.....	142
Chapter7 Conclusion and future work .....	144
7.1 Conclusion.....	144
7.2 Future work .....	146
References.....	149

## List of figures

Figure 1.1: Dielectric resonator antennas of various of shapes. ....	1
Figure 1.2 Using short magnetic dipoles to represent the magnetic field inside a rectangular DRA; (a) $TE_{115}$ (b) $TE_{119}$ .....	7
Figure 2.1: The configuration of the proposed layered CDRA. ....	24
Figure 2.2: Geometry of a single-arm spiral slot. ....	25
Figure 2.3: Simulated $ S_{11} $ with various slot widths.....	26
Figure 2.4: Simulated axial ratio with various slot widths. ....	27
Figure 2.5: Simulated Gain with various slot widths.....	27
Figure 2.6: Simulated $ S_{11} $ with various values of $g$ .....	28
Figure 2.7: Simulated axial ratio with various values of $g$ . ....	29
Figure 2.8: Simulated Gain with various values of $g$ .....	29
Figure 2.9: Simulated $ S_{11} $ for various values of $\phi_{max}$ . ....	30
Figure 2.10: Simulated AR for various values of $\phi_{max}$ . ....	31
Figure 2.11: Simulated Gain for various values of $\phi_{max}$ . ....	31
Figure 2.12: Simulated $ S_{11} $ for various values of the outer layer radius ( $a_2$ ). ....	34
Figure 2.13: Simulated AR for various values of the outer layer radius ( $a_2$ ). ....	34
Figure 2.14: Simulated Gain for various values of the outer layer radius ( $a_2$ ).....	35
Figure 2.15: The strength of the E-field inside and outside the layered CDRA.....	35
Figure 2.16: Maximum bandwidth versus outer layer thickness. ....	36
Figure 2.17: The E- and H-fields distributions inside circularly polarized single-layer and multilayer cylindrical DRA.....	36
Figure 2.18: (a) The cylindrical DRA and outer dielectric coat. (b) Feed network.....	39
Figure 2.19: Simulated and measured reflection coefficient of a CDRA without coating .....	40
Figure 2.20: Simulated and measured gain of a CDRA without coating.....	41
Figure 2.21: The axial ratio of a single layer DRA.....	41

Figure 2.22: Simulated and measured radiation patterns when $\epsilon_{r2}= 1$ at 11 GHz (a) $\phi=0^\circ$ , (b) $\phi=90^\circ$ .....	42
Figure 2.23: Simulated and measured reflection coefficients of layered CDRA. ....	44
Figure 2.24: The simulated and measured CP bandwidths of a layered CDRA.....	44
Figure 2.25: Simulated and measured radiation patterns when $\epsilon_{r2}= 3.5$ at 11 GHz (a) $\phi=0^\circ$ , (b) $\phi=90^\circ$ .....	45
Figure 2.26: Simulated and measured gain of a CDRA with coating.....	46
Figure.3.1: The slot-cross feed.....	50
Figure 3.2: The configuration of the proposed layered CDRA .....	52
Figure 3.3: Simulated $ S_{11} $ with various outer layer permittivity $\epsilon_{r2}= 1, 2, 3.5, 6$ and $10$ .....	54
Figure 3.4: Simulated realized gain with various outer layer permittivity of $\epsilon_{r2}= 1, 2, 3.5, 6$ and $10$ .....	55
Figure 3.5: Simulated axial ratio with various outer layer permittivity of $\epsilon_{r2}= 1, 2, 3.5, 6$ and $10$ .....	55
Figure 3.6: Simulated $ S_{11} $ with various slot arm length. ....	57
Figure 3.7: Simulated axial ratio with various slot arm length.....	57
Figure 3.8: Maximum bandwidth as function of the slot arm length.....	58
Figure 3.9: Simulated $ S_{11} $ with various outer layer thicknesses.....	60
Figure 3.10: Simulated axial ratio with various outer layer thicknesses .....	60
Figure 3.11: Simulated realized gain with various outer layer thicknesses.....	61
Figure 3.12: Distributions of the E-field and the H-field of circularly polarized cylindrical DRAs of higher order.....	64
Figure 3.13: The prototype of a layered CDRA (a) Feed network with highlighted layered CDRA position, (b) The inner and the outer layered of CDRA, c) Layered CDRA connects to the chamber.....	65
Figure 3.14: The simulated and measured reflection coefficient of layered CDRA. ....	66
Figure 3.15: Simulated and measured of the gain of a HDRA with coating. ....	67
Figure 3.16: The simulated and measured CP bandwidth of layered CDRA .....	68

Figure 3.17: Simulated and measured radiation pattern at 29 GHz (a) $\phi=90^0$ , (b) $\phi=0^0$ .....	69
Figure 4.1: Cylindrical DRA with a perforated dielectric coat.....	73
Figure 4.2: The configuration of the Cylindrical DRA with a perforated dielectric coat.....	74
Figure 4.3: Perforated cylindrical layer effective permittivity as a function of $t_c$ .....	76
Figure 4.4: Simulated $ S_{11} $ for cylindrical DRA with a perforated coat layer with various of $t_c$ .....	77
Figure 4.5: Axial Ratio simulated for cylindrical DRA with a perforated coat layer with various of $t_c$ .....	77
Figure 4.6: Gain simulated for perforated cylindrical DRA with a perforated coat layer with various of $t_c$ .....	78
Figure 4.7: Maximum bandwidth as function of the wall thicknesses $t_c$ .....	78
Figure 4.8: E-field and the H-field distributions inside the DRA with a perforated cylindrical coat layer .....	79
Figure 4.9: The prototype of a CDRA with perforated coat layer (a) Feed network with outlined DRA position, (b) The DRA model, c) The CDRA placed inside the chamber.....	80
Figure 4.10: The simulated and measured reflection coefficient of the perforated antenna configuration. ....	81
Figure 4.11: Simulated and measured of the gain of the perforated antenna. ....	82
Figure 4.12: The simulated and measured CP bandwidth of perforated antenna. ....	83
Figure 4.13: Simulated and measured radiation pattern at 29 GHz (a) $\phi=0^0$ , (b) $\phi=90^0$ .....	84
Figure 5.1: Hemispherical DRA. ....	87
Figure 5.2: The configuration of the proposed layered HDRA .....	92
Figure 5.3: Geometry of a single-arm spiral slot. ....	93
Figure 5.4: Simulated $ S_{11} $ , axial ratio and gain of the single layered HDRA.....	94
Figure 5.5: Radiation pattern of (a) $TE_{112}$ at 25.1GHz, (b) $TE_{511}$ at 30.8GHz for a single layer HDRA. ....	95
Figure 5.6: Simulated $ S_{11} $ with various thicknesses of the outer layer. ....	98
Figure 5.7: Simulated axial ratio with various thicknesses of the outer layer. ....	98

Figure 5.8: Simulated gain with various thicknesses of the outer layer. ....	99
Figure 5.9: Maximum bandwidth as function of the outer layer thickness .....	99
Figure 5.10: Simulated $ S_{11} $ with various slot widths ( $w_s$ ). ....	101
Figure 5.11: Simulated axial ratio with various slot widths ( $w_s$ ). ....	101
Figure 5.12: Simulated gain with various slot widths ( $w_s$ ). ....	102
Figure 5.13: Simulated $ S_{11} $ for various maximum rotation angles ( $\phi_{max}$ ). ....	103
Figure 5.14: Simulated axial ratio for various maximum rotation angles ( $\phi_{max}$ ). ....	103
Figure 5.15: Simulated gain for various maximum rotation angles ( $\phi_{max}$ ). ....	104
Figure 5.16: Simulated $ S_{11} $ with various values of $g$ . ....	105
Figure 5.17: Simulated axial ratio with various values of $g$ . ....	105
Figure 5.18: Simulated gain with various values of $g$ . ....	106
Figure 5.19: Prototype of the multi-layer hemispherical DRA. ....	107
Figure 5.20: The simulated and measured reflection coefficient of layered HDRA. ....	108
Figure 5.21: The simulated and measured axial ratio of a layered HDRA. ....	108
Figure 5.22: Simulated and measured of the radiation patterns of a layered HDRA at 22 GHz, (a) $\phi=0^\circ$ , (b) $\phi=90^\circ$ . ....	110
Figure 5.23: Simulated and measured of the radiation patterns of a layered HDRA at 29 GHz, (a) $\phi=0^\circ$ , (b) $\phi=90^\circ$ . ....	111
Figure 5.24: Simulated and measured gain of a layered HDRA. ....	112
Figure 5.25: Hemispherical Alumina DRA with a perforated Alumina dielectric coat .....	113
Figure 5.26: The configuration of the Hemispherical DRA with a perforated dielectric coat .....	114
Figure 5.27: Simulated $ S_{11} $ with various unit cell's wall thicknesses ( $t_c$ ) for the perforated coat. ....	116
Figure 5.28: Simulated Axial Ratio with various wall thickness ( $t_c$ ). ....	116
Figure 5.29: Simulated gain with various wall thickness ( $t_c$ ). ....	117

Figure 5.30: The simulated reflection coefficient of solid layered HDRA and a perforated dielectric coat HDRA.....	118
Figure 5.32: The simulated and measured reflection coefficient of an HDRA with a perforated dielectric coat.....	119
Figure 5.31: The prototype of the proposed hemispherical DRA with a perforated dielectric coat.....	119
Figure 5.33: The simulated and measured CP bandwidth of an HDRA with a perforated dielectric coat.....	120
Figure 5.34: Simulated and measured gain of an HDRA with a perforated dielectric coat. .	121
Figure 5.35: Simulated and measured radiation patterns of an HDRA with a perforated dielectric coat at 28 GHz; (a) $\phi=0^0$ , (b) $\phi=90^0$ .....	122
Figure 6.1: The configuration of the CPW-fed hemispherical DRA.....	128
Figure 6.2: Geometry of a two-arm spiral slots fed by CPW. ....	129
Figure 6.4: Simulated $ S_{11} $ , axial ratio and gain of the single layered HDRA.....	132
Figure 6.3: a) Radiation pattern of $TE_{112}$ at 45 GHz, b) Radiation pattern of $TE_{511}$ at 61GHz for a single layer HDRA .....	132
Figure 6.6: Simulated axial ratio with various radii of the outer layer.....	135
Figure 6.5: Simulated $ S_{11} $ with various radii of the outer layer.....	135
Figure 6.8: Maximum bandwidth as function of the outer layer thickness .....	136
Figure 6.7: Simulated gain with various radii of the outer layer. ....	136
Figure 6.9: (a) The prototype of a HDRA with feed network with outlined DRA position, (b) The DRA model placed inside the probe Station. (c) A screen grab of the pitch GSG probe connected to the CPW transmission line .....	139
Figure 6.10: The simulated and measured reflection coefficient of HDRA with dielectric coat .....	140
Figure 6.11: Simulated and measured of the radiation patterns of a layered HDRA at 61 GHz, (a) $\phi=90^0$ , (b) $\phi=0^0$ .....	141

## List of table

Table 1-1: Fundamental modes of various DRAs.....	3
Table 2-1: The impacts of different outer layer thicknesses $\delta a$ . ....	33
Table 2-2: Comparison between the proposed CP CDRA and previously reported designs...	46
Table 3-1: Optimum parameters of the coat layer .....	54
Table 3-2: Effect of fabrication errors on the layered CDRA's resonance frequency. ....	59
Table 3-3: Comparison between the proposed CP CDRA and previously reported designs...	70
Table 4-1: Proposed antenna performance compared to previously reported designs. ....	85
Table 5-1: The impact of different outer layer thicknesses $\delta a$ . ....	97
Table 5-2: The several of Resonance frequency TE for the layered HDRA .....	97
Table 5-3: Proposed antenna performance compared to previously reported designs. ....	123
Table 6-1: Parameters for the proposer design of the CPW slot feed.....	130
Table 6-2: The impact of different outer layer thicknesses $\delta a$ . ....	133
Table 6-3: Proposed antenna performance compared to previously reported designs. ....	142

# Chapter1 Introduction and Literature Review

## 1.1 Introduction:

Significant research attention has been devoted to dielectric resonator antenna (DRA) since its conceptualisation as a material with a high Q-factor has been demonstrated in 1939[1]. Practical applications were scarce until its utilisation as an electromagnetic radiator in 1983[2]. Subsequently, DRA has received a considerable research interest due to attractive features such as low ohmic losses, high efficiency, great power capacity, wide bandwidth and design flexibility, where the DR could be of any 3D-shape hemispherical, cylindrical, rectangular box, triangular, etc. as illustrated in Figure 1.1. The latter is dependent on the controlling parameters of fundamental shapes, such the length, or width, to height ratio of a rectangular DRAs, the height to radius ratio in a cylindrical DRAs and the radius of the hemispherical DRAs [3] .

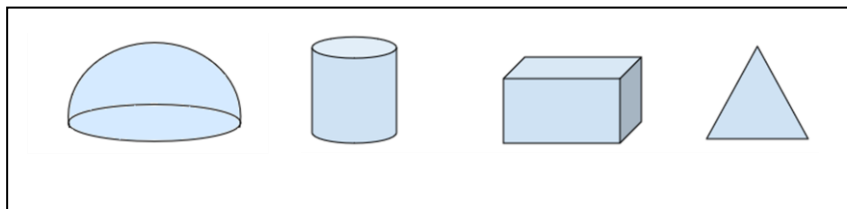


Figure 1.1: Dielectric resonator antennas of several of shapes.

Dielectric resonators (DRs) can act as effective radiators by using materials with lower dielectric properties and the removal of the metallic shield, if applicable, which has been popularised by numerous theoretical and empirical investigations exploring rectangular, hemispherical, and cylindrical DRA applications during the 1980s [4]. Furthermore, DRAs offer wide impedance bandwidths compared to microstrip antennas. This can be achieved by constructing the antennas from a material with a dielectric constant,  $\epsilon_r$ , of  $\sim 10$  [5].

This can be attributed to the fact that microstrip antenna radiates only through two narrow radiation slots. However, the DRA radiates through the whole antenna surfaces excluding the grounded part. Subsequently, DRAs have been intensively researched and applied, with cylindrical DRAs emerging as the most common geometry due to the relatively lower fabrication cost [6]. On the other hand, practical, i.e. industrial, applications of DRAs have generally lagged behind theoretical insights and there continue to be a theory-practice gap with real applications only realistically emerging since the beginning of this century. This reflects the market interests and supporting ancillary technologies associated with specific frequencies particularly at millimetre waves [7].

The emergence of millimetre wave technologies has enabled the exploration of DR radiator potential as a promising solution to address the low efficiency of metal radiators at higher frequencies. In addition, radio and microwave frequencies applications have increasingly adopted DR elements due to performance advantages in terms of bandwidth and design characteristics such as 3D flexibility and lightweight construction, low cost, variable Q-factor due to the inverse proportionality with a dielectric constant of the DR, and ease of excitation [2].

It should be noted that the DRA side and top surfaces are transparent to radio waves, thus the excitation of the resonator at the required resonating mode facilitates the penetration of the DRA surface by radio waves, which is then radiated into space. Electromagnetic field distributions within the resonator are instrumental in the excitation of a particular resonance mode, which is also affected by the chosen feed mechanism and the dielectric resonator's dimensions. The main resonance modes are mainly divided into transverse magnetic (TM), transverse electric (TE), and hybrid electromagnetic (HEM) where the hybrid modes can be further subdivided into two groups: HE and EH. For HE modes, the  $H_z$  component is considerably smaller compared to the  $E_z$  component. The other field components for HE modes

can thus be derived from a knowledge of the  $E_z$  component only. The reverse is true for EH modes [3]. The fundamental modes for these types for different DRA shapes are listed in Table 1-1 [8]:

Table 1-1: Fundamental modes of various DRAs

DRA Shaped	Modes
Rectangular	$TE_{111}^x, TE_{111}^y, TE_{111}^z$
Cylindrical	$TM_{01}, TE_{01}, HE_{11}/EH_{11}$
Hemispherical	$TM_{101}, TE_{111}$

## 1.2 DRAs and Millimetre Wave Communications

It is well-known that millimetre wavelengths are shorter than radio/microwaves and longer than infrared counterparts as they range from 1 to 10 mm. This band is also referred to as the extremely high frequency (EHF) range, which extends from 30 to 300 GHz [9]. Working in this frequency range offer advantages such as wide bandwidth that allows a high data rate, feasible compact systems with high-resolution, which enables the design of high directivity using an antenna with a reasonable size. In addition, mm Wave signals can permeate through dust, fog as well as snow, which is not possible with infrared and optical signals [10]. However, several factors need to be taken into account for certain applications such as absorption through the atmospheric gases and rain, which represents the predominant impact in the mm Wave range.

DRAs have been utilized successfully in the mmWave frequency band relying on the well-known desirable DRA properties of low losses at high frequency, making it as an effective

radiator [11-20]. For instance, on-chip high gain cylindrical DRA have been designed at 59.96 GHz with a gain of 3.2 dBi and impedance bandwidth that extends from 59 to 60.74 GHz in the  $HE_{11\delta}$  resonance mode [11]. On the other hand, E-shaped slot has been deployed for a coplanar wave guide (CPW) fed T-shaped that provided a 5.8 to 6.6 dBi gain in conjunction with an impedance bandwidth of 21% over a frequency range of 41.1 to 49.5 GHz [12]. An enhanced bandwidth of 27% has been achieved over a frequency range of 23.7 to 30.7 GHz for a slot coupled low permittivity DRA operating in the  $TE_{111}$  mode [13]. Such a wide band has been achieved by reducing the DRA dielectric constant whilst a significant coupling has been realised by optimizing the slot size and position. A low-cost high-gain hybrid DRA have been reported in the 57 to 65 GHz frequency band with impedance bandwidth and measured gain of  $\sim 15\%$  and 11.9 dBi, respectively, when the DRA is operating in the hybrid  $HEM_{15\delta}$  mode [14].

In an alternative study, a radiation efficiency of more than 95% has been achieved for RDRA using a low-cost and compact substrate integrated waveguide (SIW) with gain and impedance bandwidth of 5.51 dBi and 8.60%, respectively, when the RDRA is operating in the  $TE_{111}$  resonance mode [15]. A hybrid DRA with a superstrate has been proposed at the ISM frequency range of 57 to 65 GHz with a high gain of more than 11 dBi and an impedance bandwidth of  $\sim 18.4\%$  [16]. It should be noted that a considerable bandwidth enhancement can be achieved by changing the DRA composite materials. It should be noted that by changing DRA materials a considerable bandwidth enhancement can be achieved. As an example, a polymer-based antenna offers bandwidth enhancement by a factor of 3.5 compared to a traditional ceramic DRA that inherent hardness, which proffers difficulty to fabricate in small dimensions such as those required in the millimetre wave frequency band. A polymer rectangular DRA with  $\epsilon_r = 4$  has been designed at 26 GHz, where the  $TE_{111}$  mode was excited using a slot to improve impedance bandwidth from 8.4 to 27.7% in conjunction with a gain of  $\sim 6$  dBi [17]. Additionally, a CPW-fed stacked two rectangular DRAs targeting the Industrial,

Scientifically and Medical radio bands (ISM) frequency band was demonstrated with an impedance bandwidth of 24% that extends over the frequency range of 54.51GHz -69.73 GHz [18]. In addition, a hybrid CDRA fed by micro strip and multiple metallic strips stacked to a superstrate achieved a high gain of 15.4dBi and a 12.69% impedance bandwidth at 59.55 GHz [19]. In another study, RDRA has been fed with a T-slot-stub CPW feedline to excite the  $TE_{111}$  resonance mode with a bandwidth of 3.3% and gain of ~5dBi at 63.7GHz [20].

There has been increasing demands for applications at higher frequencies that offer much wider bandwidths with more continuous and less restricted bandwidth ability, in particular the 60 GHz band [21]. This frequency band has immense possibilities for improved flexibility and greater capacity for current and future communication systems' high data rate requirements [22]. Current regulations allow 60 GHz high transmission power as compared to other less frequency bands, which helps to overcome the problems faced due to untenable power losses associated with rain and oxygen. The network range at 60 GHz is limited to confined areas, enabling increased reuse of frequency, thus increasing the network throughput [21].

A CPW fed rectangular DRA fabricated by utilizing micromachining technology has been reported for the 54 GHz to 71.5 GHz frequency range with a wide bandwidth of 29.2% and a gain of 3.6 dBi at 60 GHz [23]. Subsequently, a circularly polarized (CP) CDRA with an axial ratio bandwidth of 4% has been reported with an impedance bandwidth of 24.2% that has been utilised with half-mode substrate integrated waveguide (HMSIW) as feed for the CDRA [24]. A 60 GHz system with enhanced gain has been demonstrated by exciting higher-order modes of a rectangular DRA, where a gain of ~10 dBi has been achieved with a bandwidth of 18% when the  $TE_{\delta 15}$  resonance mode has been excited [25]. In addition, a CPW fed CDRA has been proposed to achieve a ~10.7% bandwidth and 5.4 dBi gain at an operating frequency of 60 GHz [26]. This has been followed by proposing a cylindrical DRA fed by a microstrip line with a 5.4 dBi gain and impedance bandwidth of 7.9% bandwidth using a hollow cylindrical

conformal ground plane where the hybrid  $HE_{11\delta}$  mode has been excited inside the DR [27]. A trans-receiver silicon-integrated DRA with a CPW fed slot has been reported with a gain of up to 5 dBi and an impedance bandwidth of 5.5 GHz over the frequency range of 55.5GHz -61 GHz for the  $HEM_{11}$  resonance mode operation[28].

### 1.3 DRA Gain-enhancement Methods

The fundamental DRA mode ( $TE_{111}^y$ ) was formerly the benchmark in the majority of reported studies, where a broadside DRA radiation results in a lower directivity that is comparable to that of an  $y$  or  $x$  directed short magnetic dipole to excite the  $TE_{111}^y$  or  $TE_{111}^x$ , modes respectively. However, higher gain is one of the key requirements at high frequency communication systems. Therefore, a number of approaches have been employed to enhance the gain as listed below;

#### 1.3.1 Fundamental Mode Excitation

The DRA gain can be enhanced in numerous ways when excited in the fundamental mode by employing various approaches such as stacking to enlarge the bandwidth that can also improve the gain marginally and can be modified to increase both gain or bandwidth or only one of them [29]. On the other hand, employing a metal cavity can also improve the gain. For example, a rectangular DRA gain has been increased to  $\sim 10$  dBi using a  $1.2\lambda_0$  square aperture in a shallow pyramidal horn of 0.15 times the height of the  $\lambda_0$  as reported in[30].

In addition, the incorporation of a superstrate on top of the DRA provides a considerably higher gain of  $\sim 16$  dBi when a  $3.2\lambda$  square superstrate is utilized with a thickness of 0.85 mm and a dielectric constant of 25[31]. All of these techniques are associated with the necessity of a substantive enlargement of weight and size, which is unsuitable for hand-held mm-wave devices.

### 1.3.2 Higher-order Mode Excitation

It is widely recognized that as the operating frequency rises, the size of the required DRA correspondingly reduces to excite a particular resonance mode. As an instance, a rectangular DRA with specific respective length, width, and height of 5mm, 5mm, and 30mm at 10GHz will significantly contract to respective measurements of 1mm, 1mm, and 5mm at 60GHz operations[25, 32]. This underscores the fact that precision in DRA fabrication becomes indispensable as we venture into higher frequencies. Conversely, expanding the dimensions of a DRA fosters higher order operations at these increased frequencies. Recent research has explored the triggering of these higher order modes by adjusting the height of the RDRA to approximately  $\lambda_0/3$ ,  $\lambda_0/2$ , and  $\lambda_0$ , with the intention of exciting the  $TE_{111}$ ,  $TE_{115}$ , and  $TE_{119}$  modes, for an enhanced gain [33, 34].

Excitation of higher-order resonance modes represents a popular approach to enhance the DRA gain. For example a slot-fed rectangular has been utilised at 10.6 GHz to provide a gain of 11dBi by exciting the  $TE_{\delta 15}$  higher order mode [32]. The gain enhancement has been explained by using short magnetic dipole to represent the magnetic field inside the DRA as illustrated in Figure 1.2[33]. Combining this representation with a straightforward array theory demonstrate that the maximum gain can be achieved when the separation distance between adjacent magnetic dipoles is  $\sim 0.4\lambda_0$ .

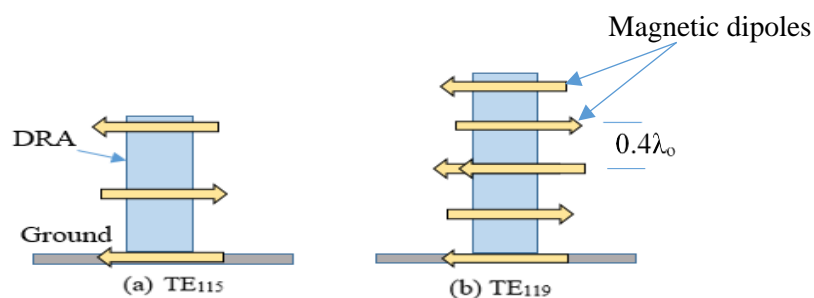


Figure 1.2 Using short magnetic dipoles to represent the magnetic field inside a rectangular DRA; (a)  $TE_{115}$   
(b)  $TE_{119}$

Single cylindrical and rectangular DRAs have been tested with higher-order mode operation. For instances, higher order modes rectangular DRA has been reported with respective gains of 8.2 and 10.2 dBi for the  $TE_{\delta 13}$  and  $TE_{\delta 15}$  modes, respectively[33]. A larger DRA with a relative permittivity  $\epsilon_r=10$  and supports the  $TE_{115}$  mode, requires approximately  $1.1\lambda_o$  as a larger dimension for DRA, where  $\lambda_o$  is the free-space wavelength. For cylindrical DRA, the higher-order mode  $HEM_{118}$  has been excited by introducing an air-filled cavity into the ground plane underneath the resonator, with a 9.5 dBi gain, albeit within an impedance bandwidth of  $\sim 7.5\%$  [35]. For another cylindrical dielectric resonator, higher-order modes operation yielded a higher gain of  $\sim 11.59$  dBi, with an impedance bandwidth that covers the ISM band of 5.8 GHz, but the broadside direction gain was less than 8 dBi due to the increased E-plane side lobe levels[36].

A metal covered cylindrical DRA has been designed with an intermediate layer in order to increase the bandwidth to 23% and gain to 11 dBi, where a strip line fed slot has been employed to excite the  $HEM_{118}$  resonance mode[37]. Furthermore, stacked CDRA variants of different sizes and permittivity have been tested with a metallic cylinder forming a cavity with a 26% impedance bandwidth that extends from 5.4 to 7.0 GHz and yielded a larger gain of 11 dBi when operating in the  $HEM_{118}$  resonance mode has [38]. A lower profile, wideband, high gain RDRA has been proposed including a centrally-fed rectangular slot for two dielectric layers of different permittivity, achieving an average gain of 9 dBi and an impedance bandwidth of 40% that covers the 3.97 to 5.98 GHz frequency range, where the  $TE_{111}$  and  $TE_{131}$  modes have been excited [39].

The DRA operation in the ISM frequency band of 57 to 65 GHz has been explored with an impedance bandwidth of more than 20% with a subterranean communications gain of 18.6 dBi that has been achieved by employing a stacked pyramid DRA with a superstrate that includes

a frequency selective surfaces (FSS) that consists of metallic strips stocked on the bottom side of the superstrate [40]. In another study, a cylindrical DRA has been tested with a periodic square ring FSS superstrate with an intermediate substrate and aperture coupled feed covering the ISM frequency band, resulting in a 14.36% bandwidth at 60 GHz , where the addition of the intermediate substrate yielded a 10 dBi gain enhancement resulting in an overall gain of 15.56 dBi [41].

## **1.4 Circularly Polarized DRAs**

Wireless communications systems have been revolutionized in the last two decades with the sudden proliferation of wireless applications. Therefore high radiation efficiency and wideband operations are required from circularly polarized (CP) antennae to meet user demands. CP antennae achieve improved connectivity between receiving and transmitting ends because the CP waves are unaffected by ionosphere Faraday rotations, enabling alignment flexibility in receiving and transmitting antennae signals, rendering CP waves particularly germane to space communications [42].

Linear, elliptical and circular antenna's polarization entails divergent far-field radiations. Circular polarization is a special case of the elliptical polarization [43], which can be facilitated in a DRA with the excitation of two quasi-degenerate modes, usually in phase quadrature, and spatially orthogonal to each other. Numerous feeding configurations facilitate this functionality including multiple or single feed points. In the latter, the geometric configuration of the resonator plays a paramount role in facilitating the emergence of spatially orthogonal modes. Concurrently, independent of the dielectric resonator, the feeding network is capable of engendering such modes via a multipoint feed. This flexibility intrinsic to the Dielectric Resonator Antenna (DRA) facilitates the radiation of a circularly polarized field, exhibiting a

broader axial ratio bandwidth when juxtaposed against its metallic counterparts[44]. Feeding mechanism or antenna geometry can be perturbed to induce circularly polarized waves, alongside certain radiating modes' excitation in some instances.

Adjustment of the feeding network to achieve circular polarization can be implemented by single-, or multi-, feeding points. The former entails less space and a simpler configuration, enabling 90° phase difference excitation with some feeding arrangements, such as single parasitic patch, 45° inclined feed and Helix conductor [45].

For example, a single feed system has been proposed over a frequency range of 14.35 to 14.80 GHz, where a rectangular DRA with a single aperture feed, which was tilted by 45°, has been employed, achieving a 3% CP bandwidth at 14.75 GHz [46]. Circular polarisation in the case of dual conformal strip fed cylindrical shaped DRA has been proposed, yielding an AR bandwidth of 20% [47]. Subsequently, a cylindrical DRA fed by a simplified microstrip line, with reduced back lobe radiation, by using two vertical stripes on the resonator surface to obtain the circular polarization, which offered up to 2.2% bandwidth [48]. A later study has departed from the earlier methods of [48] and deployed two strips of unequal length on a cylindrical resonator's surface, with no quadrature power dividers, resulting in the generation of two orthogonal modes and circular polarization bandwidth of 3.5% combined with an impedance bandwidth and gain of 15.8% and 4.9 dBi, respectively [49].

A rectangular DRA has provided CP bandwidth of 10.6% combined with an impedance bandwidth of 36.6% [50]. A coaxial fed hexagonal DRA has been reported with CP bandwidth of 14.84% in conjunction with impedance bandwidth 14.6 % [51]. An elliptical DRA fed by microstrip line has offered a CP bandwidth of 4.2% with impedance bandwidth of 26.5%. Other type of feeding has been applied in the same design, where it has been demonstrated that using a coaxial probe offers AR bandwidth of ~5.2% with return loss bandwidth of 17.3%

when exciting two orthogonal modes [52]. For a hemispherical DRA, an optimised spiral arm feed has provided an AR bandwidth of 3.9% with impedance bandwidth of 12% [53]. Utilizing a square spiral shaped micro strip line to excite a rectangular DRA with  $\epsilon_r = 9.6$  has achieved circular polarization and impedance bandwidths of 15.5% and 31.25%, respectively, with gain of  $\sim 7$  dBi for the  $TE_{\delta 11}$  and  $TE_{1\delta 1}$  resonance modes operation [54]. Off-centred micro strip feed line has been employed to excite a cylindrical DRA with  $\epsilon_r = 79$  through a circular slot revealed CP and impedance bandwidths of 3.47% and 5.8%, respectively [55].

Cylindrical DRA with 3.91% circular polarization and impedance bandwidth of  $\sim 10\%$  has been achieved by using unequal feeding and coupling for micro strip and cross slot, respectively [56]. In another study, axial ratio bandwidth of 2.2% has been reported for a cylindrical DRA with  $\epsilon_r = 9.5$ , pertinent to the two vertical stripes on the resonator's opposite wall and the micro strip feed line with impedance bandwidth and gain of 17% and 3.2 dBi, respectively [57]. A cylindrical DRA has been excited using a perturbed annular slot and offered axial ratio and impedance bandwidths of 3.4% and 19.1%, respectively, where the maximum achieved gain is  $\sim 1.5$  dBi [58]. A cavity backed and cylindrical DRA with a high dielectric constant of  $\epsilon_r = 79$  has been utilized with U-slot feed and provided axial ratio and impedance bandwidths of 2.4% and 11.7%, respectively, in conjunction with a gain of  $\sim 4$  dBi [59]. Using a micro strip line-fed rectangular, notch DRA, an axial ratio bandwidth of 5% has been achieved with a 7 dBi peak gain as well as a 20% impedance bandwidth [60]. On the other hand, utilizing a cross-slot, with unequal arm lengths, to feed a cylindrical DRA, operating at the  $HE_{11\delta}$  resonance mode, provided impedance bandwidth and gain of 28% and 3.5 dBi at 5.75 GHz, respectively, and a CP bandwidth of 4.7%. For a monofilar-spiral-slot coupled rectangular DRA, respective AR, impedance bandwidths and gain of 18.7%, 53.5% and 3.88 dBi have been achieved [61]. Experimental study to determine the impacts of L-shaped microstrip feed for a cylindrical

DRA, with  $\epsilon_r = 10.2$ , provided respective axial ratio and impedance of 15.9% and 21.3% in conduction with a gain range of 4.15 to 6.09 dBi across the operating frequency [62]. The antenna's operation utilized the  $TE_{131}$  mode for the upper band, and a combination of  $TE_{111}$  and  $TE_{121}$  modes for the lower band. This operational structure, leveraging unequal arm lengths in the cross-slot, resulted in a 3 dB Axial Ratio (AR) bandwidth of 19.8% for the upper band, and 6.2% for the lower band. Furthermore, the combination of modes in the lower band yielded an impedance bandwidth and gain of approximately 24.3% and 2.3 dBi respectively. Conversely, the upper band exhibited a gain of roughly 4.7 dBi.[63] . Applied to use as a hemi-ellipsoidal, a cross-slot fed DRA provided impedance and axial ratio bandwidths of 15.4% and 3.9%, respectively [64] .

A low-cost novel stacked DRA of four rectangular dielectric layers was proposed for respective CP and impedance bandwidth of 6% and 21% with a gain range of 6 to 6.7dBi [65]. A triple-layered hemispherical DRA with parasitic patch and conformal strip has been investigated in [66]. The positioning of the parasitic patch and conformal strip at the third and first dielectric layers have been tested for impedance matching and axial ratio, with improved performance being achieved with permittivity of 5, 1, and 3 for the outermost, middle, and innermost layers, respectively. The antennae AR and impedance bandwidths are 8% and 25.8%, respectively. Additionally, for  $HEM_{111}$  and  $HEM_{113}$  resonance modes, dual-band CP cylindrical DRA operation has been achieved with respective impedance and AR bandwidths of 23.5% and 7.4% alongside a 7 dBi maximum gain [67].

## 1.5 Multi-layered DRAs

Adding a dielectric coat to the DRA provides a substantial increase in impedance bandwidth by creating a transition region between air and the DRA resulted in a lower Q factor. The latter can also be achieved with the creation of an air gap between the DR and the ground plane, whereby

the secondary layer between the antenna and free space acts as a transitional zone, where the increased bandwidth is associated with a reduced quality factor. Multi-layer, wideband, hemispherical DRAs have been explored in numerous studies using slot aperture feeding [68, 69]. It should be noted that the maximum bandwidth enhancement can be achieved by coating the DRA with a material that has a relative permittivity, which is approximately half that of the DRA to create a transitional zone between the DRA and an air [68]. Rectangular waveguide feeding of multi-layer hemispherical DRAs was reported with an increased outer-layer permittivity, which results in a reduced resonance frequency [69]. Therefore, optimising the coating layer thickness and permittivity establish a broadband coupling between the triple-layer hemispherical DRAs and rectangular waveguide [69]. A comparative study of single and double layer hemispherical DRA has been conducted with respected bandwidths of 14% and 31.9%, respectively with a low gain of 2.5 dBi at 3.6 GHz [70].

Lower-order mode operating cylindrical DRAs have been extensively modified with numerous techniques for bandwidth enhancement, including DRA stacking, air gaps, and coating, using various materials. Initial empirical data indicated a 30% impedance bandwidth for a multi-layer wideband cylindrical DRA having an inner-layer with a dielectric constant of about 50% more than the outer layer [71]. Furthermore, 5.5 dBi gain has been achieved with broader impedance bandwidth of 66% for a stacked cylindrical DRA comprising three stacked segments with dielectric constants of 10.2, 2.32, and 6.15 for the top, middle, and bottom layers [72]. In a subsequent study, excitation of the  $TM_{018}$  mode for a four elements cylindrical DRA array has provided a gain of  $\sim 4$  dBi with a 47% impedance bandwidth [73]. Vertical double-stacking of two cylindrical DRAs achieved notable bandwidth enhancement, with 5 dBi gain and 55% impedance bandwidth [74]. Experimental investigation of a cylindrical, double-layered, wideband, transparent DRA excited in the  $HE_{118}$  mode with a conformal conducting strip,

achieving 7 dBi gain and 30% impedance bandwidth [75]. A half-cylindrical DRA with multiple layers achieved impedance bandwidth of over 52% [76].

## **1.6 3D printing Technology**

Recent interest in 3-D printing can be attributed to the lower costs and lead time associated with this technique. Moreover, 3-D printing can successfully manage complex geometrics [77]. In the period following the introduction of 3-D printing in the 1980s, several 3-D printing methods have been developed, including fused deposition modeling (FDM), electron beam melting, binder jetting, polymer jetting, selective laser melting, ceramic stereolithography apparatus, and micro-stereolithography. In addition, 3-D printing approach has been shown to effectively produce high-performance microwave and mmWave antennas, such as slot [78], horn [79], patch [80], gradient index lens [81] antennas and reflect arrays [82]. Despite this evident success, there has been limited research into 3-D-printed DRAs [83-85].

DRA is a three-dimensional (3D) antenna. Therefore, its design is more flexible than is the case with 1D linear antennae and 2D planar antennae. Irregular geometrics designs, such as the asymmetrical T-shaped [6], inverted stepped pyramid [86], and tetrahedral-shaped [87], have been proposed as a means of increasing bandwidth. Furthermore, multi segment DRA [88], and stacked DRA[39] have provided a successful approach in the design of wideband DRA. It is possible to improve multilayered DRA bandwidth by varying the permittivity of dielectric layers [76, 89]. These designs are all characterised by boresight radiation patterns. A wideband half-split conical-shaped DRA with conical radiation patterns was proposed in [90]. These designs are all characterised by the use of conventional DRAs that are created with the use of traditional techniques, including tooling, machining, and moulding. The comparative cost-effectiveness and sustainability of 3D-printing technology, otherwise known as additive manufacturing, have contributed to the recent interest in this technique. In addition, its ability

to fabricate complex shapes is also responsible for its popularity [77]. In the period following the introduction of 3-D printing technology by [91], multiple 3-D printing methods have emerged, such as fused deposition modeling (FDM), stereolithography apparatus, binder jetting, polymer jetting, and selective laser melting. Currently, 3-D printing is used for different antenna types, including lens antennae[81, 91] reflector antennae , and horn antennae. Nevertheless, only limited attempts have been made in respect of the 3Dprinted DRA.

### **1.7 Research problem:**

Current trends in communication technologies necessitate antennas with high gain, wide impedance, and axial ratio bandwidths, particularly in the high-frequency range for applications such as satellite communication, radar systems, and 5G networks. The traditional single-layer DRAs, although providing satisfactory performance, often face limitations in achieving the desired bandwidth and gain. In addition, there are issues with potential air gaps between dielectric layers in layered DRA configurations, and challenges in assigning a single effective permittivity to solid objects made of several dielectric layers. Furthermore, there is a lack of understanding on how the addition of dielectric layers and alterations in dielectric constants impact the performance of DRAs, and if these alterations can effectively enhance the impedance, axial ratio bandwidths, and gain of these antennas.

### **1.8 Research Objectives:**

The main objectives of this project are:

- To investigate the theoretical and experimental performance of circularly polarised two-layer cylindrical DRAs for X band communication system that are fed using a spiral slot, and how the addition of a dielectric coat impacts their performance.

- To experimentally study circularly polarized layered cylindrical DRA for mm-wave frequency from 20 to 30GHz and understand the influence of outer dielectric layer on the bandwidths and gain.
- To evaluate the effect of combining two layers with decreased effective dielectric constants into a single dielectric material on the performance of circularly polarized perforated cylindrical DRAs at millimetre wave band from 20GHz to 30GHz.
- To experimentally and theoretically investigate a two-layer, mm Wave hemispherical DRA emitting circular polarization, and understand the impact of the dielectric coat on the bandwidths and gain.
- To develop a hemispherical DRA that is circularly polarized and fed by a spiral slot for millimetre-wave applications operating at 60 GHz, and assess how the application of a dielectric coating enhances the performance parameters.

## **1.9 The Structure of the thesis**

This thesis is structured into seven chapters, each providing unique insights into the field of Dielectric Resonator Antennas).

### **Chapter 1: Introduction and Literature Review.**

This introductory Chapter provides a comprehensive orientation of the topic, explicating the significance of the study within the context of evolving antenna technologies. It briefly traverses the landscape of DRA, illuminating the exigencies for higher-performance antennas in contemporary technological contexts. A critical review of the extant literature and technologies associated with DRAs is conducted, identifying lacunae in current research. This culminates in a delineation of the research problem and the elucidation of the research objectives.

**Chapter 2:** A Comprehensive Examination of a Two-layer Cylindrical DRA for X-band Communication Systems.

This chapter provides an in-depth analysis of the proposed X-band two-layer cylindrical DRA design, underpinned by a combination of theoretical and empirical investigations. Conclusions are derived from a meticulous interpretation and discussion of the findings.

**Chapter 3:** Circularly Polarized Layered Cylindrical DRA for Millimetre-wave Frequencies of 20 GHz to 30 GHz.

This Chapter presents an exhaustive study of the design and application of a circularly polarized layered cylindrical DRA. It incorporates a synthesis of experimental results and theoretical observations, paving the way for rigorous analysis and discourse on the findings.

**Chapter 4:** Dissecting the Perforated Cylindrical DRA for Millimeter-wave Frequencies from 20 GHz to 30 GHz.

This Chapter introduces and explores the concept of the 3D printed perforated DRA and its pertinence to the layered CDRA. A detailed exposition on the design and examination of the circularly polarized perforated cylindrical DRA is given, corroborated by experimental results and theoretical observations. The Chapter culminates in a critical discussion of the results and their implications.

**Chapter 5:** Theoretical and Empirical Exploration of a Two-layer and Perforated Hemispherical DRA for the Millimeter-wave Band from 20 GHz to 30 GHz.

This Chapter explicates the two-layer hemispherical DRA design and illustrates the innovative use of MDF 3D printing for the fabrication of the Perforated HDRA. The Chapter encompasses an analysis of the excitation of higher-order resonance modes, supported by empirical data and theoretical predictions, followed by a discussion of the findings.

**Chapter 6:** Advancement of a Hemispherical DRA for Millimeter-wave Applications at 60 GHz.

This Chapter delineates the design protocol for the hemispherical DRA. It discusses the challenges encountered due to the dearth of specific high-frequency measurement tools, followed by the presentation of both experimental and simulated data, leading to a comprehensive analysis of the results.

**Chapter 7:** Conclusions and Future Research Directions.

The concluding Chapter of this thesis offers a synthesis of the research findings. It probes into the potential implications of the research and proffers recommendations for subsequent studies in this domain.

## **Chapter2 Layered Cylindrical DRA for X-band Applications**

### **2.1 Introduction:**

One of the most crucial components of wireless communication systems is the antenna. It serves as the last component in the transmission end and the first component in the receiving end [92]. Therefore, a poor antenna design that cannot efficiently establish the link between the endpoints reduces system performance. There are numerous antenna configurations that exist nowadays, including dipole, horn, microstrip and dielectric resonator antennas (DRA) among others. Circularly Polarised (CP) antennas are better suited to achieve communications that is less sensitive to the environment compared to their linearly polarised (LP) counterparts. In the present study, a layered circularly polarization cylindrical DRA that are supporting a multimode operation are examined.

There is a significant benefit to using CP antennas rather than linearly polarised counterparts in that it is not necessary to establish a similar orientation between the transmitter and the receiver. Therefore, there is a higher probability of receiving a transmitted CP wave provided a CP receiving antenna, with the same polarisation sense, is used. In fact, LP antenna can receive a CP wave but with 3 dB loss since they will be capable of receiving field components from a single direction. On the other hand, LP waves are largely ineffective for satellite communications. Additionally, CP waves that transmit in all planes are less vulnerable to undesired reflection and absorption. Moreover, the wave can be scattered via reflective surfaces, i.e. multipath reflections, which can ultimately generate a weak LP signal. Nonetheless, it is possible to receive a CP wave, irrespective of the multipath reflections. What's more, CP antennas can minimise the Faraday rotation impacts, which, in turn, can cause a linearly polarized wave to rotate. The extent of this rotation is determined by several factors,

including frequency, ionosphere thickness, and temperature [93, 94]. This can result in a 3dB reduction in the signal strength of linearly polarized waves [93]. Furthermore, When the reflector is a perfect conductor, the reflection coefficient is 1. This leads to a 180-degree phase change for linearly polarized waves, which might convert a right-handed CP wave into a left-handed CP wave, or vice versa, causing a polarization mismatch. Therefore, circular polarization is generally not recommended for indoor radio communications, where reflections are plentiful [94].

One regular geometry that is employed in this study is a cylindrical DRA, as its design structure is sufficiently flexible and simple in comparison to rectangular and hemispherical counterparts. An Alumina cylindrical DRA that functions in a higher-order mode will be utilized in this Chapter. The proposed antenna contains two dielectric layers with different radii and dielectric constants. It is important to note that as mentioned in the literature the maximum bandwidth enhancement can be achieved by coating the DRA with a material that has a relative permittivity, which is approximately half that of the DRA to create a transitional zone between the DRA and an air [71]. Additionally, the inner and outer layers were selected based on commercially accessible materials; the outer layer has been created through a 3D printing process involving a Polyimide powder with a dielectric constant of  $\epsilon_{r2}=3.5$ . The inner Alumina layer represents the actual DRA that has a dielectric constant of  $\epsilon_{r1}=10$ . Moreover, the suggested multilayer DRA structure provides enhanced CP and impedance bandwidths in addition to greater broadside gain when the cross-slot feed is replaced by a spiral counterpart [95].

The cylindrical geometry provides two degrees of design freedom, whilst the resonance frequency and radiation Q-factor are fully reliant on the radius  $a$ , height  $h$ , and aspect ratio [5]. Thus, a shorter and wider DRA can be created for a given dielectric constant, in order to resonate at the same frequency as a taller and thinner DRA. Thus, antenna designers can choose

between a numbers of different antenna profiles to achieve the desired resonance frequency. Moreover, it is essential to have a proper feeding mechanism to excite particular resonance modes.

The key objective of this Chapter is to demonstrate the potential of a CP layered higher-order mode cylindrical DRA at X-band frequency range. Higher order resonance mode operation can produce a higher gain with a narrower bandwidth for a single layer DRA due to the increased number of short magnetic dipoles inside the antenna. Therefore, a two-layer DRA has been employed to address these limitations with broader impedance and axial ratio bandwidths along with a higher gain by creating a transition region between air and the DRA resulted in lower the Q factor of the antenna then increase bandwidth.

It is worth mentioning that the same CDRA that is reported in [95] has been utilized in this study albeit with a different feeding slot aperture. In the presented work, a spiral slot aperture has been used, which has improved the impedance and axial ratio bandwidths. It should be noted that a spiral-slot excitation has been utilized to generate CP radiation in a number of studies, albeit for a single layer DRAs [61, 96, 97]. This Chapter demonstrates the impact on the performance of a layered DRA when the cross-slot feed is replaced by a spiral counterpart [13]. CST microwave studio has been utilized for the design and simulation and a prototype has been measured with close agreement between experimental and simulated results.

## 2.2 Cylindrical DRA modes

The cylindrical DRA support three different mode types; Transverse Electric, TE ( $E_z=0$ ), Transverse Magnetic, TM ( $H_z=0$ ), and hybrid modes ( $E_z \neq 0, H_z \neq 0$ ). The electromagnetic fields for the TE and TM modes are axially symmetric with no azimuthal, i.e.  $\phi$ , variation [98]. On the other hand, hybrid mode fields are associated with variation along the  $\phi$  direction and can be further divided into the HE and EH mode types. The HEM mode is called the HE mode if  $E_z$  is dominant, or EH when  $H_z$  is dominant [5].

The resonance modes are categorized as  $TE_{mnp}$ ,  $TM_{mnp}$ ,  $HE_{mnp}$ , and  $EH_{mnp}$ , where the  $m$ ,  $n$ , and  $p$  indices denote field variations in the azimuthal ( $\phi$ ), radial ( $r$ ), and axial ( $z$ ) directions, respectively. The index  $m$ , for instance, represents the number of full wavelength cycles along the  $\phi$  direction, whereas  $n$  and  $p$  denote the number of half-wavelength field variations in the radial and axial directions, respectively. Given the intricacy of mathematical modelling, it is a complex and time consuming process to calculate the resonance frequencies of specific higher-order modes for a cylindrical DRA [2]. Nonetheless, it is possible to determine the resonance frequencies of these modes using the CST MWS Eigenmode solver. However, there are equations to approximately calculate the resonance frequencies of particular lower order modes of cylindrical DRAs with specific dimensions combination. For example, when the aspect ratio falls in the range of  $0.4 \leq a/h \leq 6$ , the following formula can be used to calculate the  $HEM_{118}$  mode resonance frequency [2].

$$k_0 a = \frac{6.324}{\sqrt{\epsilon_r + 2}} \left[ 0.27 + 0.36 \left( \frac{a}{2h} \right) - 0.02 \left( \frac{a}{2h} \right)^2 \right] \quad (2.1)$$

where, the free space wave number is represented as  $k_0 = 2\pi f_0/c$ , whilst  $f_0$  denotes the resonance frequency and  $c$  designates the speed of light [99].

## 2.3 Design and simulation DRAs

### 2.3.1 Concept design from CST simulations

As mentioned earlier, the CST MWS [100] was employed in this study to design the DRAs. Moreover, it was critical that certain parameters were set up correctly, including the frequency range, which is essential for simulating the antenna, defining and energising the port, enhancing the mesh cells, and determining the type of simulation that would be carried out. T A hexahedral mesh type and its computational volume was discretized using rectangular cuboids of varying sizes. After all the required parameters for the simulation had been specified, the CST MWS produced visualizations depicting the outcomes. In the  $|S_{11}|$  results, the antenna performance, including impedance bandwidth and resonance frequency, can be determined. Additionally, the preliminary collection of resonator geometries is derived using the Magnetic Wall Method, formally referred to as the numerical implementation of the Dielectric Wall Method (DWM). This methodology is executed by conducting a modal analysis of the resonator utilizing the Eigenmode solver of the CST Microwave Studio (MWS). This process allows us to characterize the various modes within the DRA and understand their behaviour, thereby providing an essential foundation for subsequent design and optimization steps. The process involves using the CST MWS Eigenmode solver to carry out a modal analysis of the resonator. With the exception of the bottom wall, which is usually assumed as a perfect electric conductor (PEC), all the DRA sides are assumed to be perfect magnetic conductors (PMC). The radiation losses associated with both the antenna and its feed network have been considered and factored into this study by incorporating the loss tangent within the material properties. This approach ensures a more comprehensive understanding of the antenna's overall performance, as it includes potential energy losses due to material absorption or radiation.

### 2.3.2 Antenna Configuration

Figure 2.1 illustrates the configuration of the proposed layered CDRA with inner layer dimensions of  $a_1=3$  mm and  $c_1= 32$  mm have been determined Based on[95] as well as a relative permittivity of  $\epsilon_{r1}=10$ . The DRA is coated by a Polyimide layer that has optimized dimensions of  $a_2=20$  mm and  $c_2=36$  mm with a dielectric constant of  $\epsilon_{r2}= 3.5$  .The proposed antenna has been placed on a  $100\times 150$  mm<sup>2</sup> ground plane that has been printed on a thin Rogers RO4350 dielectric substrate having a thickness and dielectric constant of 0.8, 3.48 mm, respectively.

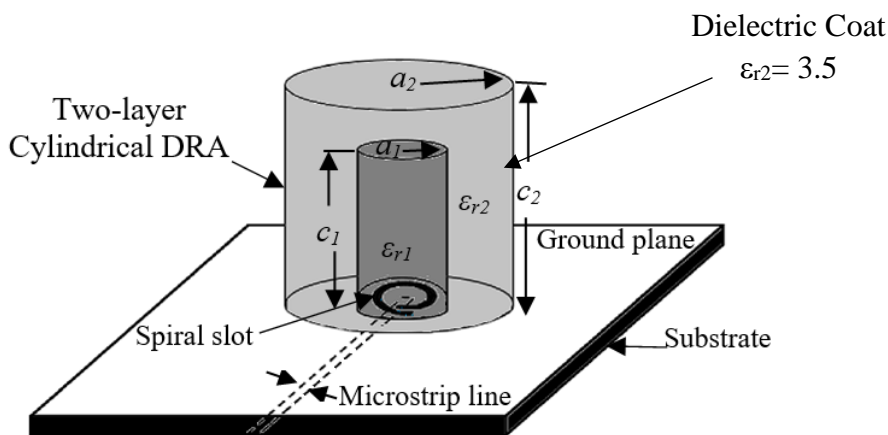


Figure 2.1: The configuration of the proposed layered CDRA.

Additionally, the feeding spiral slot has been etched on the ground plane to generate the CP radiation. The spiral is illustrated in Figure 2.2 with optimised dimensions defined by adopting the well-known Archimedean spiral function.;

$$\rho = a \varphi \quad (2.2)$$

Where  $\rho$  represents the radius of the spiral-slot arm,  $a$  is the spiral constant and  $\varphi$  is the winding angle. The chosen parameters are  $a=0.195$  mm/rad,  $0.166\pi \leq \varphi \leq 2.194\pi$  and the width of the spiral-slot arm is  $w_s=1.36$  mm with respect to a  $50 \Omega$  micro strip line containing an open stub length of  $l_{stub} = 1.27$ mm. The changes in the above spiral's parameters as well as the separation between the spiral slot arms ( $g$ ) can change the spiral's arm length [96]. Based on

the parameters mentioned above, the length of the spiral slot is 12.3435 mm is approximately  $0.9 \lambda_{\text{eff}}$  at an operating frequency of 11 GHz which has been calculated by equation 2.2 [101].

$$l = \int_{\varphi_{\min}}^{\varphi_{\max}} \sqrt{a^2 + (a \varphi)^2} d \varphi \quad (2.3)$$

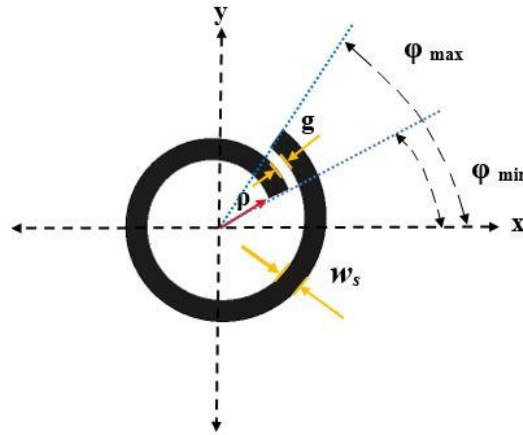


Figure 2.2: Geometry of a single-arm spiral slot.

### 2.3.3 Parametric Studies

In this section, a number of simulations have been conducted using the time domain solver in CST MWS [100]. The impact of varying the spiral slot width is studied with a fixed outer dielectric layer thickness of 20 mm and height of 36 mm. The aim is to achieve the optimum dimensions that offer wide impedance and the axial ratio bandwidths as well as the maintain the gain high.

#### ***i** The impact of slot width $w_s$ :*

In this case, the antenna has been simulated at a frequency range of 8-15 GHz with varying the width of slot  $w_s$  between 0.46 and 1.66 mm. Figure 2.3 presents the simulated  $|S_{11}|$ , where the widest impedance width of 45% can be observed at  $w_s=1.36$  mm. Figure 2.4 presents the AR variation against the width of the spiral's arm, where it is clear that the widest AR bandwidth of 18% is achieved when  $w_s =1.36$  mm. Figure 2.5 elucidates the relationship between the

antenna gain and the slot width, highlighting that the most consistent gain performance is achieved with a slot width of 1.36 mm. This specific slot width demonstrates stability in gain, exhibiting a minor fluctuation of approximately 3.5 dB across the operating frequency range, thereby underscoring the crucial role of slot width in maintaining uniform antenna performance.

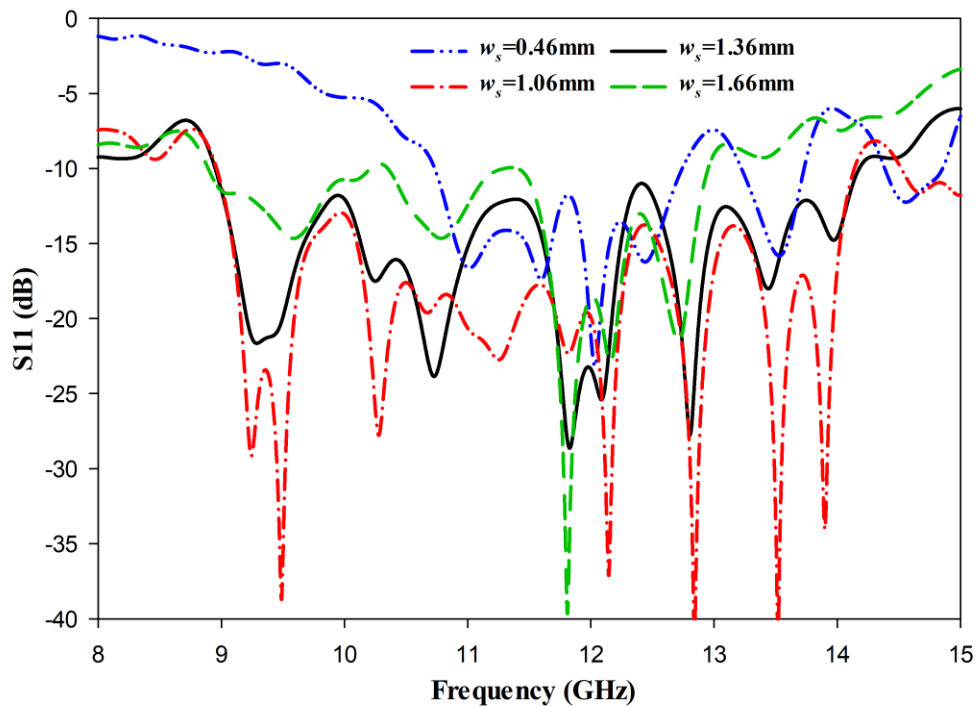


Figure 2.3: Simulated  $|S_{11}|$  with various slot widths.

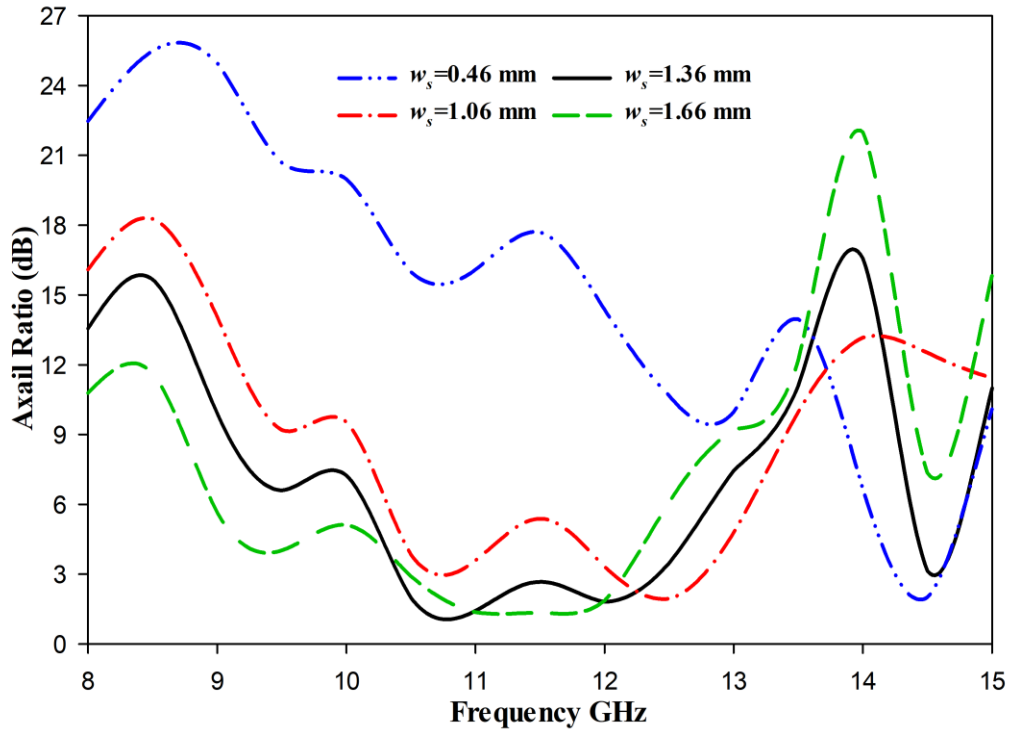


Figure 2.4: Simulated axial ratio with various slot widths.

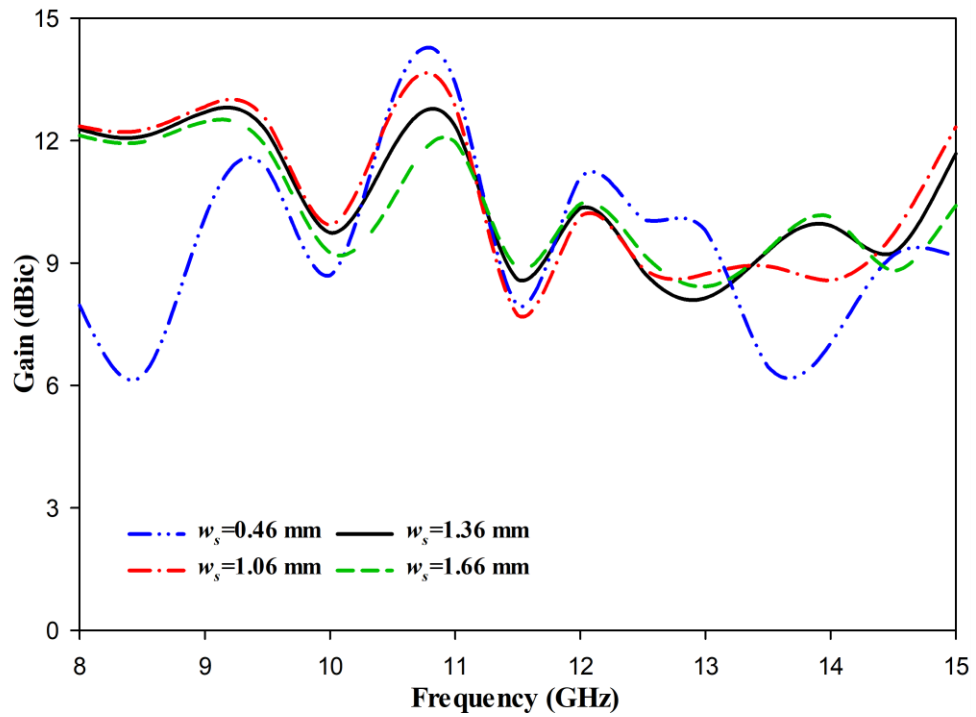


Figure 2.5: Simulated Gain with various slot widths.

## *ii The impact of separation, $g$ , between the spiral slot's arm turns.*

In Archimedean spiral slot geometry, the slot size is affected by the distance between spiral slot arm's turns,  $g$ . When  $g$  is increased for a particular spiral slot geometry, the overall length of the slot increases slightly, causing a decrease in the resonant frequency [102]. Single-arm spiral slot geometry with  $N = 1$  turns have been studied while keeping the other slot's dimensions are kept constant to study while  $g$  has been varied from 0.1mm to 0.9mm.

The  $|S_{11}|$ , AR, and Gain are presented in Figures 2.6, 2.7, and 2.8, respectively. The results indicate that the largest bandwidth is achieved when  $g=0.2$  mm, which results in exciting the following resonance modes;  $HE_{117}$  at 9.5 GHz,  $HE_{119}$  at 10.5 GHz,  $HE_{11,11}$  at 11.5GHz and  $HE_{11,13}$  at 14 GHz over a percentage impedance and AR bandwidths of 45% and 18%, respectively, in conjunction with a high gain of  $\sim 12.5$ dBic. For comparison, the narrowest S11 and AR bandwidths have been achieved when  $g=0.9$ mm with a gain of 11.5 dBi.

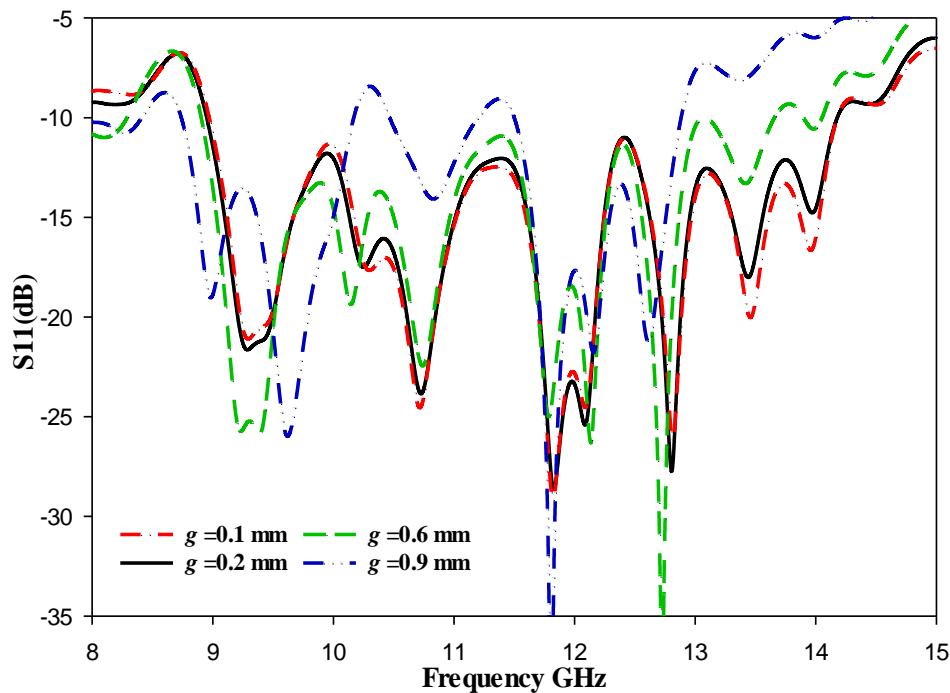


Figure 2.6: Simulated  $|S_{11}|$  with various values of  $g$ .

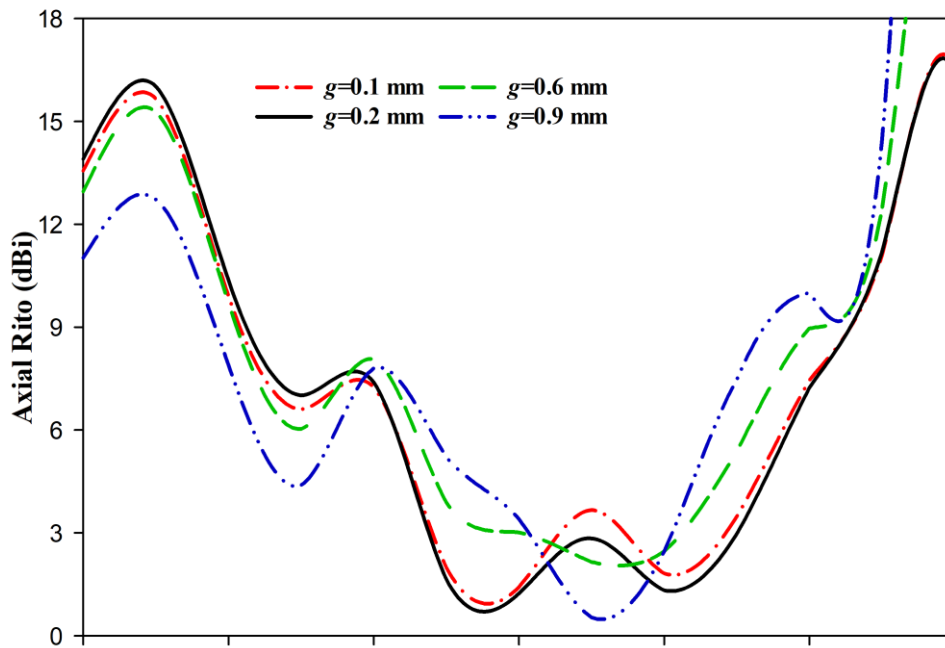


Figure 2.7: Simulated axial ratio with various values of  $g$ .

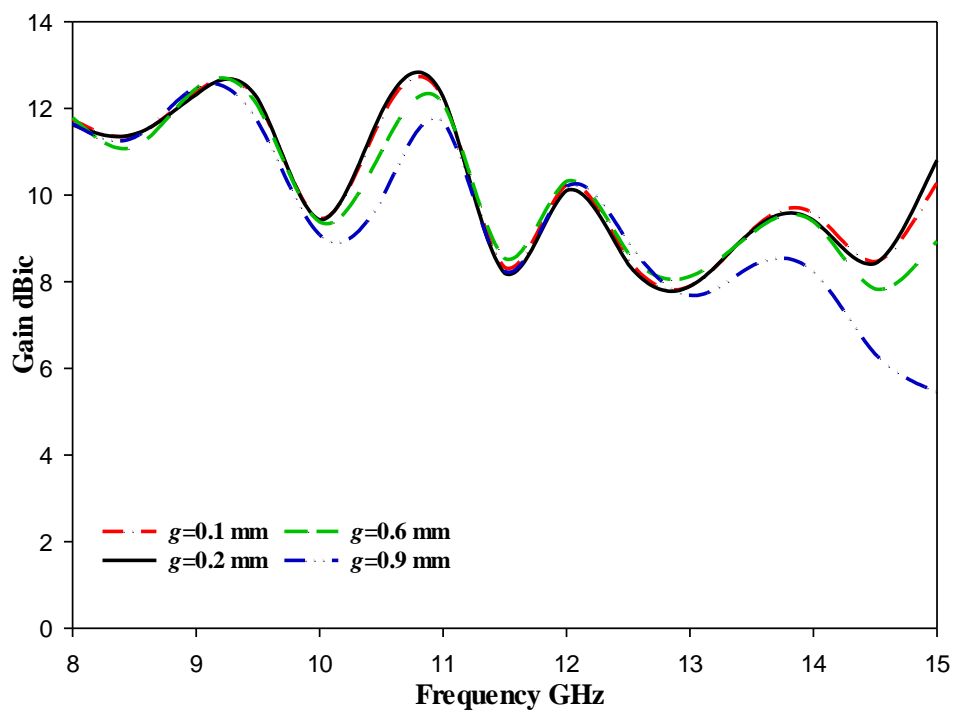


Figure 2.8: Simulated Gain with various values of  $g$ .

### iii The impacts of the maximum rotation angle

For an Archimedean spiral geometry, the maximum rotation angle,  $\varphi_{\max}$ , determines the overall arc's length. The antenna performance has been investigated when  $\varphi_{\max}$  is changed from  $2.166\pi$  to  $2.25\pi$ , which correspond to arm lengths of  $0.8\lambda_{\text{eff}}$  to  $\sim\lambda_{\text{eff}}$ . As a result, Figure 2.9 depicts the simulated  $|S_{11}|$  for various  $\varphi_{\max}$  values, with the widest impedance width observed at  $\varphi_{\max} = 2.194\pi$  and the narrowest at  $\varphi_{\max} = 2.25\pi$ . Figure 2.10 depicts the AR with the widest bandwidth observed again at  $\varphi_{\max} = 2.194\pi$  with the most suitable gain of  $\sim 12.5$  dBic is achieved at the same maximum rotation angle of  $\varphi_{\max} = 2.194\pi$  as illustrated in Figure 2.11. According to Figures 9 and 10, appropriate range for the rotation angle should be  $(0.16\pi \leq \varphi \leq 2.194\pi)$  in order to achieve optimal performance.

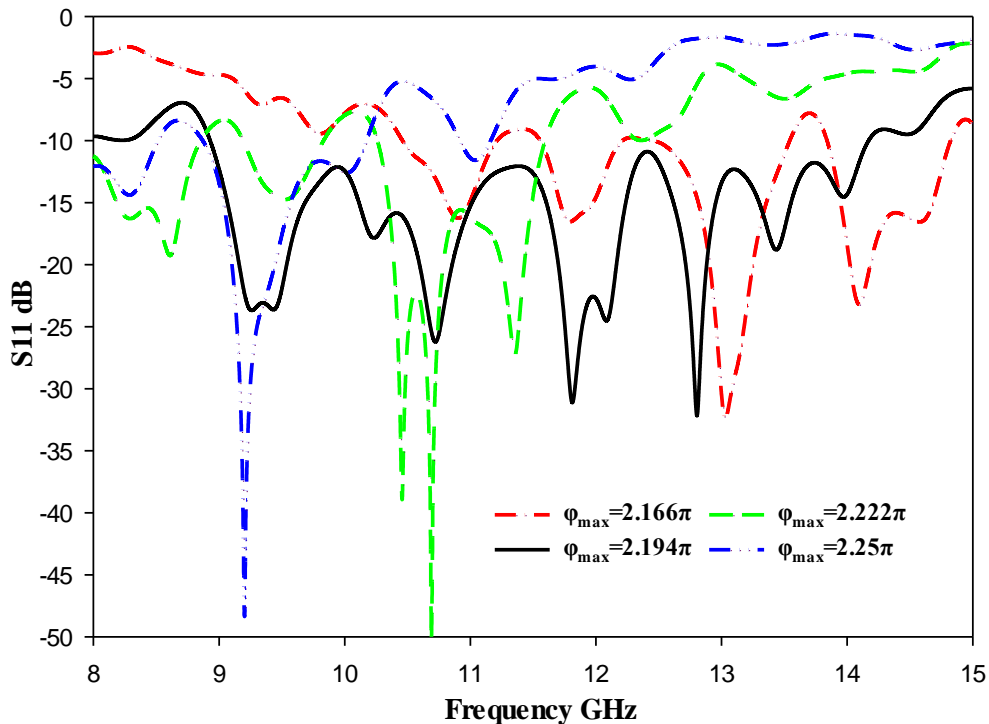


Figure 2.9: Simulated  $|S_{11}|$  for various values of  $\varphi_{\max}$ .

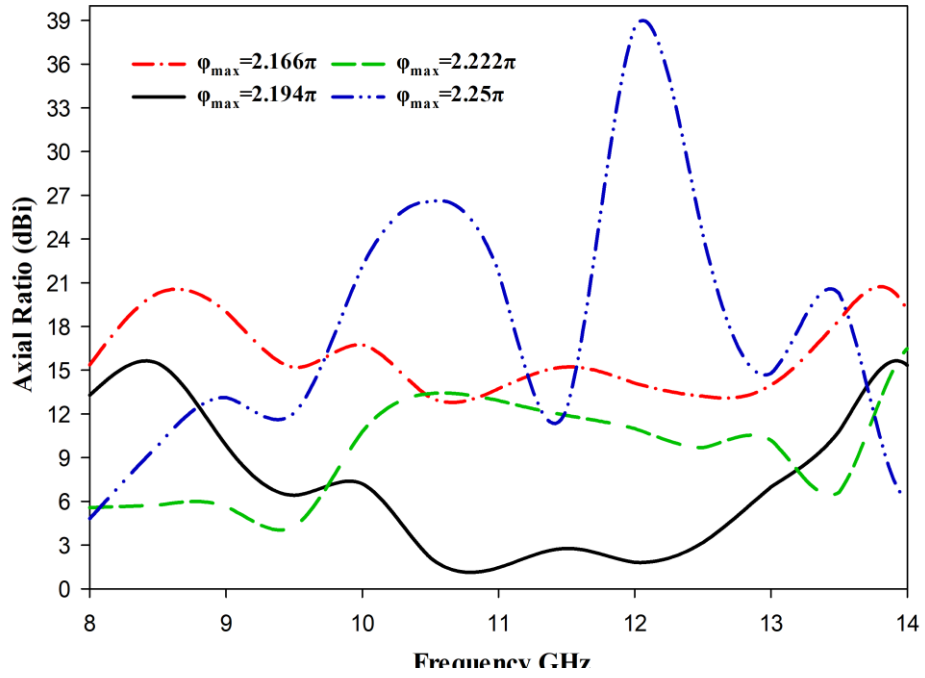


Figure 2.10: Simulated AR for various values of  $\varphi_{\max}$ .

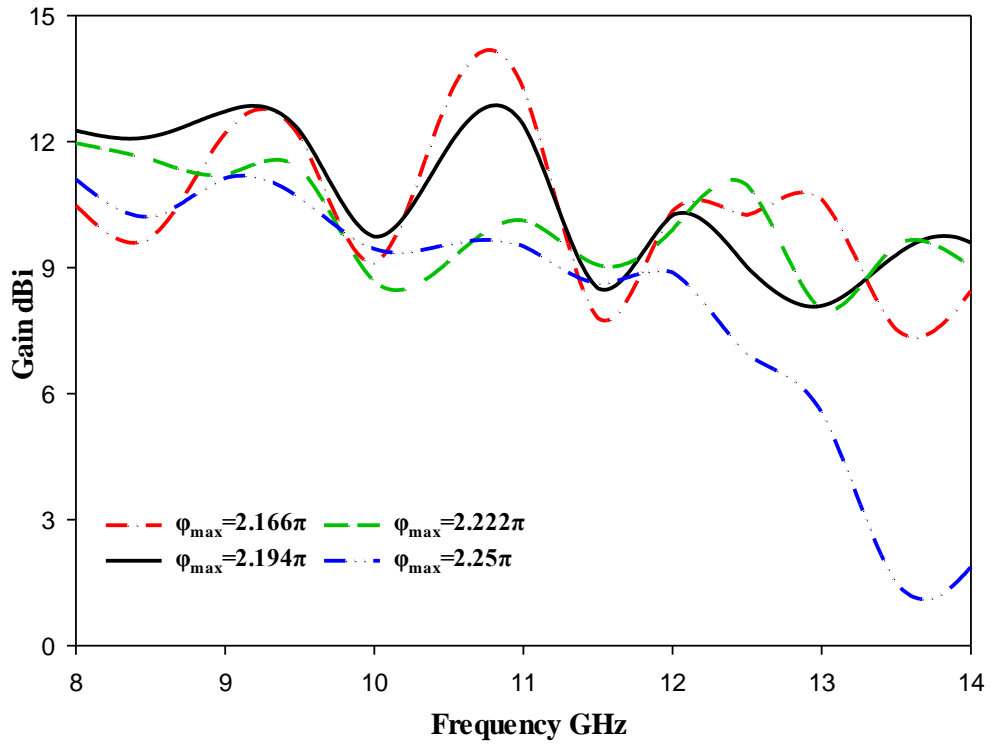


Figure 2.11: Simulated Gain for various values of  $\varphi_{\max}$ .

#### *iv The impacts of the outer layer thicknesses*

Additional simulations have been implemented to study the effects of the coating layer on the CDRA performance in terms of impedance and AR bandwidths as well as the gain. Figure 2.12 demonstrates the return losses, where it can be noted that at the absence of the dielectric coat, the DRA supports three resonance modes of  $HE_{115}$ ,  $HE_{117}$  and  $HE_{119}$  at 10.25, 11 and 12.5 GHz, respectively, with dual impedance bandwidth of 16 % and 5%.

Subsequently, the impacts of different outer layer thicknesses,  $\delta a = a_2 - a_1$ , are presented in Table 2.1 as well as Figures 2.13 and 2.14. It should be noted that  $\delta a$  has been varied from 1 mm to 17 mm when the slot dimensions are fixed at the optimum values of the previous section. These findings indicate that a thicker dielectric coat, i.e. when with  $a_2 = 20$  mm, largely improves the impedance, axial ratio bandwidths and gain because it results in exciting the following resonance modes;  $HE_{117}$  at 9.5 GHz,  $HE_{119}$  at 10.5 GHz,  $HE_{11,11}$  at 11.5 GHz and  $HE_{11,13}$  at 14 GHz over a percentage bandwidth of 45% that extends from 8.9 to 14.18 GHz as can be seen in Table 2.1. These results confirm that the already improved impedance bandwidth of a layered DRA, as reported in [95], has been improved further by replacing the cross-slot with a spiral-slot. This can be attributed to the travelling wave current distribution along the spiral slot. In addition, an increase in gain is caused by the enhanced energy confinement within the dielectric resonator layer through the excitation of higher order resonance modes. This is ultimately due to an increase in the thickness of the outer layer. As a means of confirming this point, CST MWS attached a number of probes to the CDRA at distances of 0, 2, 5, 10, 15 and 20 mm from the centre, each with a height of 2mm located along the x-axis. As can be seen in Figure 2.15, the strength of the E-field decreased outside the central CDRA as the outer layer thickness increased.

It is commonly understood that choosing a higher permittivity material can confine more energy inside it. In this case, a low permittivity material was utilised for the outer layer to avoid

this. However, increasing the outer layer thickness above 20mm may cause more energy to be trapped inside the outer layer rather than released, where the gain decreases. Furthermore, as demonstrated in Figure 2.16, the maximum bandwidth is constantly reached with an outer layer radius of  $a_2=20$  mm. The bandwidth enhancement can be attributed to the fact the dielectric coat acts as a transition layer between the DRA and free space, which minimises the reflection at the DRA-air interface that exists in a single layer DRA. The presence of the coat will also reduce the effective permittivity of the layered configuration, which also contributes to the bandwidth enhancement. Moreover, Figure 2.17 presents the simulated H-field and E -field distributions for the various hybrid modes in several planes of the resonator at a number of different targeted frequencies. The results of the comparison clearly show that modes are present within the cylindrical DRA at the frequencies that correspond to minimal  $S_{11}$  points for each DRA.

Table 2-1: The impacts of different outer layer thicknesses  $\delta a$ .

$a_1$ mm	$a_2$ mm	$\delta a$ mm	$S_{11}$ Bandwidth %	AR Bandwidth %	Gain dBic
3	3	0 (no coating)	16 and 5	0.73	9.5
3	4	1	20, 5.512.2	1.04 and 0.4	10.7
3	10	7	36	0	9
3	16	13	41	4.25	11.4
3	20	17	45	18	12.5
3	27	24	42.5	5.73	12.3
3	37	34	31	1.4	10

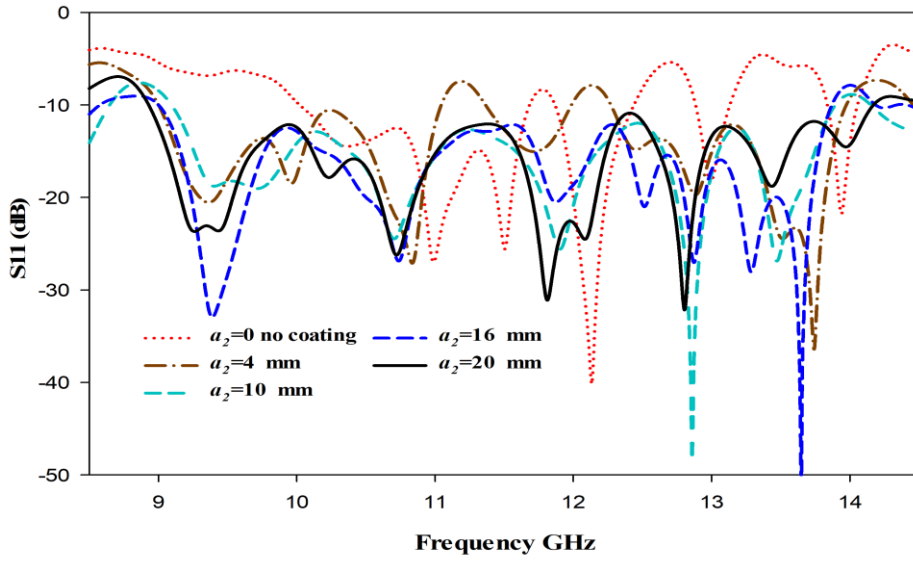


Figure 2.12: Simulated  $|S_{11}|$  for various values of the outer layer radius ( $a_2$ ).

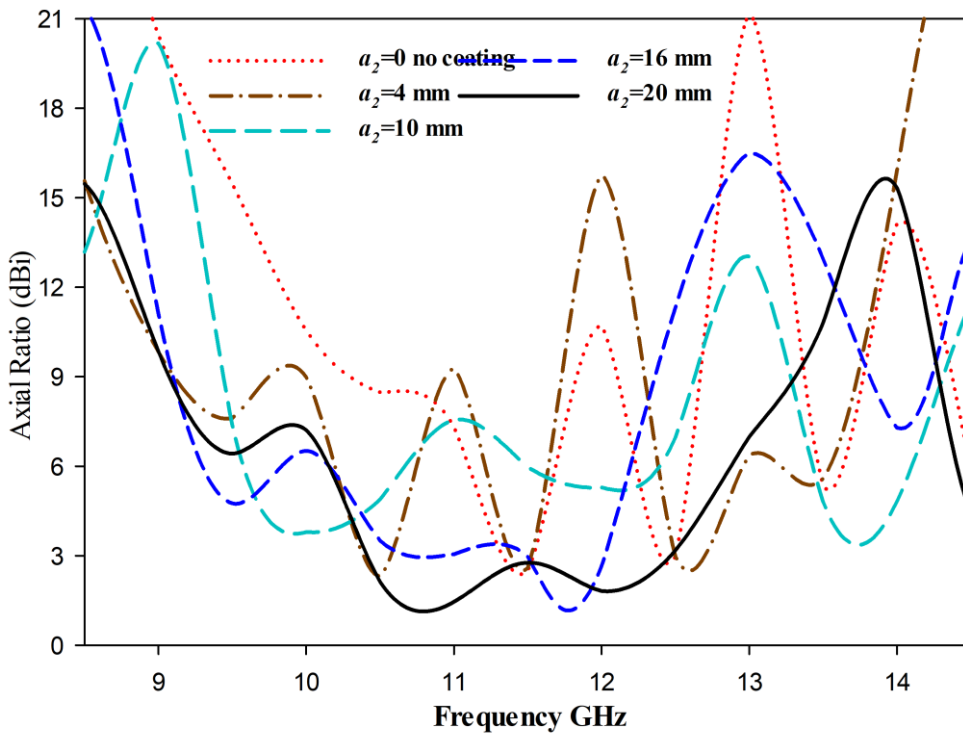


Figure 2.13: Simulated AR for various values of the outer layer radius ( $a_2$ ).

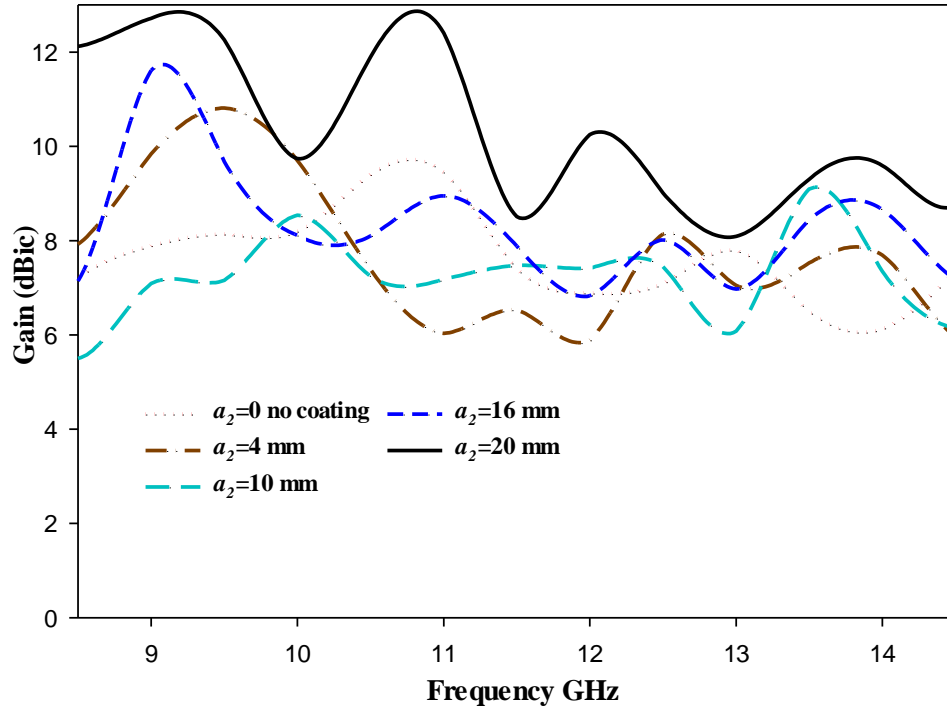


Figure 2.14: Simulated Gain for various values of the outer layer radius ( $a_2$ ).

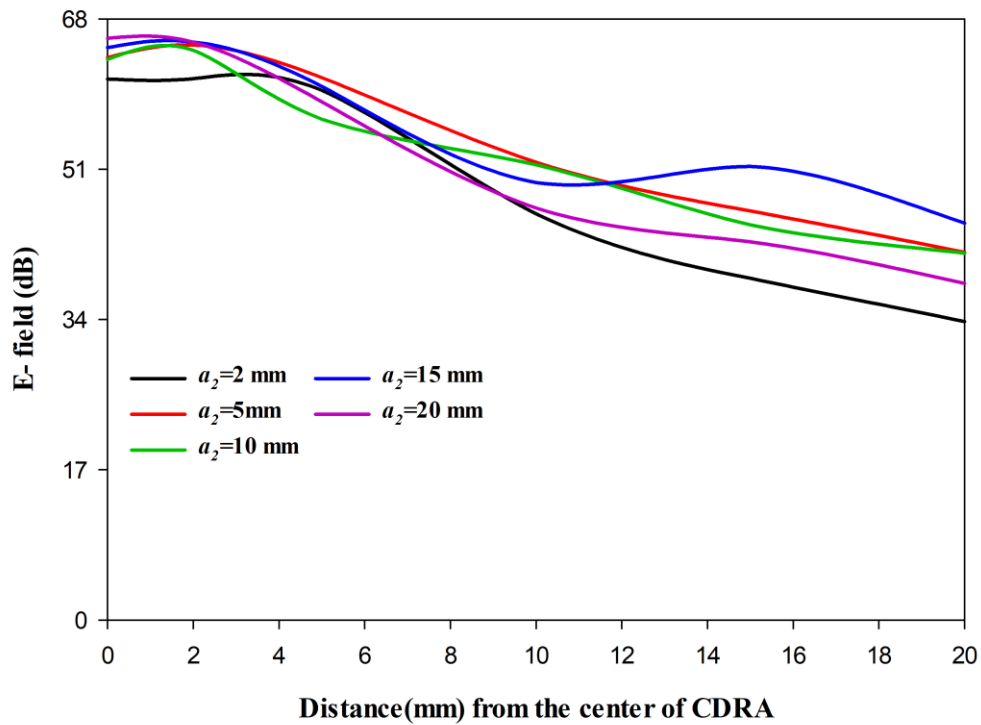


Figure 2.15: The strength of the E-field inside and outside the layered CDRA.

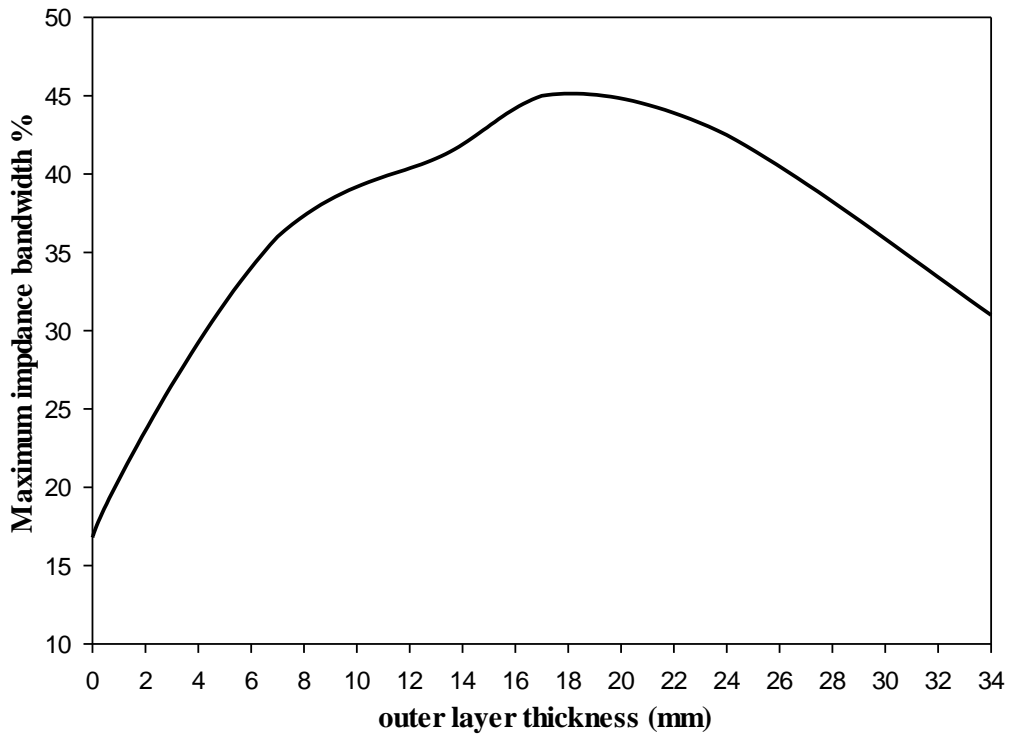
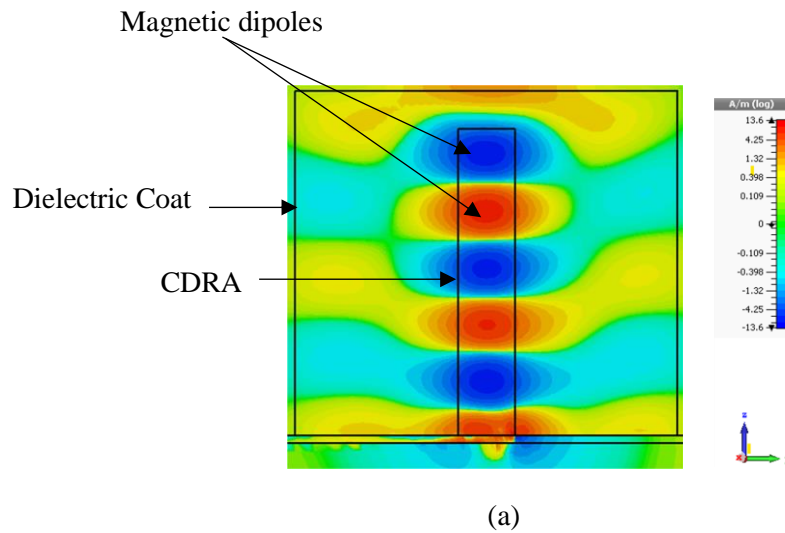
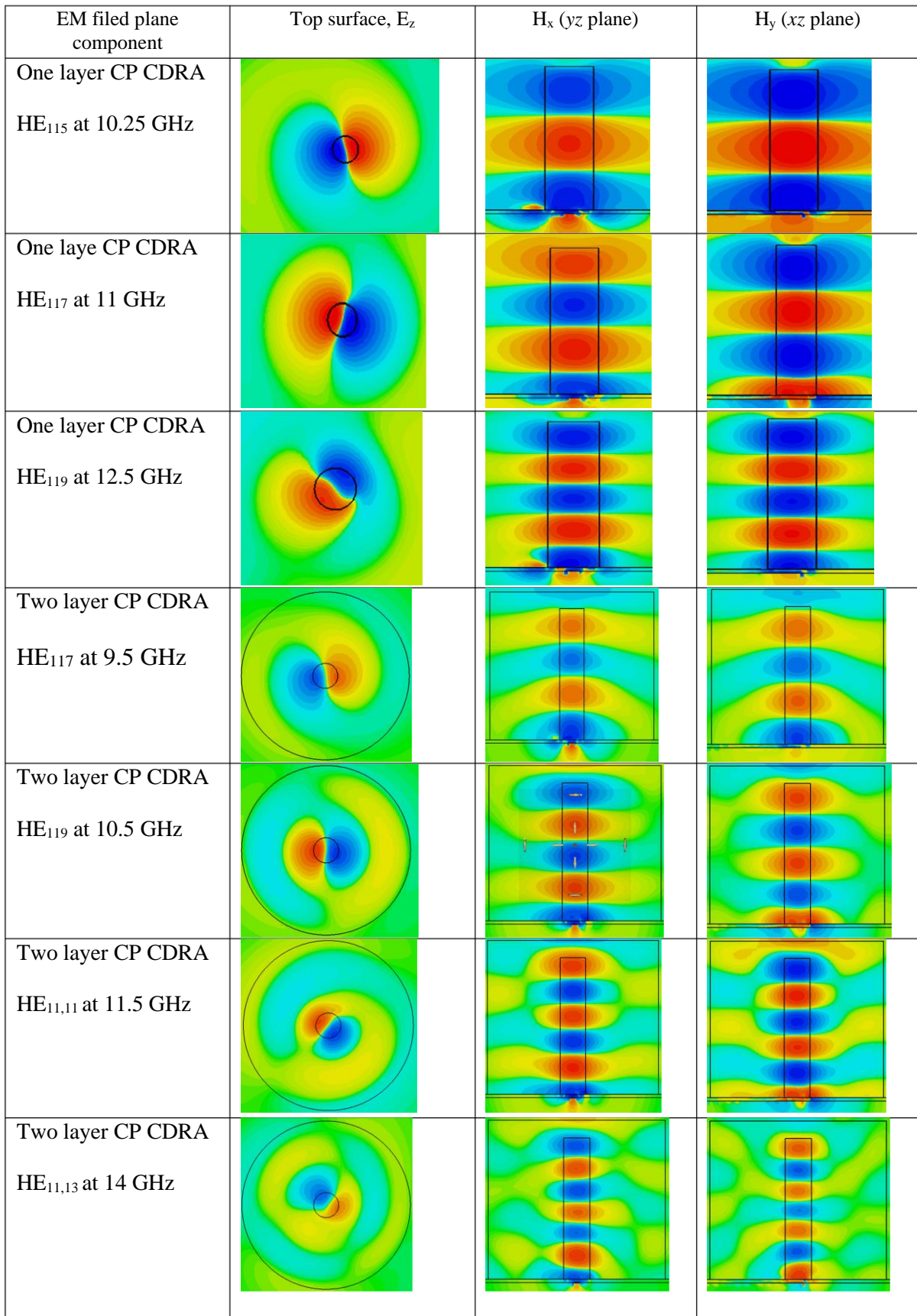


Figure 2.16: Maximum bandwidth versus outer layer thickness.

Figure 2.17: a) Magnetic field of the  $TE_{11,11}$  resonance mode , b) The E- and H-fields distributions inside circularly polarized single-layer and multilayer cylindrical DRA.



(b)



## 2.4 Fabrication and measurements

In order to validate the aforementioned simulations, the inner layer of cylindrical DRA has been manufactured by T-CERAM Company using Alumina with a fabrication tolerance of 0.06 mm with  $\epsilon_{r1}=10$  and a loss tangent of  $\tan \delta < 0.002$ . The outer dielectric coat layer has been fabricated the aid of 3D printing technology using Polyimide material with  $\epsilon_{r2}=3.5$  and loss tangent of 0.0027. In addition, the antenna has been placed on Ro4350B dielectric substrate with respective thickness of 0.8mm, permittivity of 3.5 and loss tangent of 0.0037 provided by Wrekin Circuits. The whole prototype has been fed using a microstrip line that has been printed underneath the Rogers substrate. Moreover, a 3.5 mm SMA connector that is connected to the microstrip line. The Agilent Technologies E5071C vector network analyser has been connected to the SMA thorough a 50 coaxial cable. The calibration has been conducted using the Agilent 85052D calibration kit. The radiation patterns have been measured using an NSI near field system. The antenna and its feed network are illustrated in the Figure 2.18.

The far field of the prototype has been measured, and their left-hand and right-hand radiation patterns and axial ratio are assessed as outlined below:

$$E_{RHCP} = \frac{1}{\sqrt{2}}(E_H + JE_V) \quad (2.4)$$

$$E_{LHCP} = \frac{1}{\sqrt{2}}(E_H - JE_V) \quad (2.5)$$

Where  $E_H = H_a \cos(H_p) + V_a \sin(V_p)$

$$E_V = H_a \sin(H_p) - V_a \cos(V_p)$$

$$AR = 20 \log \left( \frac{|E_{RHCP}| + |E_{LHCP}|}{|E_{RHCP}| - |E_{LHCP}|} \right) \quad (2.6)$$

( $H_a$ ,  $V_a$ ) represent the horizontal and vertical amplitude and ( $H_p$ ,  $V_p$ ) indicate the phase components measured at each  $\theta$  in the far-field [103].

Experimentally, the difference in power received from the horn antenna in  $\theta$  direction should not exceed 3 dB for circular polarisation, which is the axial ratio. To determine this, set the horn antenna in an anechoic chamber at  $\phi = 0$ , and rotate the DRA at each elevation angle  $\theta = 0^\circ, 45^\circ$  and  $90^\circ$ . With the horn antenna rotated at 90 degrees, the same approach needs to be followed to measure  $E_\theta$ .

To measure the gain, a comparison approach was utilised with another horn antenna at the receiving end, where the gain of the DRA can be calculated from the known gain of the reference horn using equation[104].

$$G_{DRA \text{ in dB}} = G_{Horn \text{ in dB}} + 10 \log_{10} \left( \frac{P_{DRA}}{P_{Horn}} \right) \quad (2.7)$$

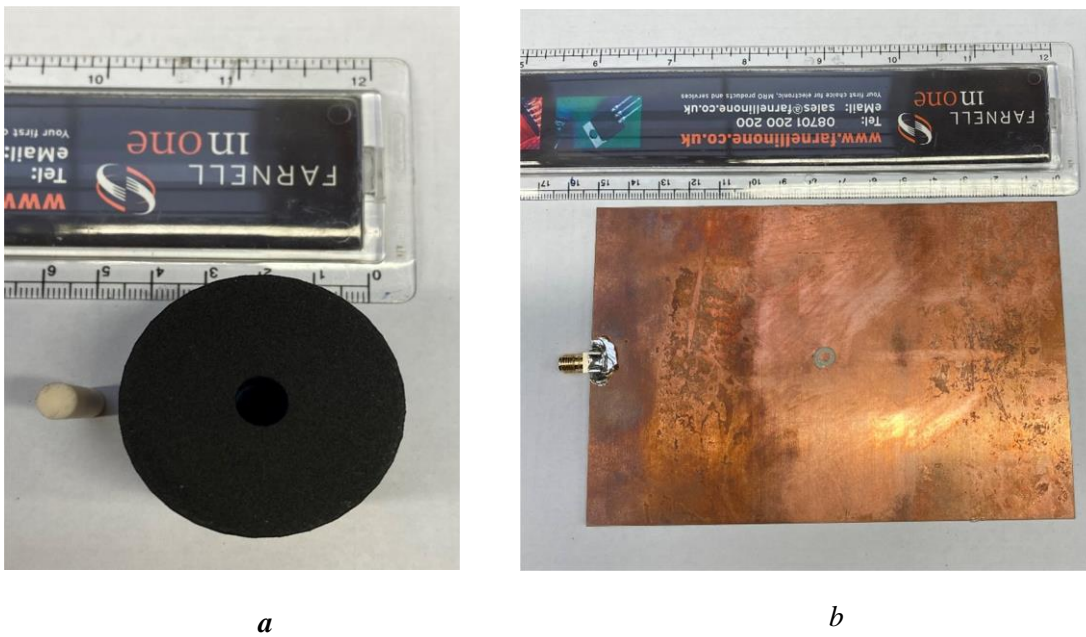


Figure 2.18: (a) The cylindrical DRA and outer dielectric coat. (b) Feed network.

### 2.4.1 Configuration of a single layer circularly polarized CDRA

Figure 2.19 presents the simulated and measured return losses at the absence of the coat with dual impedance bandwidths of 16 % from 10 to 11.75GHz and ~5% over the frequency range of 11.85 to 12.5GHz. In addition, it can be noted that at the absence of the dielectric coat, the DRA supports three resonance modes of  $HE_{115}$ ,  $HE_{117}$  and  $HE_{119}$  at 10.25, 11 and 12.5 GHz, respectively. The  $HE_{117}$  mode offers respective simulated and measured gains of 9.5dBic and 9dBic at 11GHz as illustrate in Figure 2.20. The simulated and measured AR bandwidths have been acquired over a frequency range of 11.4-11.5 GHz and from 10.95-11.1 GHz, *respectively*, which correspond to a narrow AR bandwidths of 0.73% and 1% *respectively* are shown in Figure 2.21. Figure 2.22 illustrates the normalized radiation patterns for the  $HE_{117}$  mode at 11GHz with good agreement between the simulated and measured patterns.

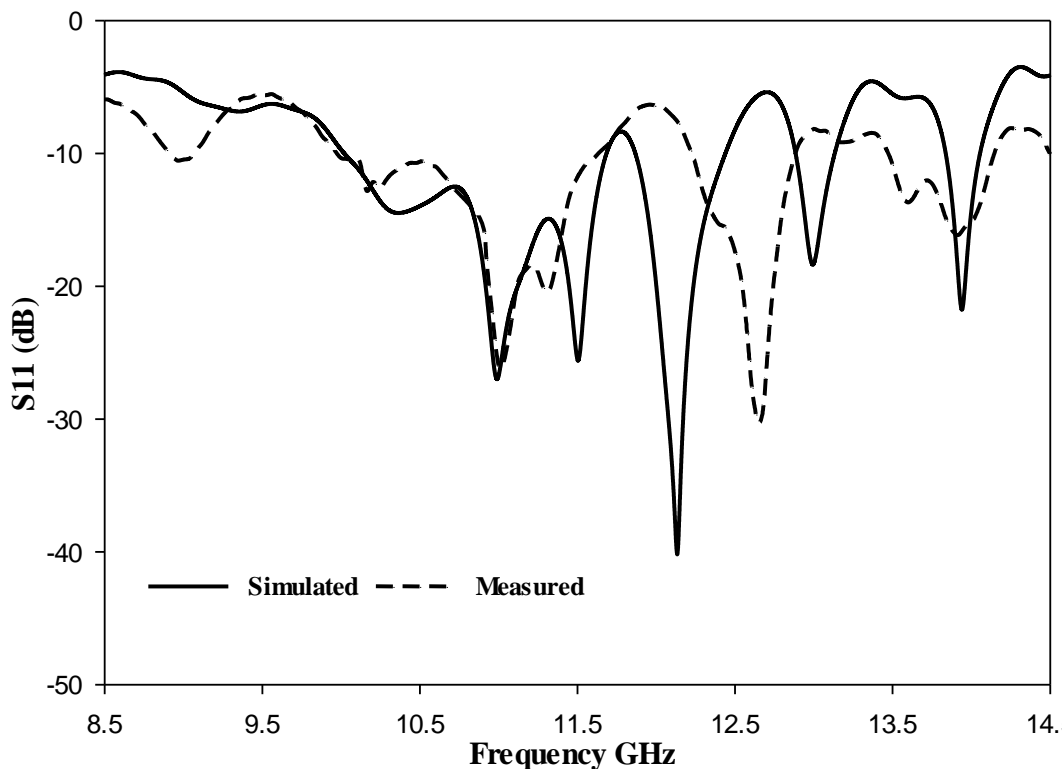


Figure 2.19: Simulated and measured reflection coefficient of a CDRA without coating

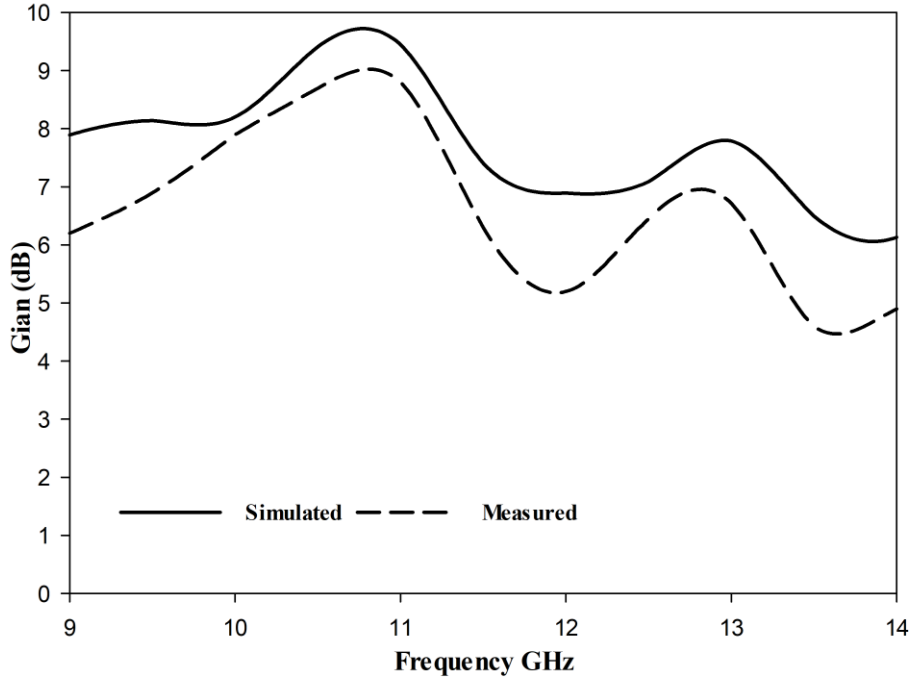


Figure 2.20: Simulated and measured gain of a CDRA without coating.

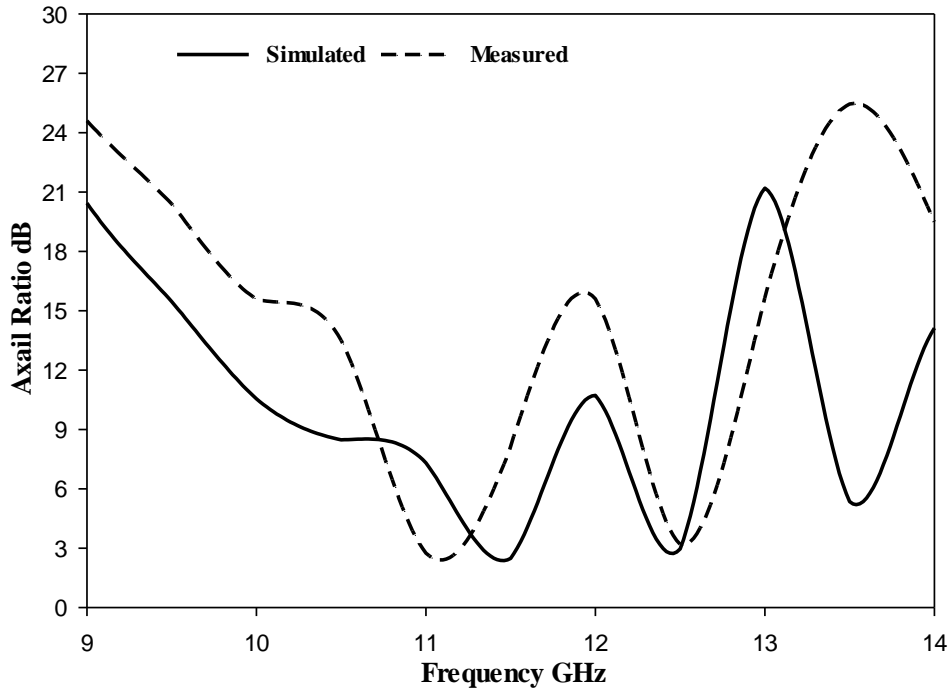


Figure 2.21: The axial ratio of a single layer DRA.

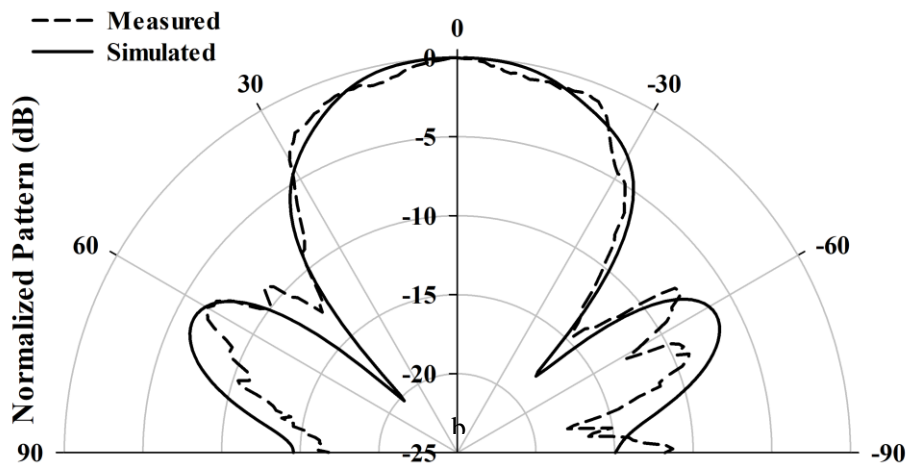
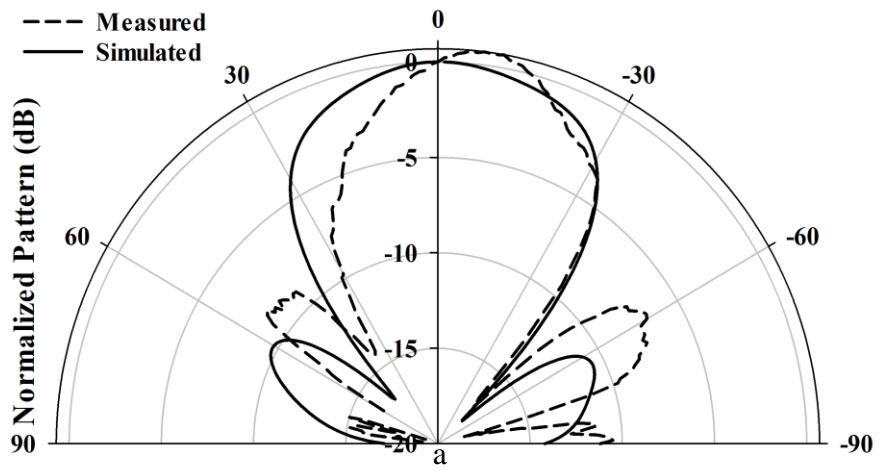


Figure 2.22: Simulated and measured radiation patterns when  $\epsilon_{r2} = 1$  at 11 GHz (a)  $\phi = 0^\circ$ , (b)  $\phi = 90^\circ$ .

## 2.4.2 A layered circularly polarized CDRA

As mentioned earlier, in order to improve the performance of the single-layer CDRA, an outer dielectric layer has been incorporated in the configuration. The respective simulated and measured reflection coefficients are 45% and 55.7% as depicted in Figure 2.23. These results demonstrate that the layered DRA supporting a multimode operation where the following modes have been excited:  $HE_{117}$  at 9.5 GHz,  $HE_{119}$  at 10.5 GHz,  $HE_{11,11}$  at 11.5GHz and  $HE_{11,13}$  at 14 GHz. In addition, adding the outer layer enhanced the AR bandwidth to 18% over a frequency range that extends from 10.4 to 12.48 GHz as shown in Figure 2.24, where it can be observed that the simulated and measured CP bandwidths cover the frequency range of 10.4-12.48 GHz and 10.3-12.6 GHz, respectively. Furthermore, these results confirm the impedance bandwidth improvement at the presence of the dielectric coat layer, which can be attributed to the fact that the added outer layer acts as a transition region between the CDRA and air, which minimizes the wave reflections and lowers the quality factor of the antenna.

Figure 2.25 illustrates a good agreement in the simulated and measured H-plane and E-plane far field patterns at the 11 GHz, it is evident that left hand circularly polarized (LHCP) has been achieved since  $E_L$  is considerably higher than  $E_R$  by ~19dB. Figure 2.26 shows the gain as a function of the frequency of layered DRA, where it is evident that when a dielectric coat is incorporated the maximum respective simulated and measured gains of 12.5 dBic and 12 dBic gain have been achieved at 11 GHz when the  $HE_{11,11}$  has excited, which illustrate the gain enhancement due to the excitation of higher order modes. It is worth pointing out that the drop in the measured gain could be attributed to experimental errors such as the losses in the cables, the SMA soldering as well as the alignment in the anechoic chambers. In Table 2-2 presents a comparison in the performance of the proposed CP layered CDRA against similar designs reported in the literature. It can be noted from this table that the combination of a spiral slot feed

and coated DRA configuration, offers an antenna that outperforms other DRAs and arrays in terms of the wide impedance and axial ratio bandwidths and higher gain.

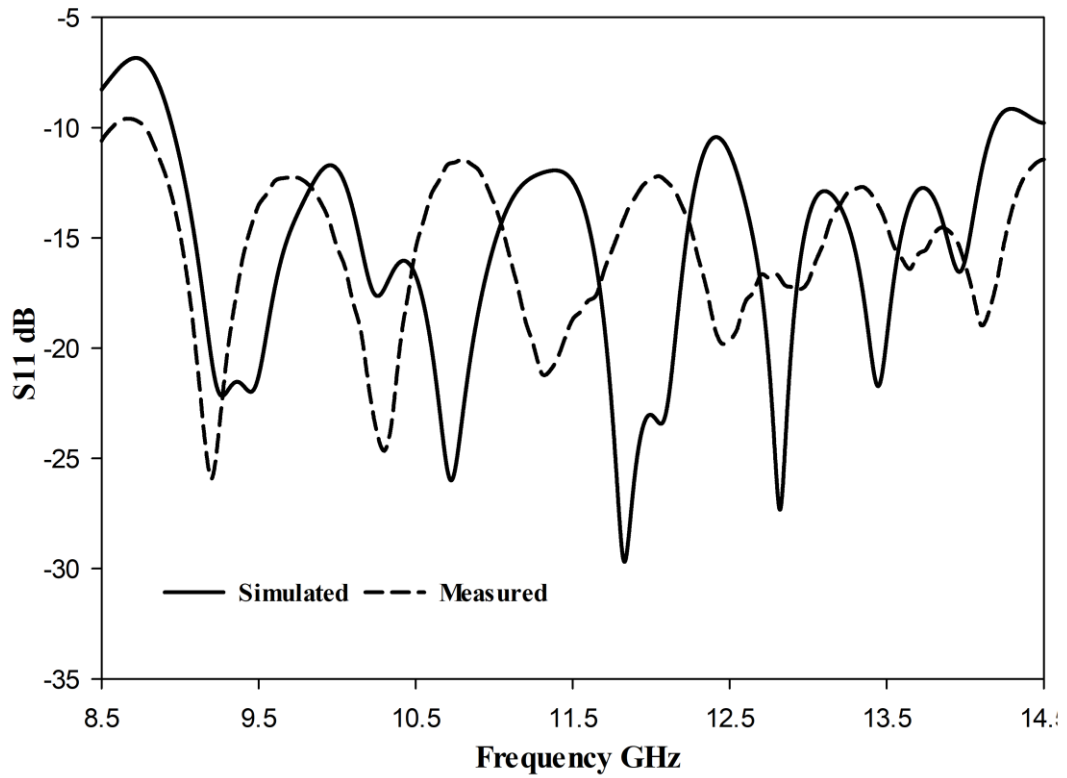


Figure 2.23: Simulated and measured reflection coefficients of layered CDRA.

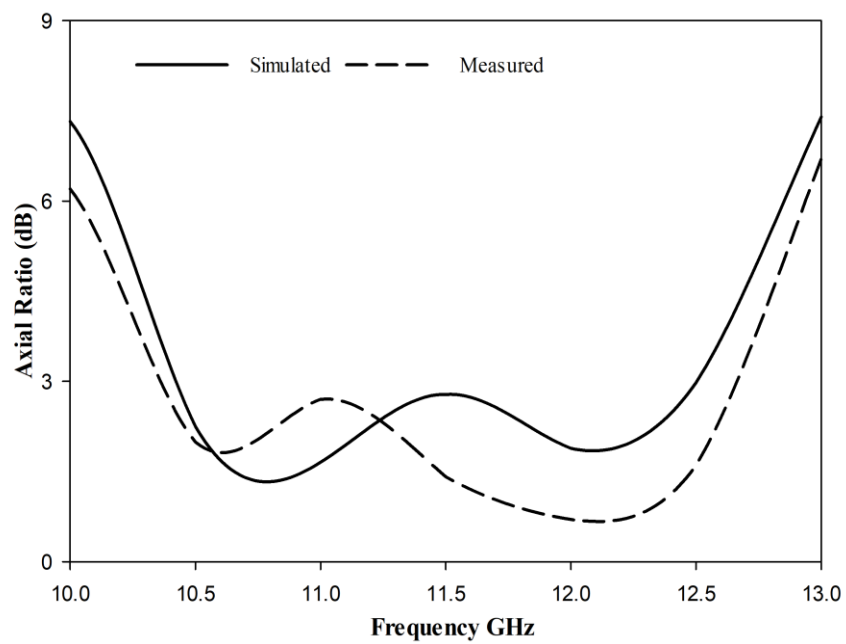
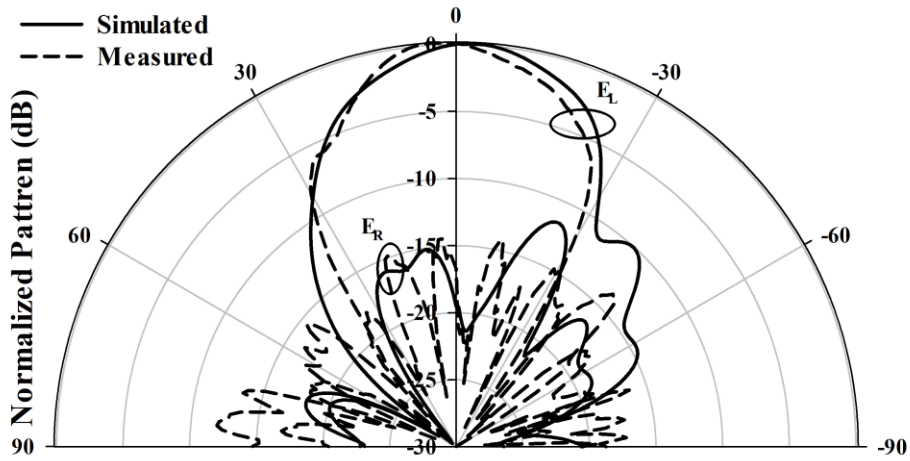
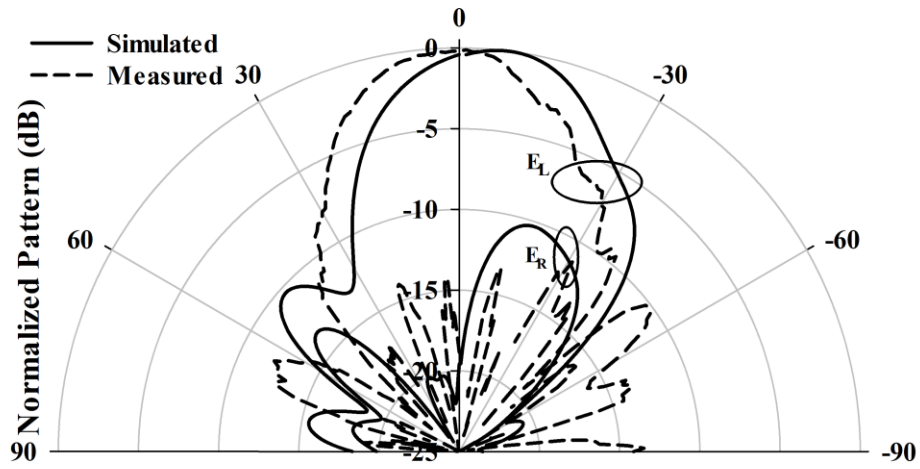


Figure 2.24: The simulated and measured CP bandwidths of a layered CDRA.



(a)



(b)

Figure 2.25: Simulated and measured radiation patterns when  $\epsilon_{r2} = 3.5$  at 11 GHz (a)  $\phi = 0^\circ$ , (b)  $\phi = 90^\circ$ .

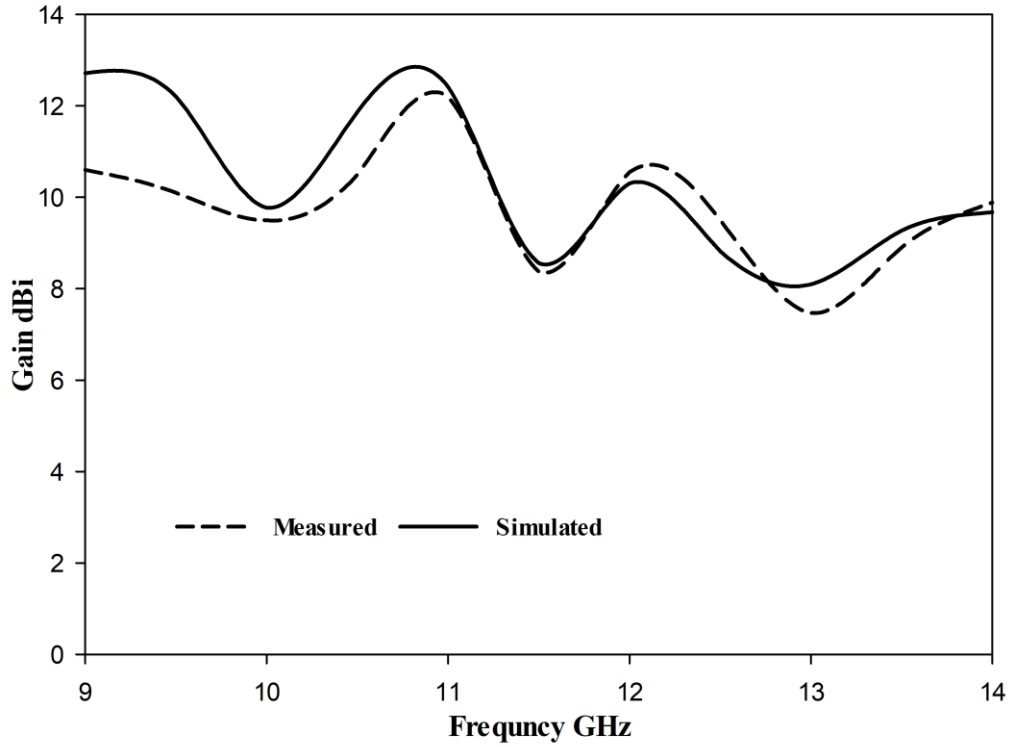


Figure 2.26: Simulated and measured gain of a CDRA with coating.

Table 2-2: Comparison between the proposed CP CDRA and previously reported designs

Antenna type	$ S_{11} $ Bandwidth %	Gain (dB <sub>ic</sub> )	Axial ratio %	Ref
Presented work	45	12.5	16	-
2 × 2 Rectangular DRA	3.4	12.9	3.1	[105]
CDRA array	30.9 (4.5–5.7 GHz)	10.0	23.52	[106]
CP CDRA	6.8(4.23–4.53GHz)	5.7	1.8	[107]
	14.9(5.95–6.9GHz)	5	1.09	
	26 (7.65–9.95GHz)	7.5	0.84	
Two layer CDRA	28.3 (9.3- 12.3 GHz)	13.9	9.5	[95]

## 2.5 Conclusions

In this Chapter, a circularly polarised two-layer cylindrical DRA that is fed using a spiral slot has been investigated theoretically and experimentally. The results demonstrate that adding the dielectric coat has improved the impedance and AR bandwidths as well as the gain. This can be explained as a result of exciting the  $HE_{119}$ ,  $HE_{11,11}$  and  $HE_{11,13}$  resonance mode in addition to the originally excited  $HE_{117}$  mode for a single layer DRA. For instance, a two-layer configuration offers respective impedance and axial ratio bandwidths and gain of 45%, 18% and 12.5 dBic compared to 16%, 0.73% and 9.5 dBic in the absence of the dielectric coat. Furthermore, a close agreement has been achieved between the simulated and measured results. In addition, the proposed antenna is most suitable for X band applications such as satellite communication and radars.

# Chapter3 High Gain Wide-Band Millimetre Wave Cylindrical DRA

## 3.1 Introduction

As a result of the potential applications of millimetre-wave (mm Wave) frequencies in 5G/B5G communication systems, mm Wave antennas are receiving increased attention due to the wide range of applications and services that are now available using mm Wave communications. Among the key technologies will be the short-range communications, mobile communications and imaging systems. As a consequence of the shorter wavelength, mm Wave signals undergo attenuation losses, which strictly limiting their transmission range. However, it is possible to compensate for the attenuation losses through the utilization of high-gain antennas, or alternatively, to increase the signal-to-noise ratio and sensitivity of systems [103]. It is well known that the commonly used metal antennas are associated with lower efficiencies at the mm Wave frequency range due to the increased Ohmic losses. . On the other hand, mm Wave directive horn antennas suffer from a number of drawbacks, including high cost and size, which make them less desirable [3]. In light of the aforementioned limitations, a mm Wave DRA represents an ideal candidate as it provides an enhanced gain with high radiation efficiency. As mentioned earlier, DRA also offers a variety of attractive features such as small size, variety of shapes, ease of excitation, low profile, and light weight [33, 108]. Further, DRA can be easily integrated with electronic circuits because of its mechanical and thermal stability. The physical size of a mm Wave DRA band is significantly smaller than those working in the microwave band, which has an impact on their practical use and creates additional challenges with respect to fabrication tolerance as well as well assembly. Nevertheless, various shapes of mm-wave DRA have been studied recently [103].

A mm Wave layered cylindrical DRA is presented in this chapter based on simulations and measurements. Based on the cylindrical DRA explained earlier for the x-band frequency range,

the antenna has been optimized for both the feed network and coat layer to improve performance. These design modifications have been carried out in response to the commercially available dielectric substrates.

### **3.2 Aperture coupling**

There are many different ways to couple electromagnetic power to a DRA structures. The coupling mechanism has a significant impact on the Q-factor and resonant frequency. As explained earlier, diverse DRA excitation methods are used in the literature, including coaxial probes, microstrip lines, and direct slot coupling.

The most common way to achieve DR coupling in microwave circuits is through this feeding technique. The DRAs are excited by the magnetic field inside by producing short horizontal magnetic dipoles. Most of the coupling is determined by the dielectric constant of the DR material. This method involves the etching of a metallic strip with a specified thickness and permittivity on one side of the substrate. Metallization and grounding are applied to the substrate. When compared with other coupling techniques, this approach is easier to fabricate. The higher permittivity of the DR allows for strong coupling, while a reduction in the DR's dielectric constant reduces the maximum amount of coupling [109].

The DR structure is placed over an aperture in the ground plane. Through the aperture, a magnetic current flow parallel to the slot length to excite the magnetic field in the DRA. The coupling from source to DRA can be controlled by ensuring the slot is properly located in strong DRA magnetic field's spots. Due to the feed network's position beneath the ground plane, aperture coupling provides the greatest isolation between the DRA and feed network, which minimizes any unwanted spurious radiation from the microstrip feed line. In addition, another advantage of aperture coupling is the ease of fabrication[110].

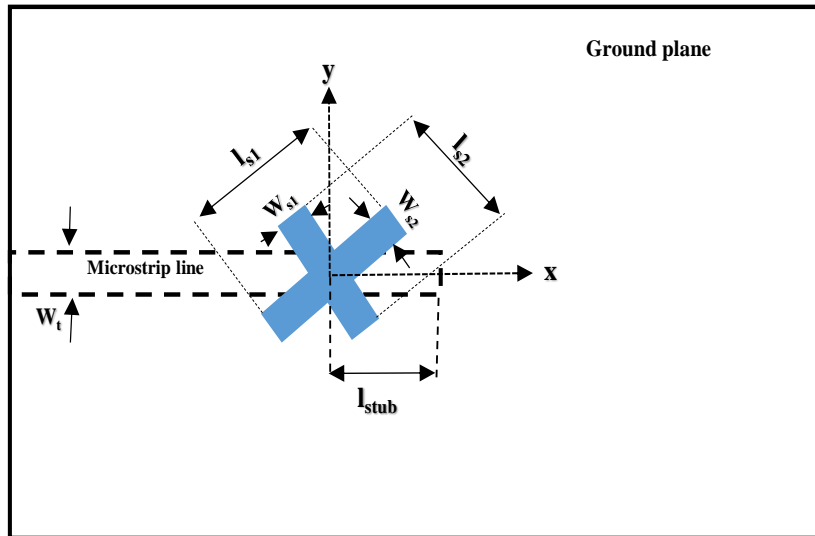


Figure.3.1: The slot-cross feed

Once more, the improvements in the impedance and circular polarization bandwidths as well as gain have been studied for the proposed two-layer cylindrical DRA. Employing a cross-slot aperture has been widely to excite circularly polarised rectangular and cylindrical DRAs with wide bandwidths [95, 111]. It is worth noting that the spiral slot feed utilized in Chapter 2 was also incorporated in this design. It successfully achieved an impedance bandwidth of 55.3% spanning the frequency range of 19.3 GHz to 34.2 GHz. Additionally, it reached an axial ratio of 11% over the frequency range of 28.3 GHz to 31.6 GHz, with a gain of 10 dBic at 29 GHz. However, certain fabrication constraints posed limitations. One such constraint was the need for the inter-arm distance of the spiral slot to exceed 0.1 mm, a criterion unmet in this design as the distance reached only 0.06 mm. This led us to explore alternative feed mechanisms for the Circularly Polarized Dielectric Resonator Antenna (CDRA) within this frequency range. Consequently, a cross slot was introduced as a substitute, the details of which will be elaborated in the following section of this chapter. The slot-cross feeding is depicted in Figure 3.1. In order to achieve the required impedance matching between the DRA and the feed micro-strip line, the slot arms' length and width need to be optimised to provide maximum coupling without increasing the back-lobe radiation. Subsequently, the slot dimensions are a trade-off between

suitable coupling to the DRA and the avoidance of excessive back lobe radiated. To offer the required coupling the dimensions of the slot size as well as the stub length can be chosen as [112]:

$$l_s = \frac{0.4\lambda_{o0}}{\sqrt{\epsilon_e}} \quad 3.1$$

where  $\epsilon_e$  denotes the effective permittivity that can be approximated as

$$\epsilon_e = \frac{\epsilon_r + \epsilon_s}{2} \quad 3.2$$

Which  $\epsilon_r, \epsilon_s$  represent the dielectric constants of the DRA and substrate, respectively.

Moreover, the width of the slot aperture,  $w_s$ , which can be chosen as  $w_s=0.2l_s$  [110].

Finally, the length of the microstrip line can be extended beyond the slot to create a matching stub section. The recommended starting length of the stub is [110]:

$$l_{stub} = \frac{\lambda_e}{4} \quad 3.3$$

Where  $\lambda_e$  is the effective wavelength.

### 3.3 Antenna configuration

This study involves the design and measurement of a mm-wave cylindrical DRA that works at higher-order modes. It should be noted that the DRA configuration of Chapter 2 has been scaled down with further optimisation to operate at the mmWave frequencies. The two-layer cylindrical DRA and feed network configurations proposed in this study are presented in Figure 3.2,. As explained in Chapter 2, the inner layer consists of the cylindrical Alumina DRA that has been fabricated by T-Ceram, with a loss tangent of 0.002 and a fabrication tolerance of 0.05mm. The DRA's radius and height have been chosen as  $R_d = 1.5$  mm,  $H_d = 10$  mm, respectively. Moreover, an outer layer of Polyimide has been applied to the DRA that has dimensions of  $R_c = 8$  mm and  $H_c = 12.15$  mm, and a dielectric constant of 3.5. Additionally, the

antenna was placed on a copper ground plane with a size of  $50 \times 50 \text{ mm}^2$ , which was located on top of a dielectric substrate measuring 0.8mm in thickness. The latter was produced using a Rogers material (RO4350B) with a dielectric constant of 3.48 and a loss tangent of 0.0037.

Additionally, unequal arms lengths for the cross slot have been etched on the ground plane to generate the CP radiation. The length of the cross-slot arms have been optimized as;  $l_{s1}=1.77$  mm and  $l_{s2}=2.85$  mm. The same width of  $w_s=0.45$  mm has been utilised for both slot arms. Each of the slots has been rotated by  $45^\circ$  with respect to a  $50 \Omega$  micro strip line that includes an open stub length of  $l_{stub} = 1.27 \text{ mm}$  for optimum matching. As a result, the following two near-degenerate perpendicular modes of equal amplitude and  $90^\circ$  phase difference have been excited to generate the circular polarisation  $\text{HE}_{117}$  at 24 GHz ,  $\text{HE}_{119}$  at 29 GHz and  $\text{HE}_{11,11}$  at 32.5 GHz.

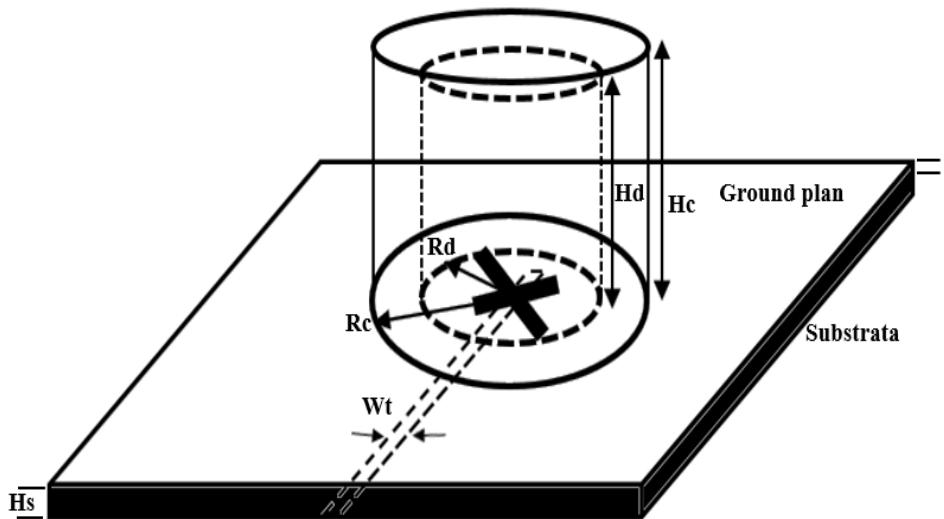


Figure 3.2: The configuration of the proposed layered CDRA

### 3.3.1 Parametric Studies

The time domain solver in CST MWS has been used to conduct the simulations. In order to determine the optimal dimensions that can offer wide impedance and axial ratio bandwidths, the length of the slot arms has been optimized and the thickness of the outer layer has been

held constant as well as the other way around when optimising the outer layer by parametrically sweeping the CST MWS.

Moreover, a study has been conducted to determine how reflection coefficient, gain and axial ratio are affected by the permittivity of the dielectric coat when the outer layer dimensions are optimized for the different values of  $\epsilon_{r2}$ . The DRA dimensions have been kept constant at  $R_d=1.5\text{mm}$  and  $H_d=10\text{mm}$ , respectively. In the absence of the dielectric coat, the highest gain was achieved at 22 GHz with excitation of resonance mode  $HE_{115}$ . With reference to Table 3.1 a coating layer with  $\epsilon_{r2}=3.5$ , the impedance bandwidth is considerably wider than with  $\epsilon_{r2}=2, 6$  and  $10$ . Considering  $\epsilon_{r2}=3.5$ , the  $S_{11}$  impedance and axial ratio bandwidths are considerably wider at 88% and 23.3% respectively. In this case, the impedance bandwidth is increased due to the fact that the second layer acts as a transition layer between the DRA and free space [113]. By increasing the permittivity of the external layer, we've achieved a consequent reduction in its optimal radius dimensions. Specifically, when the permittivity values were set to 2, 3.5, 6, and 10, the corresponding optimal radii shrank to 12.5, 8, 5.5, and 3 mm, respectively. This outcome might be due to the inherent properties of dielectric materials with higher permittivities, which typically result in smaller physical sizes. Importantly, this pattern is consistent with previous studies [114, 115], which reported a diminishing impedance bandwidth when the external layer's permittivity is reduced to approximately half that of the original DRA. Additionally, the highest gain and axial ratio bandwidth were 12.29 dBic and 23.3% respectively. Have been attained when  $\epsilon_{r2} = 3.5$ ,  $R_c = 8$  mm,  $H_c = 12.15$  mm. By contrast,

at 31GHz, the lowest gain and axial ratio bandwidth have been achieved when  $\epsilon_{r2}=6$  as 9.6 dBi and 0.93%, respectively.

Table 3-1: Optimum parameters of the coat layer

$R_c, H_c$ mm	$\epsilon_{r2}$	Frequency (GHz)	Resonance mode	$S_{11}$ BW%	Gain (dBi)	AR BW %
No coating	1	22 GHz	HE <sub>115</sub>	28.6	7.64	3.6
12.5,12.15	2	32.5 GHz	HE <sub>11,11</sub>	61	8.8	5.7,3.3
8,12.15	3.5	29 GHz	HE <sub>119</sub>	88	12.29	23.3
5.5,12.15	6	31	HE <sub>11,11</sub>	23	9.6	0.93
3,12.15	10	26.5	HE <sub>11,11</sub>	11.5	12	1.29

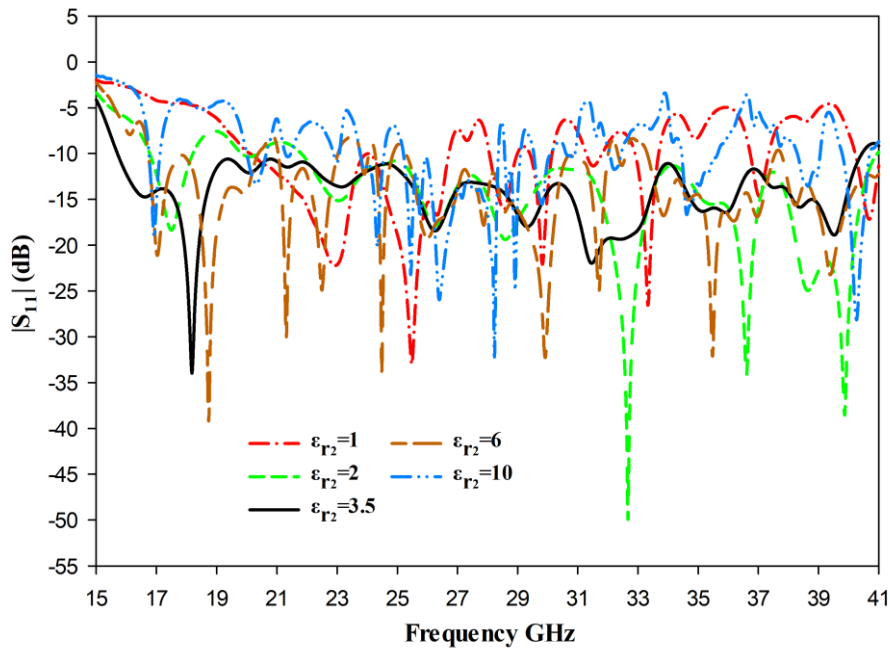


Figure 3.3: Simulated  $|S_{11}|$  with various outer layer permittivity  $\epsilon_{r2}= 1, 2, 3.5, 6$  and  $10$ .

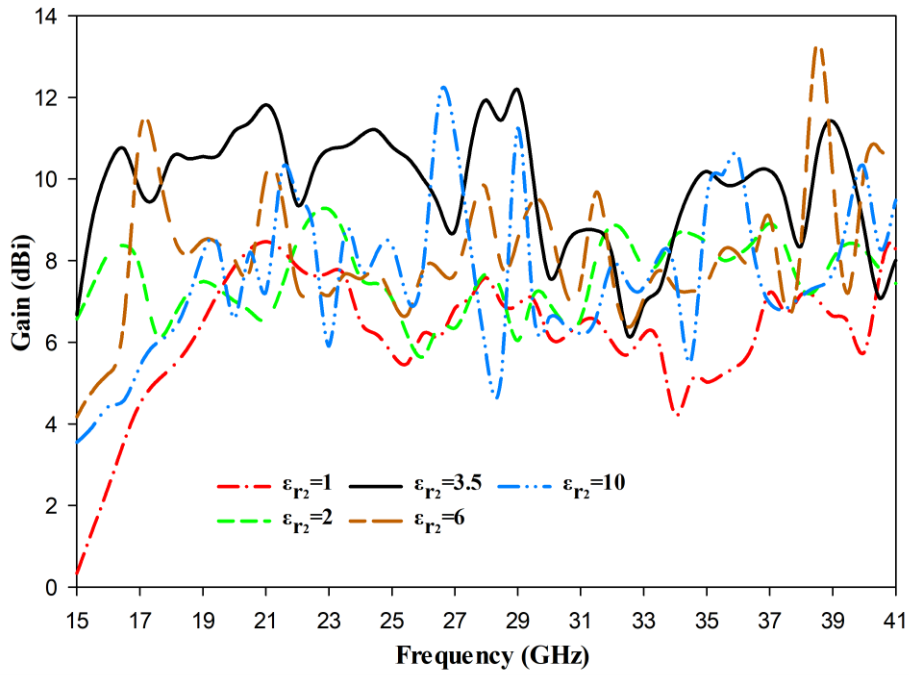


Figure 3.4: Simulated realized gain with various outer layer permittivity of  $\epsilon_{r2}= 1, 2, 3.5, 6$  and  $10$ .

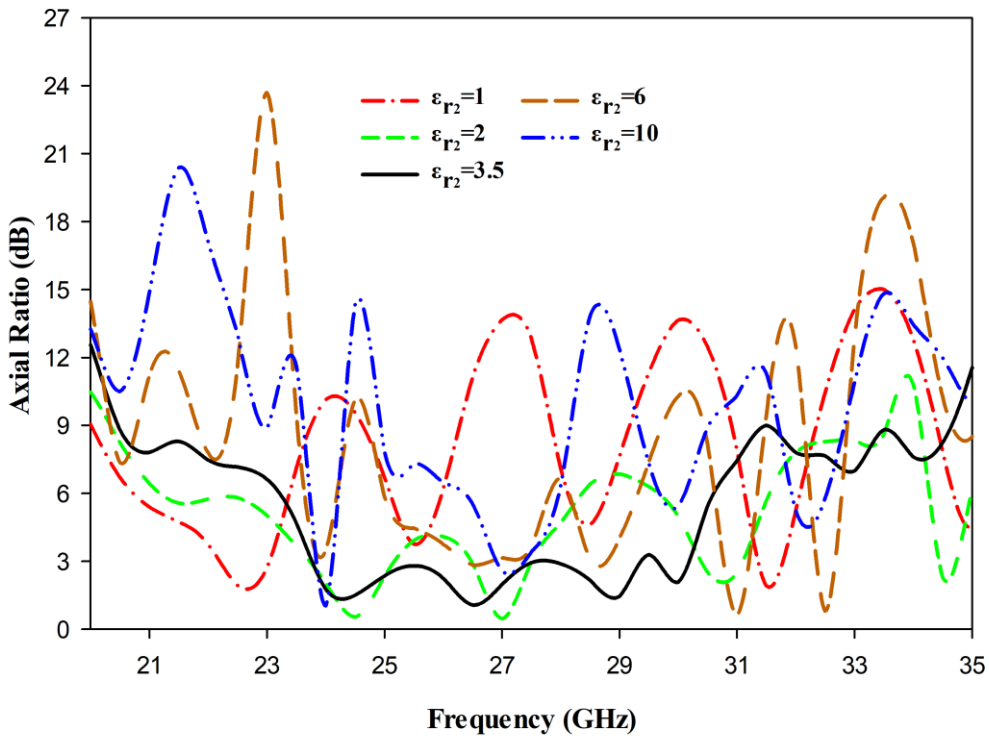


Figure 3.5: Simulated axial ratio with various outer layer permittivity of  $\epsilon_{r2}= 1, 2, 3.5, 6$  and  $10$ .

### ***i The Impact of the Slot Arm's Length***

In order to understand the impact of the slot arms length on the modes' resonance frequencies and bandwidth, the length of the first slot arm varied between 1.77mm and 2.85mm. Figures 3.6 and 3.7 illustrate the impact varying the first slot arm's length ( $l_{s1}$ ) on the  $S_{11}$  and AR, respectively, when the second stub's arm length remains fixed at 1.77 mm. As the required two orthogonal modes have not been achieved in the case of  $l_{s1} = l_{s2} = 1.77$  mm, a linear polarization has been accomplished containing triple impedance bandwidths of 7.4%, 5.3% and 7.9% that correspond to the resonance mode of  $HE_{11,11}$ ,  $HE_{11,13}$ ,  $HE_{11,15}$ , respectively. However, by increasing the length  $l_{s1}$  to 2.85 mm, it was possible to attain much broader impedance and axial ratio bandwidths of 88% and 23.6%, respectively. This is due to the fact that the following resonance modes  $HE_{11,15}$ ,  $HE_{11,17}$ ,  $HE_{11,19}$ ,  $HE_{11,11}$ ,  $HE_{11,13}$  and  $HE_{11,15}$  have been excited at 18 GHz, 22 GHz, 29 GHz, 32.5 GHz, 36 GHz and 40 GHz respectively. Furthermore,  $S_{11}$  bandwidths of 35.7%, 17.3% and 70% have been achieved when  $l_{s1}$  equals to 2.13 mm and 2.49 mm, respectively. Moreover, Figure 3.8 illustrates the variation of the  $S_{11}$  bandwidth as a function of the arm length, with the maximum  $S_{11}$  bandwidth achieved using the same arm lengths as that for the widest CP bandwidth of 2.85 mm.

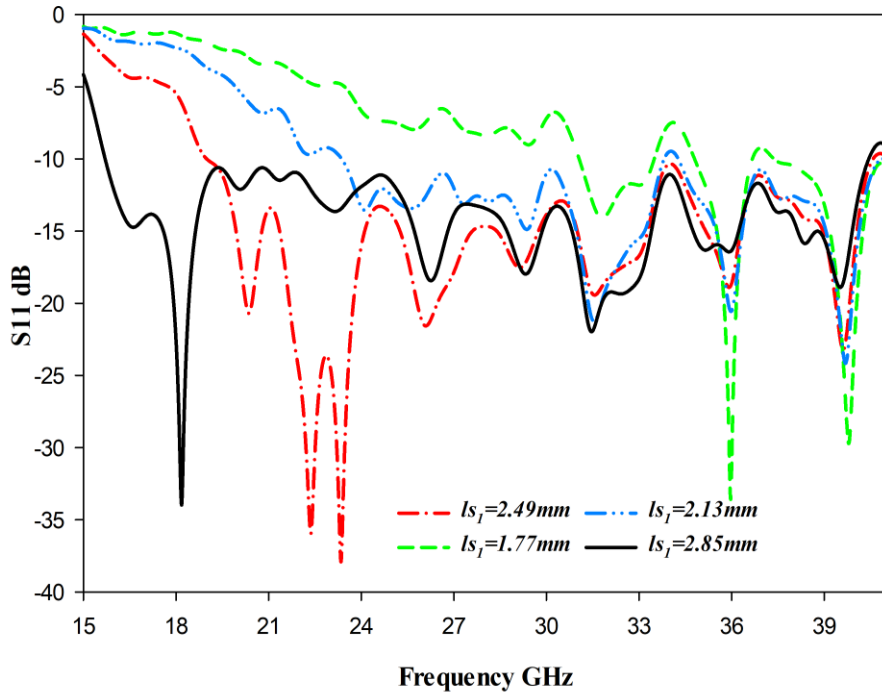


Figure 3.6: Simulated  $|S_{11}|$  with various slot arm length.

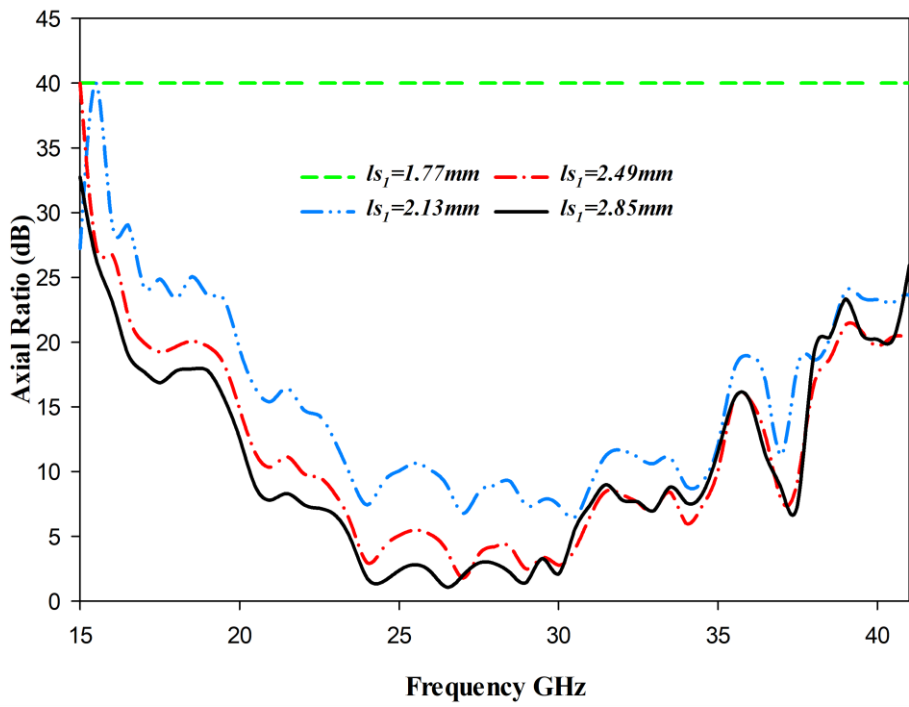


Figure 3.7: Simulated axial ratio with various slot arm length

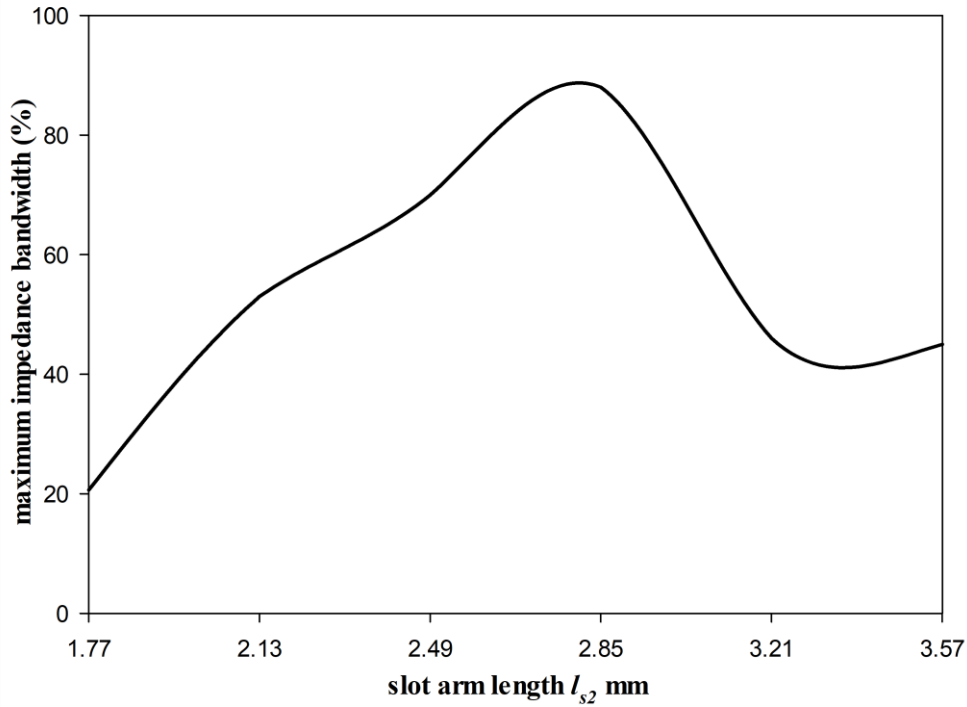


Figure 3.8: Maximum bandwidth as function of the slot arm length

### ***ii The Impact of the Outer Layer's Thicknesses***

The impact of the outer coat layer thicknesses,  $\delta a$ , have been investigated as illustrated in in Figures 3.9, 3.10 and 3.11 using the optimised cross-slot arm lengths of 2.85 and 1.77 mm. These findings demonstrate that a thicker outer layer with  $\delta a = 6.5$  mm improves the impedance and AR bandwidths as well as gain to 88%, 23.3%, 12.29 dBic, respectively, compared to 28.6%, 3.6%, and 7.64 dBic for a single layer configuration. As the outer layer serves as a transition layer between the DRA and free space, which improves the impedance matching bandwidth, by minimising the reflection at the DRA-air interface that exists in a single layer DRA. The presence of the coat also reduces the effective permittivity of the layered configuration, which also contributes to the bandwidth enhancement. The combined bandwidth brought on by multi-mode excitation at nearby resonance frequencies, where the adjacent individual bandwidths

are merged. The gain has been increased due to exciting the higher order modes of  $HE_{115}$ ,  $HE_{117}$ ,  $HE_{119}$ ,  $HE_{11,11}$ ,  $HE_{11,13}$  and  $HE_{11,15}$  at 18 GHz, 22 GHz, 29 GHz, 32.5 GHz, 36 GHz and 40 GHz, respectively, rather than just the  $HE_{115}$  and  $HE_{117}$  modes at 23 GHz and 25.5 GHz, respectively, for a single layer antenna. It is worth mentioning that when adding the coat, the higher order modes are generated by confining the electric field hence, the increment of gain is noted due to increasing the number of short magnet dipoles.

A study has been undertaken to investigate the impact of fabrication errors by analysing the mode's resonance frequency variation for fabrication errors 0.025, 0.05, 0.075, and 0.1mm for outer layers of thickness  $\delta a=6.5$ . A fixed coat dimension has been tracked for each case by adding the error to the cylindrical DRA radius. Based on Table 3-2, it can be noted that increasing the outer layer thickness minimizes the impact of fabrication errors. This may be explained as a result of the fact that in layered CDRA's, dimension variations occur in the vicinity of the DRA surface, which means that wave reflections at the cylindrical DRA surface are reduced compared to single layer DRAs, which leads to improved fabrication tolerance.

Table 3-2: Effect of fabrication errors on the layered CDRA's resonance frequency.

Fabrication error (mm)	One layer CDRA $\Delta f$ (%)	Two layered CDRA $\Delta f$ (%)
0.025	0.408	0.011
0.05	0.828	0.159
0.075	1.06	0.165
0.1	1.417	0.17

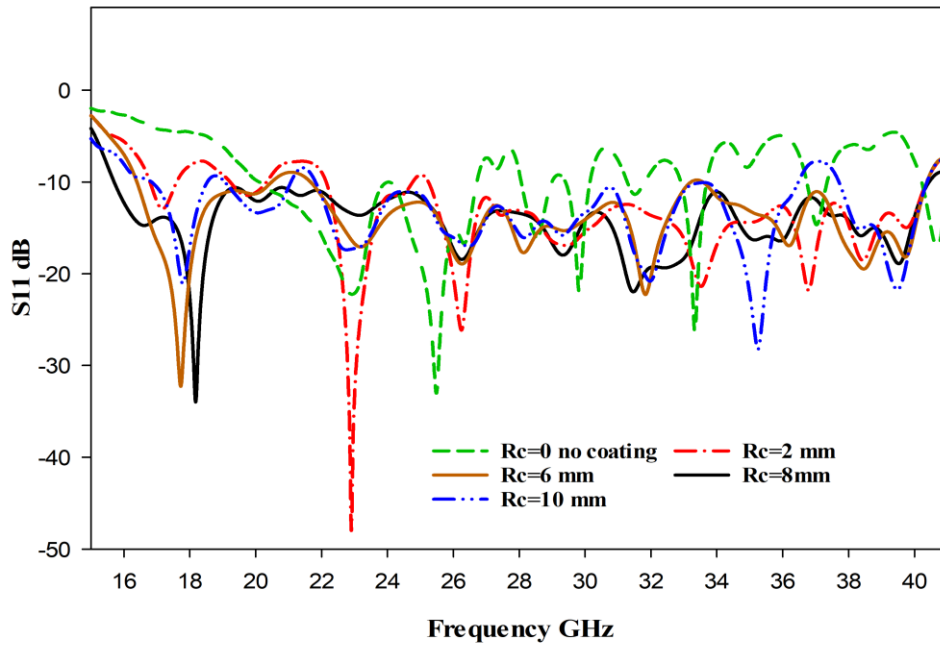


Figure 3.9: Simulated  $|S_{11}|$  with various outer layer thicknesses.

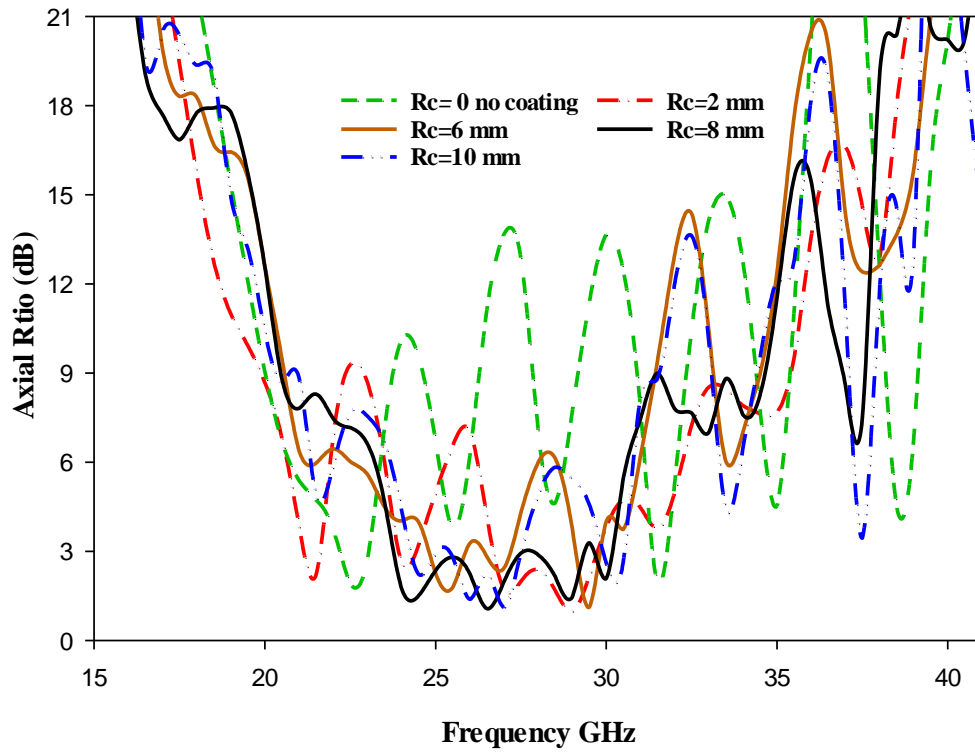


Figure 3.10: Simulated axial ratio with various outer layer thicknesses

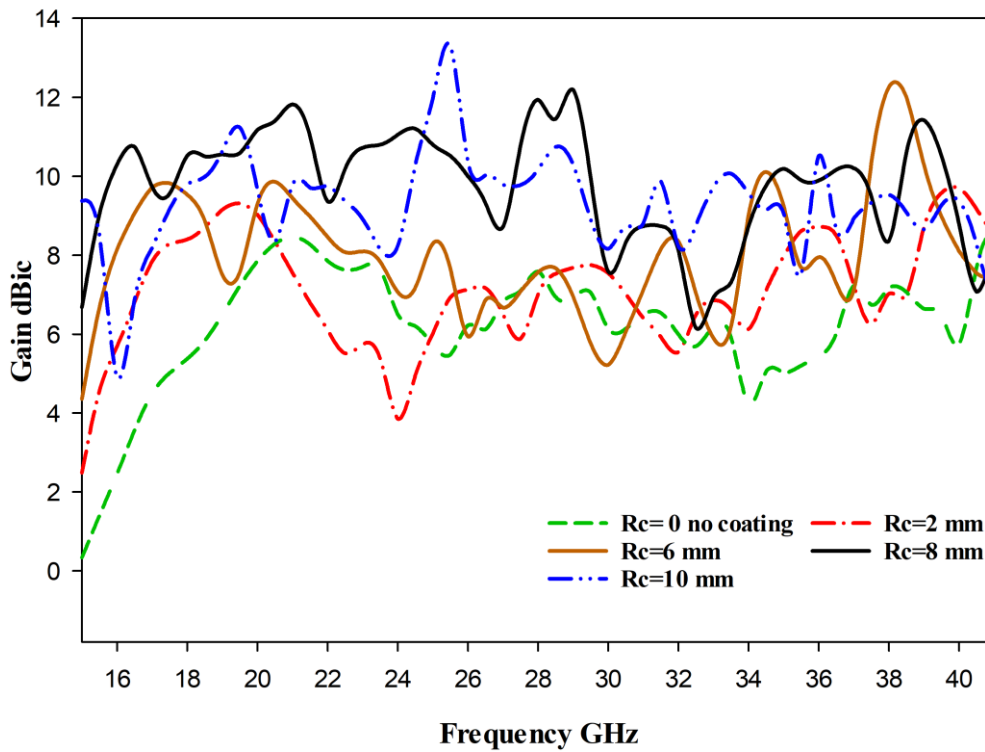
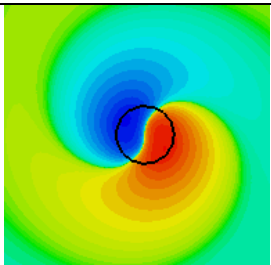
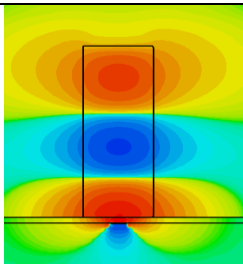
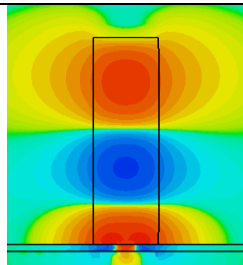
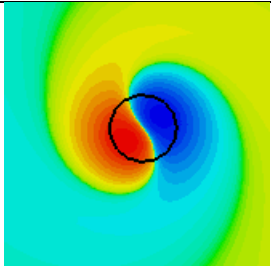
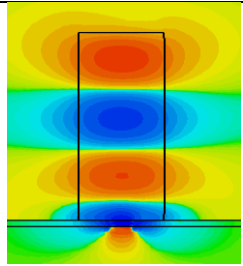
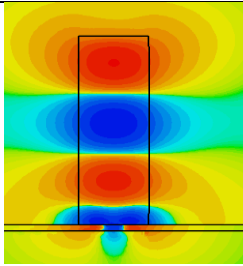
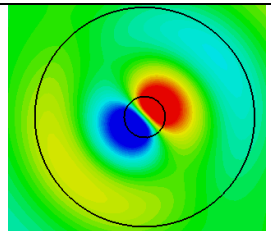
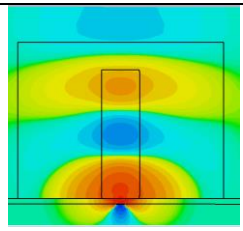
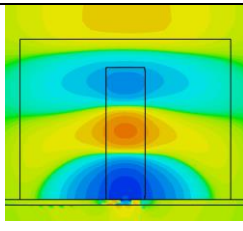
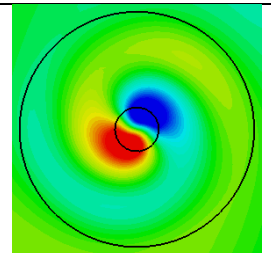
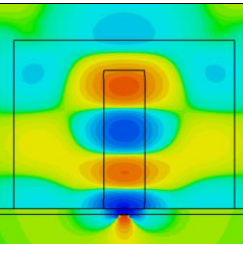
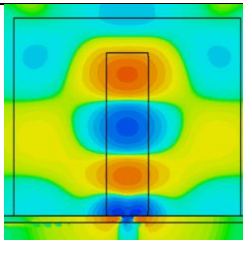
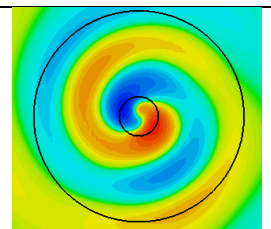
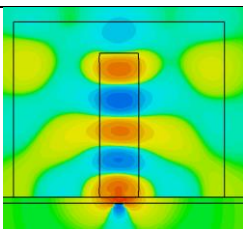
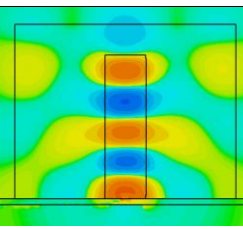
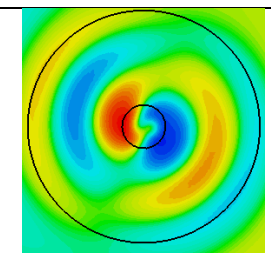
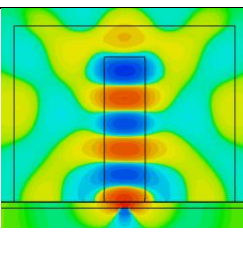
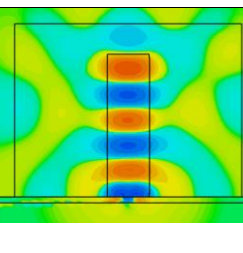


Figure 3.11: Simulated realized gain with various outer layer thicknesses

As can be observed from Figure 3.11, an increased gain has been achieved due to the enhanced energy confinement within the dielectric resonator layer as well as by increasing the number of magnetic dipoles inside the CDRA as can be observed in Figure 3.12. This is ultimately due to an increase in the thickness of the outer layer. Furthermore, as can be seen from Figures 3.9, 3.10 and 3.11, a maximum bandwidth has been consistently achieved by applying an outer layer radius of  $R_c=8\text{mm}$ . Numerous studies support that using a material with higher permittivity can store larger quantities of energy because the Dielectric Resonator Antenna (DRA) radiates across the entirety of its surface, barring the grounded area [45]. However, this can lead to a decrease in radiation efficiency. To counteract this, a low permittivity material is employed for the outer layer. In this configuration, the dielectric coating acts as a transition region between the waves inside the Dielectric Resonator (DR) antenna and those outside. This coating lessens the sudden permittivity shift between the dielectric and air[113]. Consequently,

the DR structure endures more radiation loss, leading to a wider impedance bandwidth. Moreover, Figure 3.12 illustrates the simulated H-field and E-field distributions for the various excited modes in several planes of the resonator, which were obtained from the CST Eigenmode solver and excited inside the specified CP two-layer cylindrical DRA at different targeted frequencies. The results of the comparison clearly show that the modes are present within the cylindrical DRA.

EM filed plane component	Top surface, Ez	Hx (yz plane)	Hy (xz plane)
One layer CP CDRA HE <sub>115</sub> at 22 GHz			
One layer CP CDRA HE <sub>117</sub> at 25.5 GHz			
Two layered CP CDRA HE <sub>115</sub> at 18 GHz			
Two layered CP CDRA HE <sub>117</sub> at 22 GHz			
Two layered CP CDRA HE <sub>119</sub> at 29 GHz			
Two layered CP CDRA HE <sub>11,11</sub> at 32.5 GHz			

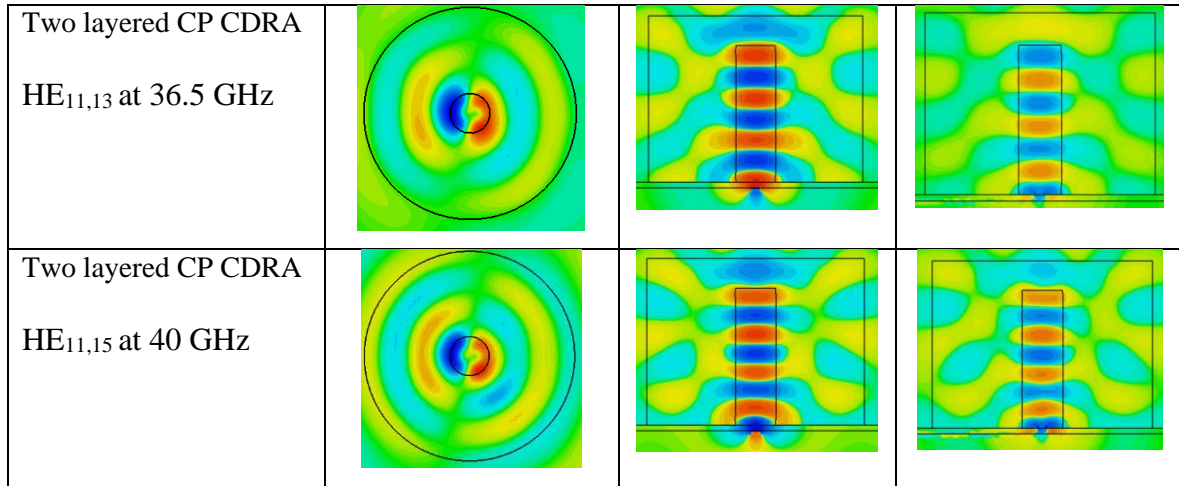


Figure 3.12: Distributions of the E-field and the H-field of circularly polarized cylindrical DRAs of higher order.

### 3.4 Experimental Results

A prototype of the proposed antenna has been fabricated in order to validate the simulations. The inner layer of cylindrical DRA has been manufactured by T-CERAM company using Alumina with fabrication tolerance of 0.06mm,  $\epsilon_r=10$  and  $\tan \delta < 0.002$ . The outer layer has been fabricated with the aid of 3D printing technology using Polyimide material with dielectric constant of 3.5 and loss tangent of 0.0027. In addition, the antenna has been placed on a copper ground plane on top of a Rogers (Ro4350B) dielectric substrate with respective thickness of 0.42mm, permittivity of 3.48 and loss tangent of 0.0037 provided by Wrekin Circuits. The whole prototype has been fed using a microstrip line that has been printed on the lower side of the Rogers substrate. The reflection coefficient has been measured using Agilent Technologies E5071C mm-wave vector network analyser that is connected through a 50 coaxial cable to the microstrip line using a 2.4 mm SMA. The radiation patterns measurements have been conducted using an (SNF-FIX-1.0) near field system. The antenna and its feed network are illustrated in the Figure 3.13.



(a)



(b)



(c)

Figure 3.13: The prototype of a layered CDRA (a) Feed network with highlighted layered CDRA position, (b) The inner and the outer layered of CDRA, (c) Layered CDRA connects to the chamber.

It is worth mentioning, the key challenges in the mm-wave range to get precise measurements are the precise alignment and bonding of the DR. The alignment has been addressed using a 3D printer to outline the coated DRA position on the copper ground plane of the fabricated feed network at the University of Sheffield as depicted in Figure 3.13 (a). Next, the antenna was bonded to the ground plane using a double-sided adhesive copper tape with a thickness of 0.08

mm that has been placed beneath the outer dielectric coat further away from the feeding cross slot.

A comparison between the simulated and measured reflection coefficients are illustrated in Figure 3.14. The simulated impedance bandwidth of 88% covers the frequency range of 15.7GHz to 40.4 GHz, correlates well with the measured counterpart of 83.4% that covers a frequency range of 16.9 GHz to 41 GHz. These results demonstrated that the layered DRA supporting a multimode operation where the  $HE_{115}$ ,  $HE_{117}$ ,  $HE_{119}$ ,  $HE_{11,11}$ ,  $HE_{11,13}$  and  $HE_{11,15}$  resonance modes were excited at 18 GHz, 22 GHz, 29 GHz, 32.5 GHz, 36 GHz and 40 GHz, respectively. Figure 3.15 illustrates the simulated and measured gains with maximum of 12.29 dBic and 11.3dBic, respectively, when the  $HE_{119}$  is excited. The achieved high gain is due to exciting the aforementioned higher order mode as a result of incorporating the dielectric coat.

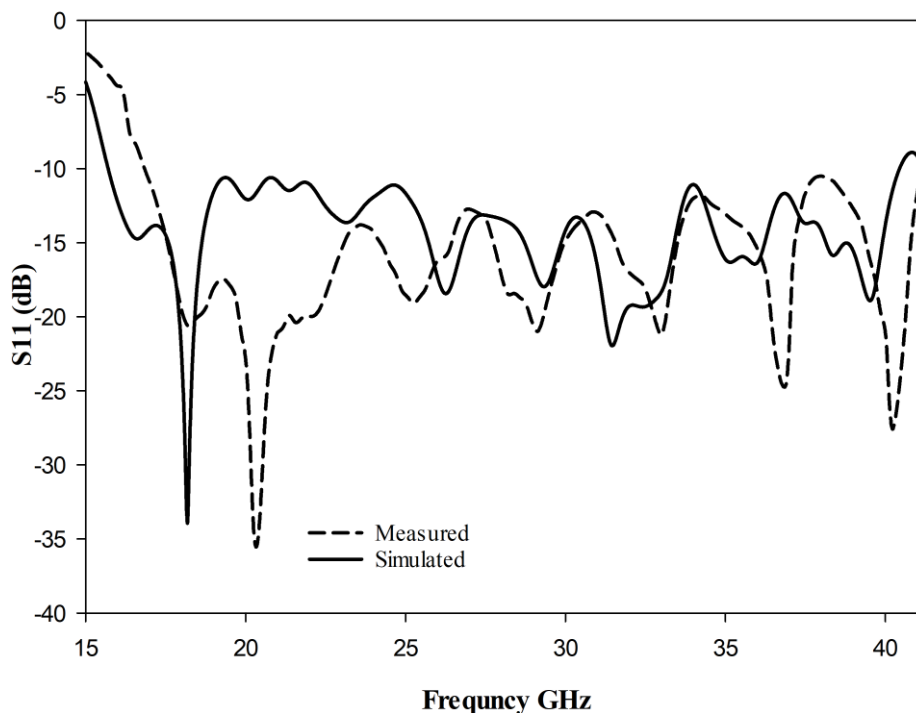


Figure 3.14: The simulated and measured reflection coefficient of layered CDRA.

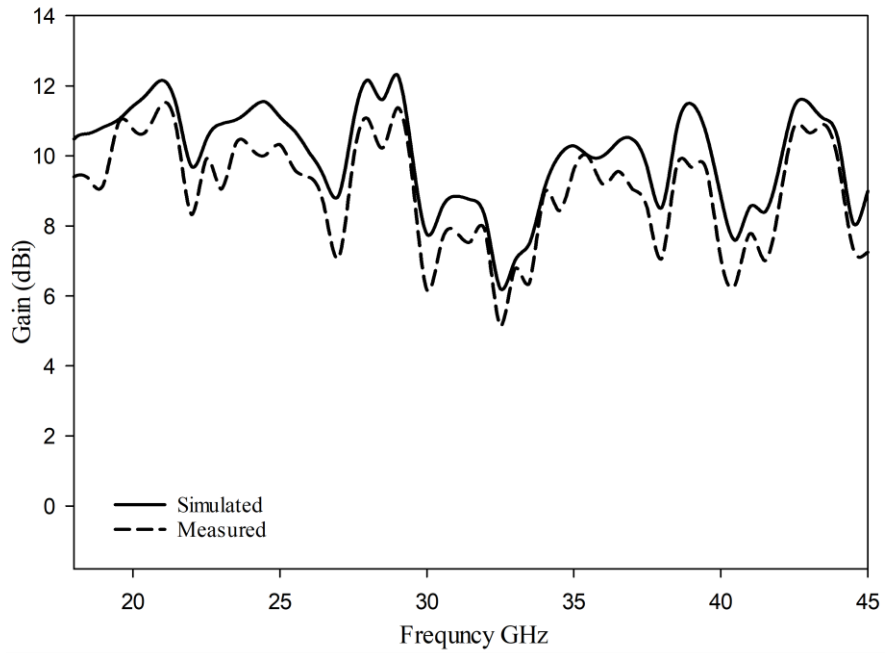


Figure 3.15: Simulated and measured of the gain of a HDRA with coating.

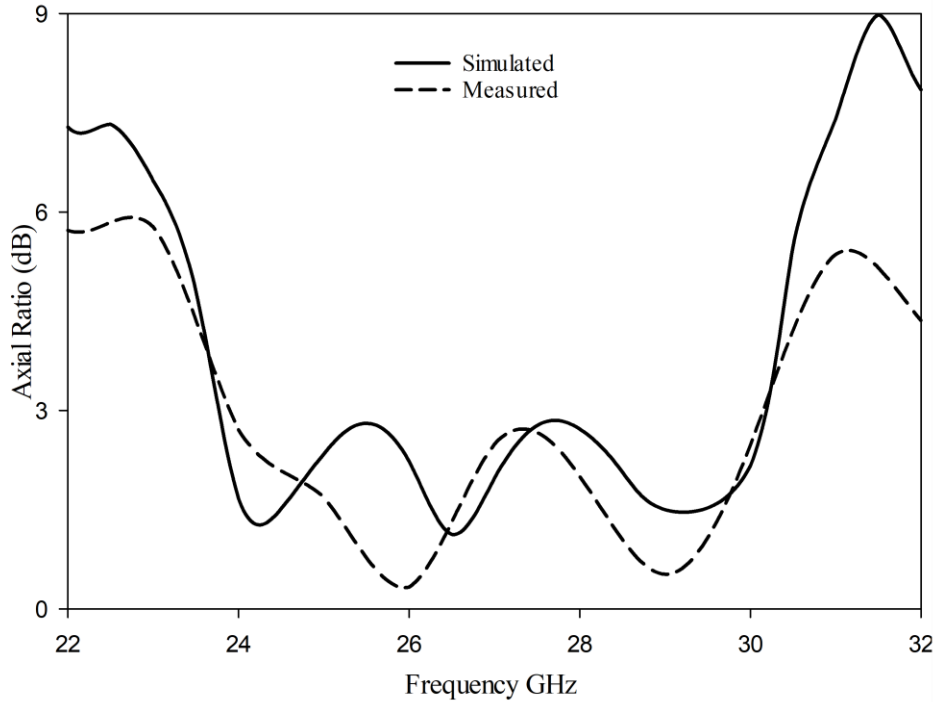


Figure 3.16: The simulated and measured CP bandwidth of layered CDRA

Figure 3.16 presents the results of simulated and measured axial ratio at the boresight,  $\theta=0^\circ$ . The simulated 3-dB AR bandwidth is 23.3%, which is comparable to the measured counterpart of 22.2%. The proposed CP CDRA's radiation patterns are presented in Figure 3.17 for the  $HE_{119}$  mode at 29 GHz, i.e. within the axial ratio bandwidth, with a good agreement between the simulated and measured patterns. A right-hand CP (RHCP) exists with respect to the far field patterns because the  $E_R$  component is  $\sim 11.66$  dB greater than the  $E_L$  counterpart. According to Table 3-3, the proposed CP layered CDRA offers a wide impedance and axial ratio bandwidth, higher gain, and is less complex than previously studied designs.

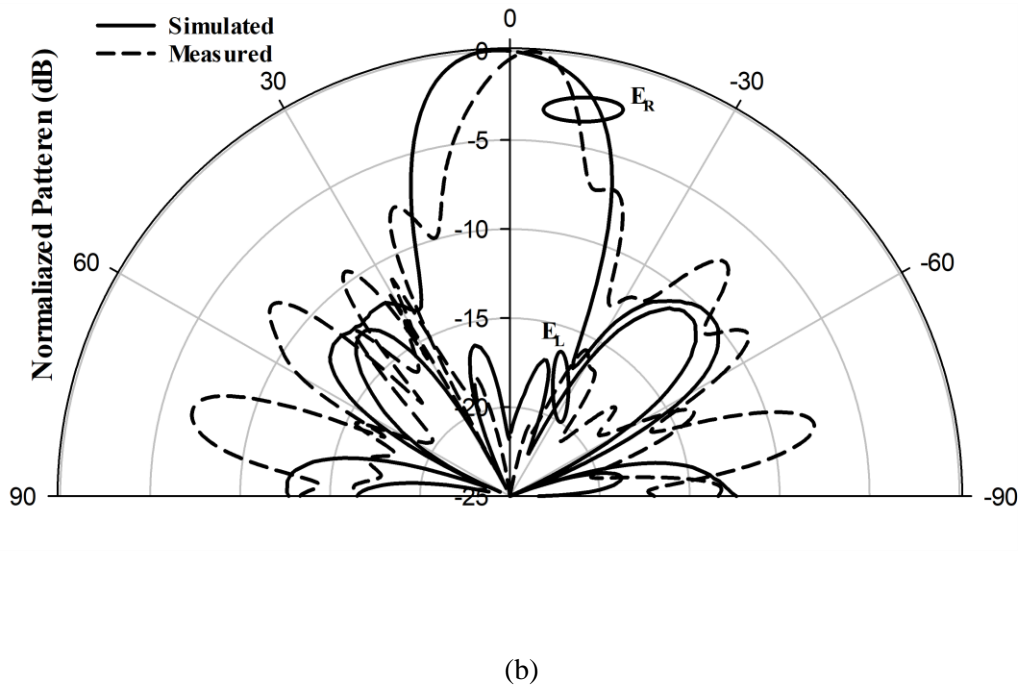
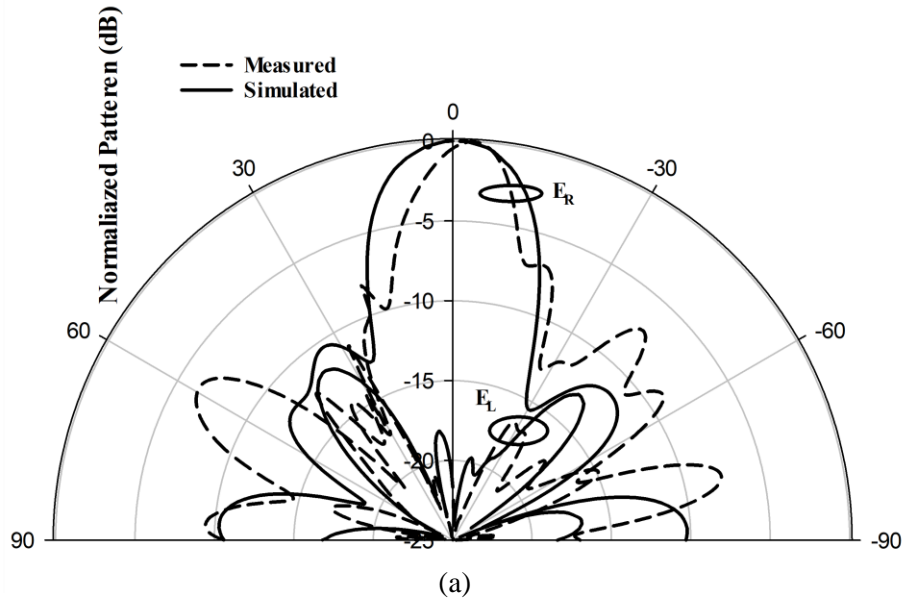


Figure 3.17: Simulated and measured radiation pattern at 29 GHz (a)  $\phi=90^\circ$ , (b)  $\phi=0^\circ$

Table 3-3: Comparison between the proposed CP CDRA and previously reported designs

Antenna type	Feeding mechanism	$ S_{11} $ Bandwidth	Gain (dBic)	AR Bandwidth	Ref
Present work	Cross slot	83% 16.9 GHz - 41.1 GHz	11.3	22.2%	-
Layered RDRA	Cross slot	36.3 % 21.5GHz-31 GHz	12.5	13.7%	[111]
2 × 2 CP DRA array	planar feeding network	16.4% 27GHz to 31.85 GHz	12.7	1.1%	[116]
4 × 4 LP CDRA array	slot	9.81% 25.77GHz-31.27GHz	15.59dBi	LP	[117]

### 3.5 Conclusion

An experimental and theoretical study of circularly polarized layered cylindrical DRA has been presented in this Chapter. The proposed simple design provided wide bandwidths of impedance and axial ratio combined with high gain due to adding the outer dielectric layer. The two-layer CDRA configuration provided 88% impedance and 23.2% axial bandwidths, along with a 12.29 dBic gain by exciting multiple hybrid modes, which would have been impossible without the outer layer. A prototype has been constructed and tested with good agreement between simulation and measurement. The measured results show an impedance bandwidth of 83% over the frequency range of 16.9 GHz to 41 GHz. Furthermore, the measured wide bandwidth of the axial ratio and a high realised gain of 22.2% and 11.3 dBic, respectively. Consequently, these appealing features of the proposed configuration are useful for 5G applications that require antennas with higher gain and wide bandwidth.

# Chapter4 High Gain Wide-Band Millimetre Wave Perforated Cylindrical DRA

## 4.1 Introduction:

With the rapid development of wireless communications has recently undergone rapid changes. With numerous wideband and multiband applications that need broadband antennas. For this reason, DRA design with improved impedance bandwidth is required. Broadening bandwidth involves the application of several precepts, including and the amalgamation of multiple resonance modes as well as the potential adoption of matching networks, [118] . For example, the utilisation of multi modes exhibits superior success in terms of improving the bandwidths of multilayered DRA stacked DRAs. Nevertheless, avoiding air gaps between the dielectric layers remains a significant challenge. Innovative 3D-printing technology is simple and cost effective with a short fabrication cycle. Hence, it has recently been considered in the context of DRA fabrications[85]. Furthermore, 3D-printing technology can be more effective in eliminating the air gaps compared to other fabrication techniques[84]. A 3D-printed multilayered cylindrical dielectric resonator antenna (CDRA) has been reported in the literature with a wideband that extend from 4.3GHz to 8 GHz GHz[84].

Recent interest in 3-D printing can be attributed to the lower costs and lead time associated with this technique. Moreover, 3-D printing can successfully manage complex geometrics [77]. In the period following the introduction of 3-D printing in the 1980s, several 3-D printing methods have been developed, including fused deposition modeling (FDM), electron beam melting, binder jetting, polymer jetting, selective laser melting, ceramic stereolithography apparatus, and micro-stereolithography. In addition, 3-D printing approach has been shown to effectively produce high-performance microwave and mm-wave antennas, such as slot [78],

horn [79], patch [80], gradient index lens [81] antennas and reflect arrays [82]. Despite this evident success, there has been limited research into 3-D-printed DRAs [83-85].

This chapter introduces and examines a 3-D-printed wideband multi-layer DRA. The comparative cost effectiveness and sustainability of 3-D-printing technology, otherwise known as additive manufacturing, have contributed to the recent interest in this technique. In addition, its ability to fabricate complex shapes has contributed to the increased popularity [77].

Therefore, the mmWave CDRA Of Chapter 3 will be replaced by an equivalent cylindrical structure with two sections that are fabricated using the same material, i.e. Alumina. The resulting structure consists of a solid single-layer DRA inner section and a perforated Alumina outer coat layer with a much lower effective dielectric constant. Consequently, by using automated 3D printing, the two dielectric layers can be assembled and bonded using an automated process without requiring any time-consuming manual assembly and bonding processes. Furthermore, using the same material for the DRA and coat simplifies and expedites the 3D printing process.

## **4.2 Antenna Configuration**

### **4.2.1 Equivalent Single Layer DRA with Perforated Outer Layer**

As previously highlighted, multilayer Dielectric Resonator Antenna (DRA) configurations are burdened with notable constraints, such as augmented physical dimensions and the requirement for sophisticated assembly processes. These processes encompass the bonding of distinct dielectric layers in a manner that averts any potential air gaps. The current research endeavours to tackle this predicament by deploying 3D printing technology in the fabrication of an Alumina-based, perforated DRA structure.

In accordance with FDM 3-D printing techniques, the proposed multilayer DRA has been created. Hence, the central DRA section consists of solid Alumina while the outer layer consists of a perforated Alumina that has a reduced effective dielectric constant. By replacing the solid outer Polyimide coat with a realistic perforated dielectric layer made from the same material as the core DRA, the proposed mm-wave cylindrical DRA becomes easier to fabricate. Additionally, the different dielectric constants of the dielectric layer [84] can be achieved with varying hole sizes, in accordance with the filling-ratio theory[119].

As shown in Figure 4.1, the 3-D-printed CDRA developed in this study is composed of two concentric dielectric sections. In particular this configuration includes a solid cylindrical DRA in the center, with different air-filling ratios in the outer dielectric providing different effective dielectric constants. The (effective) dielectric constants of the second layer is signified by  $\epsilon_{r2}$ .

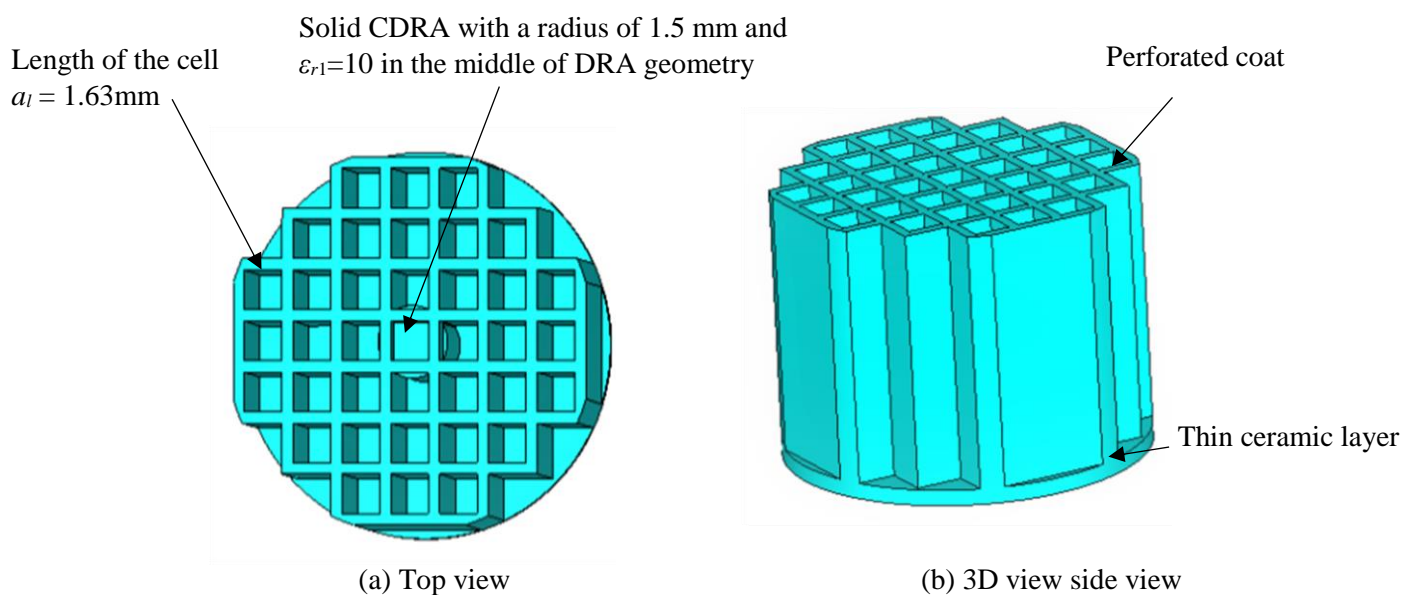


Figure 4.1: Cylindrical DRA with a perforated dielectric coat.

As depicted in Figure 4.2, the proposed antenna developed is configured using its dimensions and feed network described in the previous chapter. The figure further illustrates that the cylindrical solid DRA

is fixed within the perforated layer. The DRA has been excited using the same cross-slot as that in the solid-layered CDRA proposed in the previous Chapter.

DRA and a perforated coat with  $\epsilon_r = 10$

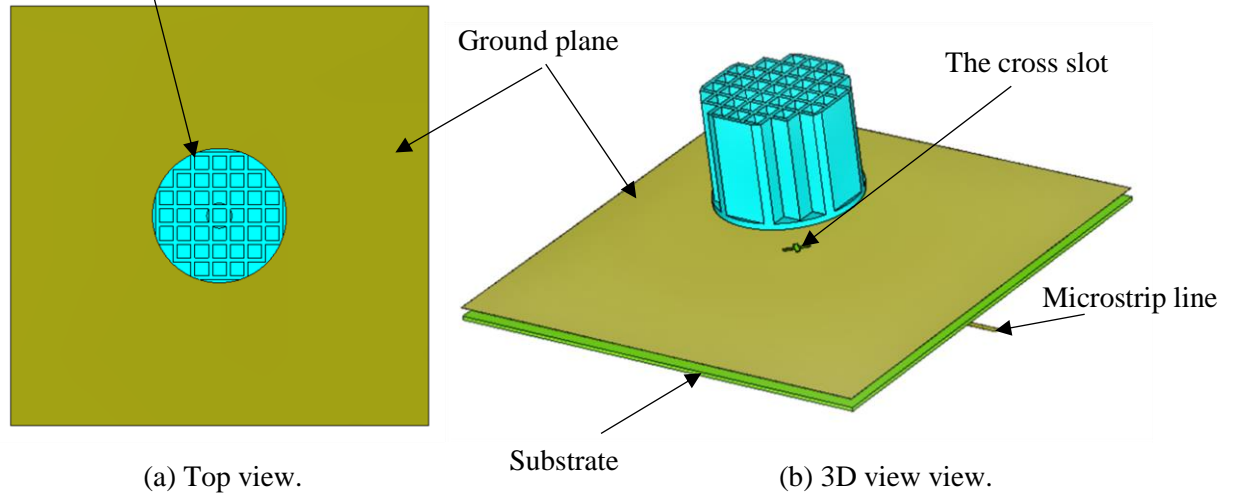


Figure 4.2: The configuration of the Cylindrical DRA with a perforated dielectric coat

#### 4.2.2 Parameter study

To create the perforated coat, a single printing material is used to print the inhomogeneous antenna. Throughout the present study, a 3-D printing material with a dielectric constant of  $10 \pm 0.35$  over 17.7-30 GHz is used. The effective dielectric constant, which has been calculated using equation 4.1  $\epsilon_{rff} = 3.58$ , whereby a cubic unit cell with a dielectric constant of 10 was introduced. The unit cell wall thickness is defined as  $t_c$  and the side length was fixed at 1.63 mm at 29 GHz. The effective dielectric constant of the perforated layer has been calculated by using equation 4.2[84].

$$\epsilon_{rff} = \frac{R_c^2}{\frac{R_d^2}{\epsilon_{r1}} + \frac{(R_c^2 - R_d^2)}{\epsilon_{r2}}} \quad (4.1)$$

$$\epsilon_{rff} = 0.55t_c\epsilon_r - 0.04\epsilon_r + 1.3 \quad (4.2)$$

Where  $R_c$ ,  $R_d$  is the radius of the inner and outer of the solid design in chapter 3 respectively as well as  $\epsilon_{r1}$  and  $\epsilon_{r2}$  are the dielectric constant of the inner and outer layer of the solid design in previous chapter 3 .

From which it can be noted that the effective dielectric constant is determined by the cell thickness  $t_c$  (mm). Figure 4.3 shows how the variation of the effective dielectric constant with unit cell wall thickness for a variety of printing materials of  $\epsilon_r = 5, 10, 15,$  and  $20$ . Therefore, the effective dielectric constant of a unit cell can be adjusted by changing its wall thickness  $t_c$ . In this design, the side length of the unit cell is set to  $a=1.63\text{mm}$ , or  $0.154\lambda_0$ , where  $\lambda_0$  denotes the free space wavelength at  $29\text{GHz}$  and a wall thicknesses of  $0.49\text{mm}$ . Three-dimensional printable unit cells have several advantages, including the ability to modify the wall thickness to regulate the effective dielectric constant, as per filling ratio theory [7]. A second characteristic of the unit cell is that it is self-supporting in the  $z$ -direction. The presence of a fixed dielectric constant for each layer characterizes the CDRA with a perforated Alumina coat presented in Figure 4.1. As a result, each layer's unit cells have equivalent wall thicknesses. In addition, these unit cells can physically support each other, so no additional supporting material is required during 3-D printing. Consequently, printing time and material costs are decreased significantly. It should be noted that for easy detachment from the building platform, a thin dielectric layer with a thickness of  $0.5\text{mm}$  and a radius of  $8\text{mm}$  was printed underneath the DRA as well as to improve the matching between the DR and the slot. Based on equation 4.2, to determine how the wall thickness affects the effective permittivity of a perforated dielectric coat as well as modes' resonance frequencies and bandwidths, the wall thickness was varied between  $0.29\text{mm}$  and  $0.69\text{mm}$ . As illustrated in Figures 4.4, 4.5 and 4.6, varying the wall thickness affects the  $S_{11}$ , gain and the gain,

respectively. The lowest impedance bandwidths of 32.2% have been achieved when  $t_c=0.69$  mm, which corresponds to the excitation of the  $HE_{115}$  and  $HE_{117}$  resonance modes, respectively, with an AR bandwidth of 1.6% and gain of 9.5 dBic. Furthermore, it was possible to attain much broader impedance, and axial ratio bandwidths and Gain of 53.3% and 16.3% and 13.13 dBic, respectively. This is due to the fact that the following resonance modes  $HE_{115}$ ,  $HE_{117}$ ,  $HE_{119}$ ,  $HE_{11,11}$  have been excited at 17.5 GHz, 21.5 GHz, 25.5 GHz and 29 GHz, respectively, when  $t_c$  equals to 0.49mm. According to Figure 4.7, the  $S_{11}$  bandwidth varies as a function of the wall thickness, with the maximum  $S_{11}$  bandwidth achieved using a thickness of the wall cell of 0.49 mm. The simulated H-field and E-field distribution for various excited modes inside the resonator are illustrated in Figure 4.8.

These results have been achieved using the CST Eigenmode solver and excited at various frequencies inside the cylindrical DRA.

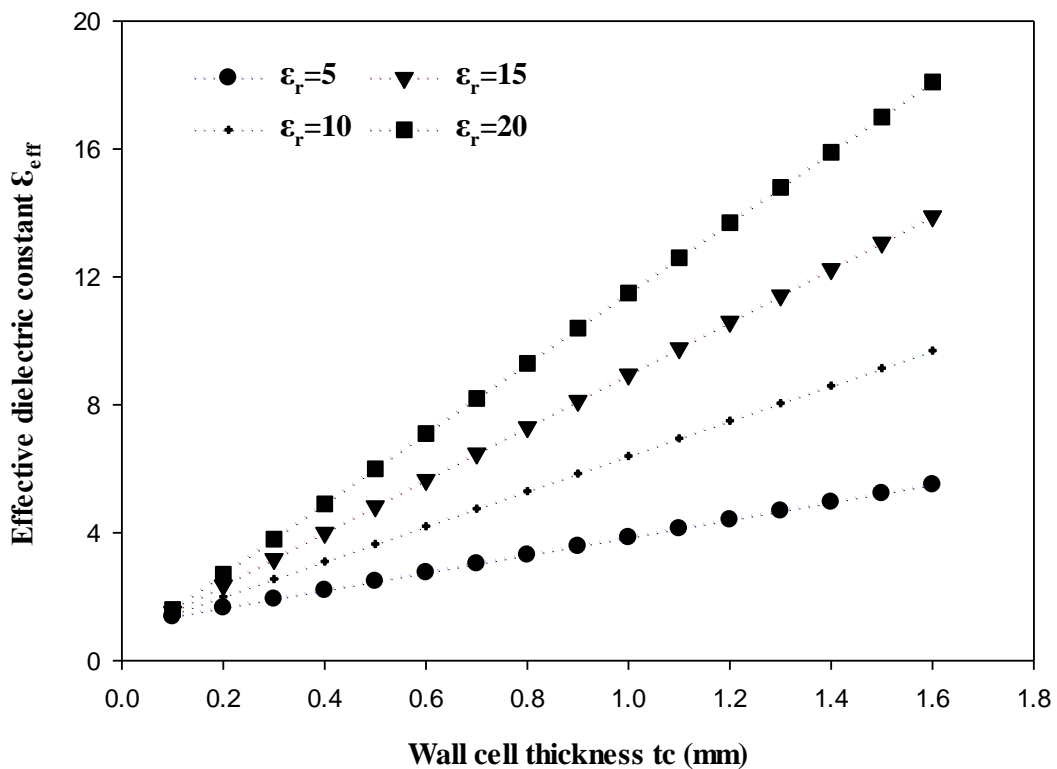


Figure 4.3: Perforated cylindrical layer effective permittivity as a function of  $t_c$

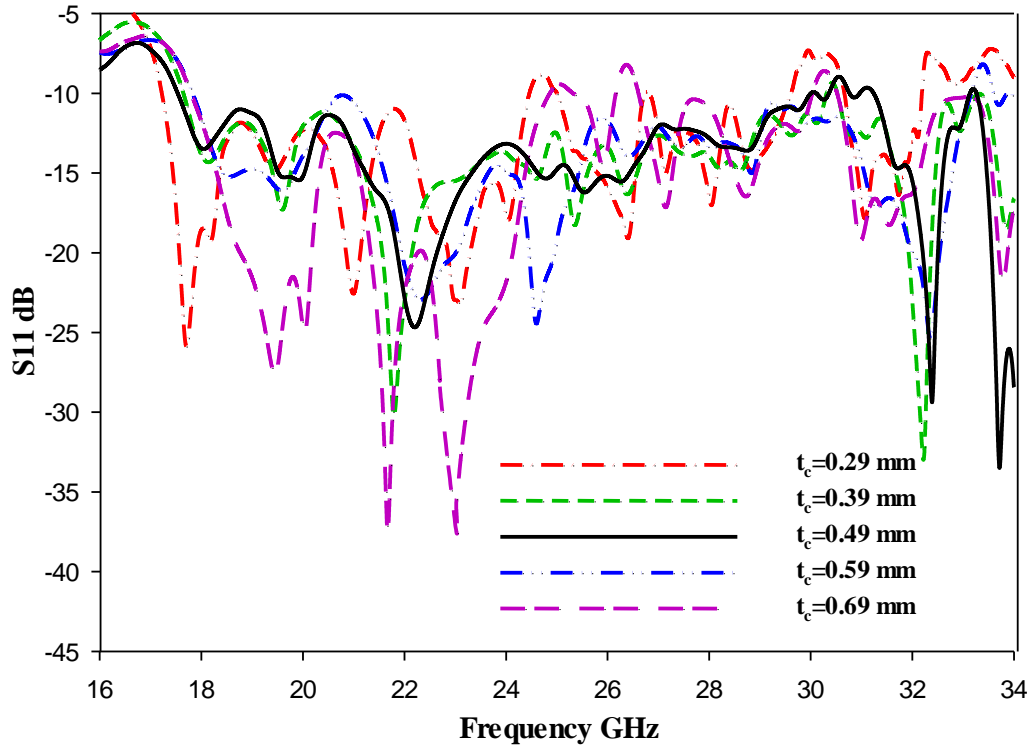


Figure 4.4: Simulated  $|S_{11}|$  for cylindrical DRA with a perforated coat layer with various of  $t_c$ .

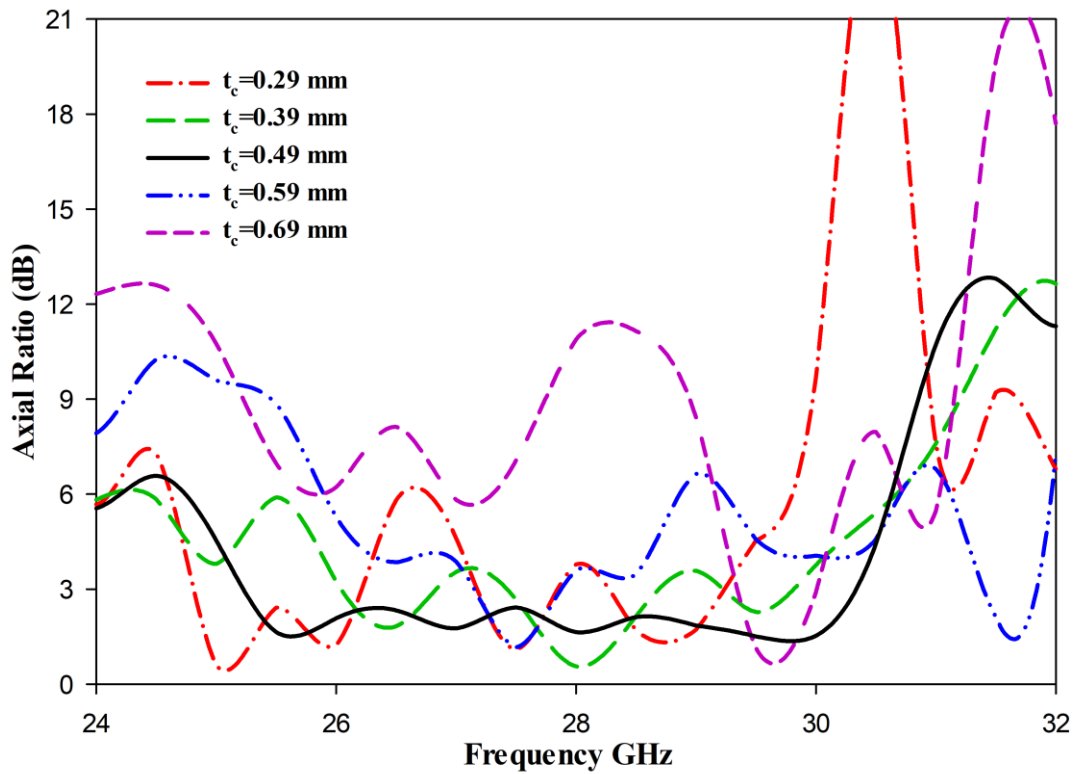


Figure 4.5: Axial Ratio simulated for cylindrical DRA with a perforated coat layer with various of  $t_c$ .

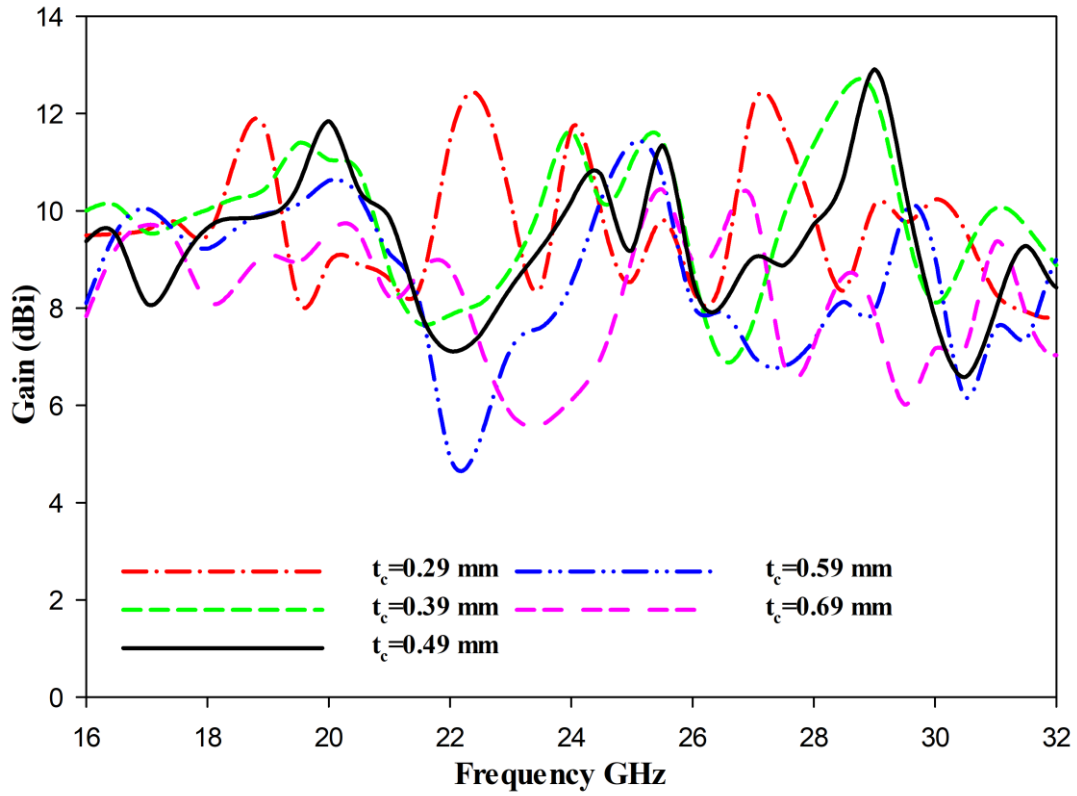


Figure 4.6: Gain simulated for perforated cylindrical DRA with a perforated coat layer with various of  $t_c$

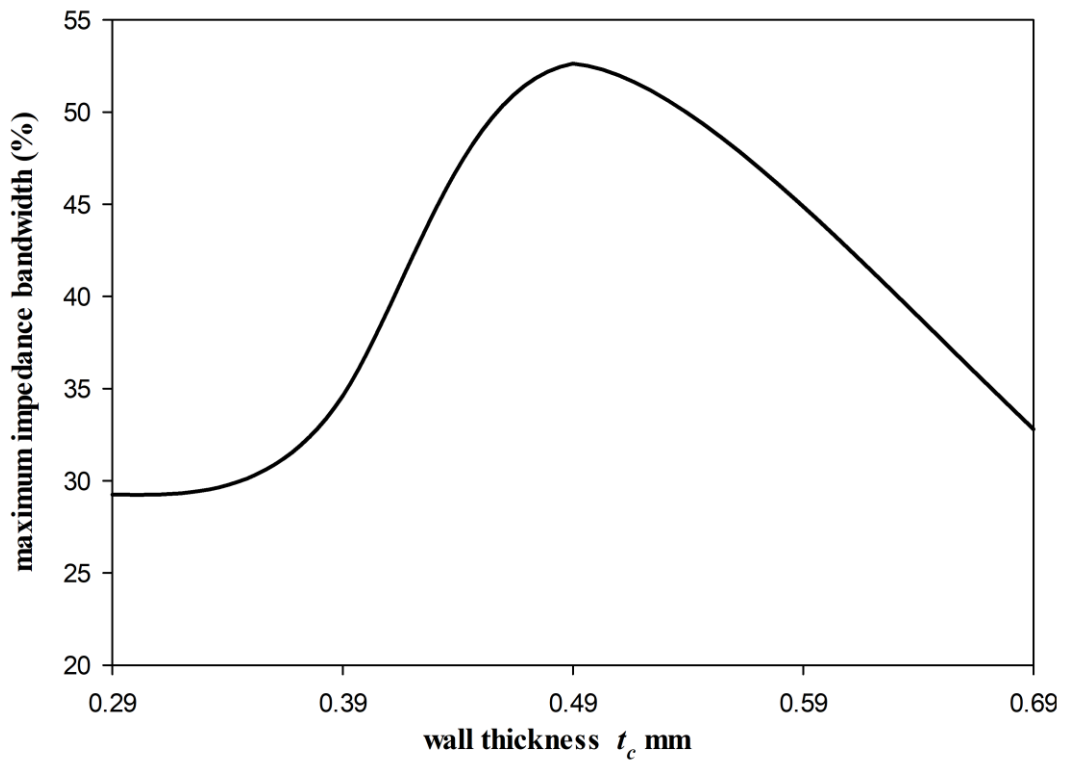


Figure 4.7: Maximum bandwidth as function of the wall thicknesses  $t_c$ .

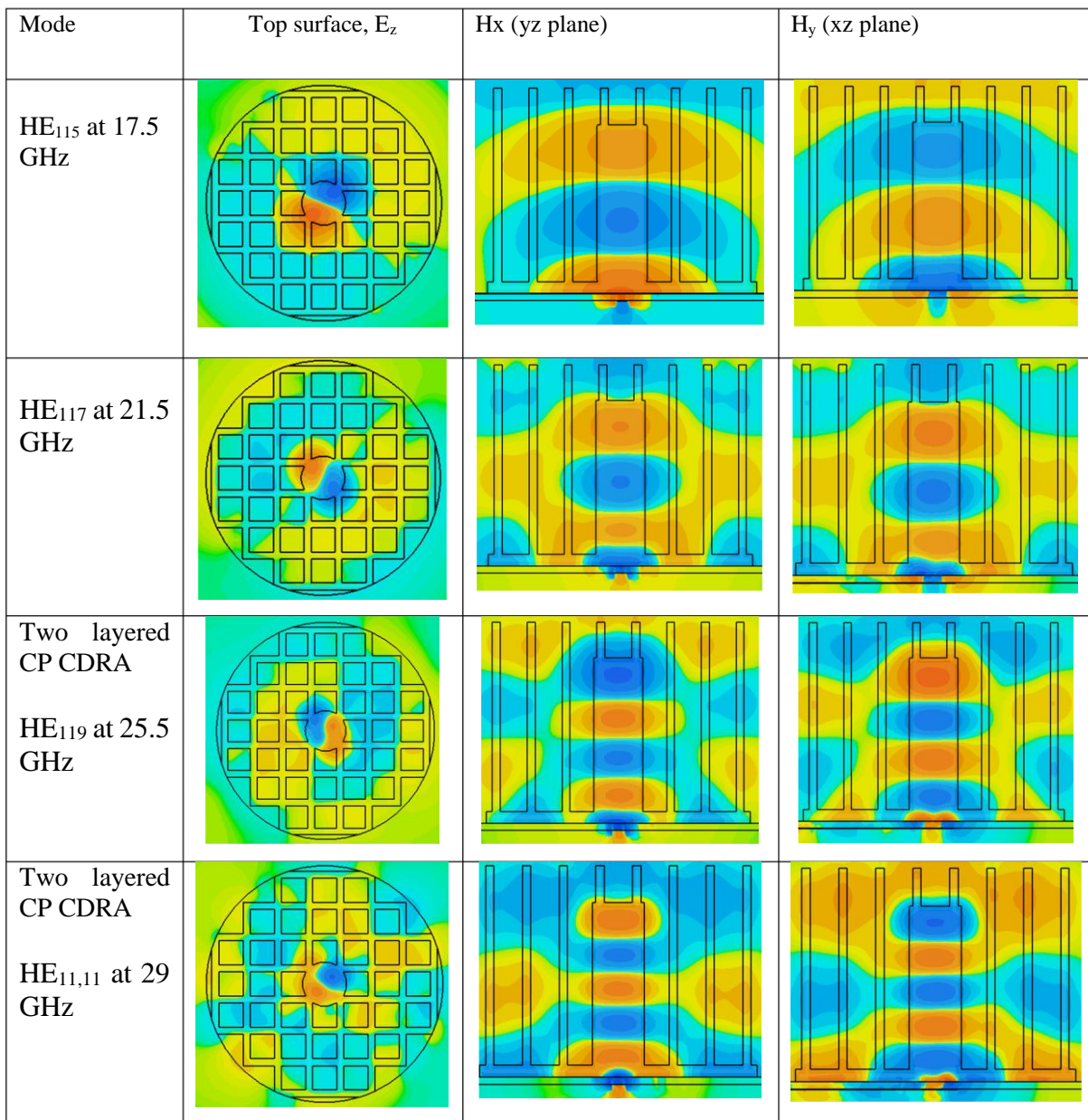


Figure 4.8: E-field and the H-field distributions inside the DRA with a perforated cylindrical coat layer

### 4.3 Experimental Results

A prototype of a cylindrical DRA with a perforated coat layer is illustrated in Figure 4.9, where both the DRA and coat are created using Alumina. The antenna has been 3-D printed by a Mattress company. The proposed antenna has been mounted on a feed network fabricated by Wrekin Circuits. The feed network consists of a Ro4350B Rogers dielectric substrate with a

thickness of 0.42mm with a relative permittivity of 3.48 and a loss tangent of 0.0037. A microstrip line was printed under the Rogers substrate. Additionally, a 2.4mm SMA connector connects to microstrip line feeding, and an Agilent Technologies E5071C mm Wave vector network analyzer has been connected to the SMA using a 50 $\Omega$  coaxial cable.

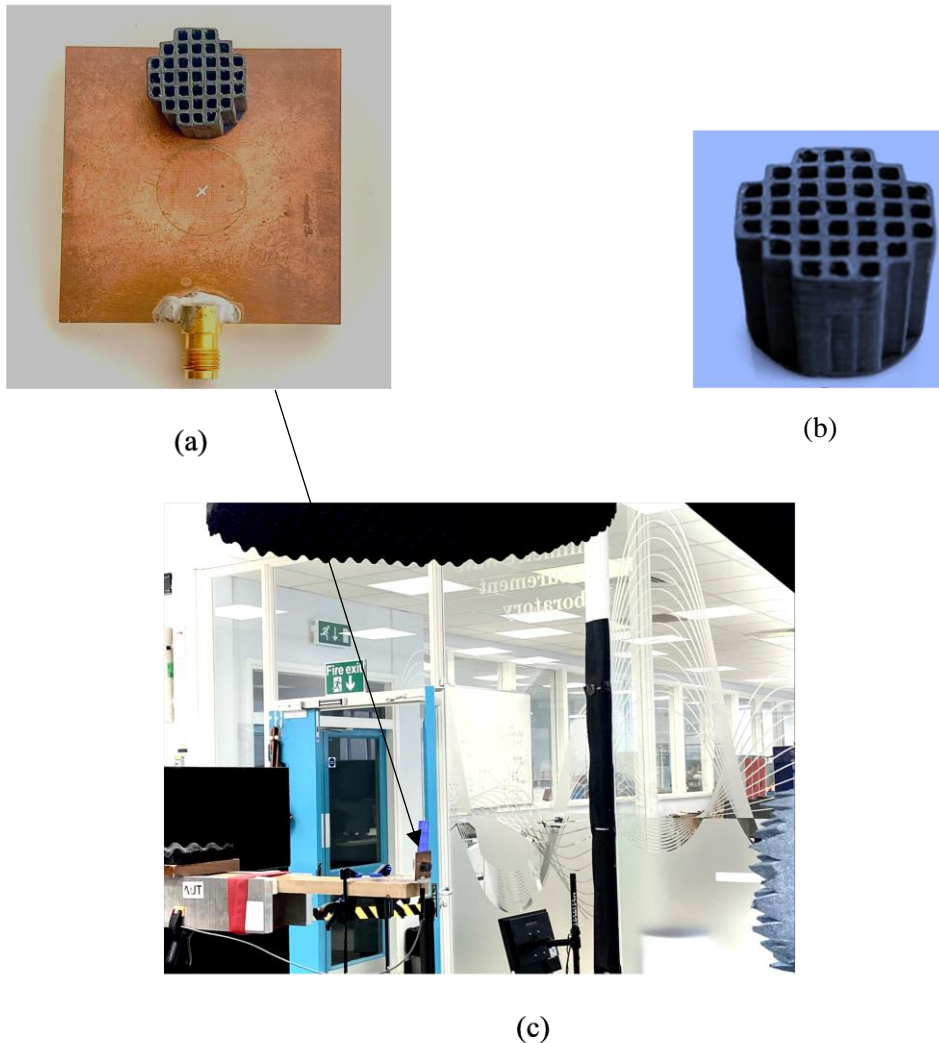


Figure 4.9: The prototype of a CDRA with perforated coat layer (a) Feed network with outlined DRA position, (b) The DRA model, (c) The CDRA placed inside the chamber.

A comparison between the simulated and measured return losses is illustrated in Figure 4.10.

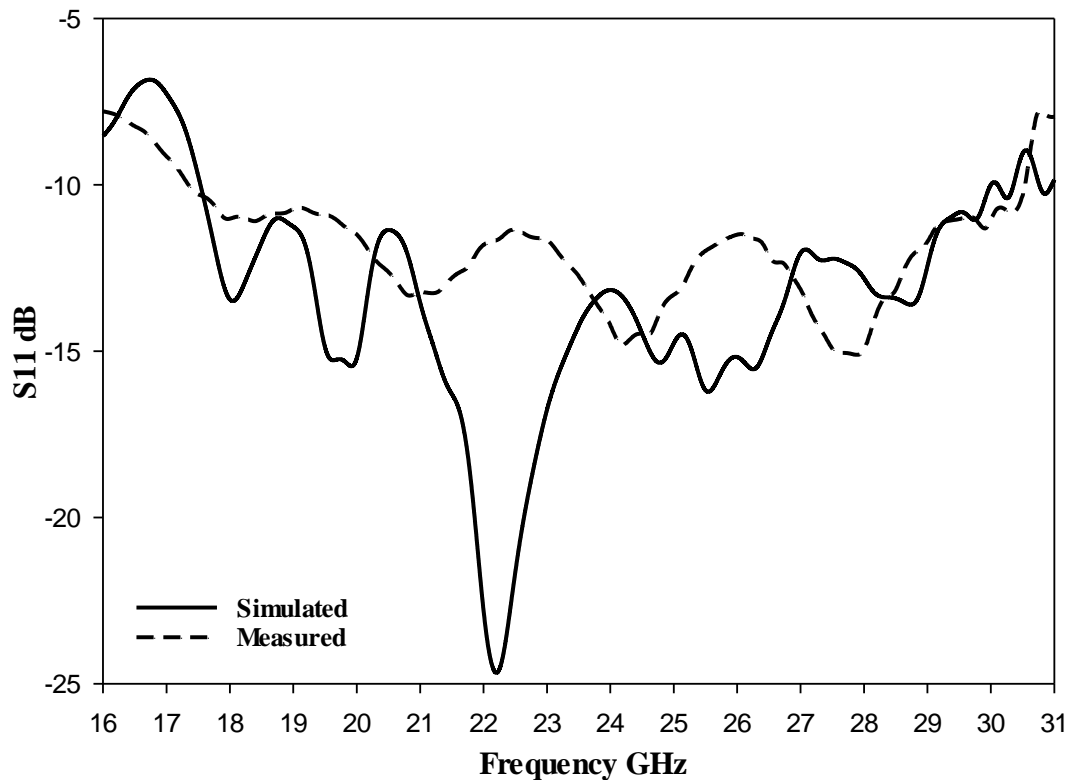


Figure 4.10: The simulated and measured reflection coefficient of the perforated antenna configuration.

The simulated impedance bandwidth of 52.6% has been achieved, which covers a frequency range of 17.5GHz to 30.5 GHz, compares well to a measured bandwidth of 53.3% that covers a frequency range of 17.4GHz to 30.3GHz. w. A multimode operation was demonstrated, where the  $HE_{115}$ ,  $HE_{117}$ ,  $HE_{119}$  and  $HE_{11,11}$  resonance modes were excited at 17.5GHz, 21.5GHz, 25.5GHz and 29GHz, respectively. According to Figure 4.11, the simulated and measured gains are 13.3 dBic and 12 dBic, respectively, when the  $HE_{11,11}$  is excited. Due to the excitement and the merging of multiple hybrid modes, the enhance bandwidths have been obtained.

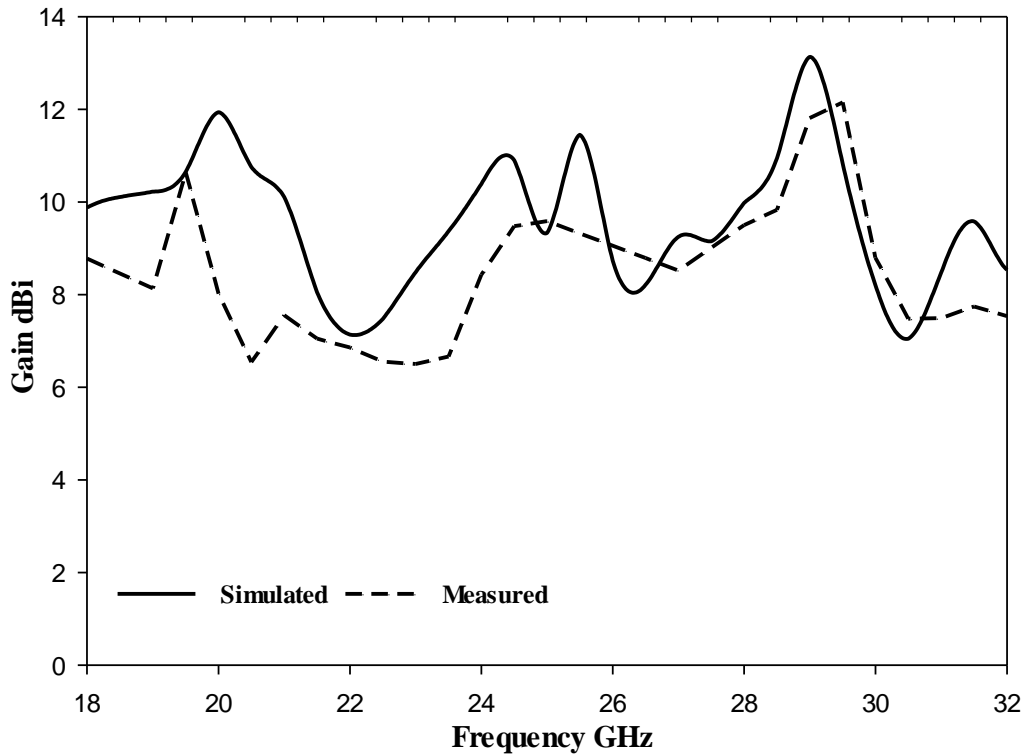


Figure 4.11: Simulated and measured of the gain of the perforated antenna.

The simulated and measured boresight axial ratios are presented in Figure 4.12. The simulation illustrates a 3-dB axial ratio bandwidth of 16.5%, which is close to the measured counterpart of 17%. The radiation patterns of the proposed circularly polarized antenna are presented in Figure 4.13, where the  $HE_{11,11}$  mode is excited at 29 GHz. The patterns demonstrate a right-hand circular polarization (RHCP) in the far field since the electric field component  $E_R$  being  $\sim 12.3$  dB greater than  $E_L$ . Table 4-1 illustrates a comparison between the performance of the proposed perforated antenna and other perforated designs, where the proposed CDRA provides CP radiation as well as a considerably higher gain in combination with a simpler design.

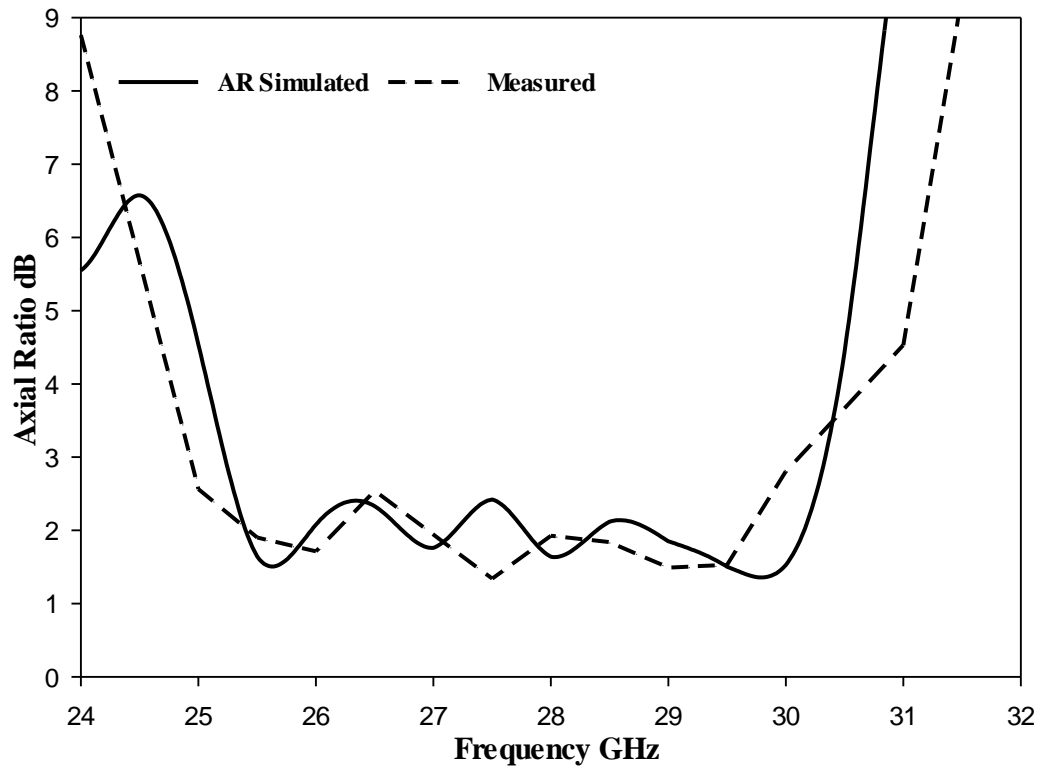
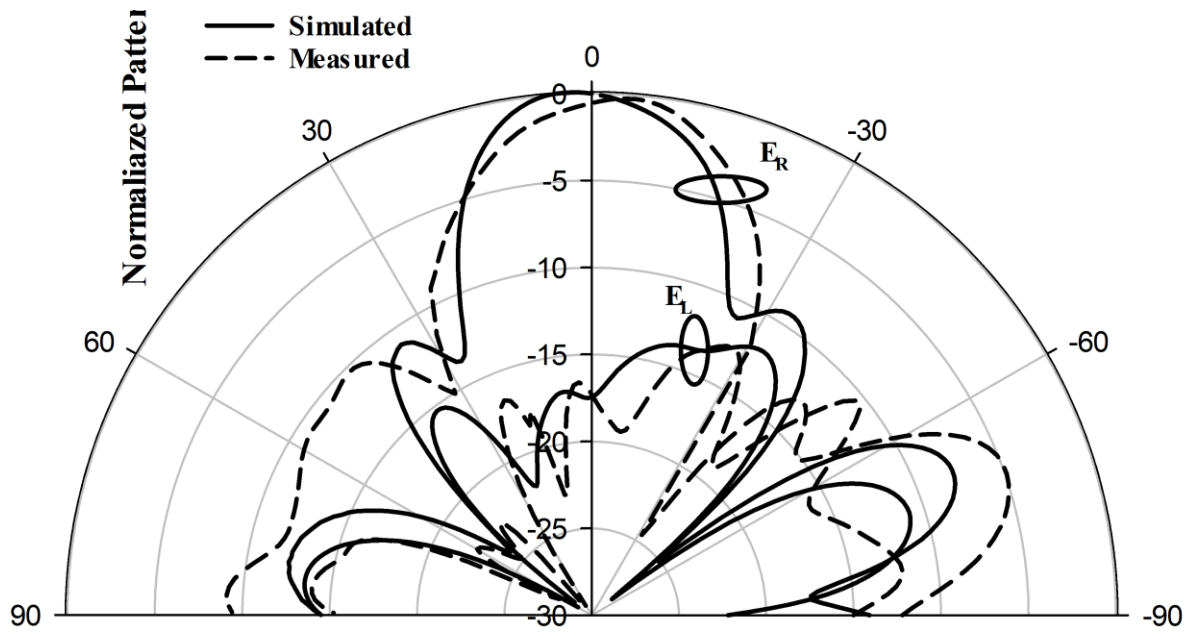
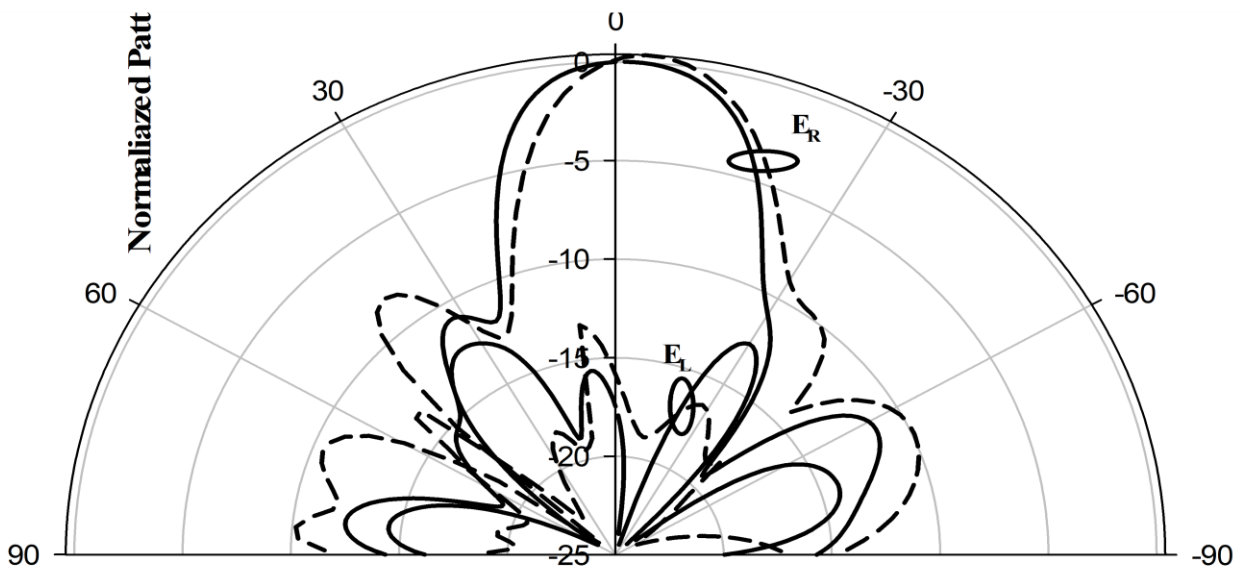


Figure 4.12: The simulated and measured CP bandwidth of perforated antenna.



(a)



(b)

Figure 4.13: Simulated and measured radiation pattern at 29 GHz (a)  $\phi=0^\circ$ , (b)  $\phi=90^\circ$

Table 4-1: Proposed antenna performance compared to previously reported designs.

Antenna type	Feeding mechanism	$ S_{11} $ Bandwidth	Gain	AR Bandwidth	Ref
Present work	Cross slot	53.3% 17.4GHz to 30.3GHz	12 dBic	17%	-
A3D-printed multi-layered CDRA	probe	65.7% 3.56GHz-7.04GHz	2.3dB	-	[118]
A3-D-printed multi-ring DRA	probe	60.2 % 3.4 GHz-8 GHz	2.45dBi	-	[84]
A3D-printed rectangular DRA	probe	44.8% 5.20 GHz-8.20 GHz	6.7 dBi	-	[120]
DRA dielectric lens antenna	Slot aperture	40.2% / 19.5%	5.8dBi / 12dBi	-	[85]

## 4.4 Conclusion

This chapter has examined the possibility of assigning a single effective permittivity to solid objects made of several dielectric layers by developing and examining the concept of internal homogenization. This concept applied to the layered CDRA, which has been examined in Chapter 3 at the mm-wave band. The equivalent single layer CDRA configuration provided an impedance bandwidth of 40.8% and an axial ratio of 15.3% with the maximum gain achieved of 11.5 dBic at 30 GHz. The second part of this chapter presented experimental and theoretical results of circularly polarized perforated cylindrical DRAs. Two layers with decreased effective dielectric constants are combined into a single piece. This facilitates automated assembly and bonding of the layered DRA and total elimination of potential air gaps between the dielectric layers. The proposed DRA offers a simulated impedance bandwidth of 52.6%,

which has been achieved by merging multiple hybrid adjacent modes. A, The measured bandwidth is 53.3%, which demonstrates a close agreement with simulated counterpart. In addition, the antenna configuration demonstrated a measured wide CP bandwidth of 17% and a high gain of 12 dBic. Consequently, these attractive features are useful for 5G applications requiring antennas with high gain and wide bandwidth.

# Chapter5 Wide-Band Layered Millimetre Wave Hemispherical DRA

## 5.1 Introduction:

Most researchers have extensively studied the geometry of hemispherical dielectric resonator antennas (HDRA), which is shown in Figure 5.1. This type of DRA primarily relies on its dielectric constant ( $\epsilon_r$ ) and radius ( $a$ ) for its design, rendering it less flexible in terms of design parameters. Additionally, fabricating a hemispherical DRA is more complex and expensive than other regular DRA geometries. Similar to cylindrical and rectangular DRAs, the A HDRA can be fed using a probe, slot aperture, or conformal strip line. However, at mm-wave frequencies, probe feeding is unsuitable due to the need to drill a hole in a solid ceramic structure, resulting in a notable air-gap size compared to the shorter wavelength [121]. Instead, slot feeding is more favourable at high frequencies, as it is easier to fabricate and isolates the antenna from the feed network, eliminating any spurious radiation. The resonance modes can be determined by numerically solving the characteristics mode equation assuming the isolated

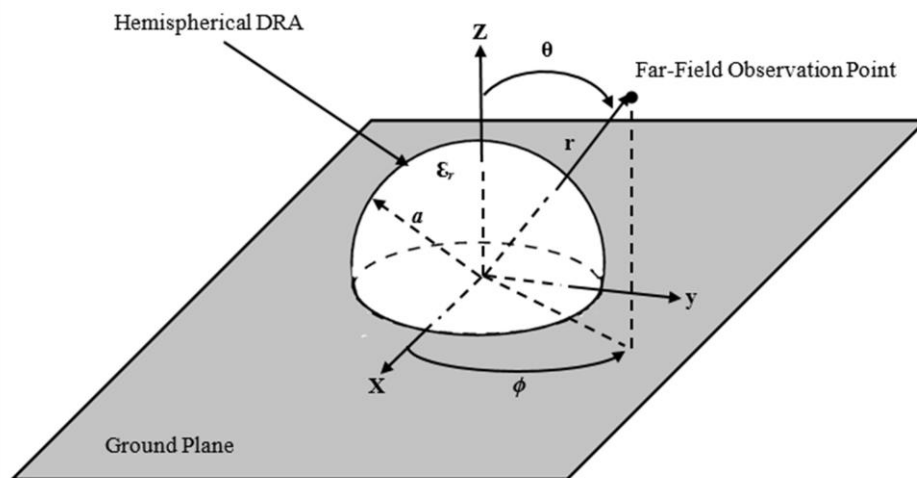


Figure 5.1: Hemispherical DRA.

DRA is placed on an infinite perfectly conducting ground plane to facilitate the utilization of image theory to determine the mode characteristics of the antenna.

The hemispherical configuration can be evaluated within the context of a dielectric sphere. This sphere's modes can be dichotomized into two primary categories, namely, Transverse Electric (TE) and Transverse Magnetic (TM) modes. The defining characteristic of TE modes is the nullity of the radial component pertaining to the electric field, denoted by  $E_r = 0$ . In contrast, TM modes are recognized by the absence of a radial component in the magnetic field, denoted by  $H_r = 0$ . [122]. The fundamental modes of a hemispherical DRA are  $TE_{111}$  and  $TM_{101}$ , which find various applications. The radiation pattern of the  $TE_{111}$  mode is similar to that of a short horizontal magnetic dipole, while the radiation pattern of the  $TM_{101}$  mode is similar to that of a short electric monopole. The subscripts of  $TE_{mns}$  modes represent variations of the fields in the radial ( $r$ ), azimuth ( $\phi$ ), and elevation ( $\theta$ ) directions of a spherical coordinate system. The resonant frequency of the fundamental mode  $TE_{111}$  can be determined by solving the following mode characteristics equation [4, 123].

$$\frac{\hat{J}_1(ka)}{\hat{J}'_1(ka)} = \epsilon_r^{1/2} \frac{\hat{H}_1(k_0a)}{\hat{H}'_1(k_0a)} \quad (5.1)$$

This equation involves  $k = \epsilon_r^{1/2} k_0$ . Where  $\hat{J}_1(x) = x j_1(x)$ ,  $j_1(x)$  is the spherical Bessel function of the 1<sup>st</sup> order,  $\hat{H}_1(x) = x h^2_1(x)$ ,  $h^2_1(x)$  is the spherical Hankel's function of the 1<sup>st</sup> order 2<sup>nd</sup> kind. To find the resonant frequency, equation (5.1) is solved for a given  $a$ , and then  $k_0$  is determined. Finally, the resonant frequency can be calculated as [123].

$$f_r = \frac{4.7713 R_e(k_0a)}{a} \quad (5.2)$$

It should be noted that equation (5.1) can be utilised to determine the modes' resonance frequencies for a coated HDRA but calculating the effective permittivity of the tow-layer structure using equation 5.3 [7].

$$\epsilon_{reff} = \epsilon_{r2} \frac{a_2^3(\epsilon_{r1}+2\epsilon_{r2})+2a_1^3(\epsilon_{r1}-\epsilon_{r2})}{a_2^3(\epsilon_{r1}+2\epsilon_{r2})-a_1^3(\epsilon_{r1}-\epsilon_{r2})} \quad (5.3)$$

The rapidly growing research interest in the millimetre-wave frequencies due to the promising applications in 5G-and-beyond communications systems triggered a stronger interest in wideband efficient antennas. Nevertheless, there remain several issues to be overcome with respect to the design of mmWave antennas, not least of which is the significant attenuation that renders it necessary to employ high gain antennae. In addition, the possible increase in Ohmic losses in metal antennas and arrays feed networks deteriorate the radiation efficiency and hence the gain [25]. Narrow impedance bandwidths in the range of 2–5% are amongst the most widely acknowledged drawbacks of microstrip antennas [124]. One appropriate solution to these disadvantages is to utilise a dielectric resonator antenna (DRA), which can remedy the aforementioned limitations through the provision of enhanced gain and increased bandwidth. DRA also has other beneficial qualities, including a comparatively small size, variety of shapes, flexible excitation options, low profile and weight [33, 108].

It is well-known that a substantial increase in the impedance bandwidth can be achieved by appending a dielectric coat to the DRA [125]. This coat functions as a transition zone between the antenna and free space. Recent reports indicate that DRA coating can increase gain as well as circular polarisation and impedance bandwidths [95, 126]. In addition, a wideband slot-fed multi-layer hemispherical DRAs have been reported with an impedance bandwidth of 55% by exciting the  $TE_{111}$  and  $TE_{221}$  resonance modes in combinations with the slot's resonance mode [68]. There have also been suggestions that a coaxial probe fed three-layer hemispherical DRA should be adopted in conjunction with materials that have relative permittivities of 9, 4 and 3

for the inner, middle and outer layers, respectively, wherein a bandwidth of 65.6% has been realised with a lower gain of 3.2 dBi when lower order modes of  $TM_{101}$  and  $TM_{102}$  are excited [127]. However, the probe feeding is impractical at mm-wave frequencies as has been explained earlier. A further design of a three-layer hemispherical DRA has been reported using a rectangular waveguide feed, whereby the optimization of the outer layer's permittivity renders the possibility of a broadband coupling to deliver impedance bandwidth and gain of 9.6% and 6.4 dBi through the excitation of the  $TE_{113}$  mode [69]. Another research study reported a wide impedance bandwidth equating to  $\sim 25\%$  in case where a conformal strip is employed to excite a three-layer hemispherical DRA operating in the  $TE_{111}$  lower order mode [66]. However, it is difficult to precisely fix a conformal strip on the DRA surface at mm-wave frequencies due to the smaller dimensions and potential airgaps between the strip and DRA. Another slot-coupled three-layer hemispherical DRA design offers a broad impedance bandwidth in the region of 29% with gain of 4.4 dBi by exciting the fundamental  $TE_{111}$  resonance mode [128]. When the performance of a two-layer hemispherical DRA is compared to that of a single layer counterpart, it becomes evident that there is a wider bandwidth of 31.9% and a modest gain of 2.5 dBi for the layered DRA compared to 14% for the single layer DRA that operates at the lower order  $TM_{101}$  mode [70].

On the other hand, multilayer DRA configurations are associated with known limitations such as the increased physical size as well as the need for a complex assembly procedure with respect to bonding the different dielectric layers together with no potential air gaps in-between. This study addresses the above issue by utilising the 3D printing technology to fabricate a perforated DRA configuration using Alumina. It should be noted that innovative 3D-printing technology is simple and cost effective, in addition to having a short fabrication cycle. Hence, it has recently been considered in the context of DRA fabrications. Furthermore, 3D-printing technology can eliminate the potential air gaps more effectively compared to other fabrication

techniques[84]. it should be noted that his technology has already been utilized to create a multilayered cylindrical dielectric resonator antenna (CDRA) ][84, 85].

Therefore, the layered hemispherical DRA geometry has been replaced by an equivalent hemispherical structure with two sections that are fabricated using Alumina. The inner section is the solid single-layer DRA and the outer coat is a perforated Alumina section with a considerably lower effective dielectric constant. As a result, an automated 3D printing process has been followed with no need for the time and labour consuming assembly and bonding of the two different dielectric layers. In addition, using the same material for the DRA and coat considerably simplifies and expedites the 3D printing process. Moreover, a prior research into multi-layer hemispherical DRAs has tended to focus on the impedance bandwidth enhancement. Hence, there has been no earlier studies focused on enhancing the circular polarisation bandwidth of a layered hemispherical DRA since the outer section offers an additional degree of freedom to achieve a wider CP bandwidth. Another factor that contributed to the enhanced CP bandwidth is the utilisation of an Archimedean spiral slot to feed the antenna by exciting multiple higher order modes. Furthermore, , the antenna operates at the 18.4-33.4 GHz mm-wave frequency band and offers an axial ratio bandwidth of ~17%, which is wider than those reported in earlier studies for a circularly polarised hemispherical DRA .A close agreement has been achieved between measured and simulated results.

## **5.2 Antenna Configuration**

### **5.2.1 Layered HDRA**

The Transverse Electric (TE) modes of the single-layer DRA have been ascertained by solving equations 5.1 and 5.2 utilizing MATLAB code. It was discovered that the single element supported dual resonance modes, namely  $TE_{112}$  and  $TE_{511}$ , at 25.1 GHz and 30.81 GHz, respectively. Figure 5.2 illustrates the two-layer hemispherical DRA and feed network

configurations proposed in this study. In addition to studying the impacts of the coating layer on the HDRA performance, simulations have been performed using CST MWS to determine the impedance and axial ratio bandwidths as well as gain. In this section, a single layer higher order mode hemispherical DRA is analysed by using a relative permittivity of 10 and a radius of  $a_1=3.8\text{mm}$ . The proposed antenna has been placed on a  $45\times 45\text{mm}^2$  ground plane printed on a thin Rogers RO4350 dielectric substrate with a thickness and dielectric constant of 0.42mm and 3.48, respectively. A feeding microstrip line has been placed on the lower side of the dielectric substrate with a length of 22.5 mm and width of 0.88mm that has been adjusted for optimum impedance matching characteristic impedance of the transmission line of  $50\Omega$ . As a starting point, the utilize x-band feed network in Chapter 2 has been optimised with further adjustments, where the spiral slot fabrication requirements have been adjusted to account for the mm Wave frequency band.

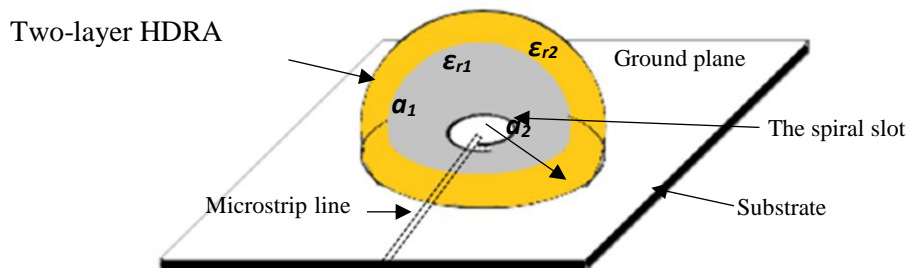


Figure 5.2: The configuration of the proposed layered HDRA

The feeding spiral is illustrated in Figure 5.3 with dimensions defined by the well-known Archimedean spiral function;

$$\rho = a \varphi \quad (5.3)$$

Where  $\rho$  represents the radius of the spiral-slot arm,  $a$  is the spiral constant and  $\varphi$  is the winding angle. The chosen parameters are  $a=0.08 \text{ mm/rad}$ ,  $0.138\pi \leq \varphi \leq 2.16\pi$  and the width of the

spiral-slot arm is  $w_s = 0.38$  mm [96], which results in a spiral-slot arm length of 3.9 mm is approximately  $0.7 \lambda_{\text{eff}}$  at an operating frequency of 29 GHz which has been calculated by equation 2.2 in Chapter 2. The changes in the above spiral's parameters as well as the separation between the spiral slot arm tuns ( $g$ ) can change the spiral's arm length.

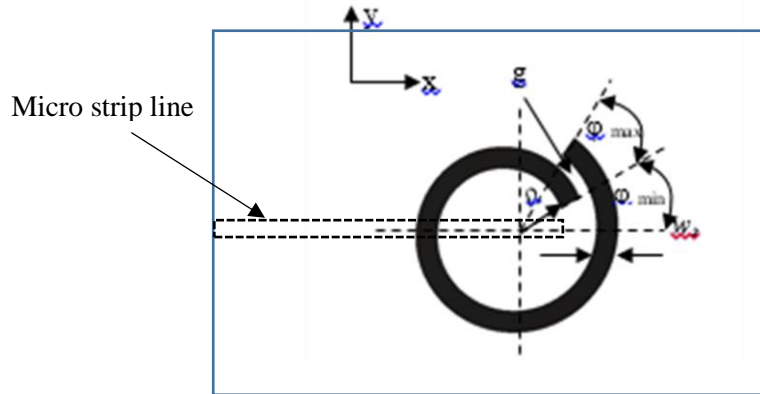


Figure 5.3: Geometry of a single-arm spiral slot.

A single layer DRA has been simulated when fed using the above-mentioned spiral-slot. The performance is illustrated in Figure 5.4, where it can be noted that a dual band is achieved with impedance bandwidths of 19.29 % and 9.37%, respectively, at the frequency range from 24.3 GHz to 29.6 GHz and 30.5 GHz to 33.5GHz. In addition, it can be noted that the single-layered DRA supports dual resonance modes of  $TE_{112}, TE_{511}$  at 25.1GHz, 30.81GHz, respectively. The simulated axial ratio bandwidth has been acquired over a frequency range of 28.3-29.5 GHz, which corresponds to a reasonable AR bandwidth of 4.15%. Figure 5.5 presents the radiation patterns of the  $TE_{112}$  mode, where it can be seen that a maximum gain of 5.7 dBi has been achieved, which can be attributed to the increased number of short magnetic dipoles of the higher-order mode.

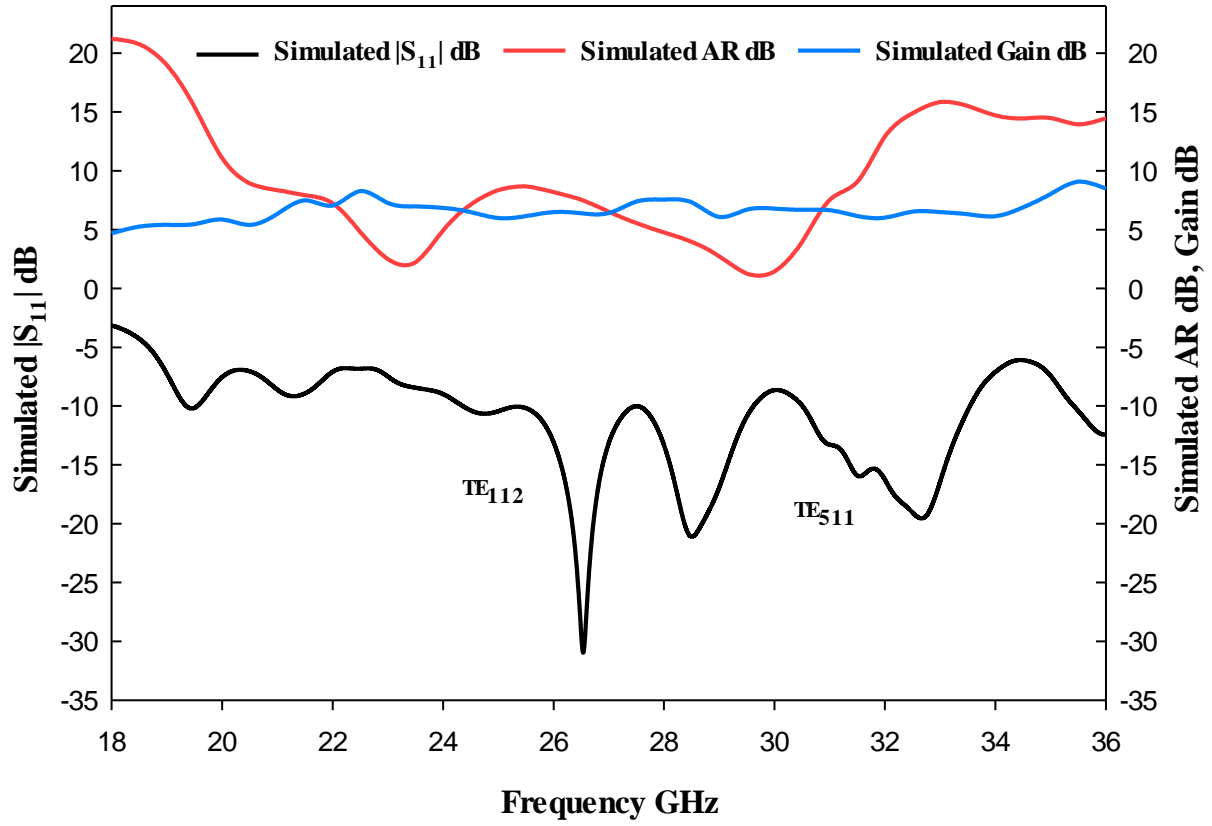
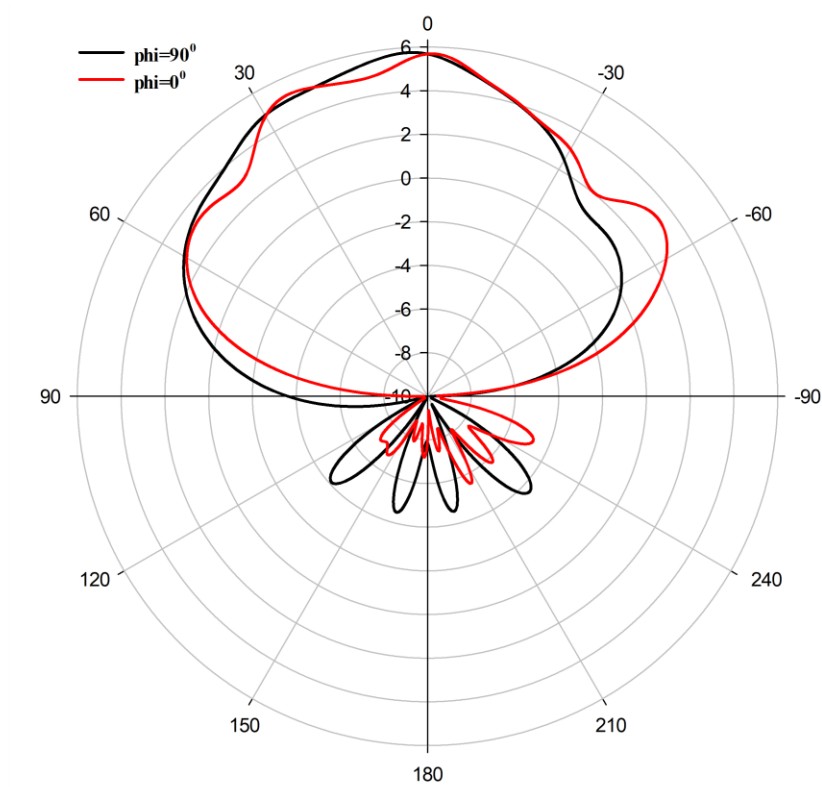
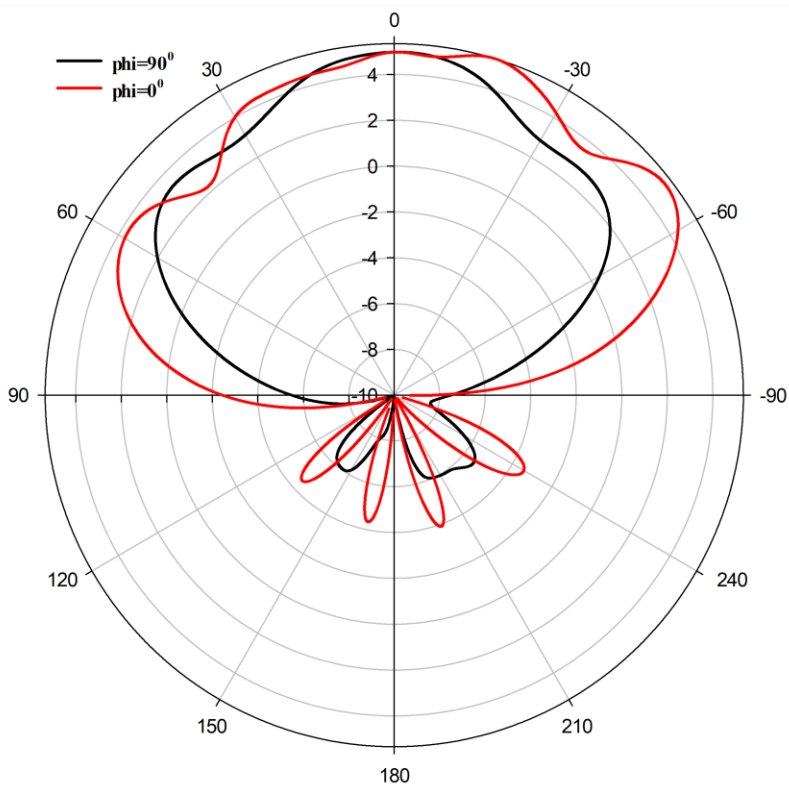


Figure 5.4: Simulated  $|S_{11}|$ , axial ratio and gain of the single layered HDRA.



(a)



(b)

Figure 5.5: Radiation pattern of (a)  $TE_{112}$  at 25.1GHz, (b)  $TE_{511}$  at 30.8GHz for a single layer HDRA.

To enhance the impedance bandwidth as well as the axial ratio AR, the proposed hemispherical DRA has been coated by a lower permittivity dielectric layer. Figure.5.2 illustrates the configuration of the proposed layered hemispherical DRA with inner layer's radius of  $a_1=3.8\text{mm}$  and a relative permittivity of  $\epsilon_{r1}=10$ . The outer Polyimide layer has a radius of  $a_2=5.7\text{mm}$  with a dielectric constant of  $\epsilon_{r2}= 3.5$ . In this case, the permittivities for the proposed DR were chosen based on their availability.

To achieve maximum coupling between the antenna and its feed network, the length of the stubs and slot dimensions are optimized using CST MWS. Furthermore, the thickness of the coated  $\delta a$  is optimized to understand its impact. In the initial configuration, the radius of the first layer was set at 3.8 mm with a relative permittivity of 10. The outer layer thickness  $\delta a=a_2-a_1$  was increased from 0.9 mm and 2.4 mm. A comparison of the effects of different outer layer thicknesses is presented in Table 5.1 and shown in Figure 5.6. From these results it can be noted that the widest impedance bandwidth was observed when the outer layer thickness is 1.9 mm and the narrowest bandwidth appeared when it was 1.4 mm. Figure 5.7 illustrates that the widest AR bandwidth exists when an outer layer thickness of 1.9 mm is used. On the other hand, an outer layer thickness of 1.4 mm yielded the narrowest AR bandwidth. Based on Figures 5.6, 5.7 and 5.8, it was found that using a thickness of 1.9 mm for the dielectric coat results in significant improvements in impedance and axial ratio bandwidths. This is because it excites the following resonance modes. Table 5.1 shows  $TE_{311}$ ,  $TE_{112}$ ,  $TE_{511}$ , and  $TE_{312}$  at 19 GHz, 24.6 GHz, 28.6GHz, and 33.4 GHz respectively with a bandwidth of 57.1% spanning from 18.6 to 33.5 GHz as shows in Table 5.2.This is due to the travelling wave currents distribution along the spiral slot. Therefore, an optimum radius of 5.7 mm has been used for the outer layer .Furthermore, Figure 5.9 illustrates the variation of the  $S_{11}$  bandwidth as a function of the coating thickness, with the maximum  $S_{11}$  bandwidth achieved using the same outer layer thickness as that for the widest CP bandwidth of 1.9 mm.

Table 5-1: The impact of different outer layer thicknesses  $\delta a$ .

$a_1$ mm	$a_2$ mm	$\delta a$ mm	$S_{11}$ Bandwidth %	AR Bandwidth %	Gain dBic
3.8	3.8	0 (no coating)	6.7 and 25.7	4.15	6.3
3.8	4.7	0.9	15.3 and 35.7	0	8.4 dB
3.8	5.2	1.4	15.3 and 35.7	0	8 dB
<b>3.8</b>	<b>5.7</b>	<b>1.9</b>	<b>57.1</b>	<b>17</b>	<b>7.5</b>
3.8	6.2	2.4	16.9 and 35	4.04 and 2.05	7.2
3.8	6.7	2.9	20.7 and 6.9	2.9	7.4
3.8	7.2	3.4	25.4	2.6	8.6
3.8	7.7	3.9	28.6	2.21	8.7

Table 5-2: The several of Resonance frequency TE for the layered HDRA

<b>Resonance TE<sub>nms</sub> mode</b>	<b>Resonance frequency <math>f_{TE_{nms}}</math> GHz</b>
<b>TE<sub>112</sub></b>	<b>24.6</b>
<b>TE<sub>311</sub></b>	<b>19</b>
<b>TE<sub>312</sub></b>	<b>33.4</b>
<b>TE<sub>511</sub></b>	<b>28.6</b>

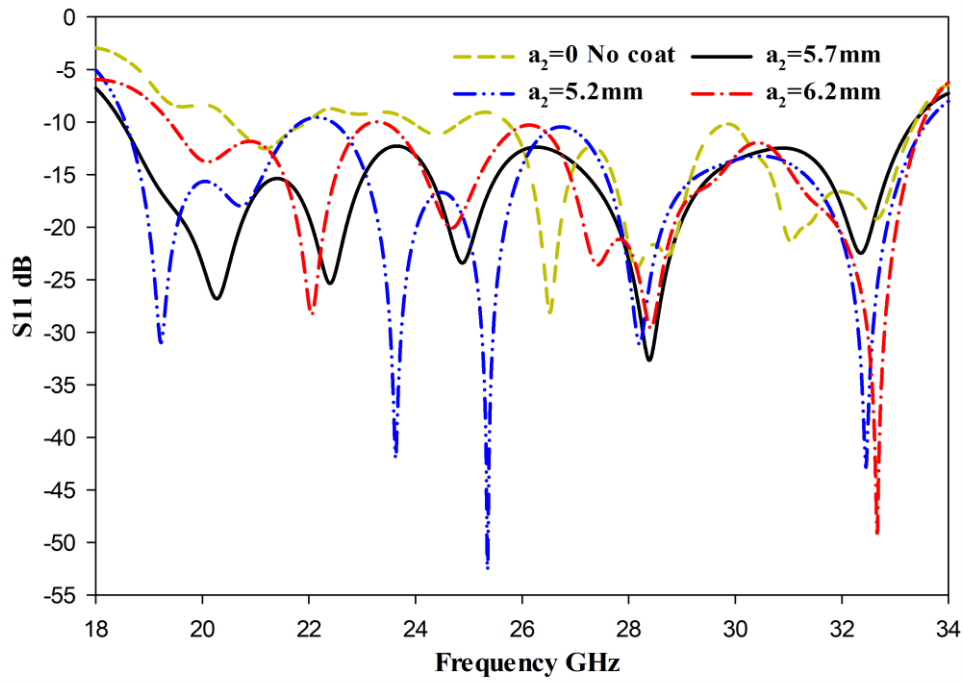


Figure 5.6: Simulated  $|S_{11}|$  with various thicknesses of the outer layer.

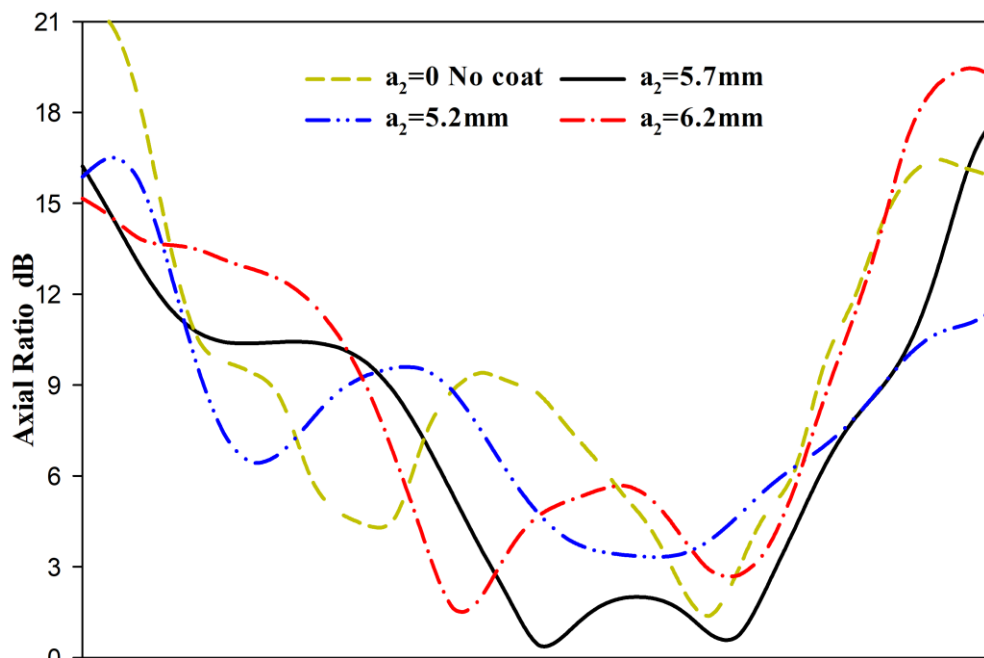


Figure 5.7: Simulated axial ratio with various thicknesses of the outer layer.

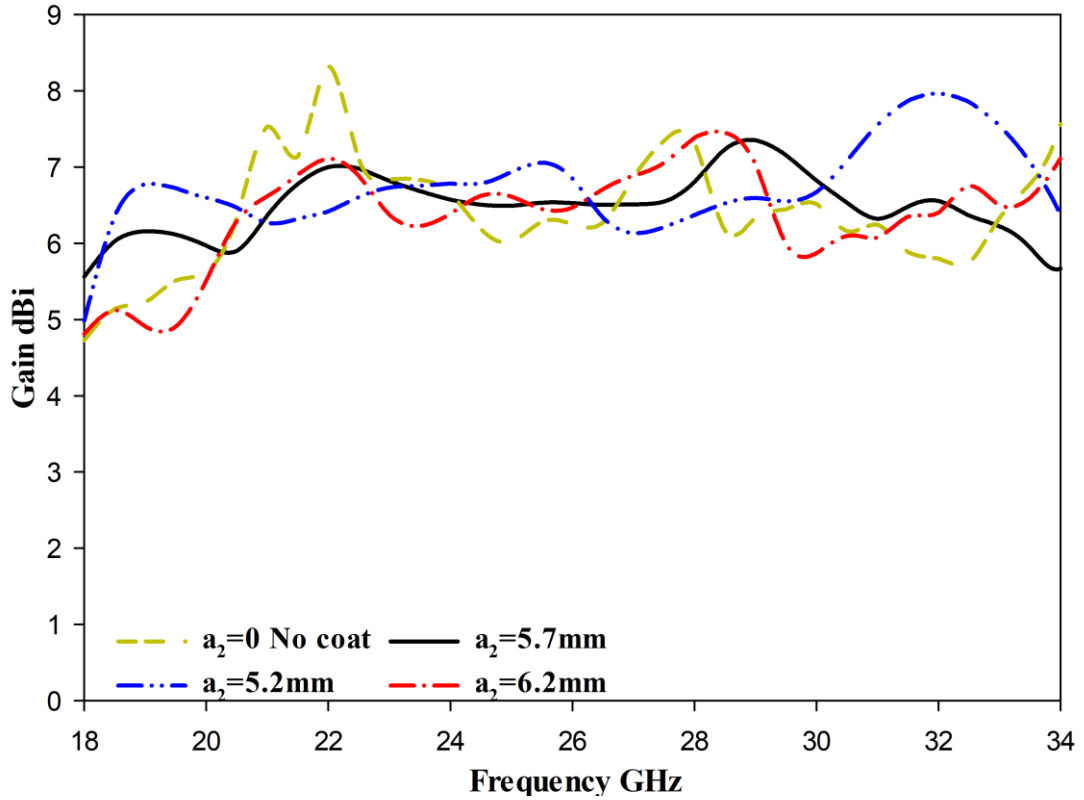


Figure 5.8: Simulated gain with various thicknesses of the outer layer.

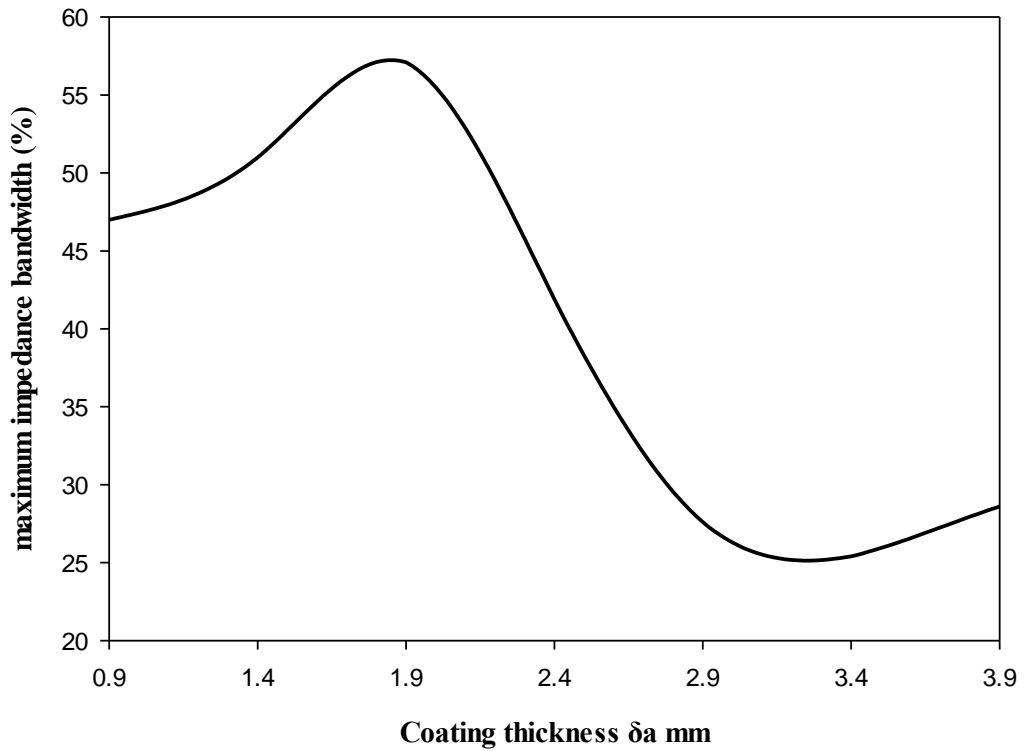


Figure 5.9: Maximum bandwidth as function of the outer layer thickness

### 5.2.2 Parametric Study

The time domain solver of CST MWS has been used to conduct simulations. In order to come up with the optimal dimensions that can offer wide impedance and axial ratio bandwidths, the spiral-slot's width and maximum rotation angle was varied when an outer layer thickness of 5.7 mm was utilized.

#### *iii Impact of spiral-slot's width ( $w_s$ )*

In order to understand the impact of the spiral slot's width on the performance,  $w_s$  was varied between 0.28mm and 0.48mm. As illustrated in Figure 5.10, The widest impedance bandwidth of 57.1% was observed when the slot width is 0.38 mm which excites the following resonance modes  $TE_{311}$ ,  $TE_{112}$ ,  $TE_{511}$ , and  $TE_{312}$  at 19 GHz, 24.6 GHz, 28.6 GHz, and 33.4 GHz, respectively these modes of the two-layer structure have been determined, by using the equivalent permittivity in MATLAB. On the other hand, the narrowest bandwidth was observed when the slot width was 0.28 mm Figure 5.11 demonstrates the impact of  $w_s$  on the achieved AR bandwidth, where it is evident that the widest AR bandwidth of 17% was achieved when the  $w_s=0.38$  mm. Figure 5.12 illustrates the gain variation when various slot's widths are utilized with the highest gain attained when  $w_s=0.38$ mm. Therefore, the optimum slot width has been chosen as 0.38 mm.

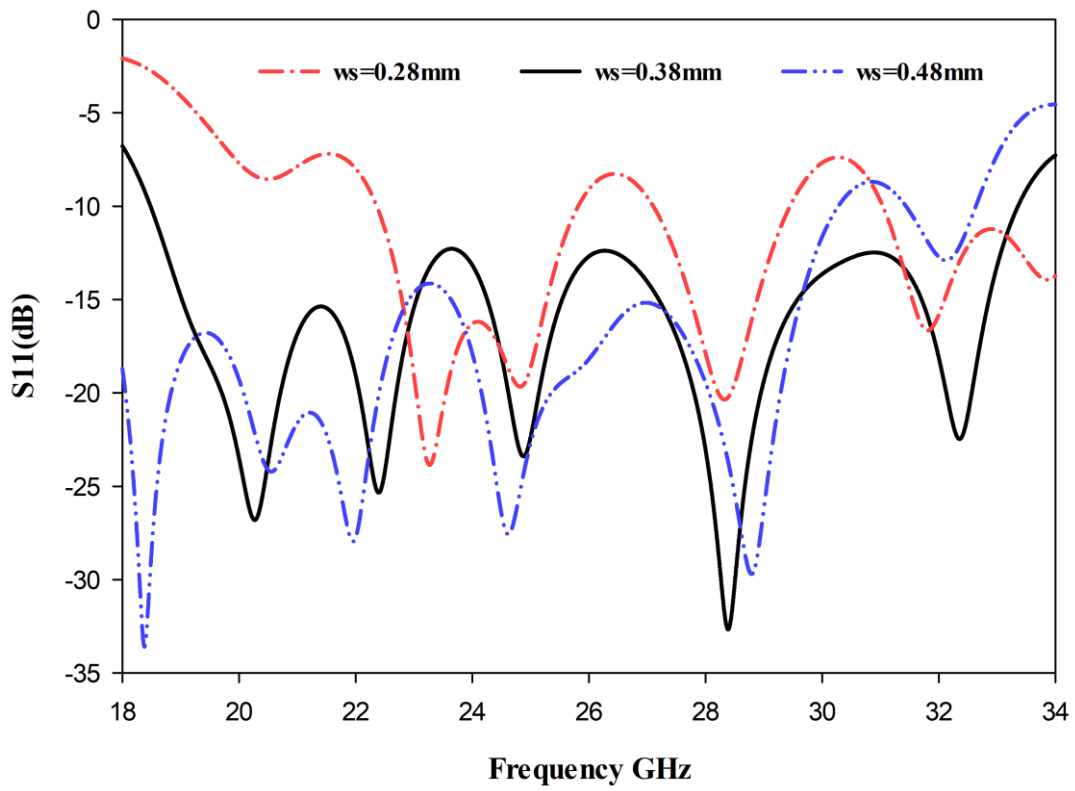


Figure 5.10: Simulated  $|S_{11}|$  with various slot widths (ws).

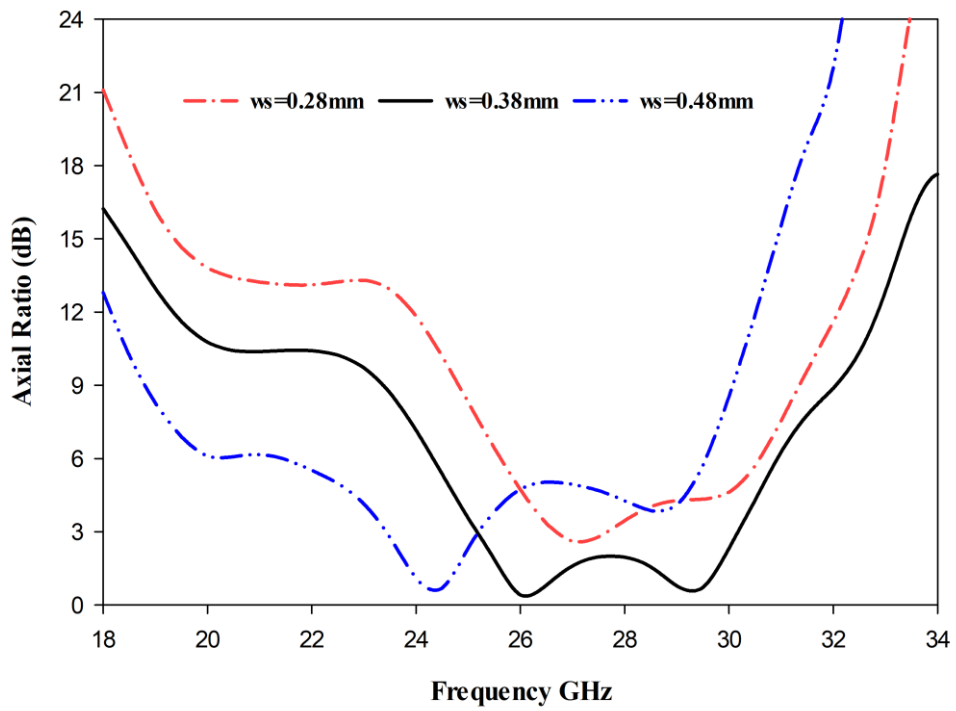


Figure 5.11: Simulated axial ratio with various slot widths (ws).

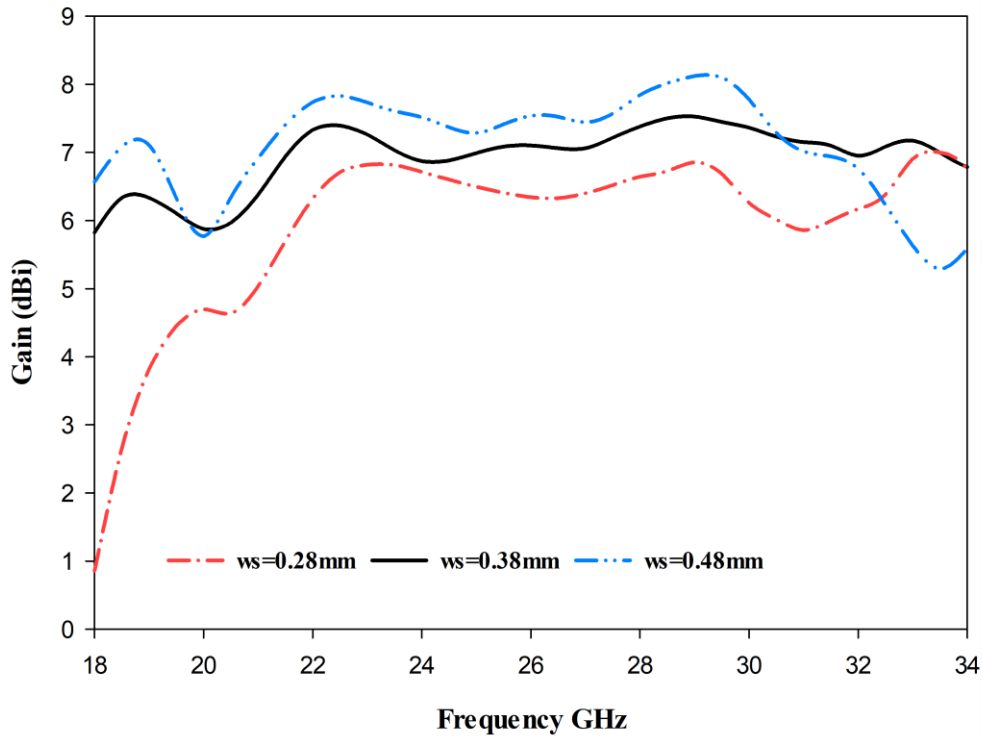


Figure 5.12: Simulated gain with various slot widths (ws).

#### *iv The impact of the maximum rotation angle ( $\varphi_{max}$ )*

For a given spiral geometry, the maximum rotation angle determines the overall arc length. This study considers the impact of changing the maximum rotation angle from  $\varphi_{max}= 2.155\pi$  to  $\varphi_{max}= 2.172\pi$  with an increment of  $0.005\pi$ . It should be noted this range of the maximum rotation angles corresponds to arm lengths of 3.87 mm to 4.36 mm which are approximately  $0.69 \lambda_{eff}$  and  $0.78 \lambda_{eff}$  respectively. The  $S_{11}|$  simulation results for various maximum rotation angles are depicted in Figure 5.13. with the broadest impedance bandwidth was observed when  $\varphi_{max} = 2.166\pi$ . Figure 5.14 demonstrates that that the widest AR bandwidth is also observed when  $\varphi_{max} = 2.166\pi$ . It's also worth emphasizing an important finding: the gain remains relatively constant, irrespective of the maximum rotation angle. This means whether we adjust

$\varphi_{\max}$  a little higher or lower, the gain we obtain remains almost unchanged. This consistency across different  $\varphi_{\max}$  values is clearly presented in Figure 5.15.

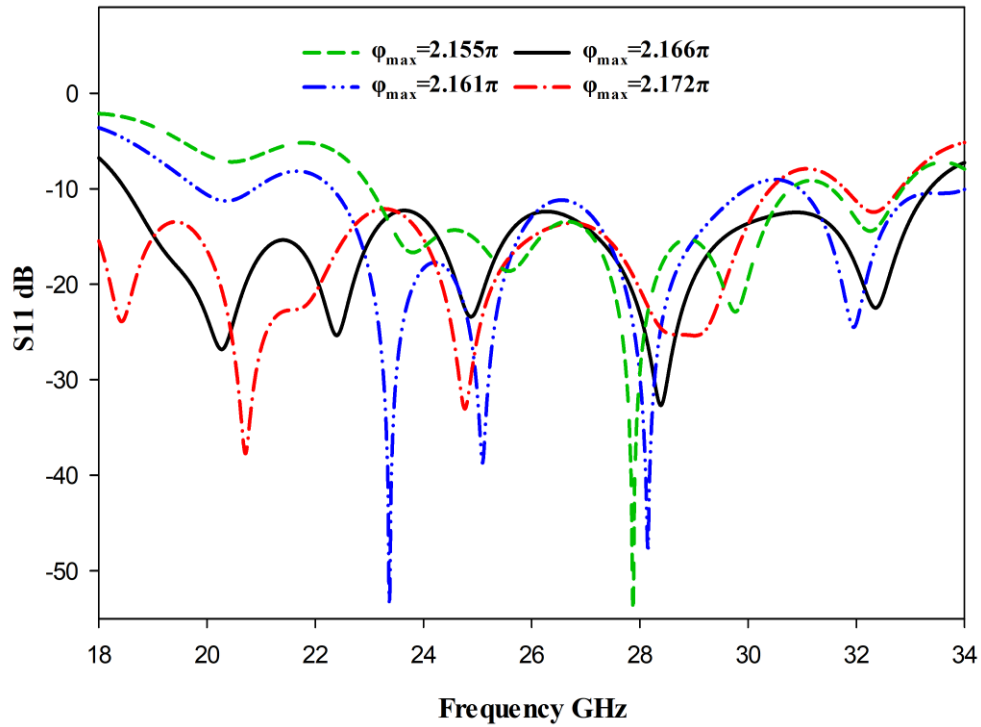


Figure 5.13: Simulated  $|S_{11}|$  for various maximum rotation angles ( $\varphi_{\max}$ ).

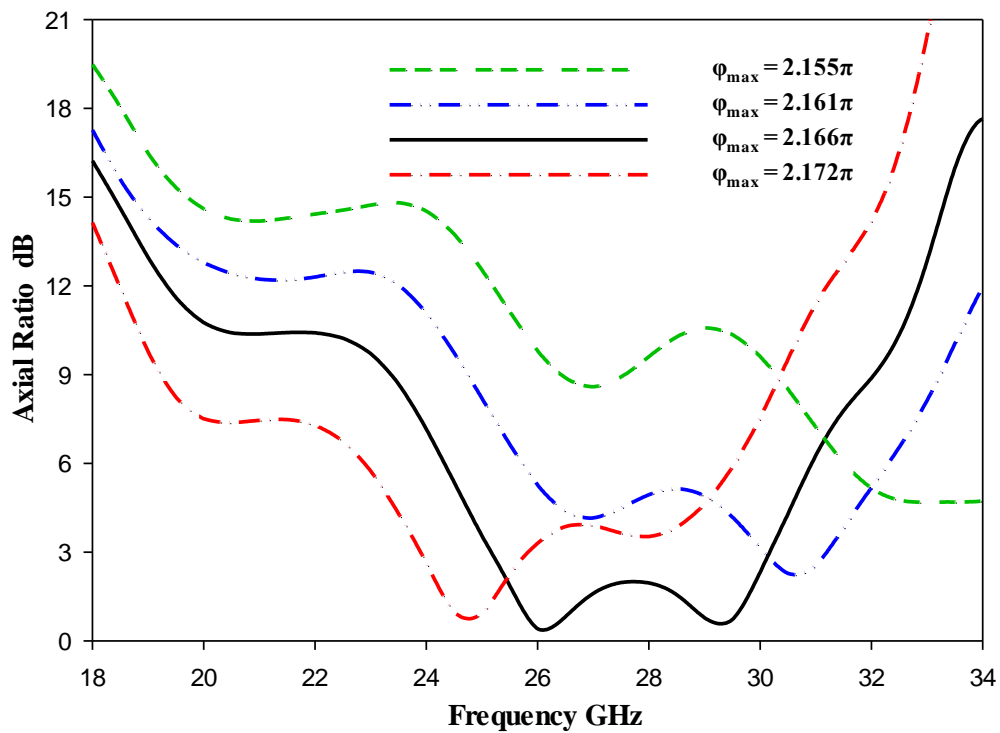


Figure 5.14: Simulated axial ratio for various maximum rotation angles ( $\varphi_{\max}$ ).

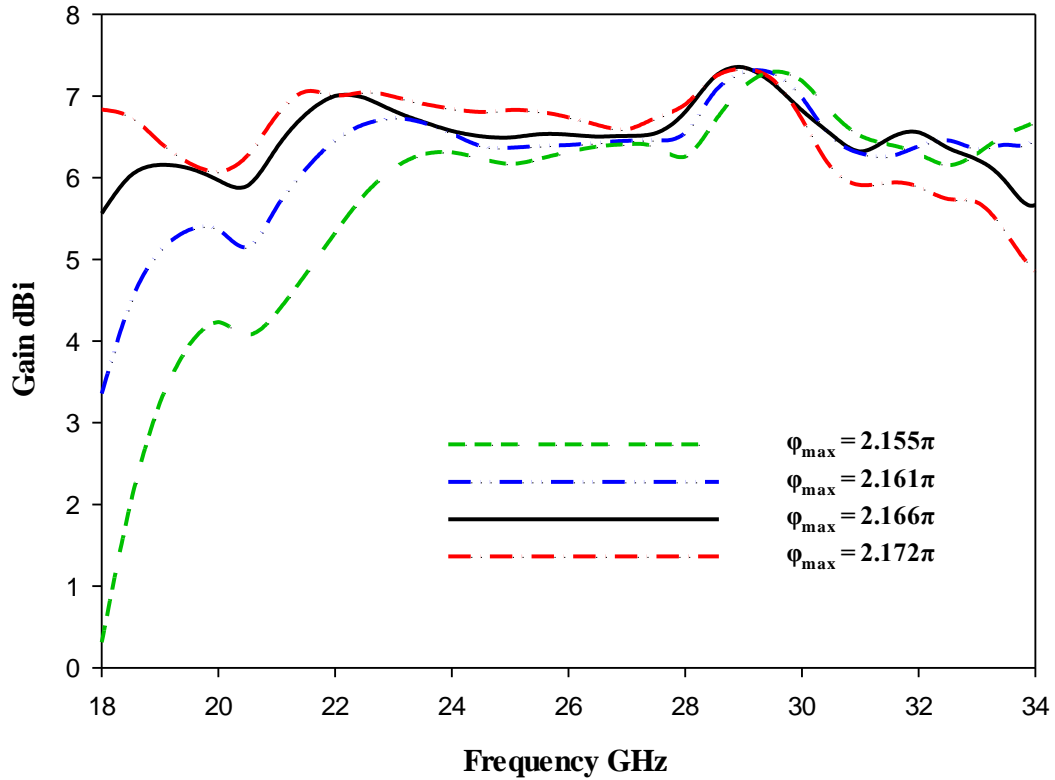


Figure 5.15: Simulated gain for various maximum rotation angles ( $\phi_{max}$ )

### ***v*** The impact of the gap ( $g$ ) between the turns of the spiral-slot's arm

This study investigated a single-arm Archimedean spiral-slot with a separation ( $g$ ) between the turn. Single-arm spiral slot geometries with  $N = 1$  turns were studied to see how  $g$  affected the DRA's performance. As mentioned in Chapter 2, for a particular spiral slot geometry, increasing  $g$  leads to an increase in the overall length of the slot, which reduces the resonant frequency [102]. According to Figure 5.16 the widest bandwidth has been achieved when  $g=0.2$  mm, which stimulates the  $TE_{311}$ ,  $TE_{112}$ ,  $TE_{511}$ , and  $TE_{312}$  at 19 GHz, 24.6 GHz, 28.6GHz, and 33.4 GHz, respectively, over an impedance bandwidth of of 57.1%. An AR bandwidth of 17%, gain of  $\sim 7.5$ dBic have been also achieved when  $g=0.2$  mm as demonstrated in Figures 5.17 and 5.18, respectively. In comparison, a narrower S11 was achieved, specifically 23% and 20%, within the frequency ranges of 23.8GHz to 30GHz and 18GHz to 22GHz respectively.

Moreover, an Axial Ratio (AR) bandwidth of 6.3% and 5.3% was accomplished when the gap (g) was set at 0.3mm, yielding a gain of 7.5 dB.

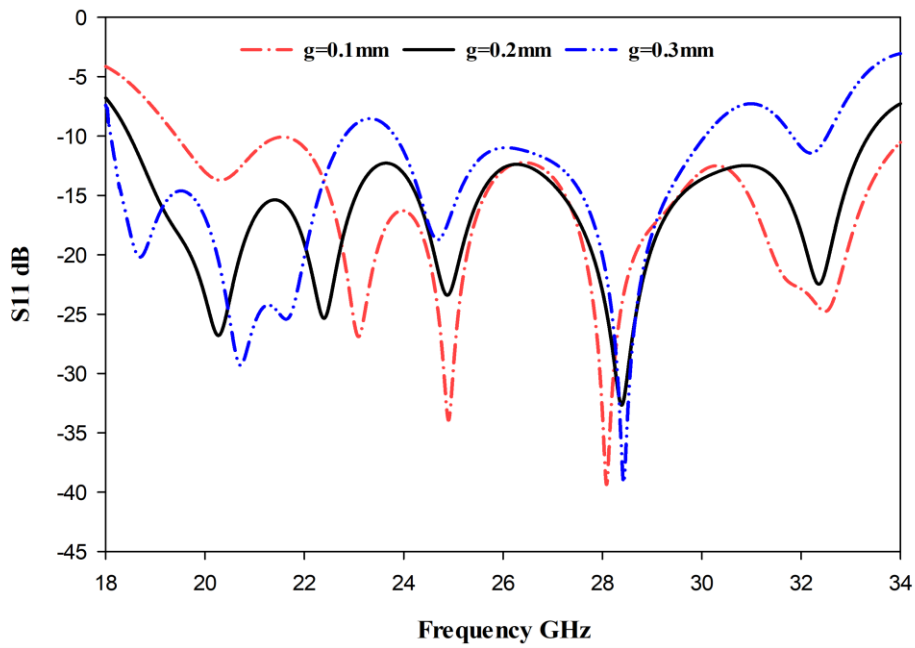


Figure 5.16: Simulated  $|S_{11}|$  with various values of  $g$ .

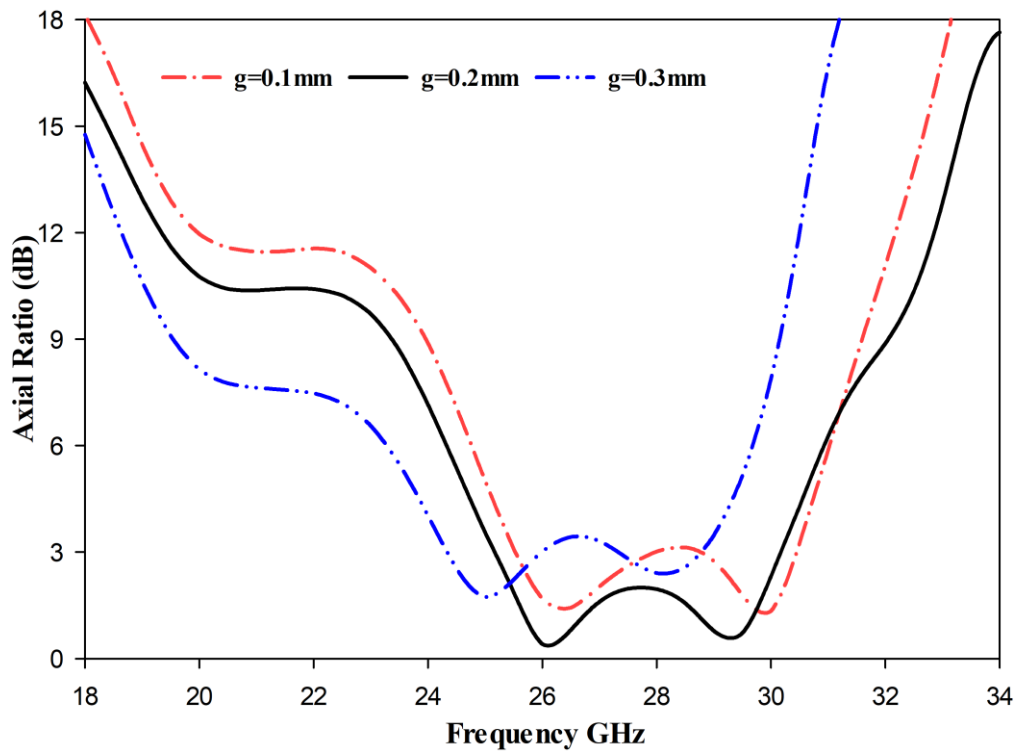


Figure 5.17: Simulated axial ratio with various values of  $g$ .

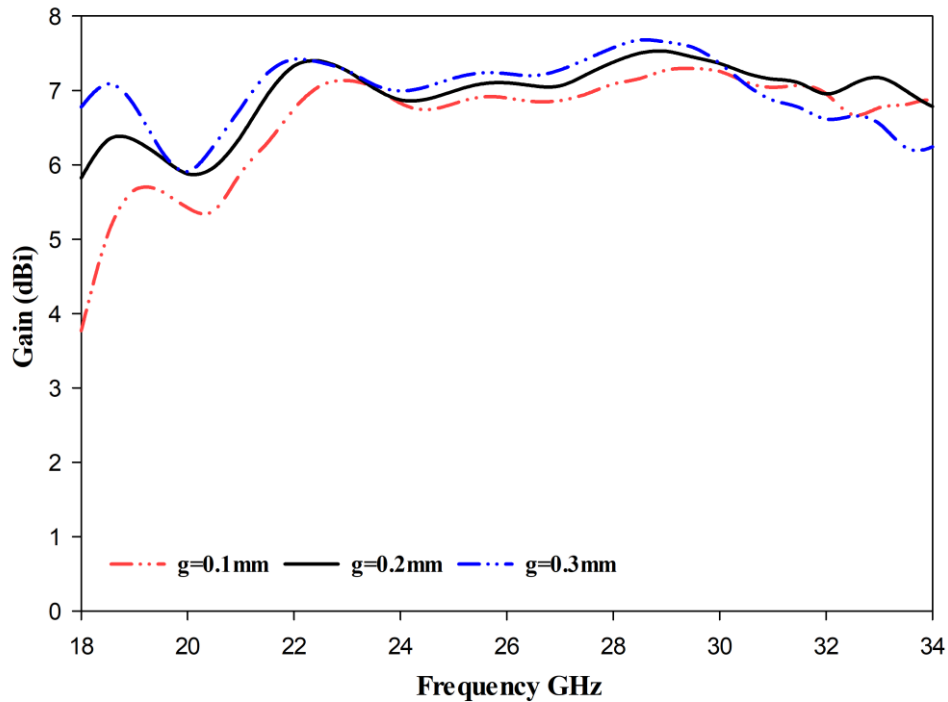


Figure 5.18: Simulated gain with various values of g.

### 5.2.3 Experimental Results

In order to validate the aforementioned simulation results, the inner layer of the hemisphere DRA has been manufactured by T-CERAM Company using Alumina with a fabrication tolerance of 0.06mm as well as a dielectric constant of  $\epsilon_r=10$  and loss tangent of  $\tan \delta < 0.002$ . The antenna outer layer (the coat) has been fabricated with the aid of 3D printing technology at the Protolabs Company using Polyimide material with dielectric constant of 3.5 and loss tangent of 0.0027. In addition, the antenna was placed on a Ro4350B dielectric substrate with respective thickness of 0.42 mm, permittivity of 3.48 and loss tangent of 0.0037 provided by Wrekin Circuits. The whole prototype has been fed using a microstrip line that was placed underneath the Roger substrate. Moreover, a 2.4 mm SMA connector was utilized to connect the feeding microstrip line to the Agilent Technologies E5071C mm wave vector network

analyser through a 50 coaxial cable. The radiation patterns measurements have been measured using an (SNF-FIX-1.0) near field system. The antenna and its feed network are illustrated in Figure 5.19

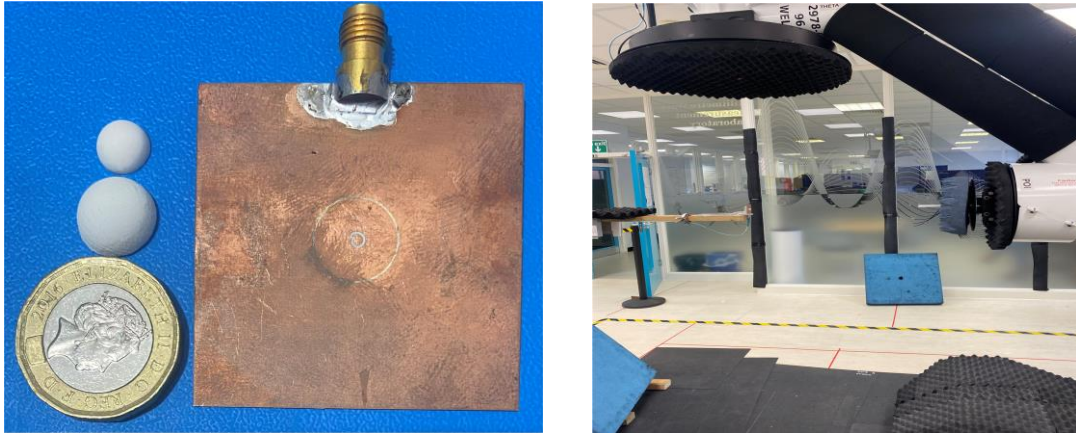


Figure 5.19: Prototype of the multi-layer hemispherical DRA.

The single-layer HDRA introduced in the previous section has been coated by an outer dielectric layer. The simulated and measured reflection coefficients are depicted in Figure 5.20 with a reasonable agreement between simulated and measured impedance bandwidths of 57.1% and 50.8%, respectively. These results demonstrated that the layered DRA supporting a multimode operation where the resonance modes of  $TE_{311}$ ,  $TE_{112}$ ,  $TE_{511}$ , and  $TE_{312}$  are excited at 19 GHz, 24.6 GHz, 28.6GHz, and 33.4 GHz, respectively. In addition, Figure 5.21 demonstrates that adding the outer dielectric layer enhances the AR bandwidth to 18.15% over a frequency range that simulated and measured AR bandwidths extend from 25.16 to 30.17 GHz and 25 to 30.6 GHz, respectively. Furthermore, the bandwidths improvement, at the presence of the dielectric coat layer, can be attributed to the fact that the added outer layer

acts as a transition region between the HDRA and air, which minimizes the wave reflections and lowers the quality factor of the antenna.

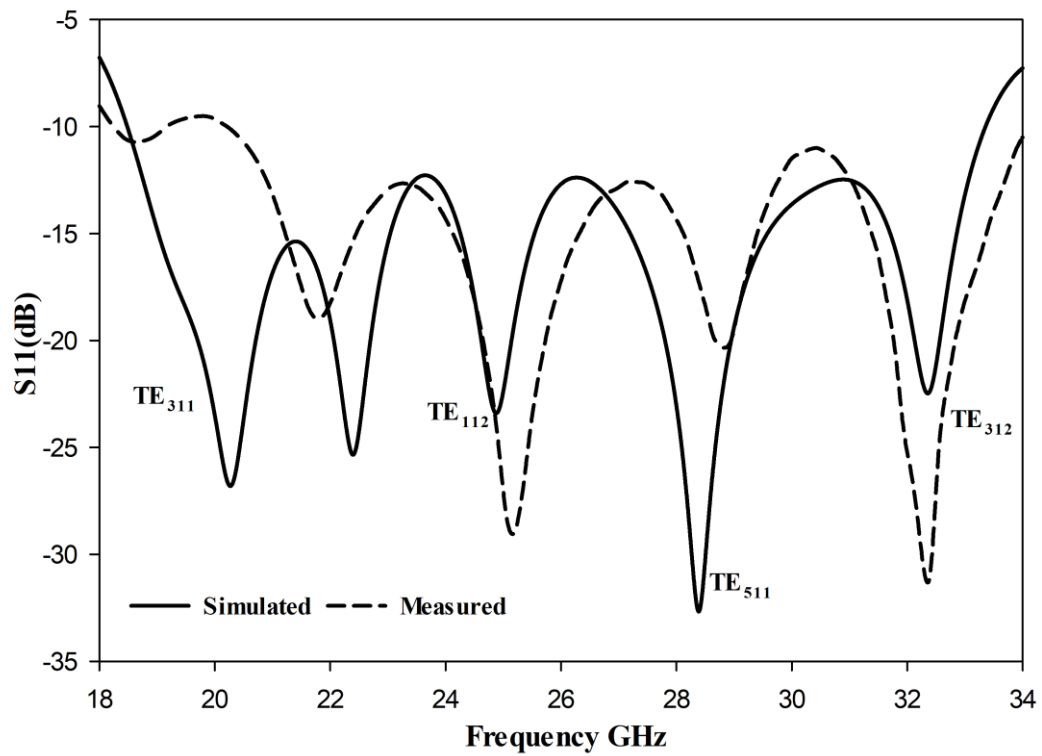


Figure 5.20: The simulated and measured reflection coefficient of layered HDRA.

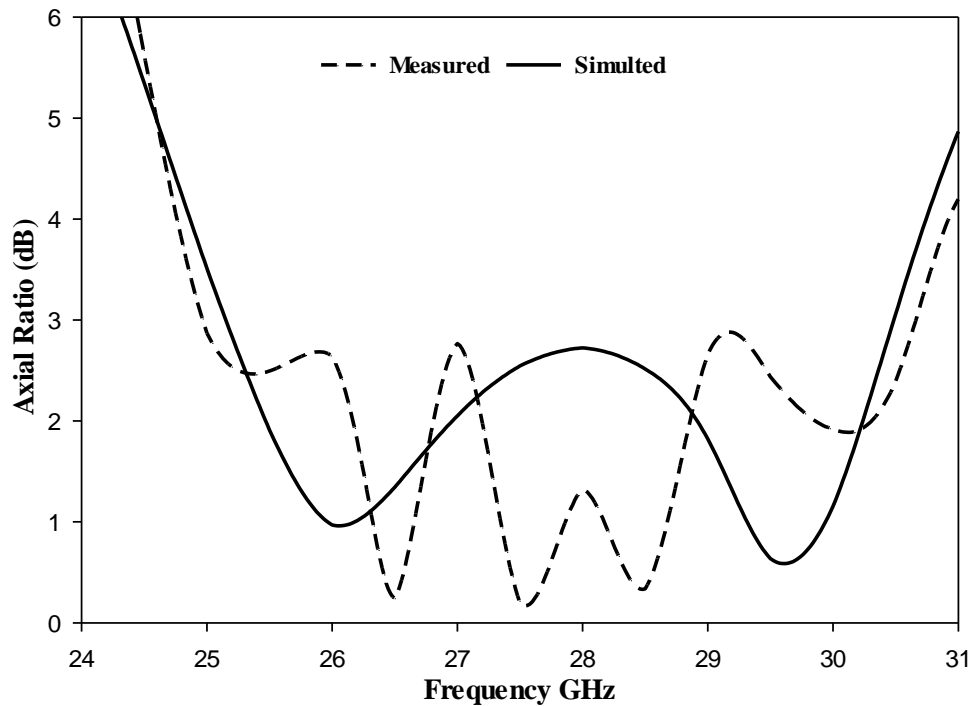


Figure 5.21: The simulated and measured axial ratio of a layered HDRA.

Figures 5.22 and 5.23 illustrate good agreement between the simulated and measured H-plane and E-plane radiation patterns at 22GHz and 29GHz, respectively. It is evident that a left hand circularly polarized (LHCP) has been achieved since  $E_L$  is higher than  $E_R$  by ~14dB. Figure 5.24 presents the layered DRA's gain as a function of frequency, from which it can be noted that. The maximum gain has been achieved at 29GHz with simulated and measured peaks of 7.57 dBic and 6.9dBic, respectively. It should be noted that the maximum gains have been achieved when the  $TE_{511}$  resonance mode is excited, which illustrate the gain enhancement due to the excitation of higher order modes. It is worth pointing out that the drop in measured gain could be attributed to experimental errors such as the loss in the cables, the SMA soldering as well as the alignment in the anechoic chambers.

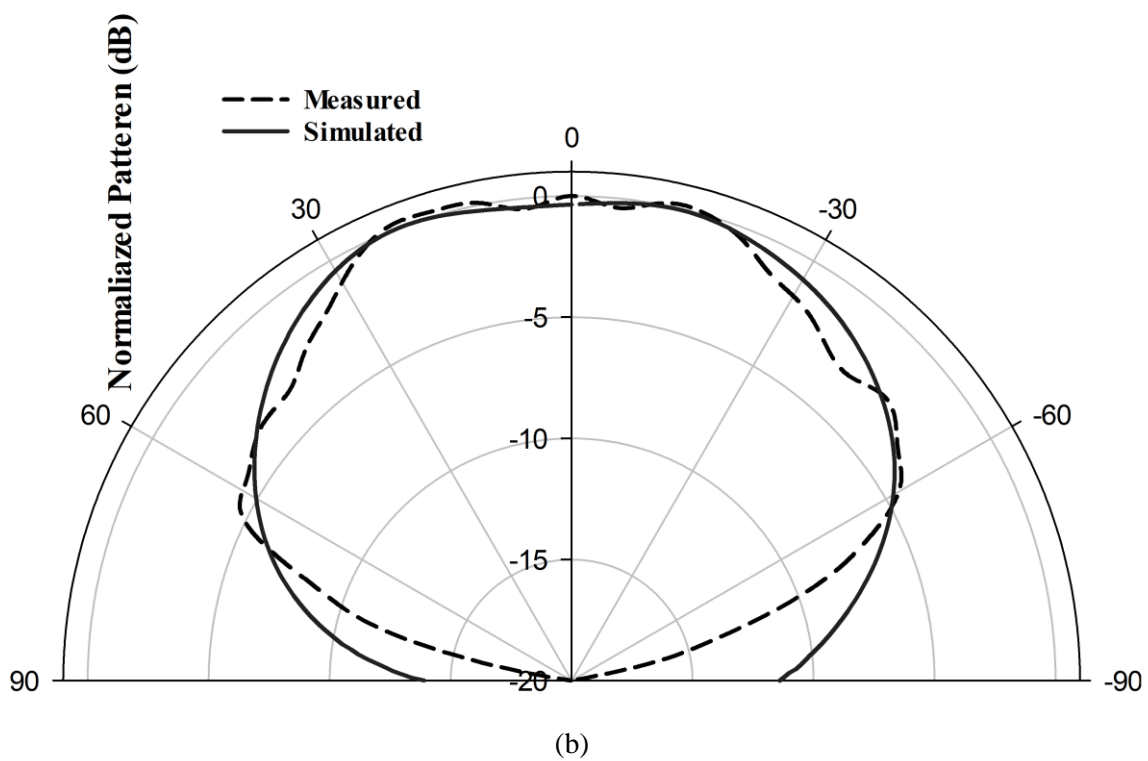
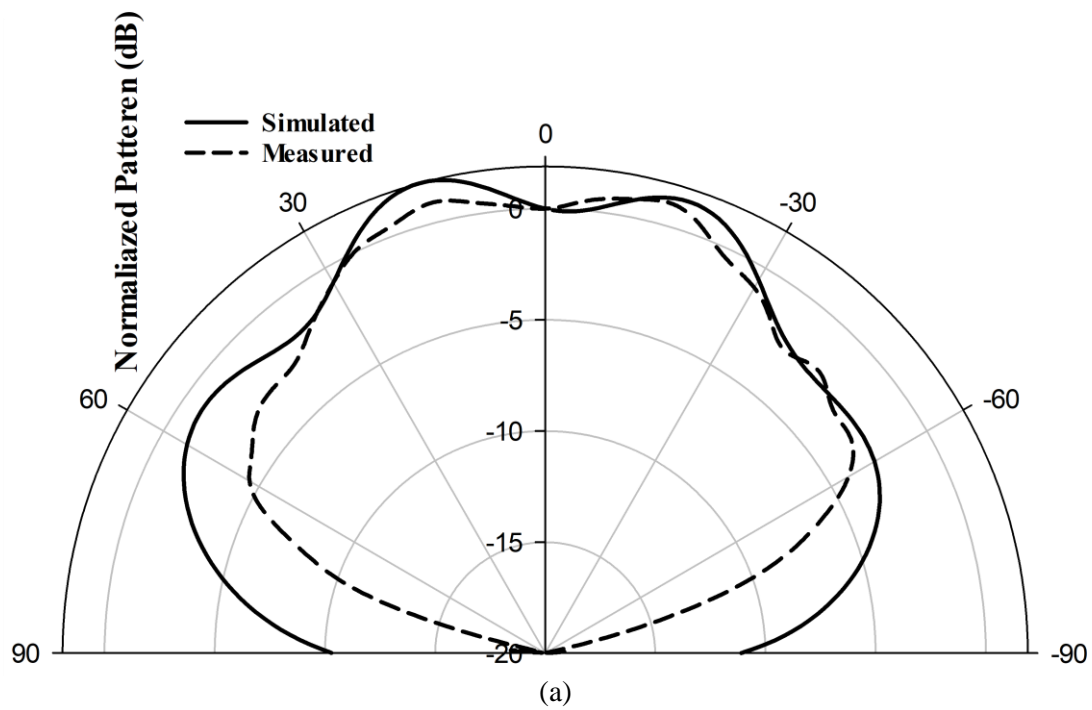


Figure 5.22: Simulated and measured of the radiation patterns of a layered HDRA at 22 GHz, (a)  $\phi=0^\circ$ , (b)  $\phi=90^\circ$ .

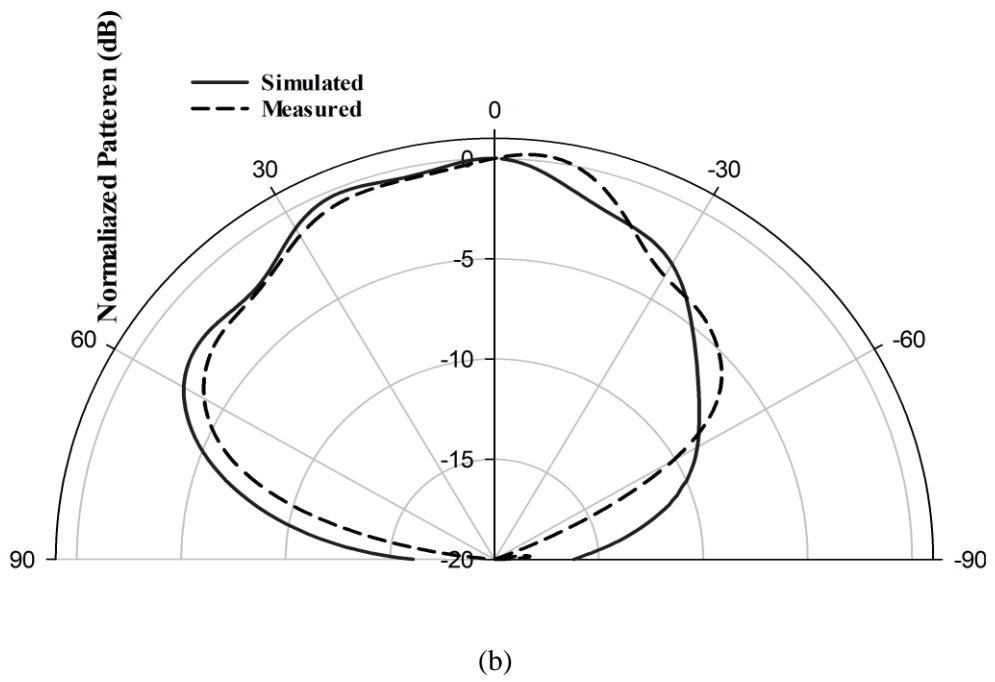
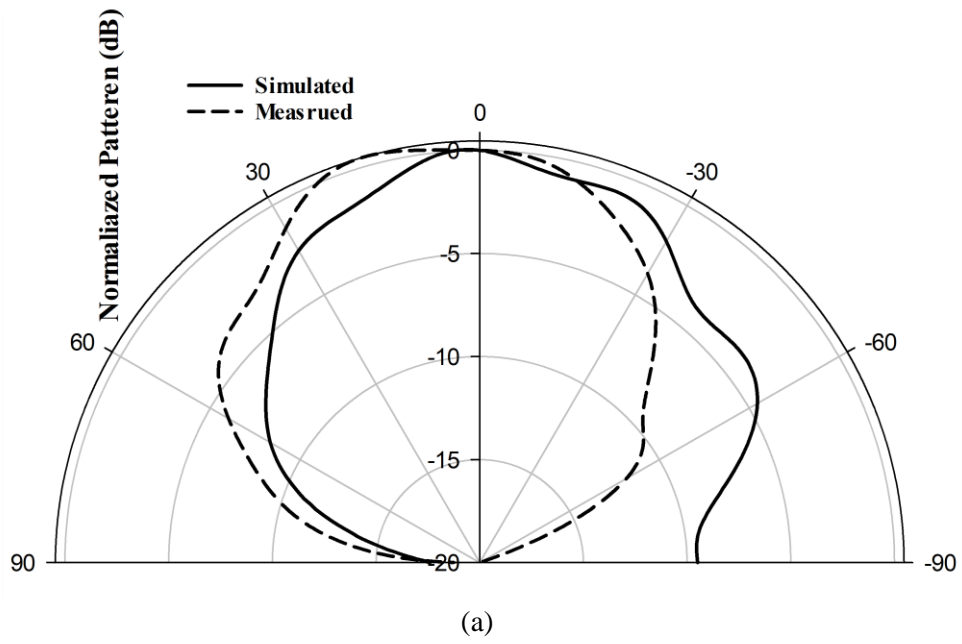


Figure 5.23: Simulated and measured of the radiation patterns of a layered HDRA at 29 GHz, (a)  $\phi=0^\circ$ , (b)  $\phi=90^\circ$ .

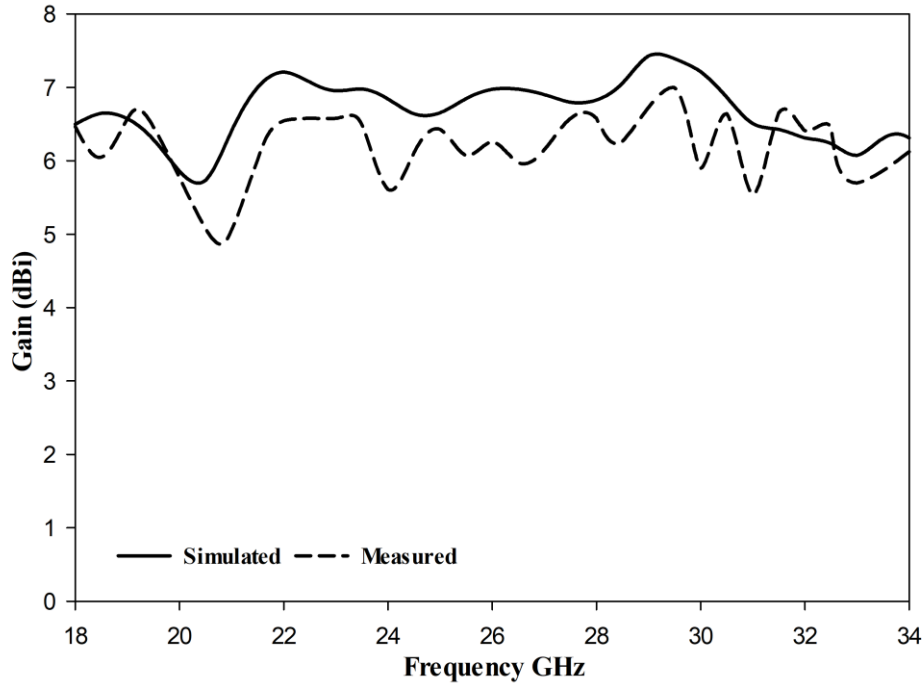


Figure 5.24: Simulated and measured gain of a layered HDRA.

### 5.3 Hemispherical DRA with a perforated Alumina coat

The proposed multilayer HDRA has been created in accordance with the FDM 3-D printing technology. Hence, the whole structure consists of a central solid Alumina DRA with a perforated Alumina layer that has a reduced effective dielectric constant of 3.5 to replace the individual Polyimide coat used earlier. Therefore, no physical assembly of the two layers is needed and there are no potential air-gaps between the DRA and the dielectric coat. This approach renders it easier to create the proposed mm Wave hemispherical DRA. Moreover, it is possible to realise the different dielectric constants of the dielectric coat [84] by using different hole sizes, as per filling-ratio theory[119].

### 5.3.1 Antenna conflagration

The proposed 3-D-printed HDRA is illustrated in Figure 5.25, which reveals that the DRA comprises two concentric Alumina sections. Specifically, the outer dielectric is characterised by different air-filling ratios designed to deliver diverse effective dielectric constants. The (effective) dielectric constants of the second layer [84].

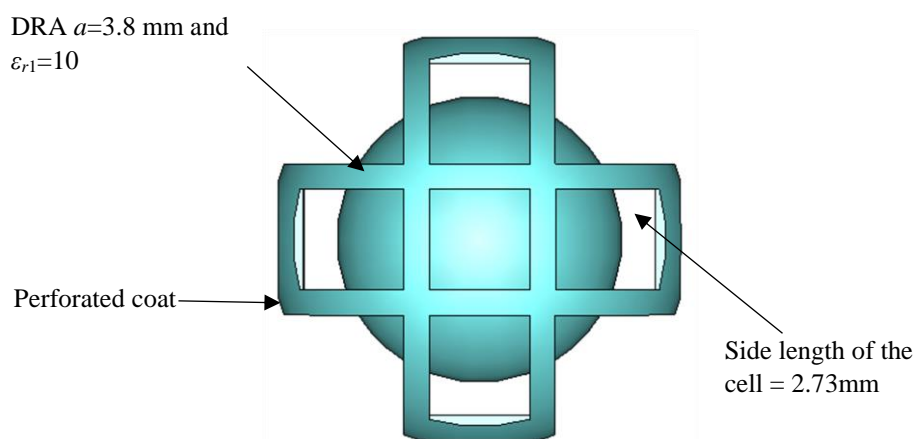


Figure 5.25: Hemispherical Alumina DRA with a perforated Alumina dielectric coat

As illustrated in Figure 5.2, the proposed antenna developed is configured using its exact dimensions and the feed network described in the previous section. Figure 5.26 demonstrates the overall 3D printed configuration that has been excited using the same feed network that was introduced in the previous section with mentioned earlier, the same dielectric material, Alumina, was utilised to print the inhomogeneous coated HDRA. The design employed in the present study uses a 3-D printing material with a dielectric constant of  $10 \pm 0.35$  over 18-34 GHz. In addition,  $\epsilon_{r1} = 10$  was used for the simulation.

To create the perforated coat, a cubic unit cell with a dielectric constant of  $\epsilon_{r1}$  was introduced. The unit cell wall thickness,  $t_c$ , and fixed side length of  $a$  were utilized  $2.73\text{mm}$  or  $0.254\lambda_0$  to calculate the resultant permittivity of the perforated coat in the following equation [84].

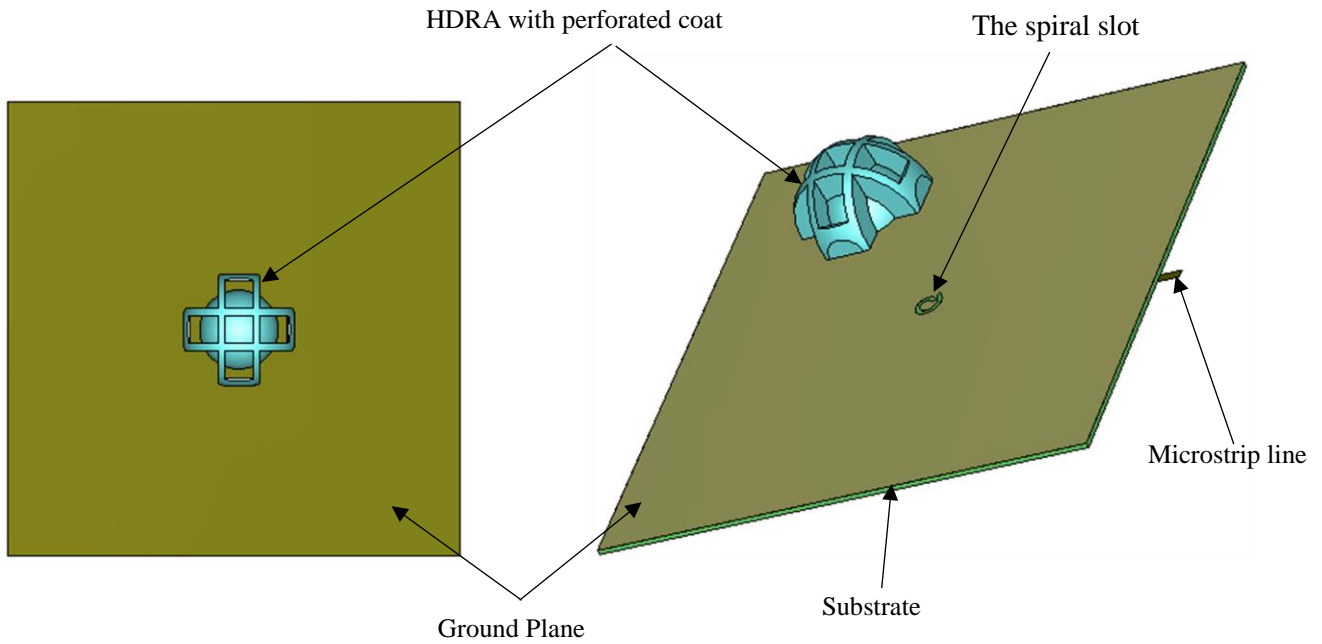


Figure 5.26: The configuration of the Hemispherical DRA with a perforated dielectric coat

$$\epsilon_{r2eff} = 0.55t_c\epsilon_{r1} - 0.04\epsilon_{r1} + 1.3 \quad (5.4)$$

The unit cell, which is intended to secure an effective dielectric constant  $\epsilon_{r2eff}$ . It has a side length of  $a$  and a wall thickness of  $t_c$ . The design presented has a side length  $a$  set as  $2.73\text{mm}$  or  $0.254\lambda_0$ , where  $\lambda_0$  denotes the wavelength in free space at  $28\text{GHz}$ . There are several advantages to this 3-D printable unit cell, the first being that the cell's effective dielectric constant can be regulated by modifying the wall thickness, as per filling ratio theory [119]. Secondly, the unit cell is self-supported in the  $z$ -direction.

### ***vi The impact of wall thickness for the unit cell:***

The control over the effective permittivity of a perforated dielectric coat can be exercised by modulating the wall thickness as stipulated in equation 5.4. An exploration into the influence of the unit cells' wall thickness was conducted to discern its optimal size. A range of thicknesses,  $t_c$ , from 0.59mm to 0.79mm, progressing in increments of 0.1, were simulated in the context of a hemispherical design adorned with a perforated dielectric coat. As illustrated in Figure 5.27, it can be noted that a wall thickness of 0.69 mm facilitates the broadest impedance bandwidth, in contrast to the thickness of 0.59 mm, which yielded the most confined bandwidth. This is expected according to equation (5.4), since a wall thickness of 0.69 mm provides the required effective permittivity of 3.5 for the perforated coat. Figure 5.28 corroborates these findings in the context of Axial Ratio Bandwidth (AR BW), revealing the maximum AR BW for a wall thickness of 0.69 mm, whilst the most restricted AR BW was associated with a wall thickness of 0.59 mm. The impact of the wall thickness on the gain is distinctly depicted in the same figure, with the most consistent gain observed at a thickness  $t_c$  of 0.69mm. This finding is further substantiated in Figures 5.27, 5.28, and 5.29.

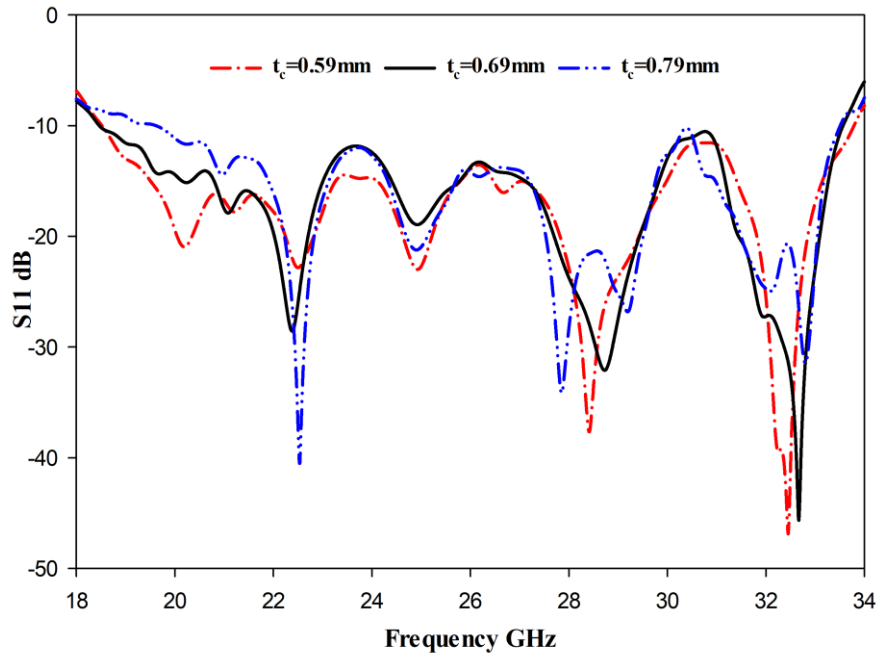


Figure 5.27: Simulated  $|S_{11}|$  with various unit cell's wall thicknesses ( $t_c$ ) for the perforated coat.

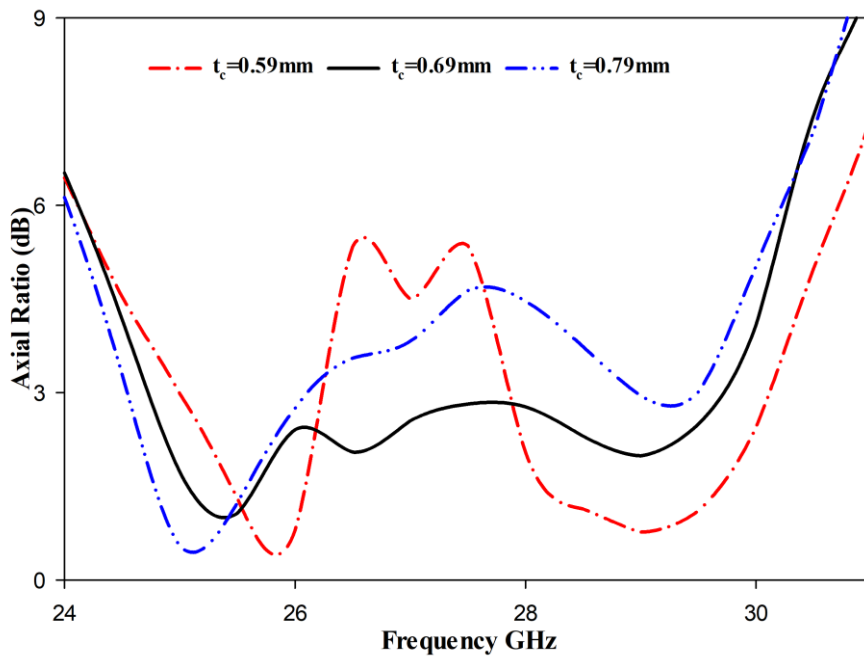


Figure 5.28: Simulated Axial Ratio with various wall thickness ( $t_c$ ).

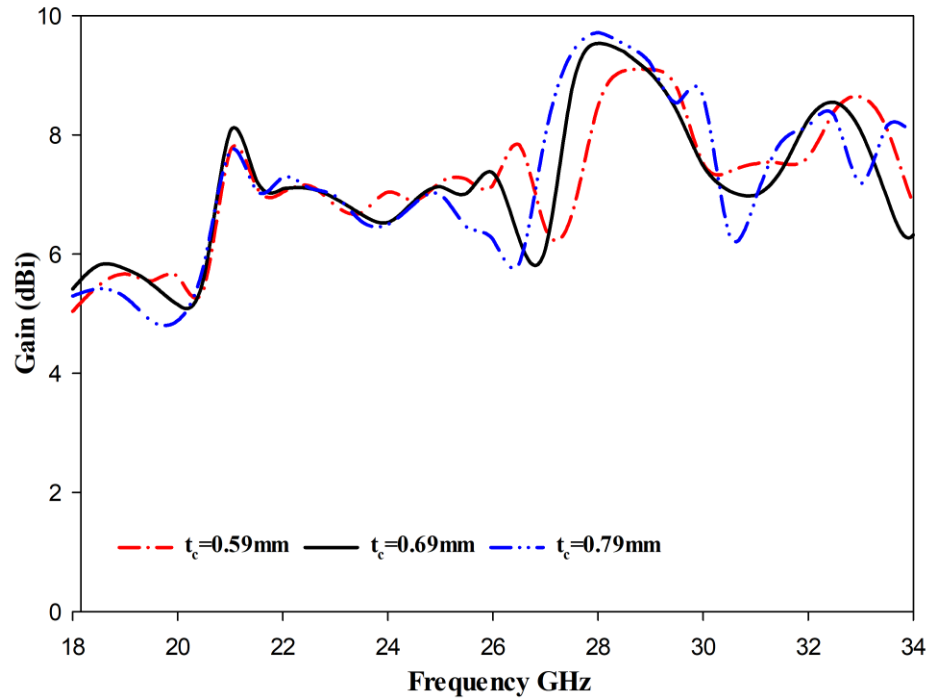


Figure 5.29: Simulated gain with various wall thickness ( $t_c$ ).

The HDRA with a perforated Alumina coat, as depicted in Figure 5.25, is marked by a constant dielectric constant within each layer. This implies that the unit cells across each layer maintain uniform wall thickness. Moreover, these unit cells possess the intrinsic capacity to provide mutual structural support, eliminating the necessity for supplementary support materials during the 3D printing process. As a direct outcome, there is a substantial diminution in both printing duration and material expenditure. Figure 5.30 presents a comparison between the return losses of the original solid structure and that of a perforated, printed version of the layered HDRA, underlining the close congruity between the two configurations. For example, an impedance bandwidth of 58.1% has been achieved for the perforated configuration compared to 57.1% for the layered structure.

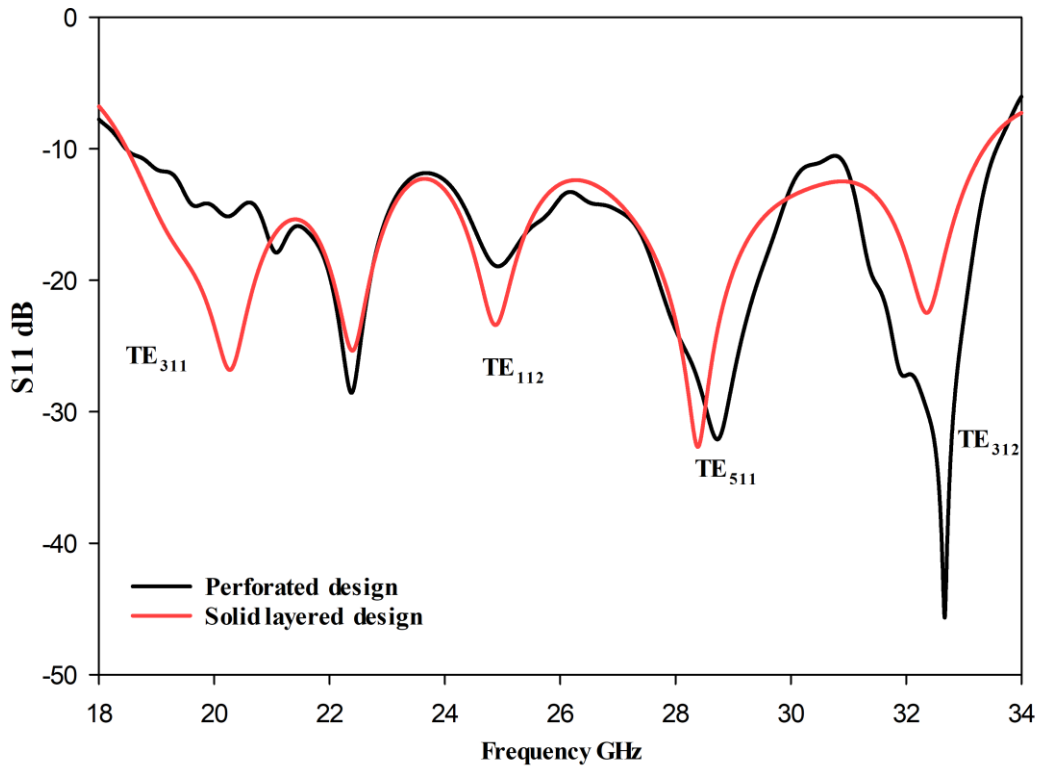


Figure 5.30: The simulated reflection coefficient of solid layered HDRA and a perforated dielectric coat HDRA.

### 5.3.2 Experimental Results

Figure 5.31 presents a prototype of the proposed 3D-printed HDRA with a perforated coat. The antenna was built by a 3D mattress company in its final configuration using a material with a dielectric constant of 10. Moreover, the proposed antenna is mounted on a Ro4350B dielectric substrate with a thickness of 0.42mm, a relative permittivity of 3.48 and a loss tangent of 0.0037, which were supplied by Wrekin Circuits. It was fed using a microstrip line printed underneath the Roger substrate. In addition, a 2.4 mm SMA connector is connected to the microstrip line feeding, and Agilent Technologies E5071C mm-wave vector network analyser is connected to the SMA via a 50 coaxial cable. According to Figure 5.32, measurement results are in good agreement with simulation results for the ( $|S_{11}| \leq -10$  dB) impedance bandwidth, which covers 59.5% and 58.05% respectively for the frequency range of 18.4 to 34 GHz and

18.4 to 33.5 GHz respectively. Results indicate that the 3D printed HDRA can operate in multiple modes, such as  $TE_{311}$ ,  $TE_{112}$ ,  $TE_{511}$ , and  $TE_{312}$  at 19 GHz, 24.6 GHz, 28.6GHz, and 33.4 GHz, respectively.



Figure 5.32: The prototype of the proposed hemispherical DRA with a perforated dielectric coat.

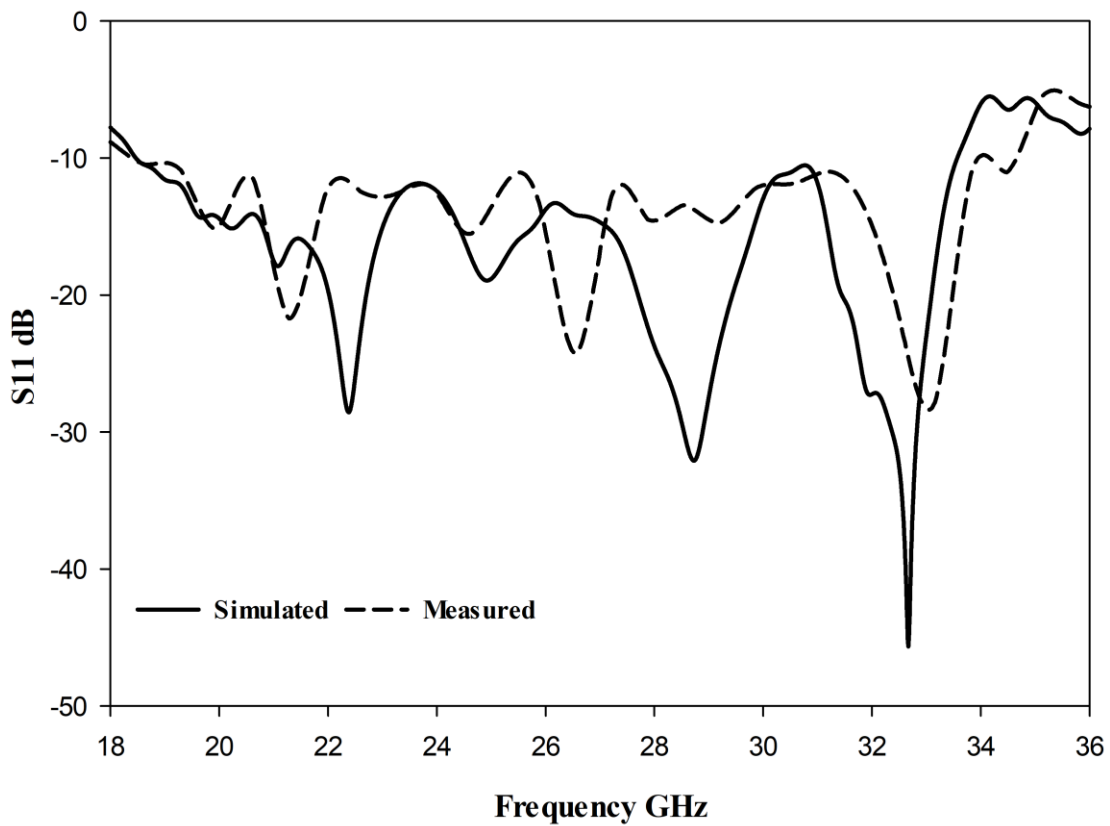


Figure 5.31: The simulated and measured reflection coefficient of an HDRA with a perforated dielectric coat.

In Figure 5.33, the simulated and measure AR are presented with respective wide bandwidths of 18% and 17.7%  $f$  covering the frequency range 24.74 to 29.66 GHz and 24.7 to 29.5 GHz, respectively. As demonstrated in Figure 5.34, a maximum gain has been achieved at 28GHz with simulated and measured values of 9.53 dBic and 8.6 dBic, respectively, when the  $TE_{511}$  resonance mode was excited, illustrating the enhanced gain due to higher order modes. In Figure 5.35, the simulated and measured H-plane and E-plane are presented with good agreement at 28GHz. It can be observed that the EL field component is higher than the ER component by 11 dB indicating that a LHCP was achieved. In the performance comparison delineated in Table 5-3, the proposed CP HDRA distinguishes itself among other similar designs. Notable features of the proposed HDRA include the ability to produce circularly

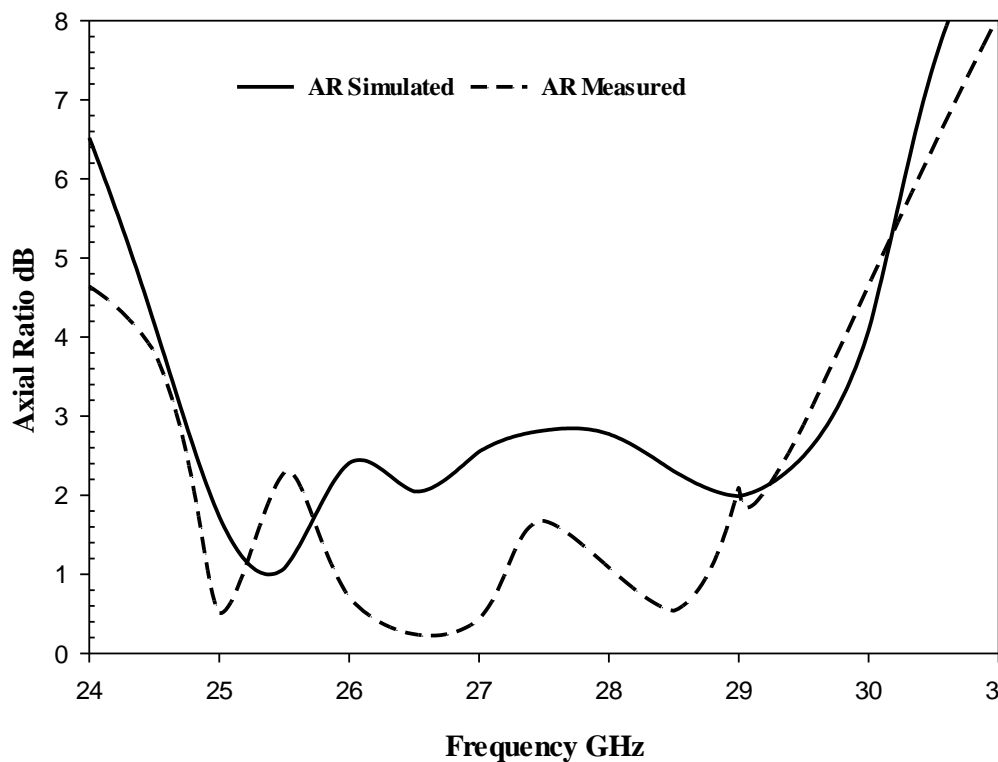


Figure 5.33: The simulated and measured CP bandwidth of an HDRA with a perforated dielectric coat

polarized radiation, with a considerably higher gain, while preserving a more streamlined architectural design.

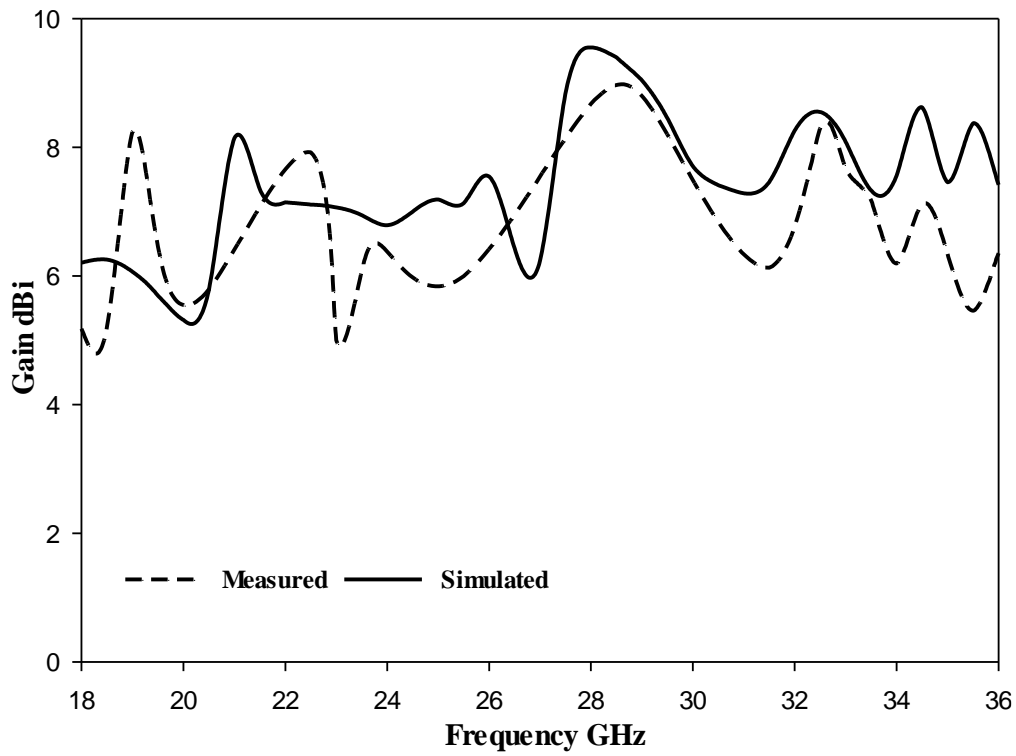
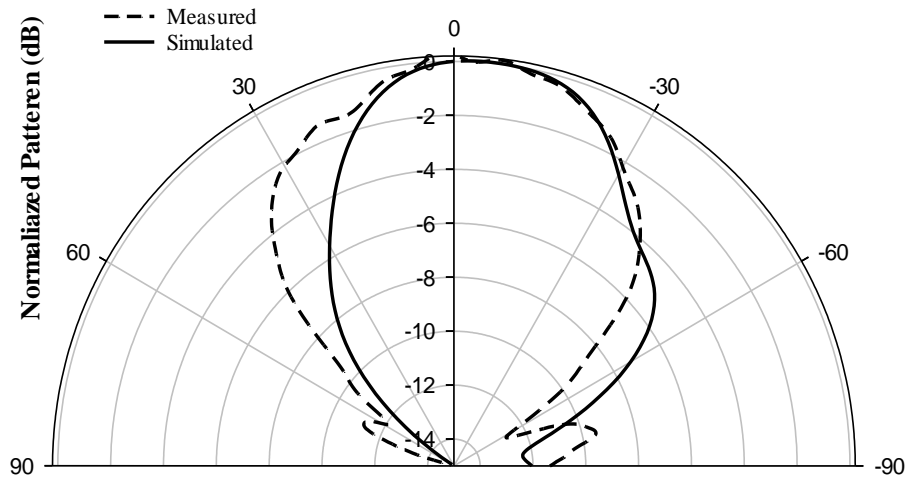
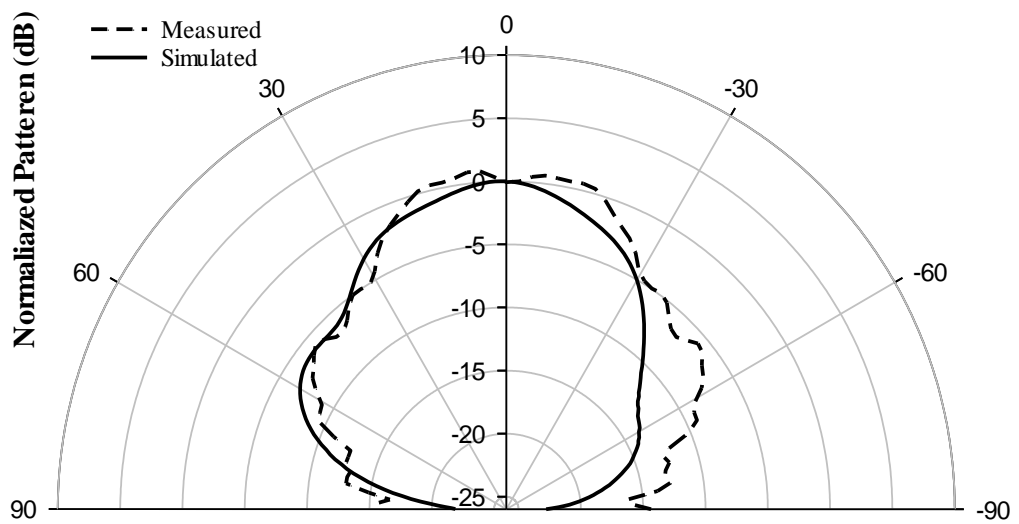


Figure 5.34: Simulated and measured gain of an HDRA with a perforated dielectric coat.



(a)



(b)

Figure 5.35: Simulated and measured radiation patterns of an HDRA with a perforated dielectric coat at 28 GHz; (a)  $\phi=0^\circ$ , (b)  $\phi=90^\circ$ .

Table 5-3: Proposed antenna performance compared to previously reported designs.

Antenna type	Feeding mechanism	$ S_{11} $ Bandwidth	Gain	AR Bandwidth	Ref
Presented work of a perforated dielectric coat HDRA	Spiral Slot	58.1% 18.4GHz to 34 GHz	9.53 dBic	17.7%	-
Presented work of two layer HDRA	Spiral Slot	57.1%	7.5	17%	-
A3D-printed multi-layered CDRA	probe	65.7% 3.56GHz-7.04GHz	2.3dB	-	[118]
A 3-D-printed multi-ring DRA	probe	60.2 % 3.4 GHz-8 GHz	2.45dBi	-	[84]
A 3D-printed rectangular DRA	probe	44.8% 5.20 GHz-8.20 GHz	6.7 dBi	-	[120]
DRA dielectric lens antenna	Slot aperture	40.2% / 19.5%	5.8dBi / 12dBi	-	[85]
Three-layer Hemispherical DRA	Cross Slot	35.8% 20.8GHz-29.9GHz	9.5dBi	-	[125]

## 5.4 Conclusions

This Chapter presented both theoretical and practical exploration of a two-layer, hemispherical DRA emitting circular polarization, which is stimulated by a spiral slot within the millimeter-wave range. The obtained results illustrate that the incorporation of a dielectric coat augments the impedance and AR bandwidths, alongside boosting the gain. This improvement is attributed to the excitation of multiple resonance modes  $TE_{311}$ ,  $TE_{112}$ ,  $TE_{511}$ , and  $TE_{312}$  at 19 GHz, 24.6 GHz, 28.6GHz, and 33.4 GHz, respectively, beyond the initial  $TE_{112}$  and  $TE_{511}$  modes at 25.1GHz and 30.81GHz, respectively. Comparatively, two-layer HDRA configurations provides increased AR and impedance bandwidths of 57.1% and 18.15%, respectively, in

combination with an enhanced gain of 7.5dBic. This needs to be compared with respective impedance and AR bandwidths 6.7% and 25.7%, 4.15%, at the absence of the outer coat layer with a gain of and 6.3dBi. Further, the successful construction and agreement between the simulated and measured results of a two-solid layer HDRA prototype were demonstrated.

It was also shown that a multilayered, wideband HDRA with a perforated dielectric coat can be fabricated through MDF 3D printing, where the two layers are combined into a single piece. This facilitates automated assembly and bonding of the layered DRA and the total elimination of potential air gaps between the dielectric layers. This structure, comprised of two concentric dielectrics, features a solid DRA at its core, while the external dielectric, characterized by varied air-filling ratios, is engineered to yield the required effective dielectric constants. The implementation of an HDRA with a perforated dielectric coat and the original solid HDRA displayed a significant correlation between the two configurations. Moreover, the 3D printed model was constructed and measured, showing a close match between simulated and measured results of impedance bandwidth, covering 59.5% and 58.05% respectively for frequencies from 18.4 to 34 GHz and 18.4 to 33.5 GHz, respectively. Simultaneously, the simulated and measured CP bandwidths of 18% and 17.7% spanned the frequency range of 24.74 to 29.66 GHz and 24.7 to 29.5 GHz, respectively. At 28GHz, the respective simulated and measured gains of 9.53 dBic and 8.6 dBic were accomplished when the modes  $TE_{311}$ ,  $TE_{112}$ ,  $TE_{511}$ , and  $TE_{312}$  were excited at 19 GHz, 24.6 GHz, 28.6GHz, and 33.4 GHz, respectively. Given these attributes, the proposed antenna is suitable for millimeter-wave applications, such as satellite communication and radar systems.

# Chapter6 60 GHz Wide-Band Axial Ratio Hemispherical DRA fed by a Coplanar Waveguide

## 6.1 Introduction

An alternate method of DRA coupling is the employment of a coplanar waveguide (CPW), which features a central strip line bordered by two slots that separate the strip from the ground plane. Direct feeding of DRAs can be achieved through open-circuit coplanar waveguides, akin to the process involving open-circuit microstrip line feeding. Enhanced control for impedance matching can be introduced by incorporating stubs or loops at the line's termination. By altering the position of the DRA over these stubs or loops, the coupling level can be adjusted [109]. The coplanar excitation brings a primary benefit, the flexibility to modify the coupling slot situated beneath the dielectric resonator, thereby optimizing the DRA's performance.

The coplanar coupling model finds extensive use in mm Wave applications, particularly when integrating the DRA in a system on chip (SoC) or on board [129]. The application of CPW transmission lines paves the way for high antenna efficiency, as the ground plane serves as a buffer between the dielectric resonator and the substrate. Unlike the case in microstrip feeding, this method prevents the undesirable formation of an air gap between the resonator and the PCB substrate[130] .

The V-band frequency, spanning a range of 40 to 75 GHz, has become a focus of interest for researchers, leading to various studies in this field. An innovative high-gain hybrid DRA and microstrip antenna were introduced at 60 GHz [14]. This configuration utilized a circular microstrip patch to power a ring-shaped DRA, grounded for effectiveness on a thin dielectric layer with a low permittivity. Exciting a higher-order mode resulted in an enhanced antenna gain. However, that study faced a few limitations. For instance, superglue connected the driving patch to the DRA, which were fabricated independently through a complicated manufacturing

process. Despite these challenges, the antenna exhibited promising results with bandwidth of 15%, gain of 11.9 dBi, and radiation efficiency of 75% [14]. In addition, a research study has unveiled an on-chip cylindrical DRA functioning at 60 GHz, fabricated using high-resistivity silicon for both the DRA and the feed circuit [131]. Power to the cylindrical DRA was supplied by a coplanar waveguide, a choice leading to a straightforward and economically efficient design. The deep reactive ion etching process was utilized to etch one side of the wafer, fashioning a cylindrical form with a radius and height of 1.18 mm and 0.4 mm, respectively. The wafer's reverse side was left unetched, serving as a substrate for the feed structure with a thickness of 0.275 mm. This design approach resulted in an impedance bandwidth of 3.78%, a gain of 7 dBi, and a radiation efficiency of 79.35% [131].

The conventional printed antennas operating at 60 GHz often exhibit significant conduction and dielectric loss, which in turn hampers the efficacy of the communication system. In this regard, a dielectric resonator is found to be a superior choice for antennas operating in the millimeter-wave band due to its characteristics such as low loss, superior radiation efficiency, comprehensive integration, and small footprint [132]. However, the literature on 60 GHz dielectric resonator antennas is relatively scarce. Investigations have been conducted on a high permittivity rectangular dielectric resonator. This was fed by a silicon-based CPW to feed the DRA, which resulted in a bandwidth of 1.897 MHz at 59.56 GHz and a gain of 3.2 dBi [132]. To augment the bandwidth, a technique of using a CPW-fed DRA situated over a patch was adopted. This method yielded a fractional bandwidth of 29.2% and a gain of 3.6 dBi at 60 GHz. In addition, high gain DRA has also been studied [23]. However, these methods have certain limitations that could restrict the bandwidth while others could elevate the fabrication costs [18].

The Chapter at hand introduces a circularly polarized hemispherical DRA, which is fed by a spiral slot, intended for applications at 60 GHz. The coplanar waveguide, as depicted in Figure

6.1, represents the ultimate coupling method to DRAs. These waveguides hold an advantage at millimeter-wave frequencies as they experience less severe conductor losses when compared to micro strips. Simulated and measured outcomes of a layered hemispherical DRA are also presented. This model is an advanced version of the hemispherical layered configuration discussed earlier, with performance enhancements due to additional optimization of the coating layer and feed network modifications to comply with the 60 GHz requirements. Consequently, the design and fabrication process become more complex compared to other DRA shapes.

Previous works have extensively researched the impedance bandwidth enhancement of the layered hemispherical DRA. Despite this, the axial ratio enhancement of hemispherical DRAs at 60 GHz remains unexplored. Attention will initially be given to the higher-order modes of a single-layer hemispherical DRA. This will be followed by the layout of a wide-band and axial ratio optimized layered hemispherical DRA. The materials for these layers have been selected based on their commercial availability, with dielectric constants  $\epsilon_{r2}=3.5$ , and  $\epsilon_{r1}=10$  for the outer and inner layers, respectively. The DRA was designed to operate within a frequency range of 40 to 65 GHz.

## **6.2 Antenna Configuration**

As previously mentioned, enhancements can be applied to the solid layer HDRA design, which was explored in the last Chapter. This can be achieved by operating at the 60 GHz band and modifying the feeding network. In this stage of the project, the DRA is energized by a coplanar waveguide situated on the wafer's top side of the ground plan.

This adjustment is necessary to meet the requirements of the V-band millimetre-wave frequency, which is interrupted by two Archimedean spiral slots centrally located below the DR. Figure 6.1 presents the structure of the proposed multi-layered HDRA, energized by the

CPW. Further to investigate the influence of the coating layer on HDRA's functionality, simulations using CST Microwave Studio (MWS) were executed to evaluate impedance and axial ratio bandwidths as well as gain. As outlined in the previous Chapter, the inner layer of the DRA comprises the hemispherical Alumina DRA with a dielectric constant of  $\epsilon_{r1}=10$  and radius that was set at  $R_d = 1.85$  mm.

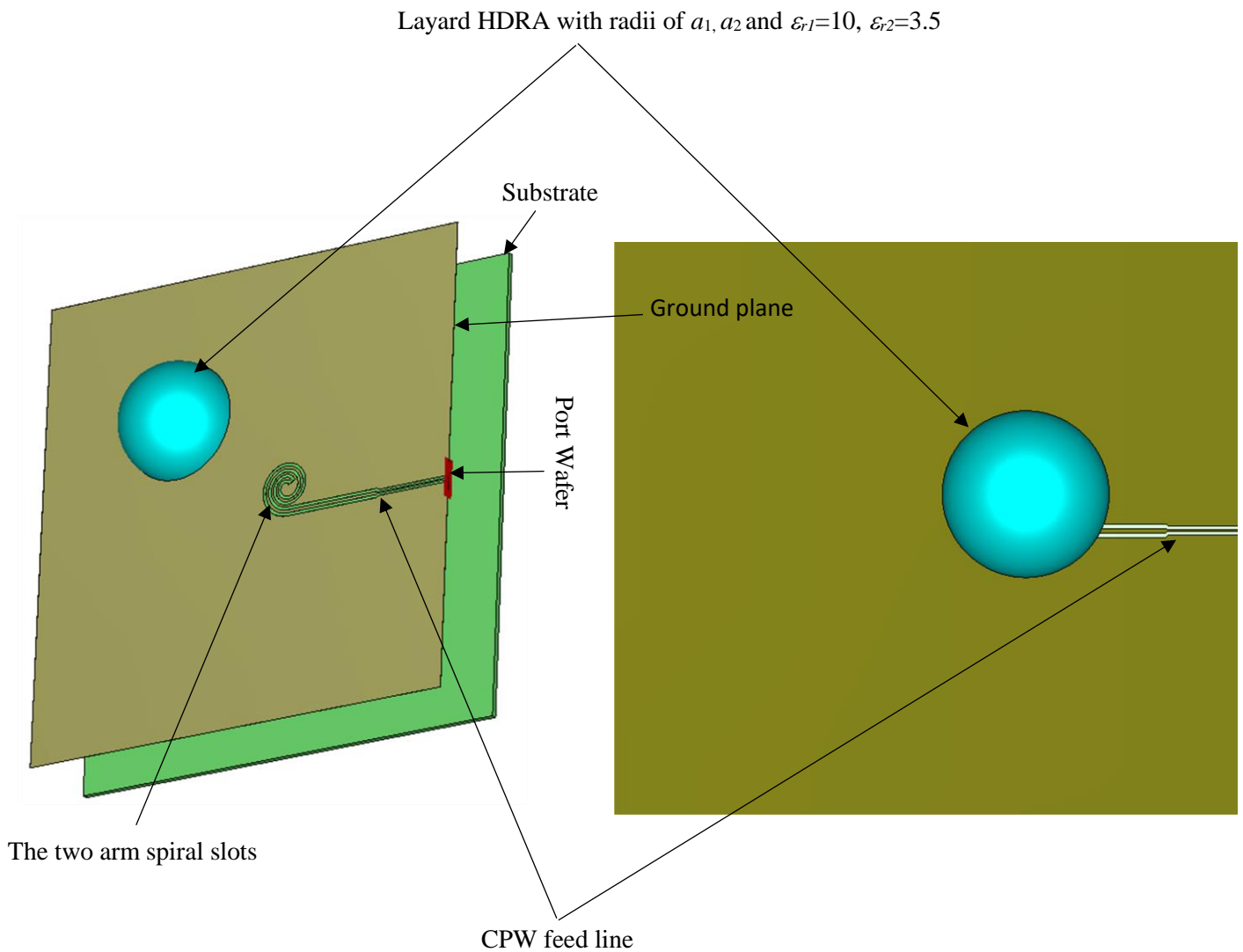


Figure 6.1: The configuration of the CPW-fed hemispherical DRA.

Figure 6.2 illustrates the configuration of the proposed CPW-fed two spiral slots. These slots, along with the feeding structure, were etched on the ground plane that was located on the top of the substrate. One significant detail to note is the gap between the turns of the slots. This gap is deliberately maintained to be no less than 0.1 mm in order to meet the fabrication requirements. A gap of this size simplifies the circuit fabrication and the alignment of the position, thereby making the manufacturing process more efficient. A noteworthy advantage of the spiral slot is its ease of realization with the port impedance closely approximating  $50 \Omega$ [133]. This feature sets it apart from other structures such as printed, wire, or microstrip structures which may not offer the same convenience.

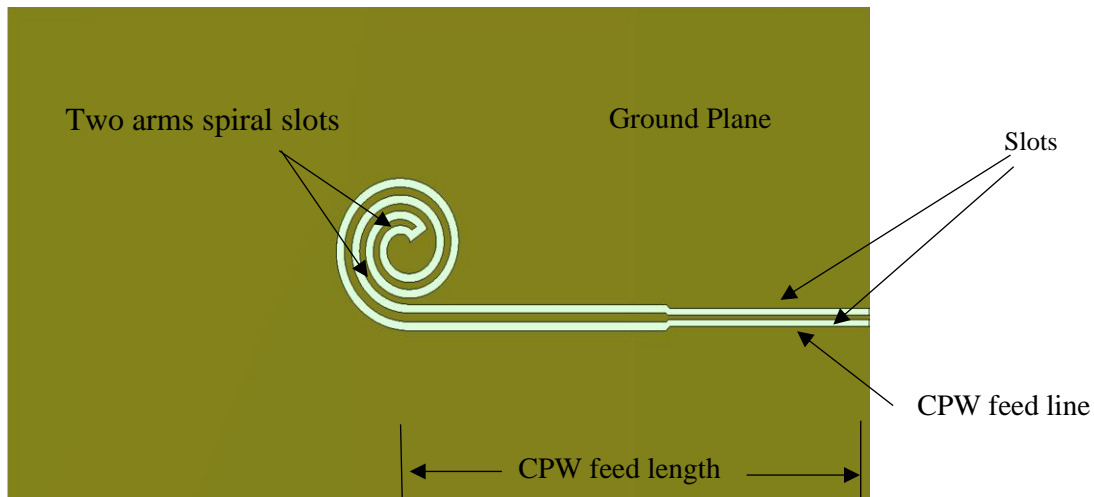


Figure 6.2: Geometry of a two-arm spiral slots fed by CPW.

Figure 6.2 illustrates the two feeding spirals with their dimensions dictated by the renowned Archimedean spiral function:

$$\rho_1 = a_1 \varphi \quad (6.1)$$

$$\rho_2 = a_2 \varphi \quad (6.2)$$

In this equation,  $\rho_1$  and  $\rho_2$  symbolize the radius of each spiral-slot arm. The constants  $a_1$  and  $a_2$  denote the respective spiral constants for arm1 and arm2.  $\varphi$  is the shared winding angle for both arms. The selected parameters include  $a_1=0.009$  mm/rad and  $a_2=0.037$ mm/rad for the range of  $0.194\pi \leq \varphi \leq 3.22\pi$ . The width of each spiral-slot arm ( $w_{s1}$  and  $w_{s2}$ ) is determined to be 0.1 mm [96]. It's worth noting that the two spiral slots are interconnected at the centre via a strip slot with a width of 0.1mm.

Each of the spiral slots was extended by a half turn, i.e.  $N=1.5$ , to create the coplanar waveguide feed line. The design of both the Archimedean spiral slots and the CPW feed line is such that they are compatible with the characteristic impedance of 50 ohms, a common specification in numerous standards as outlined in Table 6.1.

Table 6-1: Parameters for the proposer design of the CPW slot feed

<b>Elements of the Structure</b>	<b>Particular Parameters</b>	<b>Value</b>
Probe landing pads	(G-S-G) Width	50 $\mu$ m -50 $\mu$ m -50 $\mu$ m
Probe landing pads	(G-S-G) Length	1.5mm
CPW feed line	Width	0.1mm
CPW feed line	Length	3.2mm
Spiral Slots	Width	0.1mm
Slots	Length	2.5mm

There's a significant change in the dimensions of the CPW feed as it approaches the edge of the ground plane, also referred to as the probe landing pads. Specifically, the width reduces from 0.1 mm to 0.05 mm and it assumes a length of 1.5 mm. This adjustment is necessary to meet the requirements of the probe wafer equipment. Further, the probe tip is arranged in a Ground-Signal-Ground (G-S-G) configuration. The pitch between the centres of each probe tip is 150  $\mu$ m (50  $\mu$ m -50  $\mu$ m -50  $\mu$ m), offering a versatile design feature.

The simulation results of a single-layer DRA, fed using a CPW with the two spiral slots previously described, are presented in Figures 6.3 and 6.4. From Figure 6.4, it can be noted that the antenna demonstrates a dual-band performance with bandwidths of 27.7% and 6.08% that correspond to frequency ranges of 41.6 GHz-55 GHz and 59 GHz-62.7 GHz, respectively. Interestingly, the single-layered DRA is capable of supporting resonance modes of  $TE_{311}$ ,  $TE_{112}$  and  $TE_{511}$ , occurring at 45 GHz, 51.3 GHz and 61 GHz respectively. Notably, these resonant frequencies are in accordance with the results obtained from the MATLAB code.

The simulated AR bandwidth was found to be 3% over the frequency range of 58.7-60.5 GHz, indicating a satisfactory AR bandwidth. This can be considered as reasonable for this single-layered DRA design. Figure 6.5 presents the radiation patterns of the  $TE_{112}$  mode and  $TE_{511}$ . The antenna achieves a maximum gain of 5.25 dBi and 7.2dBic in these modes respectively, an outcome that can be attributed to the increased number of short magnetic dipoles in the higher-order mode. This significant gain further underlines the efficiency and performance of the DRA design.

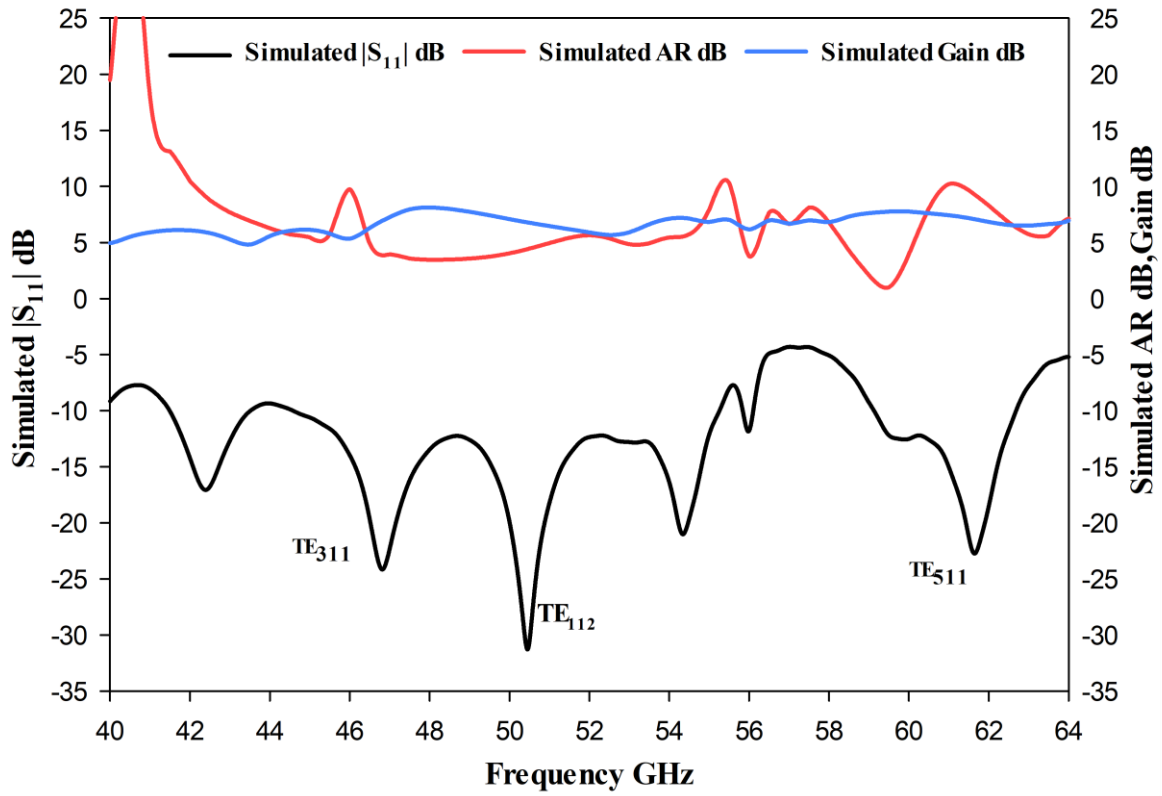


Figure 6.3: Simulated  $|S_{11}|$ , axial ratio and gain of the single layered HDRA.

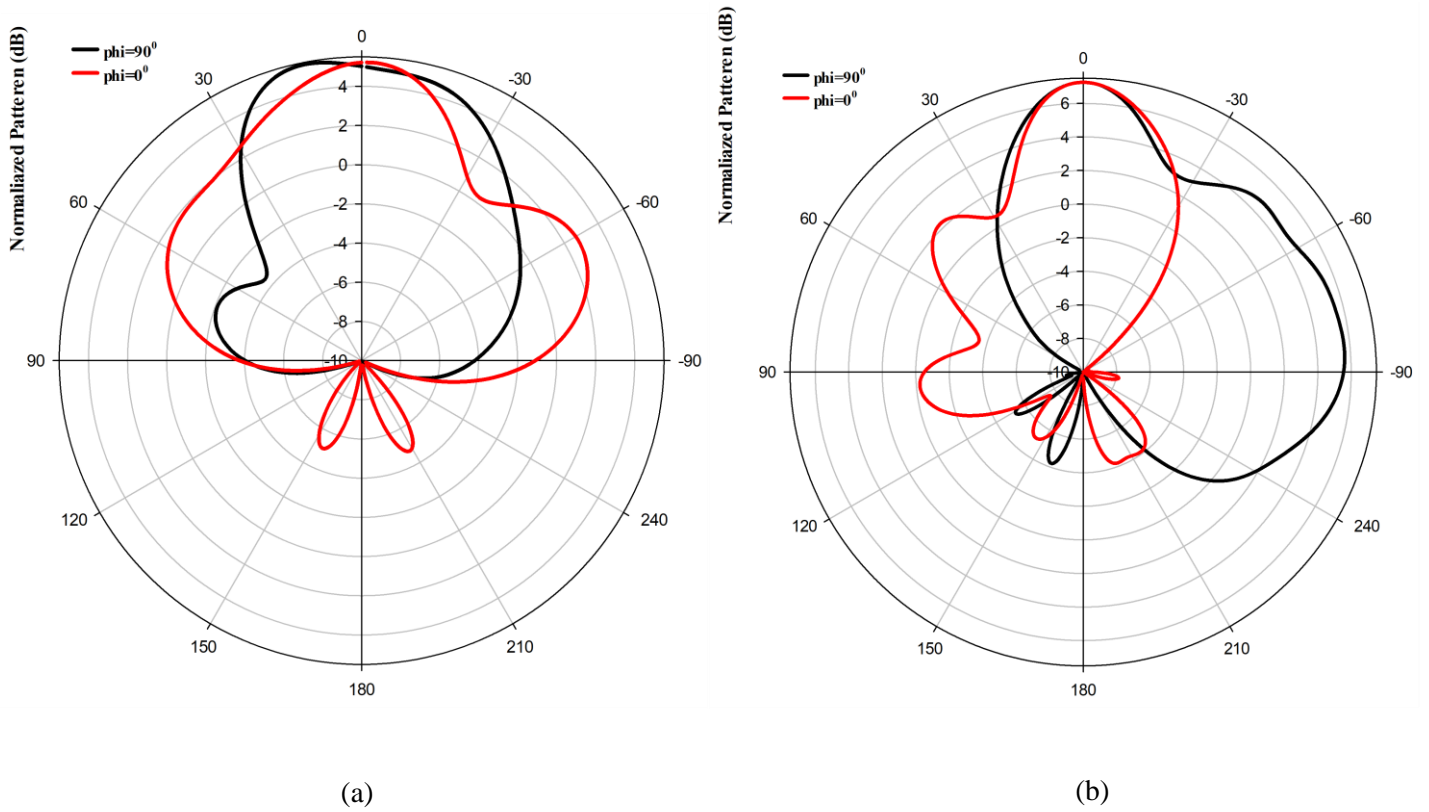


Figure 6.4: a) Radiation pattern of  $TE_{112}$  at 45 GHz, b) Radiation pattern of  $TE_{511}$  at 61 GHz for a single layer HDRA

The proposed hemispherical DRA was designed to increase the impedance and AR bandwidths. This is achieved through a coat in the form of a lower permittivity dielectric layer. The inner layer features a radius of  $a_1=1.85\text{mm}$  and a relative permittivity of  $\epsilon_{r1}=10$ . The outer Polyimide layer has a radius of  $a_2=2.85\text{mm}$  and a dielectric constant of  $\epsilon_{r2}=3.5$ . The selection of the permittivities for the proposed DR was based on their availability.

For maximum coupling between the antenna and its feed network, CST MWS was used to optimize the dimensions of the CPW feed line and spiral slots as shown in Table 6.1. Additionally, the thickness of the coating  $\delta a$  was also optimized to understand its impact. The radius of the initial configuration's first layer was set at 1.85 mm, with a relative permittivity of 10. The outer layer thickness  $\delta a=a_2-a_1$  was then incrementally increased from 0.25 mm to 1.25 mm.

Table 6.2 and Figure 6.5 present a comparison of the effects of different outer layer thicknesses. The broadest impedance bandwidth was observed with an outer layer thickness of 1 mm, while a thickness of 0.25 mm resulted in the narrowest bandwidth. Figure 6.6 indicates that the widest AR bandwidth occurs when an outer layer thickness of 1 mm is used, whereas an outer layer thickness of 1.25 mm results in the narrowest AR bandwidth.

Table 6-2: The impact of different outer layer thicknesses  $\delta a$ .

$a_1$ mm	$a_2$ mm	$\delta a$ mm	$S_{11}$ Bandwidth %	AR Bandwidth %	Gain dBi
1.85	1.85	0 (no coating)	27.7 and 6.08	3.02	5.25 dBi and 7.2
1.85	2.1	0.25	5.3, 10.5 and 3.8	3.07	7.5
1.85	2.35	0.5	29.5 and 14.2	7.4	7.9
1.85	2.6	0.75	30.5 and 16.5	4.8 and 8.8	5.5 and 7.5
<b>1.85</b>	<b>2.85</b>	<b>1</b>	<b>52.3</b>	<b>10.18</b>	<b>7.6</b>
1.85	3.1	1.25	18.5, 15 and 10.5	0	7.1 dBi

The observations drawn from Figure 6.7 indicate a notable gain enhancement. This enhancement is attributable to two primary factors: the improved energy confinement within the dielectric resonator layer and the augmentation of magnetic dipoles within the HDRA. When compared to the single-layer configuration, these changes are clearly visible. However, it's important to note that this increased gain comes with trade-offs, specifically affecting the  $S_{11}$ , axial ratio, and further gain considerations. To balance these variables, an optimal thickness of 1 mm was determined for the coating. This choice offers the best compromise between maximizing gain and managing trade-offs in other performance metrics.

Based on Figures 6.5, 6.6, and 6.7, a thickness of 1mm for the dielectric coat significantly enhances impedance and axial ratio bandwidths due to the excitation of the higher order resonance modes  $TE_{311}$ ,  $TE_{112}$  and  $TE_{511}$  at 40.29 GHz, 51.17 GHz and 61.16GHz respectively, with a bandwidth of 52.3% spanning from 38.5 to 65.8 GHz as shown in Table 6.2. This outcome can be attributed to the travelling wave currents distribution along the spiral slot. As a result, an optimum radius of 2.85 mm has been adopted for the outer layer. Moreover, Figure 6.8 shows the variation of the  $S_{11}$  bandwidth as a function of the coating thickness, with the maximum  $S_{11}$  bandwidth reached using the same outer layer thickness of 1 mm that led to the widest CP bandwidth.

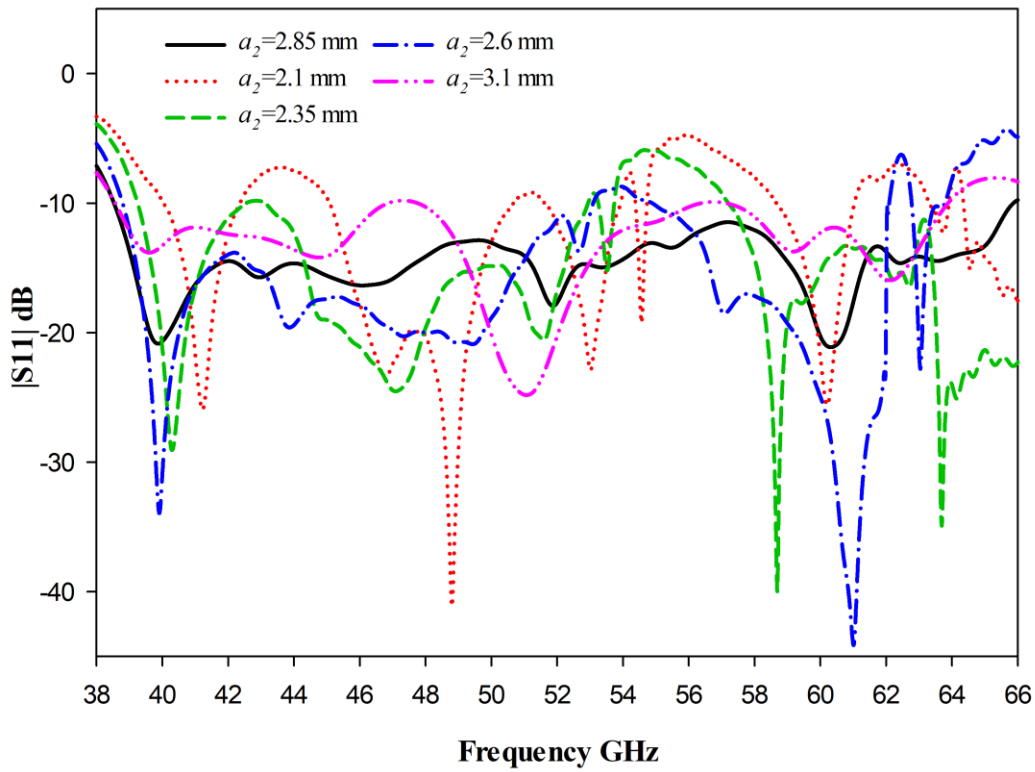


Figure 6.6: Simulated  $|S_{11}|$  with various radii of the outer layer.

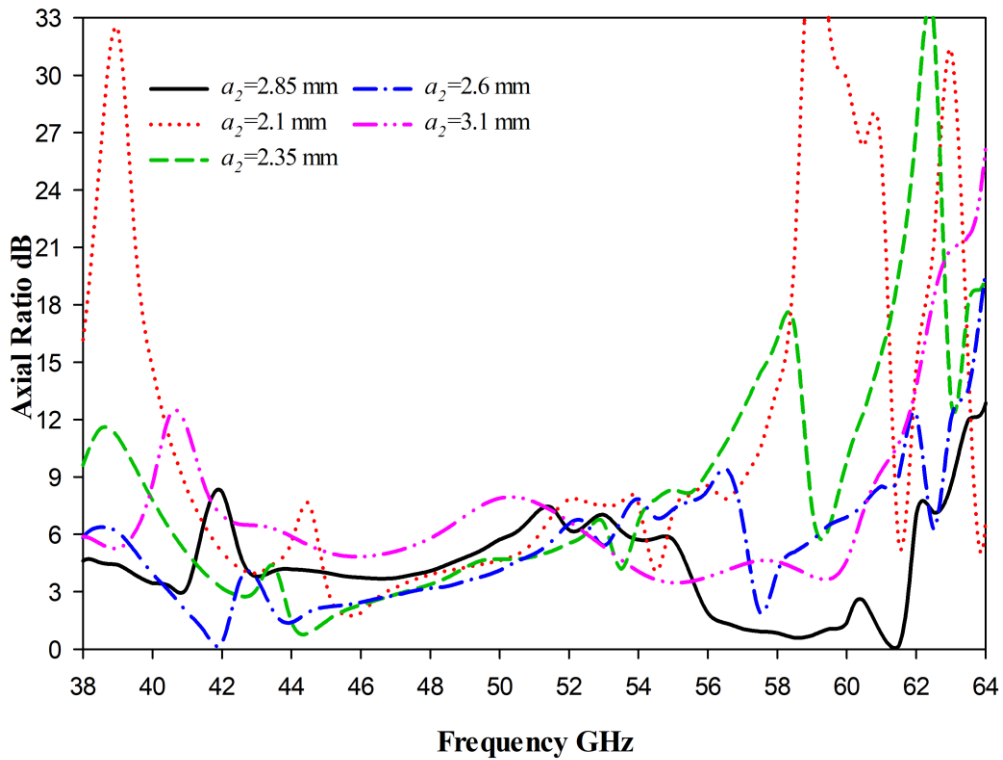


Figure 6.5: Simulated axial ratio with various radii of the outer layer.

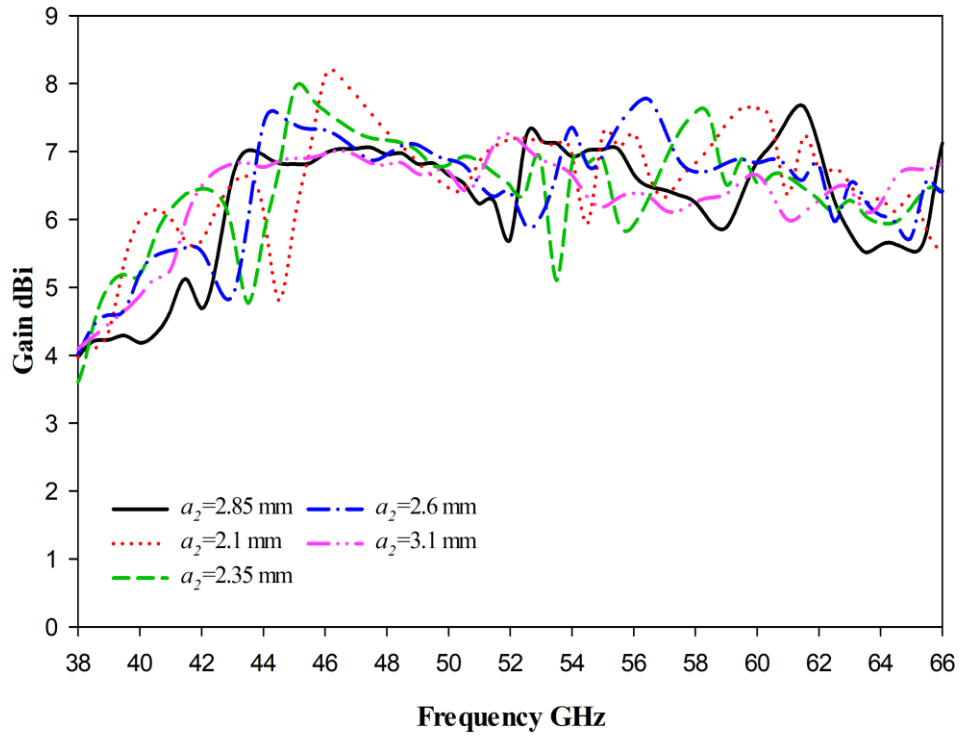


Figure 6.8: Simulated gain with various radii of the outer layer.

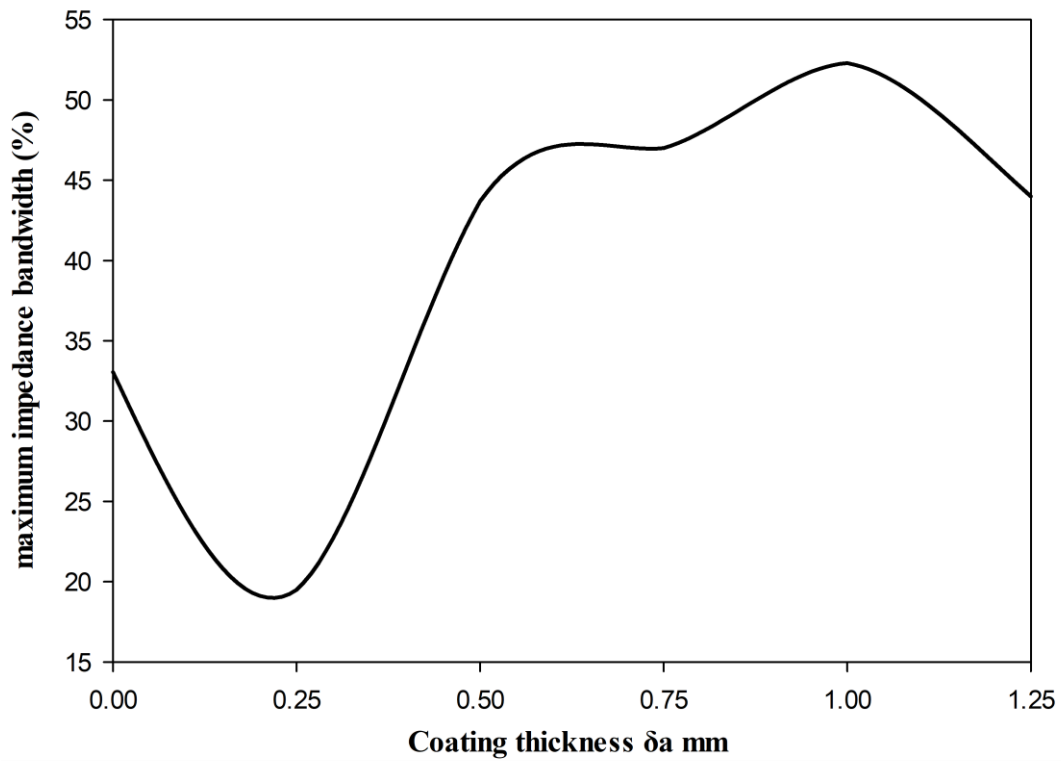


Figure 6.7: Maximum bandwidth as function of the outer layer thickness

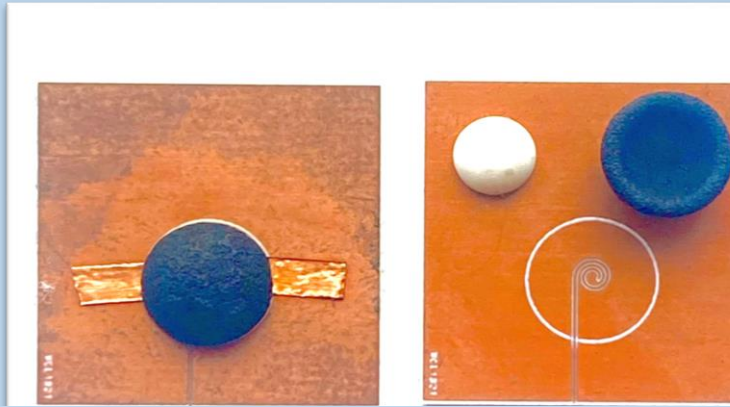
### **6.2.1 Experimental study of the layered 60 GHz HDRA**

To validate the simulations, a prototype of the actual DRA was successfully fabricated by T-CERAM company leveraging Alumina as the core material. This component was realized with a fabrication tolerance of 0.06mm, a relative permittivity of 10, and a considerably low loss tangent ( $\tan \delta$ ) of less than 0.002. In conjunction with this, we utilized 3D printing technology to build the outer layer. This procedure employed Polyimide as the prime material, due to its suitable dielectric constant of 3.5 and a reasonably low loss tangent of 0.0027.

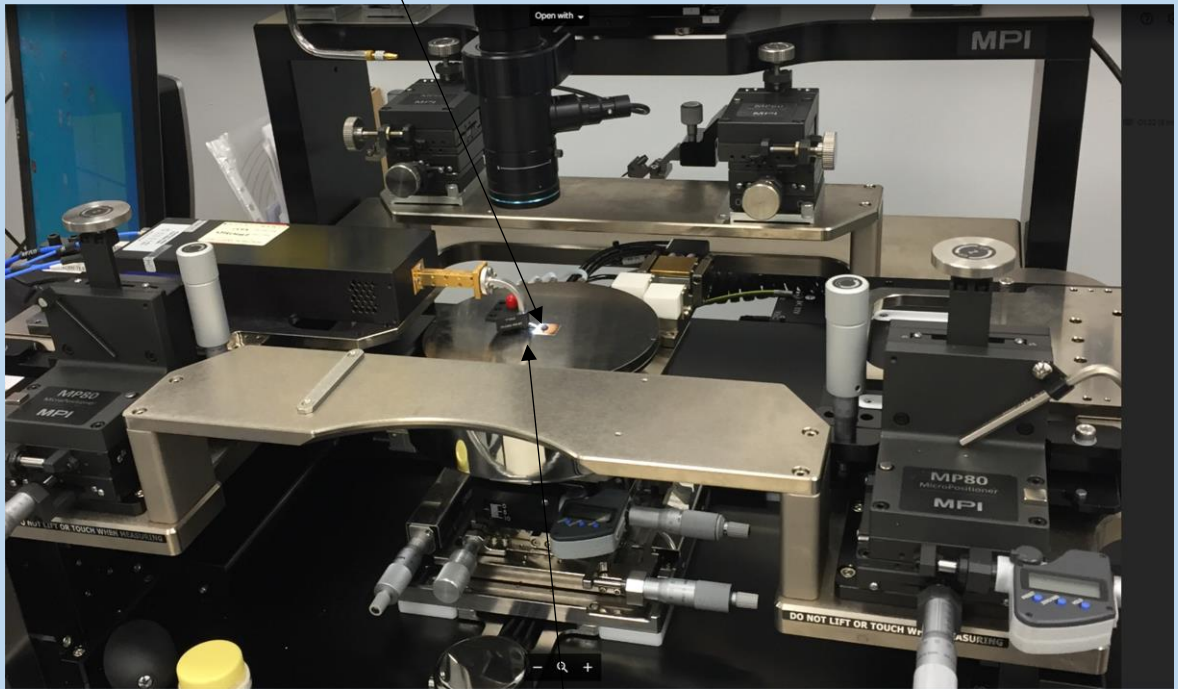
Following this, the antenna was carefully positioned on a copper ground plane, which was itself mounted atop a Rogers (Ro4350B) dielectric substrate. The substrate, provided by Wrekin Circuits, featured a thickness of 0.17mm, a relative permittivity of 3.48, and a loss tangent of 0.0037. During the fabrication, we paid special attention to the alignment process. The position of the coated DRA on the copper ground plane of the developed feed network was outlined using a 3D printer. The entire prototype was energized using a CPW, which was meticulously etched onto the surface of the ground plane. Following this, the antenna was secured to the ground plane using a double-sided adhesive copper tape with a thickness of 0.08 mm. This tape was strategically placed beneath the outer dielectric coat, away from the CPW feeding line, thereby ensuring optimal performance of the antenna.

The challenges associated with the measurement of higher frequency technologies, particularly within the millimetre-wave frequency range, stem from the compact size of these devices. To accurately gauge the measurement requirements, specific features are necessitated by the equipment, given that the manipulation of such slender dimensions can prove to be particularly intricate. To conduct tests within the 60GHz band, we utilized our 100-micron pitch GSG WR15 probes. These probes are interfaced with the Agilent Technologies E5071C mm Wave vector network analyser using premium-quality coaxial cables, as depicted in Figure 6.9.

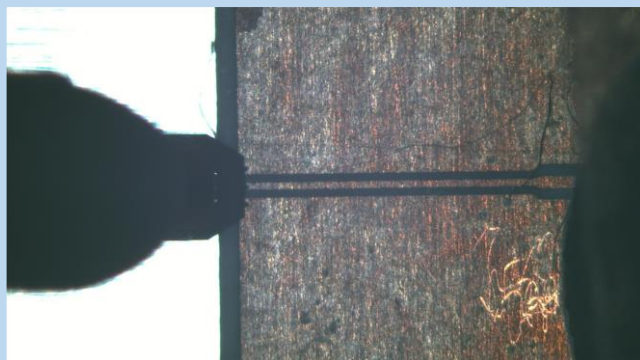
A comparison between the simulated and measured return losses is shown in Figure 6.10. The simulation achieved an impedance bandwidth of 52.3%, spanning a frequency range of 38.5GHz to 65.8 GHz. This partly aligns favourably with the measured bandwidth. Moreover, a multimode operation was manifested, where resonance modes  $TE_{311}$ ,  $TE_{112}$  and  $TE_{511}$  were excited at frequencies of 40.29 GHz, 51.17 GHz and 61.16GHz respectively. It should be noted that this novel facility installed at the University of Sheffield is still not entirely operational, as it currently lacks certain tools that are crucial for high-frequency measurements. These tools are primarily required for CPW facilities, in addition to assessing the probe wafer's lifespan. The discrepancy between the simulated and measured results can be described as a result of issues with securing a stable connection. One possible cause of this could be the absence of a smoothing coating on the board. Typically, a layer of titanium is applied over the copper to create a smooth and even surface for the probe to connect to. Furthermore, the impact of the adhesive double-sided tape between the coating and the ground plane should also be considered, as it is incorporated in the simulation results.



(a)



(b)



(c)

Figure 6.9: (a) The prototype of a HDRA with feed network with outlined DRA position, (b) The DRA model placed inside the probe Station. (c) A screen grab of the pitch GSG probe connected to the CPW transmission line

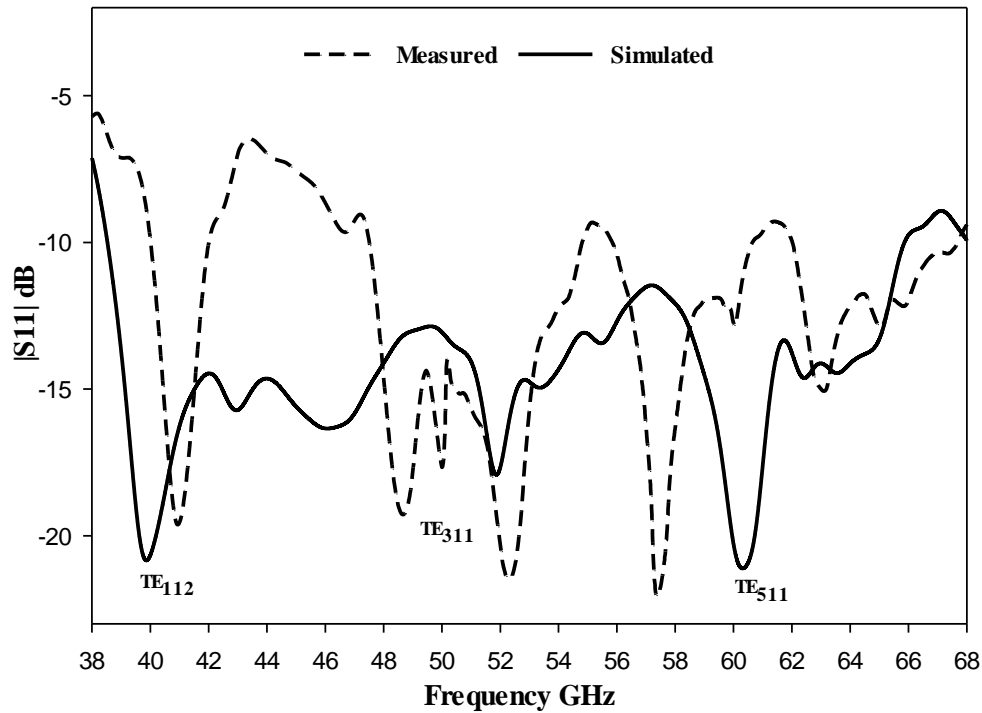
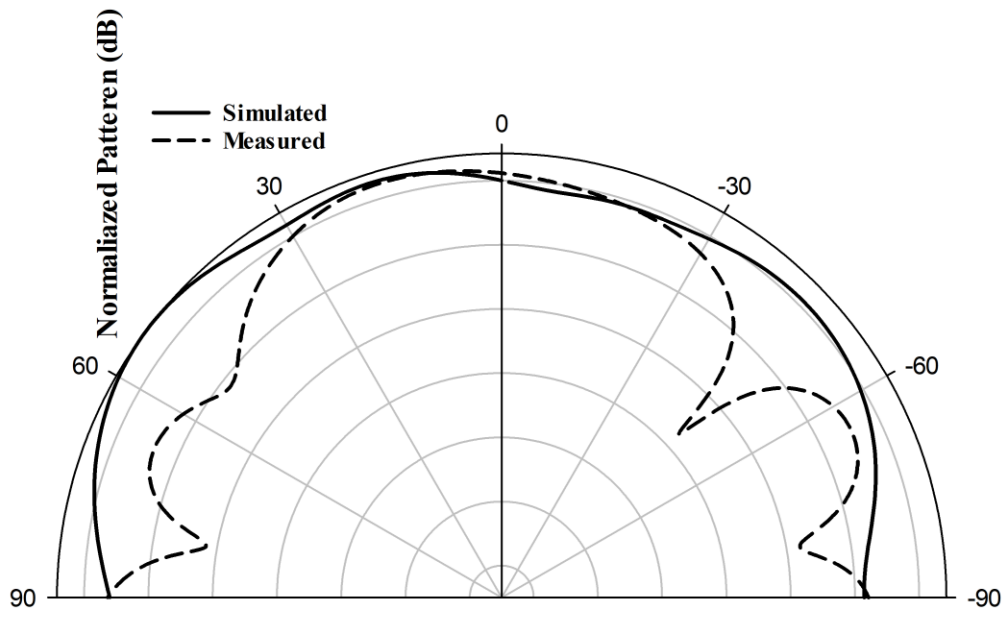


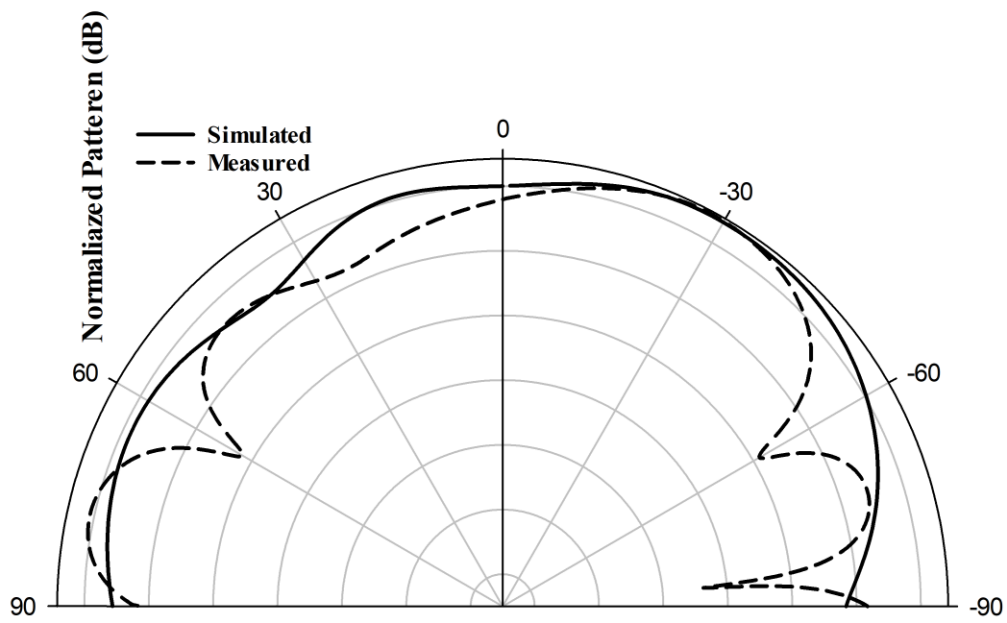
Figure 6.10: The simulated and measured reflection coefficient of HDRA with dielectric coat

The challenge lies in facilitating measurements using the spherical range, as it lacks the same level of stability as the probe station, making it difficult to manage. In addition, the probe holder for the spherical system is causing numerous false reflections within the results. As a result, the radiation patterns of the prototype could only be measured at 61 GHz. Figure 6.11 showcases the radiation patterns of the proposed circularly polarized antenna, where the  $TE_{511}$  mode is stimulated at 61 GHz. The patterns display a left-hand circular polarization (LHCP) in the far field, as evidenced by the electric field component  $E_L$  being  $\sim 10.5$  dB larger than  $E_R$ .

Table 6-3 offers a comparative analysis of the performance between the proposed HDRA and other designs at 60 GHz. It indicates that the proposed HDRA, apart from producing circularly polarized (CP) radiation, also exhibits a notably higher gain. This is achieved in conjunction with a significantly simpler design structure.



(a)



(b)

Figure 6.11: Simulated and measured of the radiation patterns of a layered HDRA at 61 GHz, (a)  $\phi=90^\circ$ , (b)  $\phi=0^\circ$ .

Table 6-3: Proposed antenna performance compared to previously reported designs.

Antenna type	Feeding mechanism	Bandwidth	Gain dBi	Axial ratio	Mode	Ref
Present work of two layer HDRA	Spiral Slot feed by CPW	52.3% 38.5GHz - 65.8 GHz	7.6 dBi	10.18% 55.7 GHz- 61.7GHz	TE <sub>511</sub>	-
CDRA	HMSIW	24.2%	5.5 dB	4 %	HEM <sub>11δ</sub>	[24]
RDRA	CPW	54 GHz -71.5	3.6 dBi	-	-	[23]
CDRA	CPW fed slot	6.4 GHz	5.4 dB	-	-	[26]
CDRA	Slot aperture	7.9 GHz	5.4 dB	-	-	[27]
Three square stacked shapes	Slot aperture	20% 57GHz-65GHz	18.6	-	-	[40]
CDRA array 2×2	Slot aperture	11.8%	11.43 dB	15.9	HEM <sub>11δ</sub>	[134]
RDRA array 1-to4 series type	ring-shape power divider network	21.6% 51.6 GHz-64.1GHz	9 dB	9.6% 57.2 GHz- 63GHz	TE <sub>111</sub>	[135]

### 6.3 Conclusion

To summarize the findings presented in this chapter, we have successfully developed a hemispherical Dielectric Resonator Antenna that is circularly polarized and fed by a spiral slot. This antenna was specially crafted to accommodate millimeter-wave applications operating at 60 GHz. The excitation of the HDRA was achieved through a coplanar waveguide feed from the spiral slot's external edge. The data obtained distinctly illustrate that the application of a dielectric coating significantly improves both the impedance and AR bandwidths while concurrently increasing the gain. This enhancement is credited to the activation of additional resonance modes TE<sub>311</sub>, TE<sub>112</sub>, and TE<sub>511</sub>, at frequencies of 40.29 GHz, 51.17 GHz, and 61.16GHz respectively. These additional modes extend beyond the initial TE<sub>112</sub> and TE<sub>511</sub> modes observed at 45.1GHz and 61GHz.

When contrasted with a single-layer configuration, two-layer HDRA designs yield broader bandwidths of 52.3% and 10.18% for impedance and axial ratios, respectively, as well as a superior gain of 7.6dBic. These results present a stark contrast to those obtained from configurations without an outer layer, which recorded 27.7%, 6.08%, 3.02%, and 5.25dBi and 7.2dBic respectively. These experimental outcomes effectively substantiate the conclusions drawn from our simulations.

However, it's crucial to note the discrepancies identified between the simulated and measured results, which can be attributed to challenges in establishing a stable connection due to the current absence of certain essential high-frequency measurement tools in our lab. Unfortunately, these connection issues with the GSG probe prevented the comprehensive measurement of the radiation pattern across all bands for the proposed HDRA within this project. Future work should aim to address these limitations and further validate our findings.

## **Chapter7 Conclusion and future work**

### **7.1 Conclusion**

This dissertation comprises six comprehensive chapters, each serving a unique purpose towards the main objectives of the study, which seeks to optimize the gain and impedance bandwidth of dielectric resonator antennas.

Chapter 1 establishes the groundwork, outlining the topic, presenting the current state of the art, and identifying gaps in the existing literature. The objective is to highlight the originality and contributions of this thesis within the larger scope of DRA studies.

Chapter 2 progresses to the theoretical and experimental analysis of a circularly polarized two-layer cylindrical DRA. It demonstrated that the application of a dielectric coat improved impedance and AR bandwidths by 45% and 18%, respectively, and the gain by 12.5 dBic, thus indicating the potential of the proposed antenna for X-band applications such as satellite communication and radars.

Chapter 3 investigates the mmWave layered cylindrical DRA, focusing on its circular polarization. The proposed design yielded 88% impedance bandwidth and 23.2% axial Ratio bandwidth, with a 12.29 dBic gain. The strong correlation between the simulation and the experimental results validate the proposed configuration's efficacy for 5G applications requiring high gain and wide bandwidth antennas.

Chapter 4 explores the feasibility of employing a 3D printer for the amalgamation of two layers using ceramic, albeit the portion that corresponds to the coat layer was perforated to achieve the required permittivity. This results in a reduced overall effective dielectric constant into a singular entity. This approach significantly streamlined the assembly process and eradicated the possibility of air gaps between the dielectric layers. Alongside this, the chapter unveils both theoretical and empirical results related to circularly polarized perforated cylindrical DRAs,

where the attained measured impedance bandwidth stood at 53.3% .This achievement underscores the antenna's aptness for 5G applications, specifically those requiring antennas with expansive bandwidth and high gain.

In Chapter 5, a detailed investigation into a two-layer hemispherical DRA is undertaken. The results show, once more, that the use of a dielectric coat significantly improved the impedance and AR bandwidths, alongside boosting the gain. In addition, a 3D printed model of a wideband HDRA was constructed and measured, displaying a close correlation between simulated and measured results of impedance bandwidth covering 59.5% and 58.05%, respectively, over a frequency range of 18.4 to 34 GHz.

Chapter 6 encapsulates the successful development of a hemispherical DRA designed for millimeter-wave applications operating at 60 GHz. When compared to a single-layer configuration, the two-layer HDRA designs displayed broader impedance bandwidth of 52.3% and 10.18% for axial ratio in combination of a higher gain of 7.6dBic. Despite some discrepancies between the simulated and measured results, mainly due to technical limitations, the chapter provided valuable insights for future research.

In summary, the thesis serves to enhance our understanding of DRA performance improvements. The introduction of innovative designs and applications for DRAs makes a significant contribution to the field of antenna technology and paves the way for future research in this domain.

## 7.2 Future work

This section delineates potential avenues for prospective research, predicated on the findings and conclusions derived from this thesis. The study's investigative trajectory has highlighted the inherent potential that layered DRAs configurations possess in offering an efficacious blend of high gain and extensive bandwidth, in addition to providing augmented structural support. The investigations encapsulated within this thesis underscore the remarkable potential of utilizing layered DRAs. Their employment presents a compelling solution to the formidable challenge of synthesizing a high gain with a wide bandwidth, thereby boosting antenna performance and opening up new opportunities for tailored design and optimization of DRAs. Moreover, our findings underscore an additional advantage of layered DRAs. They have demonstrated an enhancement in physical robustness, particularly beneficial in mitigating the brittleness associated with the elongated and slender ceramic DRA layer that characterizes the inner structure of the antenna. Considering these outcomes, future research could benefit from a more in-depth exploration of the layering techniques, material selection, and the optimization of design parameters, all with a focus on augmenting both the performance and the structural durability of DRAs. Such endeavours would not only extend our understanding of layered DRAs but could also instigate their wider application across diverse scenarios.

There was a notable disparity between the simulated and measured results in Chapter 6, primarily due to the absence of essential high-frequency measurement tools. Future research should aim to improve the precision of these measurements using more advanced equipment, which would help validate the theoretical predictions and enhance the reliability of the findings, which the University of Sheffield worked to complete the facility of the mm Wave lab facilities. A noteworthy divergence was observed between the simulated and measured results presented in Chapter 6, primarily attributable to the lack of requisite high-frequency measurement

instruments. Moving forward, future research should focus on enhancing the accuracy of these measurements by employing more sophisticated equipment. This would serve to corroborate the theoretical predictions, thereby bolstering the trustworthiness of the findings. Moreover, advancements in measurement tools could elucidate certain phenomena that remained elusive in the current study due to technical limitations. As the University of Sheffield is currently working towards augmenting the facilities within its millimetre-wave lab, there is potential for this research gap to be addressed in the near future. Enhanced lab capabilities will allow for more detailed exploration and validation of high-frequency DRA characteristics, further strengthening the body of knowledge in this field.

Furthermore, one significant development presented in this thesis is the merging of two layers into a single layer structure, leading to an automated assembly and the removal of potential air gaps between layers. These features can be exploited at high frequencies such as 60 GHz, where wider bandwidths and higher gains are key requirements in order to achieve a high data rate for mm-wave communications. However, at such high frequencies, any air gaps between the layers can impact the performance significantly. Therefore, novel manufacturing techniques need to be considered such as the 3D printing of the Alumina DRA layer as well as the coat layer in a single process in order to ensure the elimination of any potential air gaps that may exist between the two layers. These advancements prove especially beneficial at higher frequencies, such as 60 GHz, where expansive bandwidths and elevated gains are pivotal for realizing high data rates in millimetre-wave communications.

Nevertheless, at these elevated frequencies, any extant air gaps between layers can profoundly impact the antenna's performance. This process can be optimized further, possibly utilizing advanced manufacturing techniques or exploring other materials with different dielectric

properties. Engaging with such innovative manufacturing techniques will not only enhance the performance of the antenna but could also initiate a paradigm shift in the way we conceive and construct high-frequency antenna systems. The ensuing improvements in data transmission could bring us one step closer to realizing the full potential of millimetre-wave communications. Future research should, therefore, concentrate on refining these techniques and further exploring their practical applications.

## References

- [1] R. Richtmyer, "Dielectric resonators," *Journal of Applied Physics*, vol. 10, no. 6, pp. 391-398, 1939.
- [2] S. Long, M. McAllister, and L. Shen, "The resonant cylindrical dielectric cavity antenna," *IEEE Transactions on Antennas and Propagation*, vol. 31, no. 3, pp. 406-412, 1983.
- [3] K. W. Leung and S. A. Long, "Overview of the Dielectric Resonator Antenna," *Dielectric Resonator Antennas*, p. 1, 2003.
- [4] M. McAllister and S. A. Long, "Resonant hemispherical dielectric antenna," *Electronics Letters*, vol. 20, no. 16, pp. 657-659, 1984.
- [5] K. Luk and K. Leung, "Dielectric resonator antennas research studies press limited," *Hertfordshire, England, UK*, 2002.
- [6] L. K. Hady, D. Kajfez, and A. A. Kishk, "Triple mode use of a single dielectric resonator," *IEEE Transactions on Antennas and Propagation*, vol. 57, no. 5, pp. 1328-1335, 2009.
- [7] A. Petosa and A. Ittipiboon, "Dielectric resonator antennas: A historical review and the current state of the art," *IEEE Antennas and Propagation Magazine*, vol. 52, no. 5, pp. 91-116, 2010.
- [8] S. K. K. Dash, T. Khan, and A. De, "Dielectric resonator antennas: An application oriented survey," *International Journal of RF and Microwave Computer-Aided Engineering*, vol. 27, no. 3, p. e21069, 2017.
- [9] J. C. Wiltse, "History of millimeter and submillimeter waves," *IEEE Transactions on microwave theory and techniques*, vol. 32, no. 9, pp. 1118-1127, 1984.
- [10] Y. T. Lo and S. Lee, *Antenna Handbook: Volume III Applications*. Springer Science & Business Media, 2012.
- [11] R. Dickie *et al.*, "Polarisation independent submillimetre wave annular slot frequency selective surface," 2007.
- [12] T. A. Denidni and X.-L. Liang, "E-shaped slot-coupled dielectric resonator antenna for millimeter-wave applications," in *2009 3rd European Conference on Antennas and Propagation*, 2009, pp. 2581-2583: IEEE.
- [13] A. Rashidian and D. M. Klymyshyn, "Very low permittivity slot-fed dielectric resonator antennas with improved bandwidth for millimetre-wave applications," in

- 2009 3rd European Conference on Antennas and Propagation, 2009, pp. 3554-3557: IEEE.
- [14] A. Perron, T. A. Denidni, and A.-R. Sebak, "High-gain hybrid dielectric resonator antenna for millimeter-wave applications: Design and implementation," *IEEE transactions on Antennas and Propagation*, vol. 57, no. 10, pp. 2882-2892, 2009.
- [15] W. M. A. Wahab, D. Busuioc, and S. Safavi-Naeini, "Low cost planar waveguide technology-based dielectric resonator antenna (DRA) for millimeter-wave applications: Analysis, design, and fabrication," *IEEE Transactions on Antennas and Propagation*, vol. 58, no. 8, pp. 2499-2507, 2010.
- [16] Y. Coulibaly, M. Nedil, L. Talbi, and T. Denidni, "High gain cylindrical dielectric resonator with superstrate for broadband millimeter-wave underground mining communications," in *2010 14th International Symposium on Antenna Technology and Applied Electromagnetics & the American Electromagnetics Conference*, 2010, pp. 1-4: IEEE.
- [17] A. Rashidian, D. M. Klymyshyn, M. Tayfeh Aligodarz, M. Boerner, and J. Mohr, "Development of polymer-based dielectric resonator antennas for millimeter-wave applications," *Progress in Electromagnetics Research*, vol. 13, pp. 203-216, 2010.
- [18] Y. Coulibaly, M. Nedil, L. Talbi, and T. Denidni, "Design of a mm-wave broadband CPW-fed stacked dielectric resonator antenna for underground mining communication," in *2010 IEEE Antennas and Propagation Society International Symposium*, 2010, pp. 1-4: IEEE.
- [19] A. Agouzoul, M. Nedil, Y. Coulibaly, T. Denidni, I. B. Mabrouk, and L. Talbi, "Design of a high gain hybrid dielectric resonator antenna for millimeter-waves underground applications," in *Antennas and Propagation (APSURSI), 2011 IEEE International Symposium on*, 2011, pp. 1688-1691: IEEE.
- [20] K. K. So, H. Wong, K. B. Ng, and K. M. Luk, "Dielectric resonator antenna for millimeter wave applications," in *2011 International Workshop on Antenna Technology (iWAT)*, 2011, pp. 324-327: IEEE.
- [21] H. Singh, R. Prasad, and B. Bonev, "The Studies of Millimeter Waves at 60 GHz in Outdoor Environments for IMT Applications: A State of Art," *Wireless Personal Communications*, vol. 100, no. 2, pp. 463-474, 2018.
- [22] S.-K. Yong, P. Xia, and A. Valdes-Garcia, *60GHz Technology for Gbps WLAN and WPAN: from Theory to Practice*. John Wiley & Sons, 2011.

- [23] J. Oh, T. Baek, D. Shin, J. Rhee, and S. Nam, "60-GHz CPW-fed dielectric-resonator-above-patch (DRAP) antenna for broadband WLAN applications using micromachining technology," *Microwave and Optical Technology Letters*, vol. 49, no. 8, pp. 1859-1861, 2007.
- [24] Q. Lai, C. Fumeaux, W. Hong, and R. Vahldieck, "60 GHz aperture-coupled dielectric resonator antennas fed by a half-mode substrate integrated waveguide," *IEEE Transactions on Antennas and Propagation*, vol. 58, no. 6, pp. 1856-1864, 2010.
- [25] A. Petosa and S. Thirakoune, "Design of a 60 GHz dielectric resonator antenna with enhanced gain," in *Antennas and Propagation Society International Symposium (APSURSI), 2010 IEEE*, 2010, pp. 1-4: IEEE.
- [26] J. Guzman, C. Calvez, M. Ney, C. Person, R. Pilard, and F. Gianesello, "Mono-block dielectric resonator antenna with incorporated excitation for 60 ghz integrated systems," in *2012 6th European Conference on Antennas and Propagation (EUCAP)*, 2012, pp. 3260-3263: IEEE.
- [27] H. Chorfi, M. Nedil, Y. Coulibaly, T. A. Denidni, I. B. Mabrouk, and L. Talbi, "A dielectric resonator antenna mounted on a conformal structure at 60 GHz," in *2011 IEEE International Symposium on Antennas and Propagation (APSURSI)*, 2011, pp. 2577-2580: IEEE.
- [28] J. Guzman *et al.*, "Silicon integrated dielectric resonator antenna solution for 60GHz front-end modules," in *2012 IEEE 12th Topical Meeting on Silicon Monolithic Integrated Circuits in RF Systems*, 2012, pp. 53-56: IEEE.
- [29] Y. Hwang, Y. Zhang, K. Luk, and E. Yung, "Gain-enhanced miniaturised rectangular dielectric resonator antenna," *Electronics Letters*, vol. 33, no. 5, pp. 350-352, 1997.
- [30] K. Esselle, "Antennas with dielectric resonators and surface mounted short horns for high gain and large bandwidth," *IET Microwaves, Antennas & Propagation*, vol. 1, no. 3, pp. 723-728, 2007.
- [31] Y. M. Antar, "Antennas for wireless communication: Recent advances using dielectric resonators," *IET circuits, devices & systems*, vol. 2, no. 1, pp. 133-138, 2008.
- [32] A. Petosa, S. Thirakoune, and A. Ittipiboon, "Higher-order modes in rectangular DRAs for gain enhancement," in *Antenna Technology and Applied Electromagnetics and the Canadian Radio Science Meeting, 2009. ANTEM/URSI 2009. 13th International Symposium on*, 2009, pp. 1-4: IEEE.

- [33] A. Petosa and S. Thirakoune, "Rectangular dielectric resonator antennas with enhanced gain," *IEEE Transactions on Antennas and Propagation*, vol. 59, no. 4, pp. 1385-1389, 2011.
- [34] R. S. Yaduvanshi and H. Parthasarathy, *Rectangular dielectric resonator antennas*. Springer, 2016.
- [35] D. Guha, A. Banerjee, C. Kumar, and Y. M. Antar, "New technique to excite higher-order radiating mode in a cylindrical dielectric resonator antenna," *IEEE Antennas and Wireless Propagation Letters*, vol. 13, pp. 15-18, 2013.
- [36] M. Mrnka and Z. Raida, "Enhanced-gain dielectric resonator antenna based on the combination of higher-order modes," *IEEE Antennas and Wireless Propagation Letters*, vol. 15, pp. 710-713, 2016.
- [37] Y.-F. Wang, T. Denidni, Q.-S. Zeng, and G. Wei, "Design of high gain, broadband cylindrical dielectric resonator antenna," *Electronics Letters*, vol. 49, no. 24, pp. 1506-1507, 2013.
- [38] Y. Wang, T. A. Denidni, Q. Zeng, and G. Wei, "A wideband high-gain stacked cylindrical dielectric resonator antenna," *Progress In Electromagnetics Research*, vol. 43, pp. 155-163, 2013.
- [39] Y. Pan and S. Zheng, "A low-profile stacked dielectric resonator antenna with high-gain and wide bandwidth," *IEEE Antennas and Wireless Propagation Letters*, vol. 15, pp. 68-71, 2015.
- [40] T. Elkarkraoui, G. Y. Delisle, N. Hakem, and Y. Coulibaly, "New hybrid design for a broadband high gain 60-GHz Dielectric Resonator Antenna," in *2013 7th European Conference on Antennas and Propagation (EuCAP)*, 2013, pp. 2444-2447: IEEE.
- [41] Y. Coulibaly, M. Nedil, L. Talbi, and T. A. Denidni, "Design of high gain and broadband antennas at 60 GHz for underground communications systems," *International Journal of Antennas and Propagation*, vol. 2012, 2012.
- [42] B. Y. Toh, R. Cahill, and V. F. Fusco, "Understanding and measuring circular polarization," *IEEE Transactions on Education*, vol. 46, no. 3, pp. 313-318, 2003.
- [43] C. A. Balanis, *Antenna theory: analysis and design*. John wiley & sons, 2016.
- [44] U. Ullah, M. F. Ain, and Z. A. Ahmad, "A review of wideband circularly polarized dielectric resonator antennas," *China Communications*, vol. 14, no. 6, pp. 65-79, 2017.

- [45] S. K. K. Dash, T. Khan, and Y. M. Antar, "A state-of-art review on performance improvement of dielectric resonator antennas," *International Journal of RF and Microwave Computer-Aided Engineering*, p. e21270, 2018.
- [46] K. P. Esselle, "Circularly polarised low-profile rectangular dielectric-resonator antenna: FD-TD and experimental results," in *IEEE Antennas and Propagation Society International Symposium. 1996 Digest*, 1996, vol. 1, pp. 577-580: IEEE.
- [47] K. Leung, W. Wong, K. Luk, and E. Yung, "Circular-polarised dielectric resonator antenna excited by dual conformal strips," *Electronics Letters*, vol. 36, no. 6, pp. 484-486, 2000.
- [48] M. Lee, K. Luk, E. Yung, and K. Leung, "Microstrip-line feed circularly polarized cylindrical dielectric resonator antenna," *Microwave and Optical Technology Letters*, vol. 24, no. 3, pp. 206-207, 2000.
- [49] W. Wong and K. Leung, "Circularly polarized dielectric resonator antenna excited by dual conformal strips of unequal lengths," *Microwave and Optical Technology Letters*, vol. 29, no. 5, pp. 348-350, 2001.
- [50] R. Chair, S. L. S. Yang, A. A. Kishk, K. F. Lee, and K. M. Luk, "Aperture fed wideband circularly polarized rectangular stair shaped dielectric resonator antenna," *IEEE transactions on antennas and propagation*, vol. 54, no. 4, pp. 1350-1352, 2006.
- [51] V. Hamsakutty, A. Praveen Kumar, J. Yohannan, and K. Mathew, "Coaxial fed hexagonal dielectric resonator antenna for circular polarization," *Microwave and Optical Technology Letters*, vol. 48, no. 3, pp. 581-582, 2006.
- [52] S. S. Yang, R. Chair, A. Kishk, K. Lee, and K. Luk, "Single-feed elliptical dielectric resonator antennas for circularly polarized applications," *Microwave and Optical Technology Letters*, vol. 48, no. 11, pp. 2340-2345, 2006.
- [53] S. Khamas, "Circularly polarized dielectric resonator antenna excited by a conformal wire," *IEEE Antennas and Wireless Propagation Letters*, vol. 7, pp. 240-242, 2008.
- [54] L. Zhang, Y.-C. Jiao, and Z.-B. Weng, "Wideband circularly polarized dielectric resonator antenna with a square spiral microstrip feedline," *Progress In Electromagnetics Research*, vol. 41, pp. 11-20, 2013.
- [55] C.-C. Lin and J.-S. Sun, "Circularly polarized dielectric resonator antenna fed by off-centered microstrip line for 2.4-GHz ISM band applications," *IEEE Antennas and Wireless Propagation Letters*, vol. 14, pp. 947-949, 2014.

- [56] C.-Y. Huang, J.-Y. Wu, and K.-L. Wong, "Cross-slot-coupled microstrip antenna and dielectric resonator antenna for circular polarization," *IEEE Transactions on Antennas and Propagation*, vol. 47, no. 4, pp. 605-609, 1999.
- [57] M. Lee, K. Luk, E. Yung, and K. Leung, "Circularly polarised dielectric resonator antenna with a microstrip feed," in *1999 Asia Pacific Microwave Conference. APMC'99. Microwaves Enter the 21st Century. Conference Proceedings (Cat. No. 99TH8473)*, 1999, vol. 3, pp. 722-723: IEEE.
- [58] K. Leung and S. Mok, "Circularly polarised dielectric resonator antenna excited by perturbed annular slot with backing cavity," *Electronics Letters*, vol. 37, no. 15, pp. 934-936, 2001.
- [59] B. Li, K. So, and K. Leung, "A circularly polarized dielectric resonator antenna excited by an asymmetrical U-slot with a backing cavity," *IEEE Antennas and wireless propagation letters*, vol. 2, pp. 133-135, 2003.
- [60] S.-M. Deng and C.-L. Tsai, "A broadband slot-coupled circularly polarized rectangular notch dielectric resonator antenna fed by a microstrip line," in *2005 IEEE Antennas and Propagation Society International Symposium*, 2005, vol. 4, pp. 246-249: IEEE.
- [61] M. Zou, J. Pan, Z. Nie, and P. Li, "A wideband circularly polarized rectangular dielectric resonator antenna excited by a lumped resistively loaded monofilar-spiral-slot," *IEEE Antennas and Wireless Propagation Letters*, vol. 12, pp. 1646-1649, 2013.
- [62] Z. Zhang, X.-M. Wang, Y.-C. Jiao, and Z.-B. Weng, "Broadband circularly polarized dielectric resonator antenna with annular slot excitation," *Progress In Electromagnetics Research*, vol. 40, pp. 105-117, 2013.
- [63] M. Zhang, B. Li, and X. Lv, "Cross-slot-coupled wide dual-band circularly polarized rectangular dielectric resonator antenna," *IEEE antennas and wireless propagation letters*, vol. 13, pp. 532-535, 2014.
- [64] B. Li and K. W. Leung, "On the circularly polarized hemi-ellipsoidal dielectric resonator antenna," *Microwave and optical technology letters*, vol. 48, no. 9, pp. 1763-1766, 2006.
- [65] S. Fakhte, H. Oraizi, and R. Karimian, "A novel low-cost circularly polarized rotated stacked dielectric resonator antenna," *IEEE Antennas and Wireless Propagation Letters*, vol. 13, pp. 722-725, 2014.

- [66] A. B. Kakade and M. Kumbhar, "Wideband circularly polarized conformal strip fed three layer hemispherical dielectric resonator antenna with parasitic patch," *Microwave and Optical Technology Letters*, vol. 56, no. 1, pp. 72-77, 2014.
- [67] X. S. Fang and K. W. Leung, "Linear-/circular-polarization designs of dual-/wide-band cylindrical dielectric resonator antennas," *IEEE Transactions on Antennas and Propagation*, vol. 60, no. 6, pp. 2662-2671, 2012.
- [68] K. W. Leung and K. K. So, "Theory and experiment of the wideband two-layer hemispherical dielectric resonator antenna," *IEEE Transactions on Antennas and Propagation*, vol. 57, no. 4, pp. 1280-1284, 2009.
- [69] A. Kakade and B. Ghosh, "Analysis of the rectangular waveguide slot coupled multilayer hemispherical dielectric resonator antenna," *IET microwaves, antennas & propagation*, vol. 6, no. 3, pp. 338-347, 2012.
- [70] X. S. Fang and K. W. Leung, "Design of wideband omnidirectional two-layer transparent hemispherical dielectric resonator antenna," *IEEE Transactions on Antennas and Propagation*, vol. 62, no. 10, pp. 5353-5357, 2014.
- [71] S. Shum and K. Luk, "Numerical study of a cylindrical dielectric-resonator antenna coated with a dielectric layer," *IEE Proceedings-Microwaves, Antennas and Propagation*, vol. 142, no. 2, pp. 189-191, 1995.
- [72] W. Huang and A. Kishk, "Compact wideband multi-layer cylindrical dielectric resonator antennas," *IET Microwaves, Antennas & Propagation*, vol. 1, no. 5, pp. 998-1005, 2007.
- [73] R. K. Chaudhary, K. V. Srivastava, and A. Biswas, "Four element multilayer cylindrical dielectric resonator antenna excited by a coaxial probe for wideband applications," in *2011 National Conference on Communications (NCC)*, 2011, pp. 1-5: IEEE.
- [74] R. D. Maknikar and V. G. Kasabegoudar, "Circularly polarized cross-slot-coupled stacked dielectric resonator antenna for wireless applications," *International Journal of Wireless Communications and Mobile Computing*, vol. 1, no. 2, pp. 68-73, 2013.
- [75] Y. Sun, X. Fang, and K. W. Leung, "Wideband two-layer transparent cylindrical dielectric resonator antenna used as a light cover," in *2015 IEEE International Conference on Computational Electromagnetics*, 2015, pp. 286-287: IEEE.
- [76] R. K. Chaudhary, K. V. Srivastava, and A. Biswas, "Variation of permittivity in radial direction in concentric half-split cylindrical dielectric resonator antenna for wideband

- application," *International Journal of RF and Microwave Computer-Aided Engineering*, vol. 25, no. 4, pp. 321-329, 2015.
- [77] B. Zhang, Y.-X. Guo, H. Zirath, and Y. P. Zhang, "Investigation on 3-D-printing technologies for millimeter-wave and terahertz applications," *Proceedings of the IEEE*, vol. 105, no. 4, pp. 723-736, 2017.
- [78] S. Alkaraki *et al.*, "Compact and low-cost 3-D printed antennas metalized using spray-coating technology for 5G mm-wave communication systems," *IEEE antennas and wireless propagation letters*, vol. 17, no. 11, pp. 2051-2055, 2018.
- [79] G. Addamo *et al.*, "3-D printing of high-performance feed horns from Ku-to V-bands," *IEEE Antennas and Wireless Propagation Letters*, vol. 17, no. 11, pp. 2036-2040, 2018.
- [80] M. Liang, C. Shemelya, E. MacDonald, R. Wicker, and H. Xin, "3-D printed microwave patch antenna via fused deposition method and ultrasonic wire mesh embedding technique," *IEEE Antennas and Wireless Propagation Letters*, vol. 14, pp. 1346-1349, 2015.
- [81] Y. Li, L. Ge, M. Chen, Z. Zhang, Z. Li, and J. Wang, "Multibeam 3-D-printed Luneburg lens fed by magnetoelectric dipole antennas for millimeter-wave MIMO applications," *IEEE Transactions on Antennas and Propagation*, vol. 67, no. 5, pp. 2923-2933, 2019.
- [82] P. Nayeri *et al.*, "3D printed dielectric reflectarrays: Low-cost high-gain antennas at sub-millimeter waves," *IEEE Transactions on Antennas and Propagation*, vol. 62, no. 4, pp. 2000-2008, 2014.
- [83] J. Huang, S. J. Chen, Z. Xue, W. Withayachumnankul, and C. Fumeaux, "Impact of infill pattern on 3D printed dielectric resonator antennas," in *2018 IEEE Asia-Pacific Conference on Antennas and Propagation (APCAP)*, 2018, pp. 233-235: IEEE.
- [84] Z.-X. Xia, K. W. Leung, and K. Lu, "3-D-printed wideband multi-ring dielectric resonator antenna," *IEEE Antennas and Wireless Propagation Letters*, vol. 18, no. 10, pp. 2110-2114, 2019.
- [85] Z.-X. Xia, K. W. Leung, P. Gu, and R. Chen, "3-D-Printed Wideband High-Efficiency Dual-Frequency Antenna for Vehicular Communications," *IEEE Transactions on Vehicular Technology*, 2022.
- [86] A. Kishk, K. Lee, and C. Smith, "Wideband flipped staired pyramid dielectric resonator antennas," *Electronics Letters*, vol. 40, no. 10, p. 1, 2004.

- [87] A. A. Kishk, "Wide-band truncated tetrahedron dielectric resonator antenna excited by a coaxial probe," *IEEE Transactions on Antennas and Propagation*, vol. 51, no. 10, pp. 2913-2917, 2003.
- [88] C.-E. Zebiri *et al.*, "Offset aperture-coupled double-cylinder dielectric resonator antenna with extended wideband," *IEEE Transactions on Antennas and Propagation*, vol. 65, no. 10, pp. 5617-5622, 2017.
- [89] R. K. Chaudhary, K. V. Srivastava, and A. Biswas, "A practical approach: design of wideband cylindrical dielectric resonator antenna with permittivity variation in axial direction and its fabrication using microwave laminates," *Microwave and Optical Technology Letters*, vol. 55, no. 10, pp. 2282-2288, 2013.
- [90] A. A. Kishk, Y. Yin, and A. W. Glisson, "Conical dielectric resonator antennas for wide-band applications," *IEEE Transactions on Antennas and Propagation*, vol. 50, no. 4, pp. 469-474, 2002.
- [91] J.-P. Kruth, M.-C. Leu, and T. Nakagawa, "Progress in additive manufacturing and rapid prototyping," *Cirp Annals*, vol. 47, no. 2, pp. 525-540, 1998.
- [92] C. A. Balanis, "Antenna theory analysis and design, A JOHN WILEY & SONS," *Inc., Publication*, vol. 811, 2005.
- [93] S. S. Gao, Q. Luo, and F. Zhu, *Circularly polarized antennas*. John Wiley & Sons, 2013.
- [94] H. Yi and K. Boyle, "Antennas: from theory to practice," *A John Wiley and Sons, Ltd, Publication*, pp. 263-272, 2008.
- [95] A. A. Abdulmajid and S. Khamas, "Higher Order Mode Layered Cylindrical Dielectric Resonator Antenna," *Progress In Electromagnetics Research*, vol. 90, pp. 65-77, 2019.
- [96] Z. Qian, K. W. Leung, and R.-S. Chen, "Analysis of circularly polarized dielectric resonator antenna excited by a spiral slot," *Progress In Electromagnetics Research*, vol. 47, pp. 111-121, 2004.
- [97] M. Zou, J. Pan, and Z. Nie, "A wideband circularly polarized rectangular dielectric resonator antenna excited by an archimedean spiral slot," *IEEE Antennas and Wireless Propagation Letters*, vol. 14, pp. 446-449, 2014.
- [98] A. Kapoor and G. Singh, "Mode classification in cylindrical dielectric waveguides," *Journal of lightwave technology*, vol. 18, no. 6, pp. 849-852, 2000.

- [99] R. De Smedt, "Correction due to a finite permittivity for a ring resonator in free space," *IEEE transactions on microwave theory and techniques*, vol. 32, no. 10, pp. 1288-1293, 1984.
- [100] M. Studio, "Computer simulation technology (CST)," *Online: www.cst.com*, vol. 124, 2015.
- [101] S. K. Khamas and G. G. Cook, "Moment-method analysis of printed wire spirals using curved piecewise sinusoidal subdomain basis and testing functions," *IEEE Transactions on Antennas and Propagation*, vol. 45, no. 6, pp. 1016-1022, 1997.
- [102] P. b. K. Sharma and J. T. Bernhard, "Analysis of Archimedean Spiral Slot Antennas in Infinite Ground Planes Using the Theory of Characteristic Modes," *IEEE Access*, 2022.
- [103] A. Kesavan, M. a. Al-Hassan, I. Ben Mabrouk, and T. A. Denidni, "Wideband circular polarized dielectric resonator antenna array for millimeter-wave applications," *Sensors*, vol. 21, no. 11, p. 3614, 2021.
- [104] W. H. Kummer and E. S. Gillespie, "Antenna measurements—1978," *Proceedings of the IEEE*, vol. 66, no. 4, pp. 483-507, 1978.
- [105] B. Rana and C. K. Ghosh, "High gain circularly polarized rectangular dielectric resonator antenna array with helical-like exciter," *Progress In Electromagnetics Research*, vol. 46, pp. 95-100, 2014.
- [106] S. Gupta, A. Sharma, G. Das, R. K. Gangwar, and M. Khalily, "Wideband circularly polarized dielectric resonator antenna array with polarization diversity," *IEEE Access*, vol. 7, pp. 49069-49076, 2019.
- [107] L. Usha and K. Krishnamoorthy, "Linearly Polarized and Circularly Polarized Cylindrical Dielectric Resonator Antenna," *Progress In Electromagnetics Research Letters*, vol. 102, pp. 57-65, 2022.
- [108] R. K. Gangwar, S. Singh, and D. Kumar, "Comparative studies of rectangular dielectric resonator antenna with probe and microstrip line feeds," *Archives of applied science research*, vol. 2, no. 3, pp. 1-10, 2010.
- [109] A. Petosa, *Dielectric resonator antenna handbook*. Artech House Publishers, 2007.
- [110] R. S. Yaduvanshi and G. Varshney, *Nano Dielectric Resonator Antennas for 5G Applications*. CRC Press, 2020.
- [111] A. A. Abdulmajid, S. Khamas, and S. Zhang, "Wide Bandwidth High Gain Circularly Polarized Millimetre-Wave Rectangular Dielectric Resonator Antenna," *Progress In Electromagnetics Research*, vol. 89, pp. 171-177, 2020.

- [112] A. Sharma, K. Khare, and S. Shrivastava, "Simple and Enhanced Gain Dielectric Resonator Antenna for ku band Application," *International Journal of Scientific & Engineering Research*, vol. 4, no. 9, pp. 1066-1070, 2013.
- [113] A. Abumazwed, "Broadband dielectric resonator antennas for WLAN applications," Concordia University, 2009.
- [114] K. L. Wong and N. C. Chen, "Analysis of a broadband hemispherical dielectric resonator antenna with a dielectric coating," *Microwave and Optical Technology Letters*, vol. 7, no. 2, pp. 73-76, 1994.
- [115] N. C. Chen, H. C. Su, K. L. Wong, and K. W. Leung, "Analysis of a broadband slot-coupled dielectric-coated hemispherical dielectric resonator antenna," *Microwave and Optical Technology Letters*, vol. 8, no. 1, pp. 13-16, 1995.
- [116] H. Chu and Y.-X. Guo, "A novel approach for millimeter-wave dielectric resonator antenna array designs by using the substrate integrated technology," *IEEE Transactions on Antennas and Propagation*, vol. 65, no. 2, pp. 909-914, 2016.
- [117] M. Niayesh and A. Kouki, "LTCC-integrated dielectric resonant antenna array for 5G applications," *Sensors*, vol. 21, no. 11, p. 3801, 2021.
- [118] Y. Chen, X. Yuqi, and K. W. Leung, "A 3D-Printed Wideband Multilayered Cylindrical Dielectric Resonator Antenna With Air Layers," in *2020 IEEE Asia-Pacific Microwave Conference (APMC)*, 2020, pp. 561-563: IEEE.
- [119] M. Liang, W.-R. Ng, K. Chang, K. Gbele, M. E. Gehm, and H. Xin, "A 3-D Luneburg lens antenna fabricated by polymer jetting rapid prototyping," *IEEE Transactions on Antennas and Propagation*, vol. 62, no. 4, pp. 1799-1807, 2014.
- [120] Z.-X. Xia and K. W. Leung, "3D-printed Wideband Rectangular Dielectric Resonator Antenna," in *2019 Photonics & Electromagnetics Research Symposium-Fall (PIERS-Fall)*, 2019, pp. 285-289: IEEE.
- [121] H. Ng and K. Leung, "Circular-polarized hemispherical dielectric resonator antenna excited by dual conformal-strip," in *IEEE Antennas and Propagation Society International Symposium (IEEE Cat. No. 02CH37313)*, 2002, vol. 3, pp. 442-445: IEEE.
- [122] R. K. Chaudhary, R. Kumar, and R. Chowdhury, *Circularly Polarized Dielectric Resonator Antennas*. Artech, 2021.
- [123] G. A. Sarkar, S. Ballav, A. Chatterjee, S. Ranjit, and S. K. Parui, "Four element MIMO DRA with high isolation for WLAN applications," *Progress In Electromagnetics Research Letters*, vol. 84, pp. 99-106, 2019.

- [124] N. M. Nor, M. H. Jamaluddin, M. R. Kamarudin, and M. Khalily, "Rectangular dielectric resonator antenna array for 28 GHz applications," *Progress In Electromagnetics Research*, vol. 63, pp. 53-61, 2016.
- [125] A. A. Abdulmajid, S. Khamas, and S. Zhang, "Wideband high-gain millimetre-wave three-layer hemispherical dielectric resonator antenna," *Progress In Electromagnetics Research*, vol. 103, pp. 225-236, 2020.
- [126] A. A. Abdulmajid, Y. Khalil, and S. Khamas, "Higher-Order-Mode Circularly Polarized Two-Layer Rectangular Dielectric Resonator Antenna," *IEEE Antennas and Wireless Propagation Letters*, vol. 17, no. 6, pp. 1114-1117, 2018.
- [127] A. B. Kakade and B. Ghosh, "Mode excitation in the coaxial probe coupled three-layer hemispherical dielectric resonator antenna," *IEEE Transactions on Antennas and Propagation*, vol. 59, no. 12, pp. 4463-4469, 2011.
- [128] B. Ghosh and A. B. Kakade, "Mode excitation in the microstrip slot-coupled three-layer hemispherical dielectric resonator antenna," *IET Microwaves, Antennas & Propagation*, vol. 10, no. 14, pp. 1534-1540, 2016.
- [129] R. Khan, "MultiBand-Rectangular Dielectric Resonator Antenna (M-RDRA)," 2014.
- [130] R. Lan, "Dielectric Resonator Antenna on Printed Circuit Board," Queen's University (Canada), 2019.
- [131] M. O. Sallam *et al.*, "Micromachined on-chip dielectric resonator antenna operating at 60 GHz," *IEEE Transactions on Antennas and Propagation*, vol. 63, no. 8, pp. 3410-3416, 2015.
- [132] K. M. Luk and K. W. Leung, "Dielectric resonator antennas," Research studies press 2003.
- [133] C. J. Wang, "A CPW-fed wideband spiral slot antenna with circular polarization," *Microwave and Optical Technology Letters*, vol. 52, no. 5, pp. 1204-1208, 2010.
- [134] Y.-X. Sun and K. W. Leung, "Circularly Polarized Substrate-Integrated Cylindrical Dielectric Resonator Antenna Array for 60 GHz Applications," *IEEE Antennas and Wireless Propagation Letters*, vol. 17, no. 8, pp. 1401-1405, 2018.
- [135] T.-Y. Lin, Y.-C. Chang, C. H. Chang, D.-C. Chang, and T. Chiu, "A 60 GHz High-Gain Circularly Polarized Dielectric Resonator Antenna Array Using Bondwire Feeding Structure," in *2018 IEEE CPMT Symposium Japan (ICSJ)*, 2018, pp. 121-122: IEEE.